THE COMPOSITION, VERTICAL STRUCTURE AND GLOBAL VARIABILITY OF THE LOWER CLOUD DECK ON VENUS AS DETERMINED BY RADIO OCCULTATION TECHNIQUES

Thesis by

Josephine Beatrice Cimino

In Partial Fulfillment of the Requirements

for the Degree of

Doctor of Philosophy

California Institute of Technology

Pasadena, California

1982

(submitted 15 October 1981)

To my Father,

for his birthday

ACKNOWLEDGMENTS

It is with great pleasure that I acknowledge the many people who assisted in the production of this thesis and contributed to my overall experience in the field of Planetary Science. I am particularly grateful to Dr. Duane Muhleman, my thesis advisor, for his guidance, valuable criticism and basic belief in the power of the radio occultation technique. I have gained not only from his knowledge of the basic principles governing radio science, but from his careful and precise methods for analyzing and interpreting data.

I am also grateful to Dr. Andrew Ingersoll, my academic advisor, for his guidance in understanding the whole picture of a planetary atmosphere and for his positive outlook in the wake of much criticism. I would also like to thank Dr. Yuk Yung for providing a link to the chemical aspects of atmospheric research, for providing many thoughts on the Venus cloud system and for introducing me to Van de Hulst, to whom I am also indebted for including a small section on the polarization of spherical shells in his famous book.

Without the Pioneer Venus and Mariner 10 data provided by Dr. Arvydas Kliore, this thesis would not have been possible. His generosity with the data and his time go beyond the call of duty. I would also like to thank Dr. Charles Elachi for his continuous support, optimism and friendship. I would particularly like to acknowledge Dr. Elachi for providing the original idea and incentive for this thesis. I am grateful to Dr. Fred Shair for providing a valuable understanding of chemical engineering and for his much welcomed positive attitude.

I am additionally indebted to many people outside of Caltech. Dr. William Ho, Dr. William Hall and Dr. Dwight Landis at Rockwell Science Center have not only contributed excellent dielectric constant data, but have provided invaluable discussions on the properties of dielectrics. Indu Patel has provided

endless hours of data processing and I am particularly grateful for his cheerful attitude no matter how extravagant or rushed the request. Drs. Mike Janssen and Robert Poynter were extremely helpful in calculating sulfuric acid absorption coefficients. Dave Tristram and John Cowley at Pioneer Missions at Ames have been extremely helpful in providing trajectory data and command tables. Dr. Thomas Jukes and Dr. Richard Holmquist at Berkeley provided the original incentive to attend Caltech, have always shown much appreciated interest in my work and my future and have offered invaluable friendship. I would also like to thank Mr. Kenneth Carroll for his inspiration in high school and throughout my career.

I am forever indebted to Donna Lathrop for her time and talents in producing a final version of this thesis which looks so good it has to be right. I would also like to thank Kay Campbell for for her assistance in the many administrative details required to complete a thesis.

The completion of this work would not have been possible without the immeasurable support and encouragement of my family and friends. I would like to especially thank my parents and my sisters for the love, laughter, confidence and especially their understanding. I would like to thank my husband, Jim for teaching me how to express my thoughts on paper and for helping me through the many rough spots encountered in doing this thesis. Without him I would have been done two years ago. I would like to thank my friends Ed and Theresa Fall and Mike Kobrick for very special friendships, encouragement, distractions and for the care and feeding of my husband through the final months of this thesis, and Rick Lewis and Chuck Douthitt for all the baked beans and bunnies. And I would like to thank my fellow graduate students for their interest, assistance and for answering the telephone. Finally I would like to thank my godchild, Erin, for waiting until I was finished to arrive.

This research was funded by Grant NAS7-100 sponsored by the Planetary Atmospheres Program Office, Office of Space Sciences, National Aeronautics and Space Administration.

ABSTRACT

The opportunity to determine the planetwide temperature and cloud structure of Venus using radio occultation techniques arose with Pioneer Venus. This orbiting spacecraft contained a dual frequency radio system which was used to collect radio occultation data for more than two years.

Amplitude and Doppler data provided by the radio occultation experiment provide a unique and powerful means of examining atmospheric properties in a region of Venus which may otherwise be observed only by means of a probe.

The extraction of atmospheric properties from the received occultation data is a complicated non-linear process for which careful account of all contributing uncertainties must be taken. Such atmospheric phenomena as turbulence, oblateness due to winds, perturbations in the temperature, atmospheric density or gaseous composition affect both the Doppler and the amplitude data. Uncertainties inherent in the experiment itself and the data collection and processing procedures, such as trajectory errors, fluctuations in the power profile, averaging of the data and spacecraft wobble, result in additional uncertainties which must be considered.

Absorption coefficient and temperature profiles were analyzed in detail for the effects of major sources of uncertainty. Inasmuch as the power loss due to refractive defocussing is determined from the Doppler data, uncertainties in the refractivity as well as the received power are considered. Power fluctuations are found to produce the greatest uncertainty in the S-band absorption coefficient profiles. Power fluctuations and spacecraft wobble contribute the greatest uncertainty to the X-band data. In fact, in many cases the spacecraft wobble has rendered the X-band data useless.

Absorption due to gaseous components of the atmosphere are subtracted from the measured absorption coefficient profiles before they are used to compute cloud mass contents. The H_2O mixing ratio profile used is that measured by the Venera 11 and 12 spectrophotometers. The SO_2 profile was determined from the Venera 11 and 12 and Pioneer probe gas chromatograph and mass spectrometer results. The sulfuric acid saturation vapor mixing ratio used is the equilibrium vapor pressure above a concentrated sulfuric acid-water solution at the temperatures of the lower cloud deck.

The absorption due to the gaseous components is found to represent a small part of the total absorption. In the main cloud deck, gaseous absorption contributes 10 to 20% and at the bottom of the detected absorption layer the sulfuric acid vapor contributes 60 to 100% to the absorption due to increased acid vapor pressures resulting from higher temperatures in this region. The clouds are the primary contributing absorbers in the 1 to 3 bar level of the Venus atmosphere. Below about 3 bars, absorption due to sulfuric acid vapor dominates.

As a first attempt, mass content profiles were produced from the absorption coefficient data assuming the clouds were composed of concentrated sulfuric acid-water liquid. The resulting mass contents were on the order of several grams per cubic meter. Although planetwide variability in the lower cloud deck may account for differences in these radio occultation mass contents and those determined by the Pioneer probes, a second factor discounting purely liquid clouds has arisen. The dielectric constants of liquid sulfuric acid were measured in the laboratory at S-and X-band wavelengths and the results suggest the wavelength dependence for absorption by the liquid is $1/\lambda^2$. The wavelength dependence measured by the radio occultation experiment is about $1/\lambda^{1.2}$. In addition, the wavelength dependence required to fit the opacity determined from the 1.35 cm microwave emission data is $1/\lambda^{1.2}$ to $1/\lambda^{1.5}$. Apparently the liquid sulfuric acid droplet model does not satisfy the observed wavelength dependence or mass content.

If, however, a cloud particle model consisting of a solid non-absorbing dielectric sphere with a concentric liquid sulfuric acid coating is invoked, the absorptivity of the particles increases and the mass content derived from the absorption coefficient profiles decreases. As the ratio of the core radius to the total radius (q) increases, absorption increases by more than a factor of 10 for high values of q. In the case of pure sulfuric acid droplets, the conductivity is sufficiently high that some of the field is excluded from the interior of the droplet thereby reducing the absorption. When a dielectric core of non-absorbing material is introduced, two effects occur which contribute to the increase in the electric field which penetrates the drop. First, the relative volume filled by sulfuric acid decreases and the number of available free charges decreases. Second, the dielectric core, which is also polarized in the presence of the electric field, affects the arrangement of the free charges by attracting them to the inner surface and by acting as a barrier in the presence of the rapidly alternating electric field.

The mass contents for all orbits in the equatorial region of Venus are calculated using values of q of from 0 to 1. The resulting profiles match the probe mass content profiles at similar locations when a q of 0.98 is chosen. Values for q of 0.97 to 0.99 change the absorptivity of the cloud particles by as much as 50%.

The wavelength dependence of the absorption for the spherical shell model varies with q from $1/\lambda^2$ for pure liquid to $\lambda^{0.2}$ for a large core. A q of 0.98 results in a wavelength dependence of $1/\lambda^{1.0}$ to $1/\lambda^{1.4}$ which matches the radio

occultation absorption wavelength dependence and the microwave opacity wavelength dependence.

Mass content profiles using a q of 0.98 were determined for occultations in the polar, collar, midlatitudinal and equatorial regions assuming q remains constant over the planet. The results show considerable variability in both the level and the magnitude of the lower cloud deck. The cloud layer is lowest in altitude in the polar region. This might be expected as the temperature profile is cooler in the polar region than over the rest of the planet. The mass content is greatest in the polar and collar regions; however, many of the collar profiles are cut off due to fluctuations resulting from increased turbulence in the collar region. The mass contents are least dense in the midlatitude regions.

These results support the value of using radio occultation techniques to obtain temporal and spatial coverage of the planet Venus in terms of cloud composition and mass content.

TABLE OF CONTENTS

LIST OF FIGURES

LIST OF TABLES

CHAPTER I

INTRODUCTION

The most outstanding feature of the planet Venus is its cloud covering. The most frustrating aspect of studying Venus is that it is difficult, if not impossible, to sense anything below the uppermost layer of the cloud cover. Excluding the insertion of a probe into the lower Venus atmosphere, which is limited in spatial and temporal coverage, the only means of examining the atmospheric properties below the upper cloud layer is by radio occultation techniques. From the amplitude and Doppler data of a signal which has been refracted by the dense Venus atmosphere, temperature, pressure, atmospheric density, cloud mass content and some knowledge of the cloud composition may be determined. These make up a complete set of parameters necessary to study atmospheric structure and dynamics. If the spacecraft is orbiting, the entire planet may be probed over long periods of time. Temporal and spatial variations in the temperature and cloud structure are obtained as a result.

The extraction of these atmospheric properties from the Doppler and amplitude data is a complicated non-linear process for which careful account of all contributing uncertainties must be taken. Such atmospheric phenomena as turbulence, oblateness due to winds, perturbations in the temperature, atmospheric density or gaseous composition of the atmosphere affect both the Doppler and the amplitude data. Uncertainties inherent in the experiment itself and the data collection and processing procedures such as trajectory errors, fluctuations in the power profile, averaging of the data and spacecraft wobble result in additional uncertainties which must be considered.

Once all uncertainties have been taken into account, temperature and absorption coefficient profiles at each occultation location may be derived. From the absorption coefficient profiles, mass content profiles may be determined for a proposed cloud material. The proposed cloud material is likely to be correct if the mass content profiles at the locations of measured probe mass content profiles are consistent. If absorption data for more than one wavelength are available, the absorption wavelength dependence of the proposed cloud material must match that of the measured absorption. Finally, the wavelength dependence must be consistent with opacities determined by Earth-based microwave emission measurements.

The opportunity to determine the planetwide temperature and cloud structure arose with Pioneer Venus. This orbiting spacecraft contained a dual frequency radio system which has been used to collect radio occultation data for more than two years. The primary goals of this thesis are to determine the uncertainties inherent in the absorption coefficient profiles derived from the radio occultation experiment and use the resulting profiles to determine the mass content and composition of the Venusian lower cloud deck.

Before Pioneer Venus, all available information about the Venus atmosphere and cloud system was based on Earth-based measurements, the Venera results, the Mariner 5 flyby and the Mariner 10 flyby. The results of Earth based observations suggested the cloud tops were featureless at visible and infrared wavelengths, however ultraviolet contrasts were apparent. From the UV contrasts, cloud motions and morphological changes were observed and a four day cloud top circulation was determined. The microphysics of the upper cloud tops were determined by polarimetry (Hansen and Hovenier, 1974). The cloud particles were determined to be monodispersed spherical droplets with an index of refraction of 1.44 ± 0.01 and a radius of 1.05 μ with a variation of 0.07. Sill (1972), Pollack et al (1974) and Young (1973) proposed hydrated sulfuric acid as a likely candidate for the cloud particles based on these observations. In addition, very little water vapor was detected in the Venus atmosphere; again hydrated sulfuric acid cloud particles were a promising candidate as the vapor pressure above such particles is extremely low at the temperatures of the upper clouds. Venera 9 and 10 supported this proposed cloud composition to several optical depths. Enhanced backscatter detected by Venera 9 and 10 at lower attitudes suggested an increase in the cloud liquid content or a change in composition.

The lower cloud of Venus was first observed by the Mariner 10 radio occultation experiment. A region of increased absorption was interpreted as a cloud of dense mass content assuming the particle were concentrated liquid sulfuric acid (Kliore et al, 1979).

The goal of the Pioneer Venus mission was to determine the cloud properties in the lower levels of the atmosphere and observe global variations in the cloud properties at the cloud tops. In order to accomplish this goal, four probes and an orbiter were sent to Venus. The Sounder probe contained a nephelometer, a Particle Size Spectrometer (LCPS), a mass spectrometer and a gas chromatograph which could be used to directly observe the properties of the clouds and associated atmospheric chemistry. The three small probes contained only nephelometers. The nephelometers detected the 175° backscatter cross-section as a function of altitude. The LCPS counted particles in different size bins. Particles in the size range of 0.5 to 5 μ were detected using single particle scattering techniques and particles in the size range from 5 to 500 μ were detected using shadow graph imaging. In addition, aspect ratios for particles greater than 50 μ could be determined.

The results of the nephelometer experiment are shown in Figure 1 and the results of the LCPS experiment are shown in Figure 2. Table I summarizes the results. The upper cloud extends from above 70 km, where the instruments began operating, to 56 km. The backscatter is variable and weak. A bimodal particle distribution was observed by the LCPS with a maximum density at about

Figure 1. Nephelometer results (Ragent and Blamont, 1980)

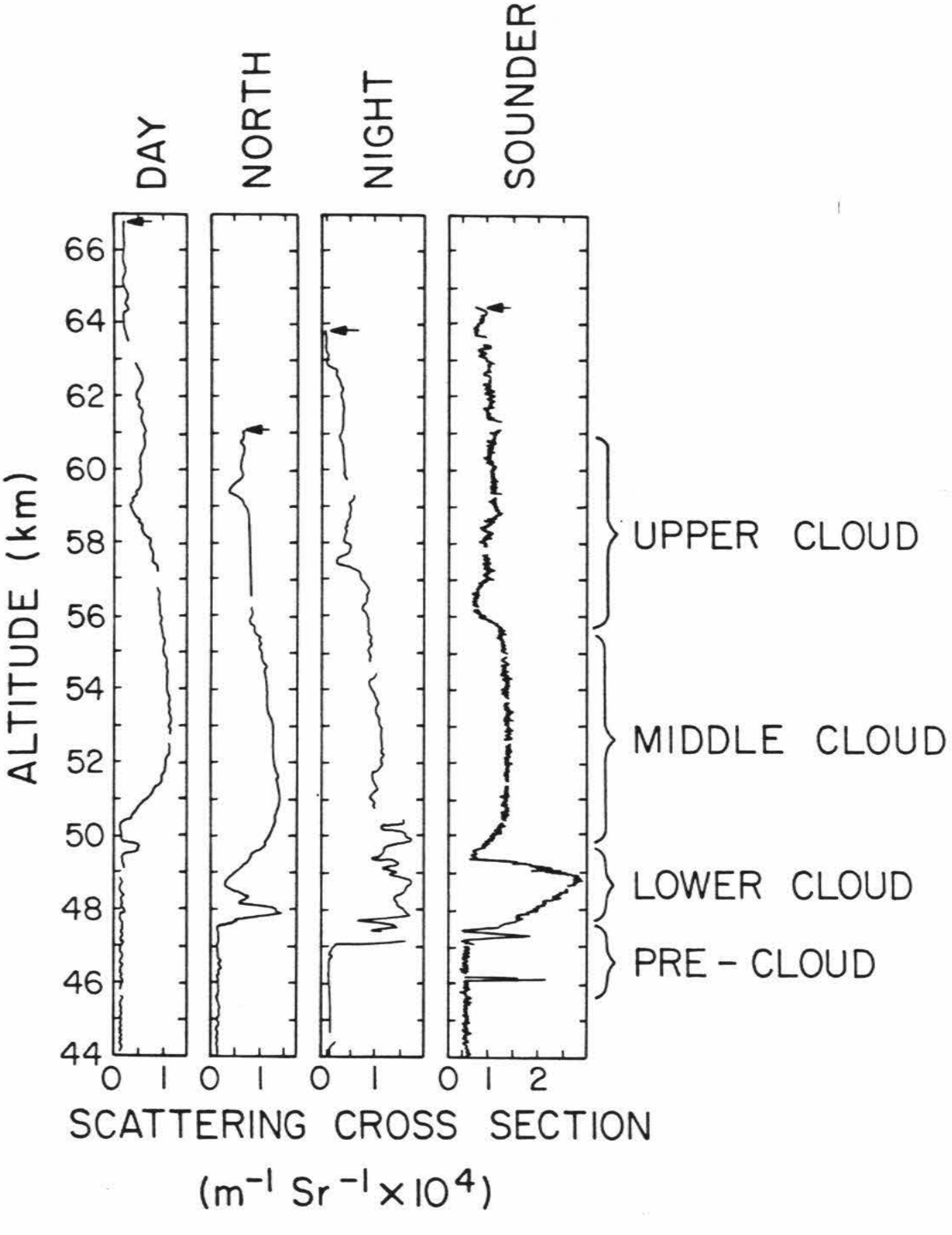
DAY
NORTH
NIGHT
SOUNDER
ALTITUDE (km)
44
46
48
50
52
54
56
58
60
62
64
66
0 1
0 1
0 1
0 1 2
SCATTERING CROSS SECTION
(m^{-1} Sr^{-1} × 10^4)
UPPER CLOUD
MIDDLE CLOUD
LOWER CLOUD
PRE - CLOUD

Figure 2. Particle Size Spectrometer results (Knollenberg and Hunten, 1980)

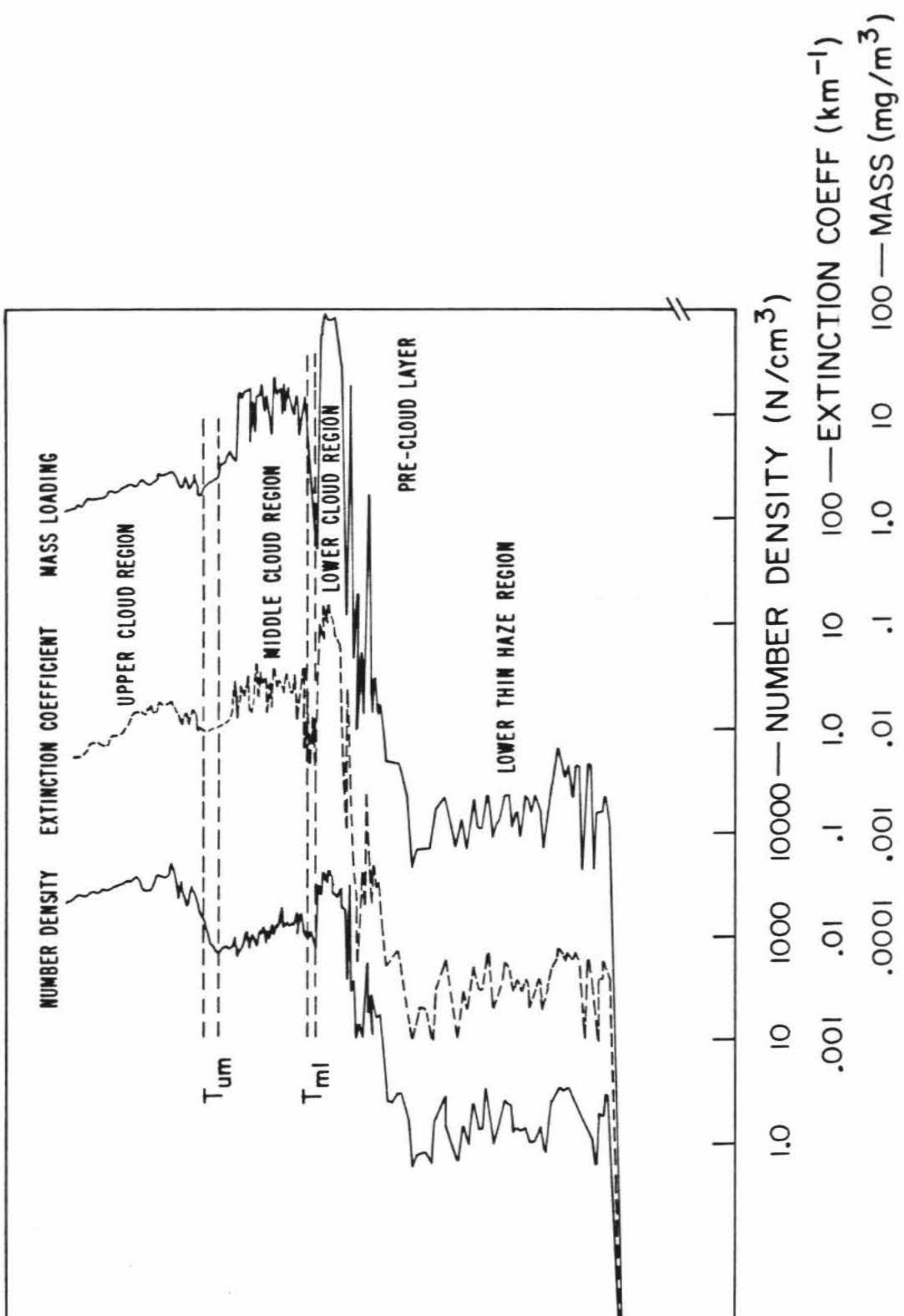
NUMBER DENSITY
EXTINCTION COEFFICIENT
MASS LOADING
UPPER CLOUD REGION
MIDDLE CLOUD REGION
LOWER CLOUD REGION
PRE-CLOUD LAYER
LOWER THIN HAZE REGION
T_{um}
T_{ml}
ALTITUDE (km)
68
64
60
52
48
44
40
36
32
28
2
0
1.0
10
1000
10000 — NUMBER DENSITY (N/cm^3)
.001
.01
.1
1.0
10
100 — EXTINCTION COEFF (km^{-1})
.0001
.001
.01
.1
1.0
10
100 — MASS (mg/m^3)

60 km. At about 56 km, a decrease in the cloud mass content was observed (T_{um}) by both the nephelometer and the LCPS. The mode 1 and mode 2 particles are depleted at this level. Just below T_{um}, the mode 2 particles increase in diameter from 2.1.ps 10 μ to 2.7 μ.

The middle cloud region extends to 50 km in altitude. The backscatter signal is stronger, however the number density has decreased. The cloud in this region contains a trimodal particle distribution. The smallest mode remains depleted and mode 3 appears with the number densities of both mode 2 and mode 3 increasing with depth.

Table I
SUMMARY OF CLOUD PROPERTIES

Region	Altitude	T (K)	Average N (cm^{-3})	Mean Diam (μ)	Composition
Upper Cloud	56.5-70.	286-225	(1) 1500 (2) 50	Bimodal 0.4 and 2.0	H_2SO_4 + ?
Middle Cloud	50.5-56.5	345-286	(1) 300 (2) 50 (3) 10	Trimodal 0.3, 2.5, 7.0	H_2SO_4 + ? + crystals
Lower Cloud	47.5-50.5	367-345	(1) 1200 (2) 50 (3) 50	Trimodal 0.4, 2.0, 8.0	H_2SO_4 + ? + crystals
Lower Haze	31.-47.5	482-367	2-20	0.2	H_2SO_4 + ?
Precloud Layers	46 and 47.5	378 and 367	50 and 150	Bimodal 0.3 and 2.0	H_2SO_4 + ?

At 50 km, another discontinuity in the cloud structure, T_{ul}, appears. Below T_{ml}, mode 3 increases in number density and size. This lower cloud deck contains the greatest mass and largest backscatter cross-section, except at the Day probe location. Below the lower cloud deck are two pre-cloud layers. The smallest mode extends below the lower cloud deck to about 31 km.

Optical properties of the clouds were determined by calculating the backscatter cross-sections of the clouds from the LCPS particle distributions assuming an index of refraction. When the calculated backscatter cross-section matched that measured by the nephelometer, it was assumed the correct index of refraction had been chosen. The index of refraction for the mode 2 particles was determined to be 1.44 throughout the cloud layers. The mode 1 particles are probably also sulfuric acid. The index of refraction of the lower cloud layer mode 3 particles was determined to be 1.2 to 1.3. This index does not fit any known liquid or solid. The index may be increased if the mode 3 particles have a reduced probability of scattering in the backward direction. This will occur for four possible types of cloud particles (Knollenberg and Hunten, 1980) including absorbing, irregularly shaped, composite (clusters) and diffusely scattering particles (entrained smaller particles). Ragent and Blamont (1980) favor absorbing particles however this disagrees with the solar flux radiometer results which observe a constant flux and therefore conservative scattering (Tomasko, 1980). Knollenberg and Hunten (1980) favor irregularly shaped particles and suggest the mode 3 particles are solid. As will be seen, this author favors entrained smaller particles.

Additional inputs into the properties of the cloud particles are the results of the mass spectrometer and gas chromatograph (Hoffman et al, 1980 a and b and Oyama et al, 1980, respectively). Several gases were detected including H_2O, SO_2 and N_2. The gas chromatograph inlet was clogged while passing through the lower cloud layers and products of concentrated sulfuric acid solutions were observed when the clog evaporated. The Venera 11 and 12 spacecraft also carried a spectrophotometer (Maroz, 1980) which detected water vapor. The mixing ratio determined by this instrument was lower than that detected by the Pioneer mass spectrometer and gas chromatograph experiments, however it is believed the spectrophotometer results are superior. A final input into the chemistry of the lower cloud deck was made by Surkov (1980) on Venera 11 and 12. The atmosphere and clouds were sampled through an open inlet throughout the cloud region. The collected sample was measured by X-ray fluorescence techniques and the results showed a Cl/S ratio of 10 to 1.

These results as well as many others will be incorporated into the work presented here in an effort to understand the composition of the lower cloud region on Venus.

CHAPTER II

EXPERIMENT DESCRIPTION

The temperature and absorption coefficient data used in this thesis were obtained primarily from the Pioneer Venus Orbiter Radio Occultation Experiment. A detailed discussion of the Pioneer Venus experiment is presented in this chapter along with a map describing the planetary coverage thus far obtained.

The basic techniques used to analyze the data, however, were initially developed using the Mariner 10 Radio Occultation data, which are also included in this thesis. A brief description of the Mariner 10 experiment, along with a detailed discussion of several problems that arose after initial publication of the results, is presented in this chapter.

1. Pioneer Venus

The Pioneer Venus spacecraft has been orbiting Venus every 24 hours since December 4, 1978. The orbit is near polar and highly eccentric with an apoapsis altitude of about 66,900 km and a periapsis altitude of from 140 to 260 km (see Figure 3). When the geometry is such that the spacecraft is occulted by Venus, two occultation measurements, entry and exit, are obtained with each orbit. This occurred for the first 71 orbits during the first occultation season. As of November, 1981, approximately 290 orbits have provided data resulting in a possible 580 occultation profiles (see Table II). Approximately half of the available occultations thus far processed have provided useful data; the others are not useful due to operational problems.

Figure 3. Geometry of the orbit and periapsis altitude as a function of time (from Colin, 1980)

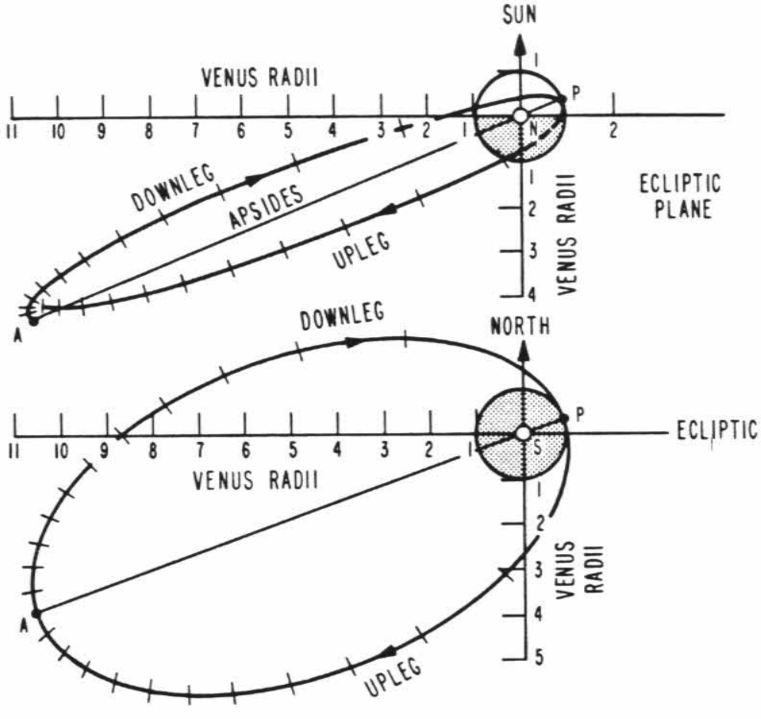
SUN
VENUS RADII
11 10 9 8 7 6 5 4 3 2 1
1 2
P
N
DOWNLEG
APSIDES
UPLEG
ECLIPTIC PLANE
1 2 3 4
VENUS RADII
A
DOWNLEG
NORTH
P
ECLIPTIC
11 10 9 8 7 6 5 4 3 2 1
S
VENUS RADII
1 2 3 4 5
VENUS RADII
A
UPLEG

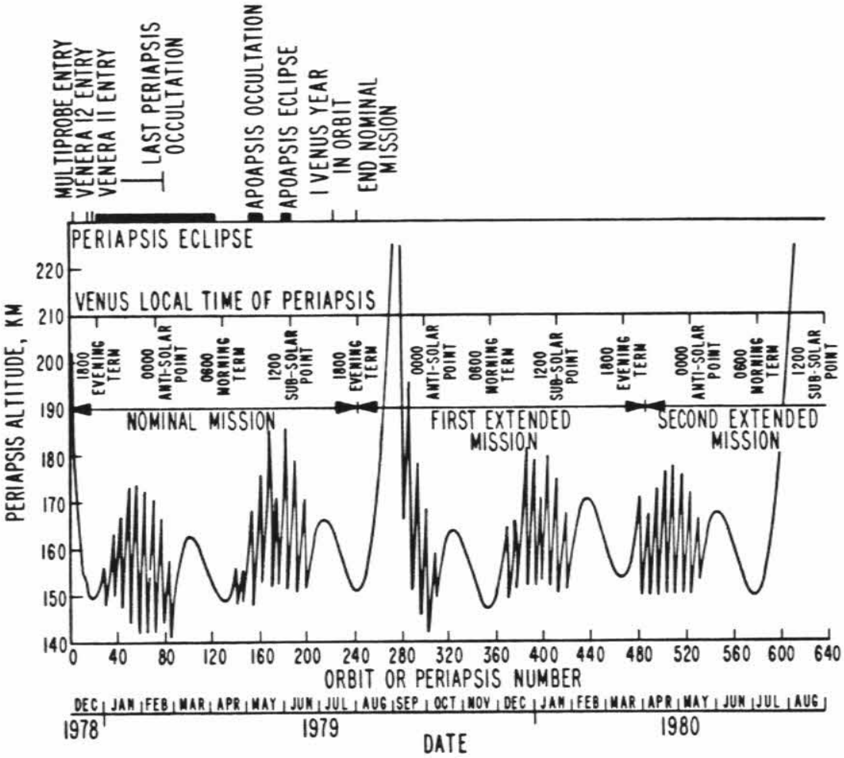
MULTIPROBE ENTRY
VENERA 12 ENTRY
VENERA 11 ENTRY
LAST PERIAPSIS OCCULTATION
APOAPSIS OCCULTATION
APOAPSIS ECLIPSE
1 VENUS YEAR IN ORBIT
END NOMINAL MISSION
PERIAPSIS ECLIPSE
VENUS LOCAL TIME OF PERIAPSIS
1800 EVENING TERM
0000 ANTI-SOLAR POINT
0600 MORNING TERM
1200 SUB-SOLAR POINT
1800 EVENING TERM
0000 ANTI-SOLAR POINT
0600 MORNING TERM
1200 SUB-SOLAR POINT
1800 EVENING TERM
0000 ANTI-SOLAR POINT
0600 MORNING TERM
1200 SUB-SOLAR POINT
NOMINAL MISSION
FIRST EXTENDED MISSION
SECOND EXTENDED MISSION
PERIAPSIS ALTITUDE, KM
140 150 160 170 180 190 200 210 220
0 40 80 120 160 200 240 280 320 360 400 440 480 520 560 600 640
ORBIT OR PERIAPSIS NUMBER
DEC JAN FEB MAR APR MAY JUN JUL AUG SEP OCT NOV DEC JAN FEB MAR APR MAY JUN JUL AUG
1978 1979 1980
DATE

Table II

Dates of Occultation Season

Occultation Season	Dates	Orbits	Total Orbits
1	12/78 - 2/79	1 - 71	71
2	10/79 - 12/79	305 - 379	75
3	9/80 - 10/80	657 - 691	35
4	7/81 - 11/81	955 - 1063	109

The Pioneer Venus spacecraft is spin stabilized with its spin axis approximately normal to the plane of the ecliptic (see Figure 4). The spin rate is about 5 revolutions per minute. The high gain radio antenna used in the occultation experiments is despun and steerable through a preprogrammed series of antenna slews designed to counteract bending of the radio beam away from the virtual position of Earth.

The radio system includes an S-band (2111 MHz, 14.21 cm) receiver which provides a phase coherent output to drive two transmitters, one operating at S-band (2293 MHz, 13.08 cm) and one at X-band (8408 MHz, 3.57 cm). These two signals are simultaneously received on Earth by the NASA/Jet Propulsion Laboratory Deep Space Net (DSN) stations at Goldstone, California (DSS-14) and Tidbinbilla, Australia (DSS-43). The receiver signals are split between closed-loop and open-loop receivers. The closed-loop receivers extract Doppler data which are available soon after an occultation. The primary data, however, are the open-loop data (Berman and Ramos, 1980). These data must be digitized, bandwidth reduced, and filtered (see Kliore et al., 1979 and Kliore and Patel,

Figure 4. Spacecraft configuration (from Colin, 1980)

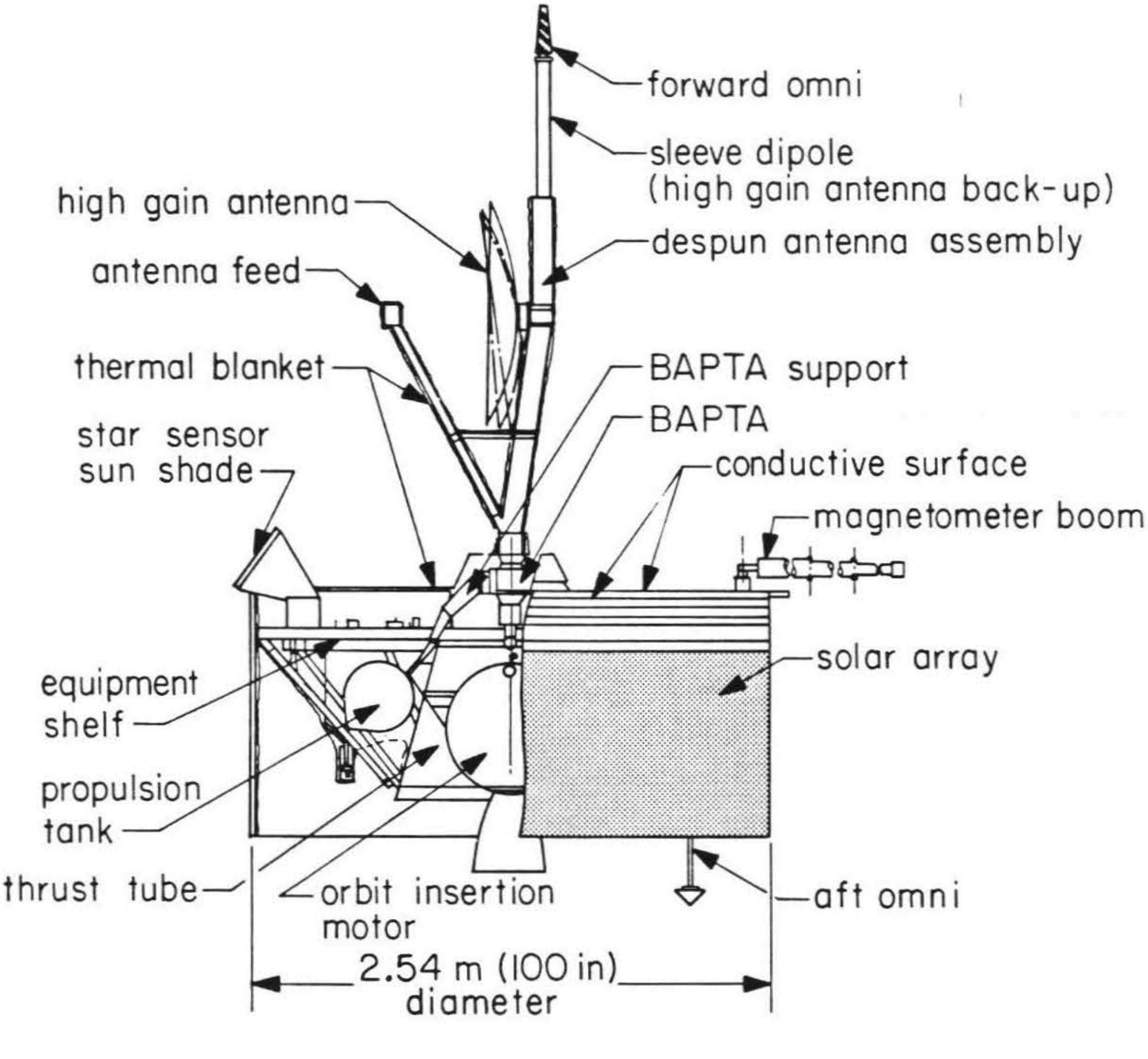
forward omni
sleeve dipole
(high gain antenna back-up)
high gain antenna
despun antenna assembly
antenna feed
thermal blanket
BAPTA support
BAPTA
star sensor
sun shade
conductive surface
magnetometer boom
solar array
equipment
shelf
propulsion
tank
thrust tube
orbit insertion
motor
aft omni
2.54 m (100 in)
diameter

1980 for detailed procedures for Mariner 10 and Pioneer Venus, respectively). The resulting output are frequency and amplitude of the S- and X-band signals as functions of time.

The frequency data are affected only by the refraction in the atmosphere. These data are used to obtain the refractive index profile of the Venus atmosphere by means of the Abel integral transform (Fjeldbo and Eshleman, 1968; Kliore, 1972). From the refractive index data, pressure-temperature profiles may be derived assuming that the refractive index is proportional to the atmospheric density, hydrostatic equilibrium, and an ideal atmosphere. The refractive index data may also be used to determine the power loss due to defocussing resulting from bending of the radio beam by the atmosphere. These data are essential to the analysis of the amplitude data.

The amplitude data are affected not only by absorption by the clouds and gaseous components of the atmosphere and refractive defocussing as mentioned above, but by all spacecraft and antenna motions. The extraction of the component of the attenuation due to absorption, and its relation to the composition of the atmosphere, are the primary goals of this thesis.

The latitude, the solar zenith angle and the date for all occultation orbits which have been analyzed as a part of this thesis are listed in Table III. Also included are the latitudes, solar zenith angles and dates of the Pioneer Venus probes (Colin, 1980), Venera 11 and 12 (Kurt and Zhegulev, 1979), Mariner 5 (Fjeldbo et al, 1971), and Mariner 10 (Kliore, 1979). Figure 5 shows the locations of these occultations on the planet in latitude vs. solar zenith angle. Also shown is the approximate location of the collar region (Taylor et al., 1980).

The polar occultations are located near the terminator while occultations located in the collar region occurred during both daytime and nighttime.

Figure 5. Location of the Pioneer Venus occultations in terms of solar zenith angle. Also shown are the locations of the Pioneer probes, Mariner 5 and 10, and Venera 11 and 12.

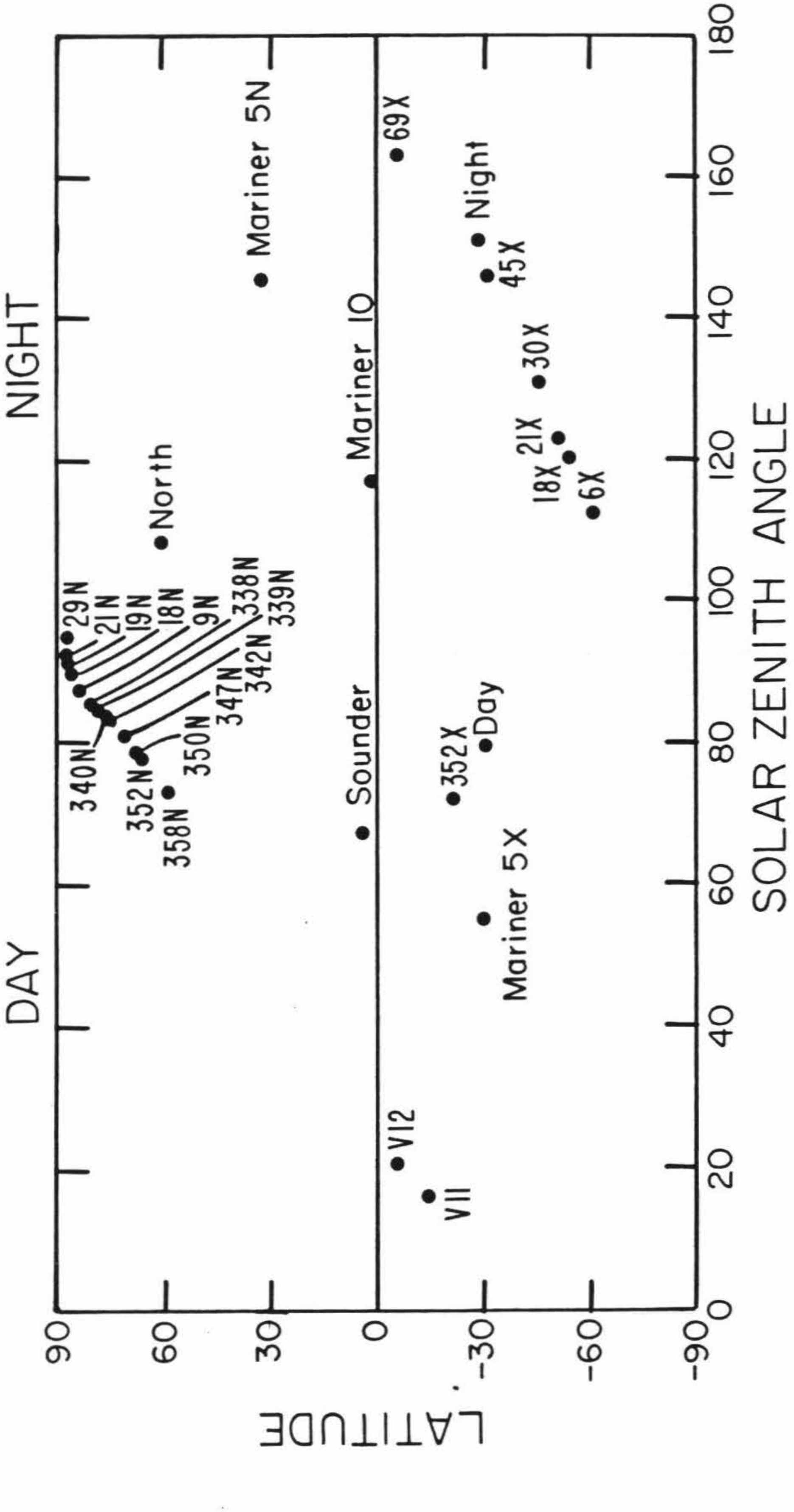
DAY
NIGHT
LATITUDE
SOLAR ZENITH ANGLE
90
60
30
0
-30
-60
-90
0
20
40
60
80
100
120
140
160
180
VI2
VII
Mariner 5X
352X
Day
Sounder
Mariner 10
358N
352N
350N
340N
347N
342N
338N
339N
9N
18N
19N
21N
29N
North
Mariner 5N
6X
18X
21X
30X
45X
Night
69X

The more equatorial occultations between 60° and the equator are all in the southern hemisphere and occur during the night with the exception of orbit 352X which is a daytime occultation.

Table III

Latitude, Longitude and Solar Zenith Angle
of all Analyzed Orbits

Orbit	Latitude*	SZA	Date
6X	-60.1	112.7	12/10/78
9N	83.9	87.3	12/13/78
18N	86.2	89.9	12/22/78
18X	-54.3	120.4	12/22/78
19N	86.5	90.2	12/23/78
21N	87.0	91.0	12/25/78
21X	-52.2	122.9	12/25/78
29N	87.2	94.4	01/02/79
30X	-45.5	130.8	01/03/79
45X	-31.2	146.4	01/18/79
69X	-5.4	165.4	02/11/79
338N	80.3	85.5	11/08/79
339N	79.3	85.0	11/09/79
340N	78.4	84.5	11/10/79
342N	76.6	83.4	11/12/79
347N	71.7	80.6	11/17/79
350N	68.7	78.8	11/20/79
352N	66.5	77.4	11/22/79
352X	-22.3	61.2	11/22/79
358N	59.4	72.9	11/28/79
Mariner 10N	0.9	117.6	02/05/74
Mariner 5N	32.0	145	10/19/67
Mariner 5X	-30.0	55	10/19/67
Sounder	4.4	65.7	12/09/78
Night	-28.0	150.7	12/09/78
North	59.3	108.0	12/09/78
Day	31.2	79.9	12/09/78
Venera 11	-14	20	12/25/78
Venera 12	-7	25	12/21/78

*Negative latitudes are in southern hemisphere

2. Mariner 10

The first attempt to analyze absorption coefficient data received from a radio occultation experiment in terms of atmospheric properties was made using Mariner 10 data. The Mariner 10 spacecraft flew by Venus on February 5, 1974. The spacecraft was three axis stabilized with a fixed altitude relative to the sun and Canopus. The radio system included an S-band receiver (2115 Mhz) and two transmitters, one operating at S-band (13.06 cm) and the other at X-band (3.56 cm). At a radius of 6093 km during the entry occultation the signal from Earth to the spacecraft which drove the S- and X-band transmitters became critically weakened by refraction. At this time the S- and X-band exciters were switched to an on-board oscillator which was several orders of magnitude less stable than the Deep Space Net (DSN) station frequency standards which referenced the uplink signal. These exit data and the entry data at radii below 6093 km were proven to be useless due to a serious instability in the on-board oscillator.

The entry occultation at radii greater than 6093 km provided frequency and amplitude data for both S- and X-band wavelengths as a function of time. These data were used to derive temperature-pressure (Howard et al., 1974) and absorption coefficient (Kliore et al., 1979) profiles (see Figure 6) for the middle atmosphere of Venus. A complete discussion of the amplitude data reduction including a detailed description of the power corrections due to both programmed and unplanned antenna motions is given by Kliore et al. (1979).

Since the publication of that paper, several problems have been brought to the attention of the authors. First, the uncertainty with which the antenna motions could be mapped was underestimated by Kliore et al. due to a possible antenna offset. The X-band signal strength began to decrease prior to any significant atmospheric refraction effects. The magnitude of the offset reached 2.5 dB before the beginning of the entry occultation but was reduced to about 1 dB or a 0.05 dB/sec drift, after power corrections were made. Kliore et al. men-

Figure 6. Absorption coefficients in the lower Venus atmosphere as a function of altitude for Mariner 10 (a) S-band and (b) X-band.

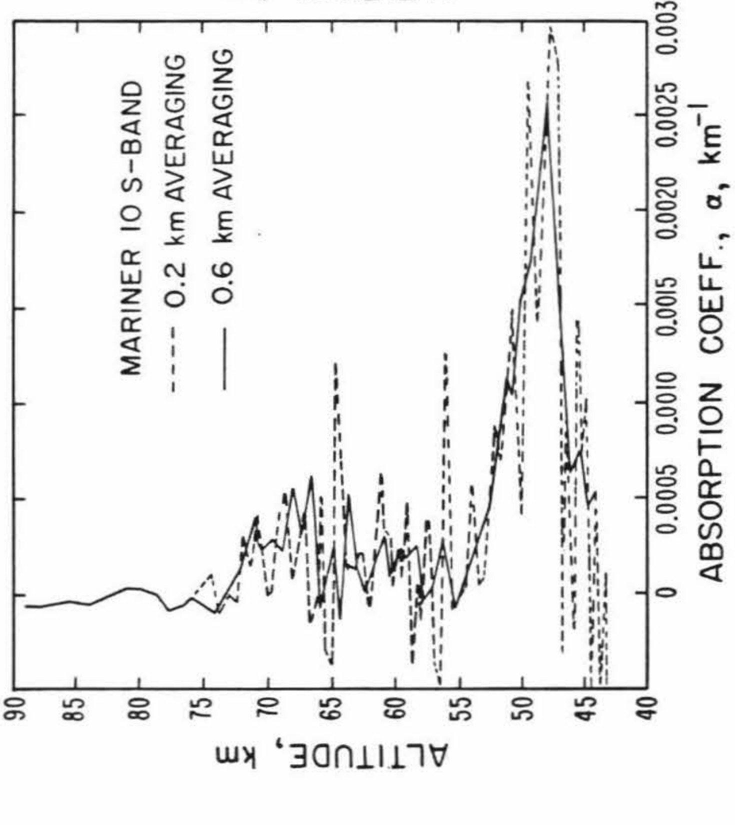
MARINER 10 S-BAND
0.2 km AVERAGING
0.6 km AVERAGING
ALTITUDE, km
90
85
80
75
70
65
60
55
50
45
40
ABSORPTION COEFF., α, km⁻¹
0
0.0005
0.0010
0.0015
0.0020
0.0025
0.0030

a

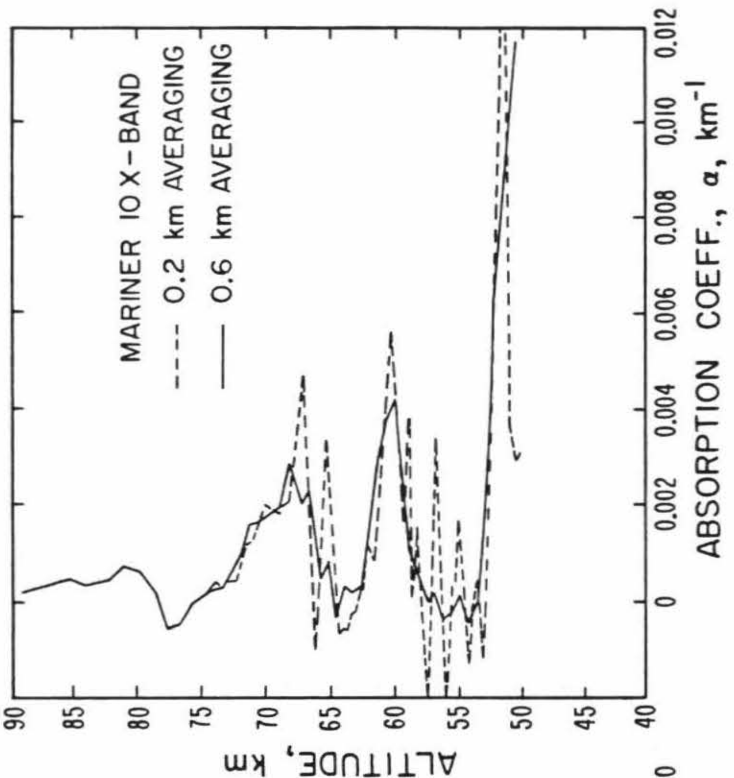
MARINER 10 X-BAND
0.2 km AVERAGING
0.6 km AVERAGING
ALTITUDE, km
90
85
80
75
70
65
60
55
50
45
40
ABSORPTION COEFF., α, km⁻¹
0
0.002
0.004
0.006
0.008
0.010
0.012

b

tion this problem and suggest the residual could have been caused by either the incorrect knowledge through telemetry of the initial position of the antenna or by inaccuracies in the reconstruction of the spacecraft limit-cycle motion. If this offset continued at a rate of 0.05 dB/sec, a total decrease in the received power of about 4 dB would result toward the end of the occultation from unknown and therefore uncorrectable sources. Such antenna offsets produce large errors in the power profiles due to the steep nature of the X-band antenna gain profile. Figure 7 describes the problem in detail. The antenna patterns for S- and X-band are plotted as relative gain vs. antenna off-axis angle. The actual position of the antenna center line, or ray, relative to Earth (antenna off-axis angle) is shown as a function of time. Also shown is the antenna off-axis angle as a function of time assuming a 0.05 dB/sec residual drift as observed in the X-band power profile. Thus at any given time, t, during the occultation, the loss in power due to antenna offset, or relative gain, may be determined for S- or X-band wavelengths by determining the antenna off-set angle at t and the corresponding gain. Also noted in the figure are the times during occultation of S- and X-band signal loss.

At the time of X-band signal loss (approximately 57 seconds from entry into occultation) it is possible the antenna drifted to an antenna off-axis angle of 1.0 degrees. This would result in a total gain, or power loss, of 3.8 dB. In addition to this gain uncertainty, an additional uncertainty is introduced because at a one degree offset the antenna position is on a steep portion of the X-band gain curve.

At the time of S-band signal loss (approximately 185 seconds from entry occultation), the antenna off-axis angle was 1.5 degrees assuming the 0.05 dB drift. The corresponding power loss in this case is only about 0.6 dB —

Figure 7. S- and X-band power profiles are shown along with the actual position of the Mariner 10 antenna as a function of time. The antenna position assuming a 0.05 dB/sec drift is also shown.

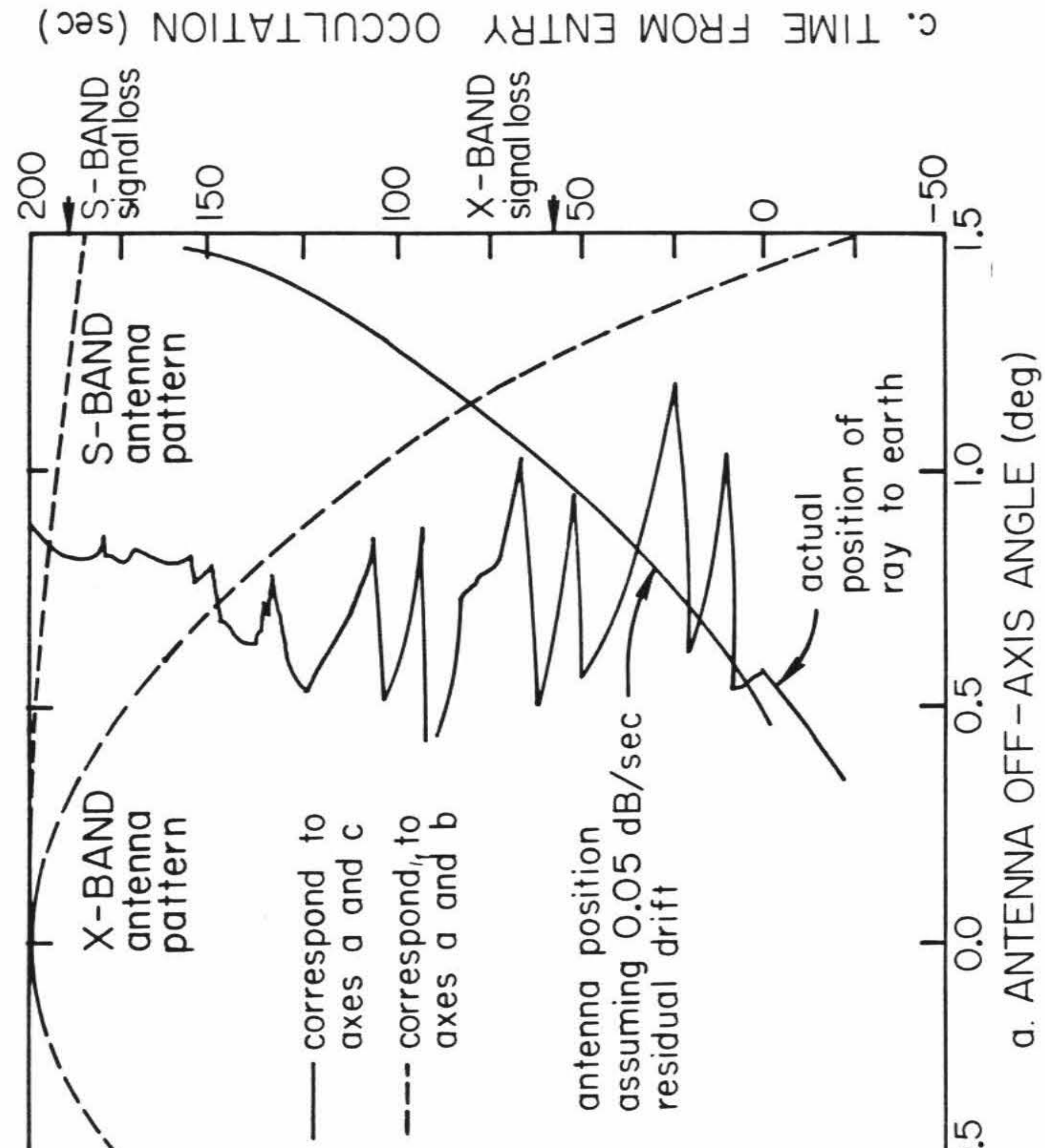
c. TIME FROM ENTRY OCCULTATION (sec)
200
150
100
50
0
-50
S-BAND signal loss
X-BAND signal loss
S-BAND antenna pattern
X-BAND antenna pattern
— correspond to axes a and c
- - - correspond to axes a and b
antenna position assuming 0.05 dB/sec residual drift
actual position of ray to earth
a. ANTENNA OFF-AXIS ANGLE (deg)
-0.5
0.0
0.5
1.0
1.5
b. RELATIVE GAIN (dB)
0
-1
-2
-3
-4
-5
-6
-7
-8
-9
-10

significantly less than that observed in the X-band gain profiles. The antenna offset is still on the flat portion of the gain pattern thus introducing no additional uncertainties as in the case of the X-band offset.

Eshleman et al. (1980) provide a detailed analysis of the X-band absorption data and suggest the upper and middle cloud layers observed by Kliore et al. could have been artificially created by known motions of the spacecraft antenna if its axial direction was biased by the offset described above. The most important evidence favoring the possibility of uncorrected X-band antenna motions is the results of the Pioneer-Venus probes and orbiter radio occultation experiments. The probe particle size spectrometer (Knollenberg and Hunten, 1980) in conjunction with the nephelometer (Ragent and Blamont, 1980) have determined the mass content and identified the cloud particles for the upper and middle clouds. The mass contents derived from these data are insufficient to produce any observable absorption layers above about 55 km in the Venus atmosphere. In addition, the Pioneer-Venus radio occultation absorption coefficient profiles contain no absorption layers above about 52 km in altitude. It is therefore likely the cloud layers observed in the Mariner 10 X-band data were a result of antenna motions as suggested by Eshleman et al.

The lower absorption layer observed in the Mariner 10 S-band data was not affected by the possible antenna drift due to the broader nature of the S-band antenna gain pattern. An antenna off-axis angle capable of producing several decibels of offset in an X-band power profile produced only a few tenths of a decibel offset in the S-band power profile as described earlier. Therefore the S-band absorption coefficient profile for Mariner 10 is believed to be correct as presented by Kliore et al.

The second problem concerning the analysis of the Mariner 10 data was the refractive defocussing equation used in analyzing the data. Eshleman et al. (1980) stated the refractive defocussing equation used by Kliore et al. was incorrect in two respects. First, Kliore et al. used a cylindrically symmetric approximation for the atmosphere thereby neglecting a focussing effect of the curved limb of the planet perpendicular to the ray propagation direction. A spherically symmetric approximation has been used in all Pioneer Venus work (see equation 28). Second, the refractive defocussing in the plane of the ray propagation path was miscalculated. The nature of this error is discussed in detail below. Fortunately, the error in the absorption coefficient profiles resulting from the use of the incorrect equation was minimal in the case of the Mariner 10 data.

The following will describe, using detailed diagrams, the derivation of the refractive defocussing equation using both Eshleman et al.'s (1980) method and Kliore's et al. (1979) method for defocussing in the plane of the ray path. The two methods produce the same refractive defocussing equation as presented here. In examining the derivation by Kliore et al., it is evident that the equation presented in the original paper on the Mariner 10 analysis neglected to include the term $b \tan(\psi/2)\, d\psi$ which is just the difference in the distance from the planet center to the refracted ray assuming two adjacent rays are parallel and assuming they are diverging by an angle $d\psi$. ψ is the bending angle and b is the ray asymptote. The magnitude of that error will be discussed.

Figure 8a describes the geometry used in Eshleman et al.'s derivation. The refractive defocussing, I^{-1}, is equal to the ratio of the beam width after refraction to the beam width before refraction (Δb), or

Figure 8. The geometry used in deriving the refractive defocussing in the plane containing the ray. (a) is for Eshleman's derivation and (b) is for Kliore's derivation.

ESHLEMAN DERIVATION

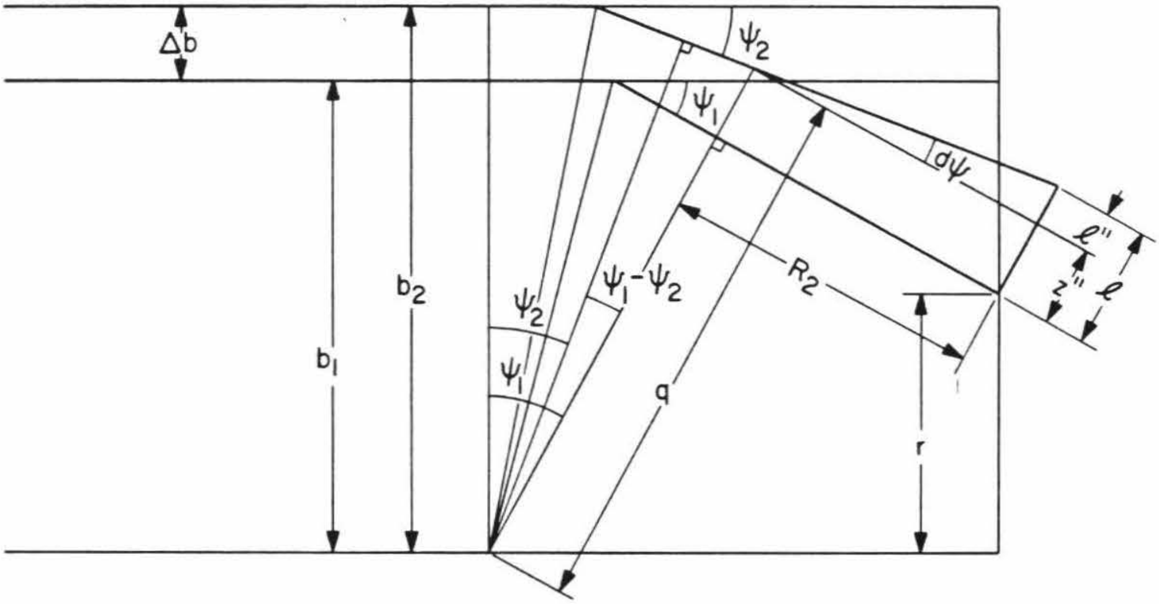

a.

KLIORE DERIVATION

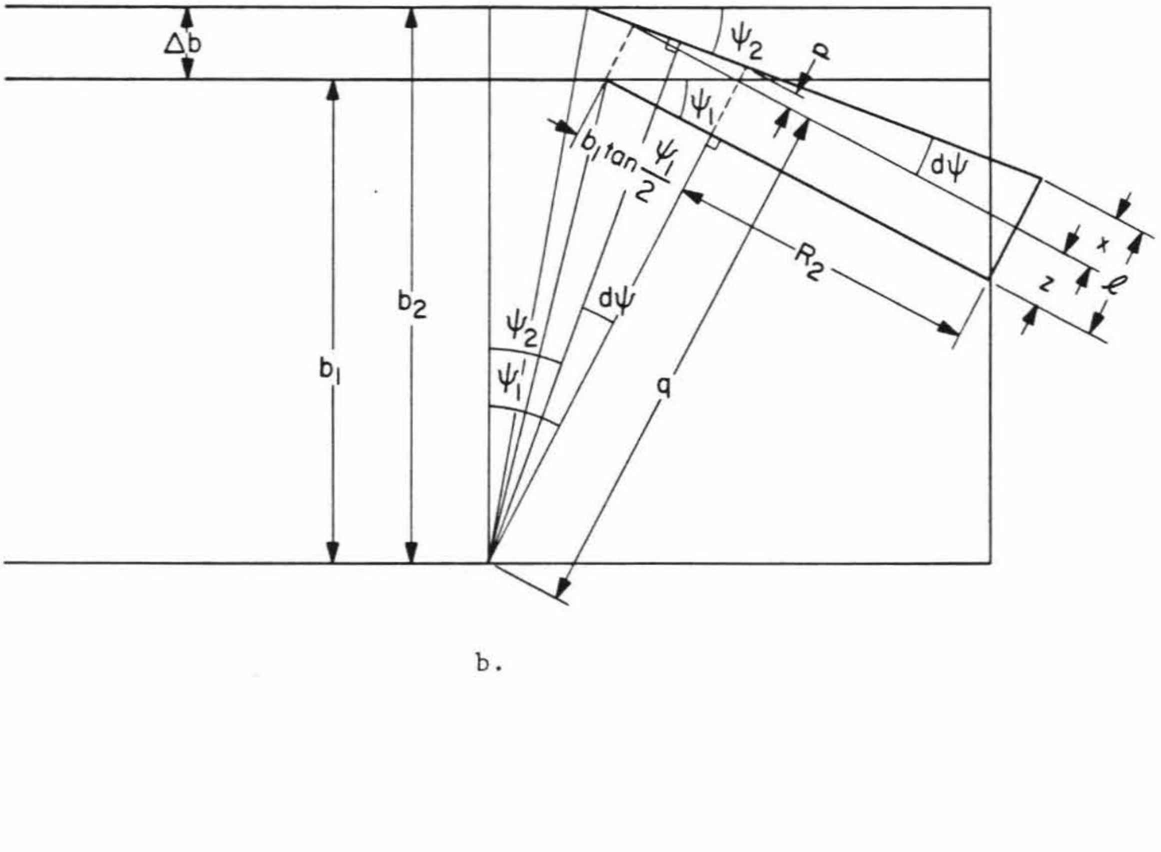

b.

$$I^{-1} = \frac{z'' + l''}{\Delta b} \tag{1}$$

where $\Delta b = b_2 - b_1$ $(b_2 > b_1)$.

$$z'' = \left[\frac{b_2}{\cos d\psi} - b_1\right] \tag{2}$$

and $l'' = -R_2 \tan d\psi$ where $d\psi = \psi_2 - \psi_1$ $(\psi_1 > \psi_2)$. Inserting z'' and l'' into equation (1) results in

$$I^{-1} = \frac{\dfrac{b_2}{\cos d\psi} - b_1 - R_2 \tan d\psi}{\Delta b} \tag{3}$$

Assuming $d\psi$ is small,

$$I^{-1} = \frac{b_2 - b_1 - R_2 d\psi}{\Delta b} \tag{4}$$

or,

$$I^{-1} = 1 - R_2 \frac{d\psi}{db} \quad . \tag{5}$$

Figure 8b describes the geometry used by Kliore et al. In this case, the refractive defocussing is

$$I^{-1} = \frac{l}{\Delta b} = \frac{x + z}{\Delta b} \tag{6}$$

where $\Delta b = b_2 - b_1 (b_2 > b_1)$, z and x are described in the figure and

$$x = -\left[b_1 \tan\frac{\psi^1}{2} + R_2\right] \tan\psi \tag{7}$$

$$z = (q - b_1) - p \tag{8}$$

$$p = -b_1 \tan\frac{\psi_1}{2} \tan d\psi \tag{9}$$

$$q = \frac{b_2}{\cos d\psi} \tag{10}$$

where $d\psi = \psi_2 - \psi_1 (\psi_1 > \psi_2)$. Substituting x and z into equation (6) results in

$$I^{-1} = \frac{-\left[b_1 \tan\frac{\psi_1}{2} + R_2\right] \tan d\psi + \left[\frac{b_2}{\cos d\psi} - b_1\right] + b_1 \tan\frac{\psi_1}{2} \tan d\psi}{\Delta b} \tag{11}$$

Again, assuming $d\psi$ is small, I^{-1} is simplified to

$$I^{-1} = \frac{-\left[b_1 \tan\frac{\psi_1}{2} + R_2\right] d\psi + (b_2 - b_1) + b_1 \tan\frac{\psi_1}{2} d\psi}{\Delta b} \tag{12}$$

After cancelling the $b_1 \tan\frac{\psi_1}{2} d\psi$ terms,

$$I^{-1} = \frac{\Delta b - R_2}{\Delta b} d\psi \tag{13}$$

or

$$I^{-1} = 1 - R_2 \frac{d\psi}{db} \tag{14}$$

Originally, Kliore et al. (1979) assumed $z = \Delta b$ instead of $z = \Delta b + b_1 \tan\frac{\psi_1}{2} d\psi$. The $b_1 \tan\frac{\psi_1}{2} d\psi$ term subtracted when calculating x was therefore not added in calculating z resulting in an equation for I^{-1} which contained an extra $b \tan\frac{\psi}{2} d\psi$ term.

Kliore et al. (1980) calculated the refractive defocussing obtained using both the correct (equation 5 or 14) and the incorrect (Kliore et al, 1979) equation including the r/b factor introduced by the spherical approximation $\frac{r}{b}\left[1 - R_2 \frac{d\psi}{db}\right]$. The results show a maximum difference of less than 5% in the refractive defocussing. This corresponds to less than a 10% difference in the excess attenuation in the region of the lower cloud deck (see Figure 9). For occultations where the atmosphere is penetrated to a greater depth than for Mariner 10, it is likely a greater error would result from the use of the incorrect equation.

Figure 10 shows the Mariner 10 absorption coefficient as calculated by Kliore et al. (1979) and Lipa and Tyler (1979). The primary difference between the two Mariner 10 profiles is the extra absorption observed in the Kliore et al. profile between 6100 and 6103 km. The remainder of the profiles are remarkably similar. The error in excess attenuation is greatest at the cloud top due to the small difference between the total attenuation and the refractive defocussing in this region. It is therefore likely the difference above 6100 km could be due to the refractive defocussing equation used. The Mariner 10 absorption coefficient data used to analyze the lower cloud deck will be an average of the two curves below 6100 km, and that calculated by Lipa and Tyler above 6100 km.

Figure 9. Attenuation profile for the total attenuation, the refractive defocussing using Kliore's equation and the refractive defocussing using Eshleman's equation.

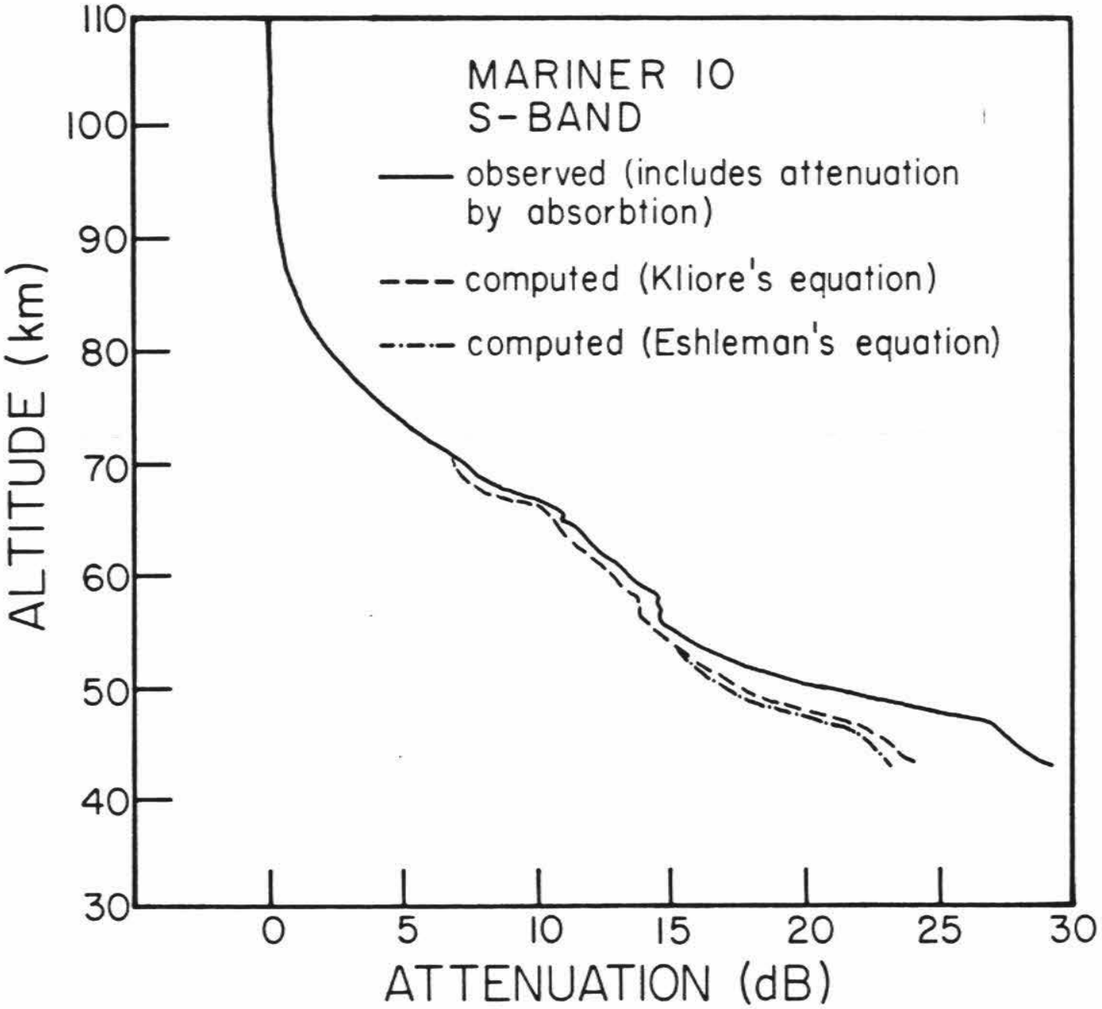
MARINER 10
S-BAND
observed (includes attenuation by absorbtion)
computed (Kliore's equation)
computed (Eshleman's equation)
ALTITUDE (km)
110
100
90
80
70
60
50
40
30
0
5
10
15
20
25
30
ATTENUATION (dB)

Figure 10. Absorption coefficient profiles derived for Mariner 10 by Kliore et al. (1979) and Lipa and Tyler (1979).

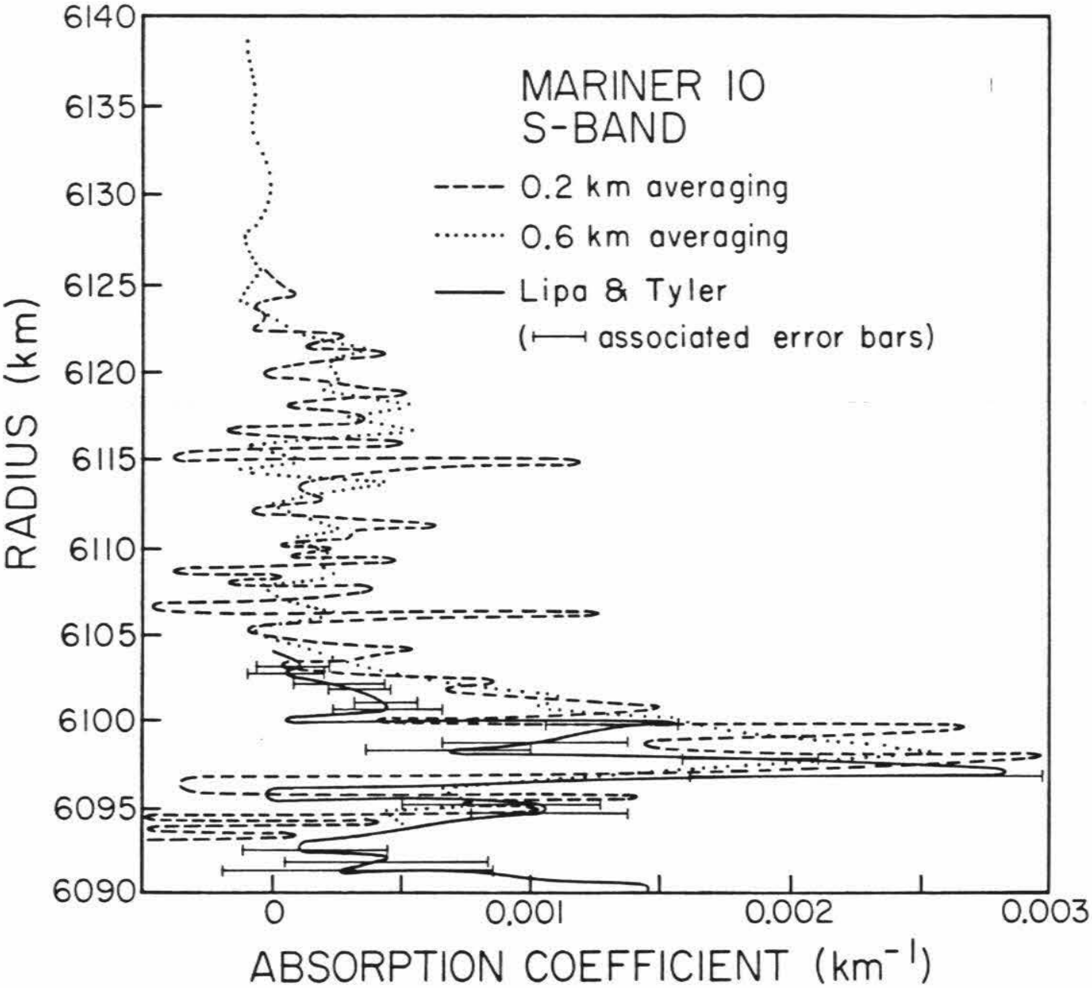
MARINER 10
S-BAND
0.2 km averaging
0.6 km averaging
Lipa & Tyler
(associated error bars)
RADIUS (km)
6140
6135
6130
6125
6120
6115
6110
6105
6100
6095
6090
0
0.001
0.002
0.003
ABSORPTION COEFFICIENT (km^{-1})

CHAPTER III

PRESSURE-TEMPERATURE AND REFRACTIVE DEFOCUSSING PROFILES FROM DOPPLER DATA

1. Refractivity Data from the Doppler Data

A signal received from a spacecraft contains two basic pieces of information — the frequency and the amplitude. If there is relative motion between the spacecraft and the earth, a Doppler shift is associated with the frequency. If in addition the signal passes close to another planet and is refracted by that planet's atmosphere, there is an additional Doppler shift associated with the bending of the ray. Since the relative velocities of the spacecraft and the Earth are known, the residual Doppler due to bending of the ray may be extracted and used to determine the refractive index profile of the atmosphere which produced the Doppler shift. From this refractivity profile the density, pressure and temperature profiles of the atmosphere are easily determined if the composition of the atmosphere is known. It is the goal of this chapter to describe the derivation of these profiles from the Doppler data and the associated uncertainties.

Chapter IV will describe the use of the amplitude data and its associated loss to study absorption in the atmosphere. In order to attribute losses in the power data to atmospheric phenomena, losses due to spreading of the beam as it is refracted must first be taken into account. This refractive defocussing is determined from the Doppler data and therefore its derivation and associated uncertainties are included in this chapter.

Occultation orbit 9 entry (9N) will be used as an example of each step in the analysis of errors and uncertainties associated with the calculation of pressure-temperature and refractive defocussing profiles. The data from this orbit are typical of all occultation profiles. It is used only because it was one of the first orbits processed and has therefore been used throughout the error analysis procedure.

2. Procedure: Refractivity Profiles from Doppler Data

The geometry of a radio occultation experiment is described in Figure 11a. A radio signal of given amplitude and frequency is sent from the spacecraft to Earth via a path which is bent as it passes through the atmosphere due to refraction of the ray. The path is described by b, the asymptote impact parameter, r_0 the radius of closest approach, and ψ, the bending angle. On Earth, the received signal is Doppler shifted due to a change in the projected velocity of the ray as it is bent. The time delay, or additional time required for the ray to travel from the spacecraft to Earth along the longer bent path, may also be measured and used to determine the refractivity. Doppler shifts, however, are measured more accurately and are therefore used in all occultation experiments.

In addition to the amplitude and frequency, or Doppler shift, several other quantities are available from the trajectory data. Figure 11b describes these quantities which include R_E, the distance from the spacecraft to Earth, r_{SC}, the distance from Venus to the spacecraft, α, the angle between R_E and r_{SC}, $\bar{v}_{SC}$, the velocity vector of the spacecraft, and $\varphi_{\oplus}$, the angle between the Earth and v_{SC}. The quantity $\dot{r}$, or the velocity of the spacecraft projected in the direction of the ray, is obtained from the Doppler shift, which to first order is

$$\Delta f = \frac{-2\dot{r} f_o}{c} \tag{15}$$

where f_o is the original frequency of the signal and c is the speed of light. From

Figure 11. (a) The radio occultation geometry showing the path of the refracted radio wave relative to Venus. (b) and (c) Geometry used in deriving the refractive index profile.

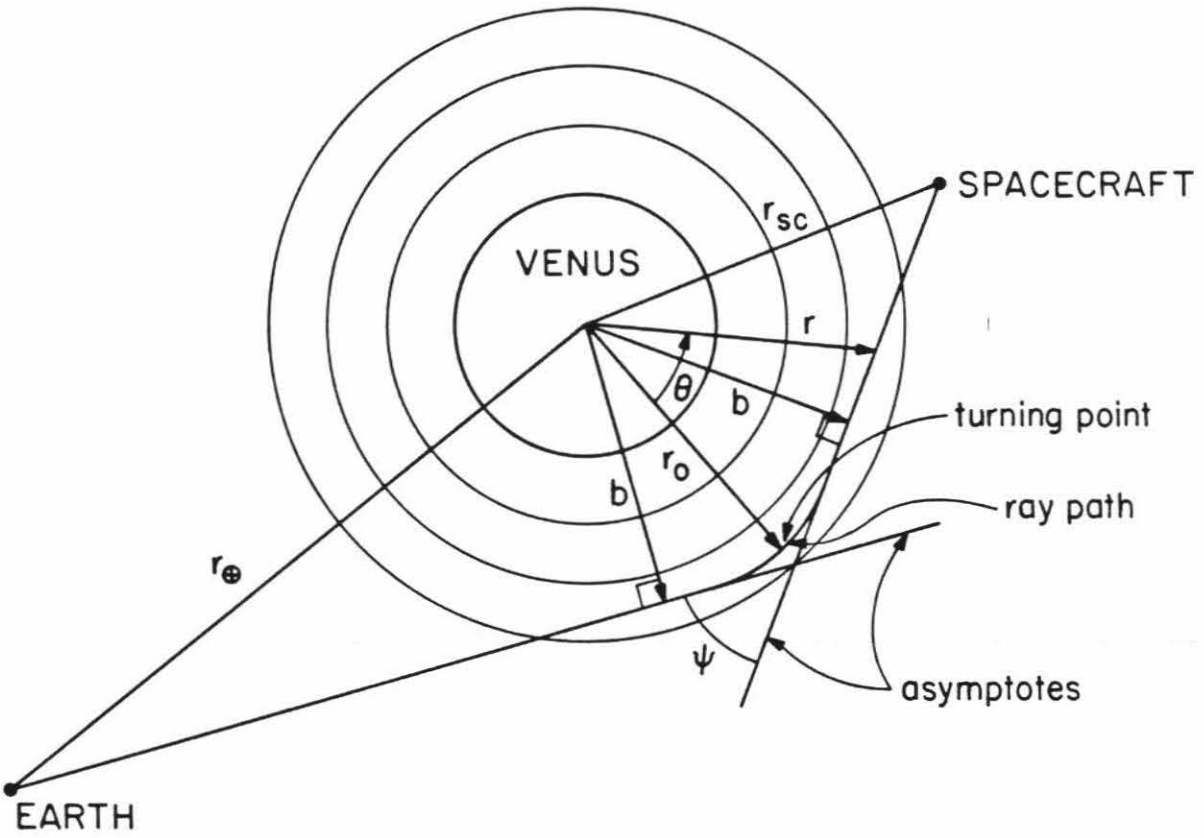

b = asymtote impact parameter

r_o = radius of closet approach

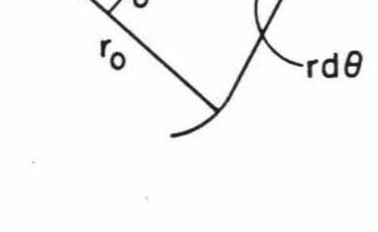

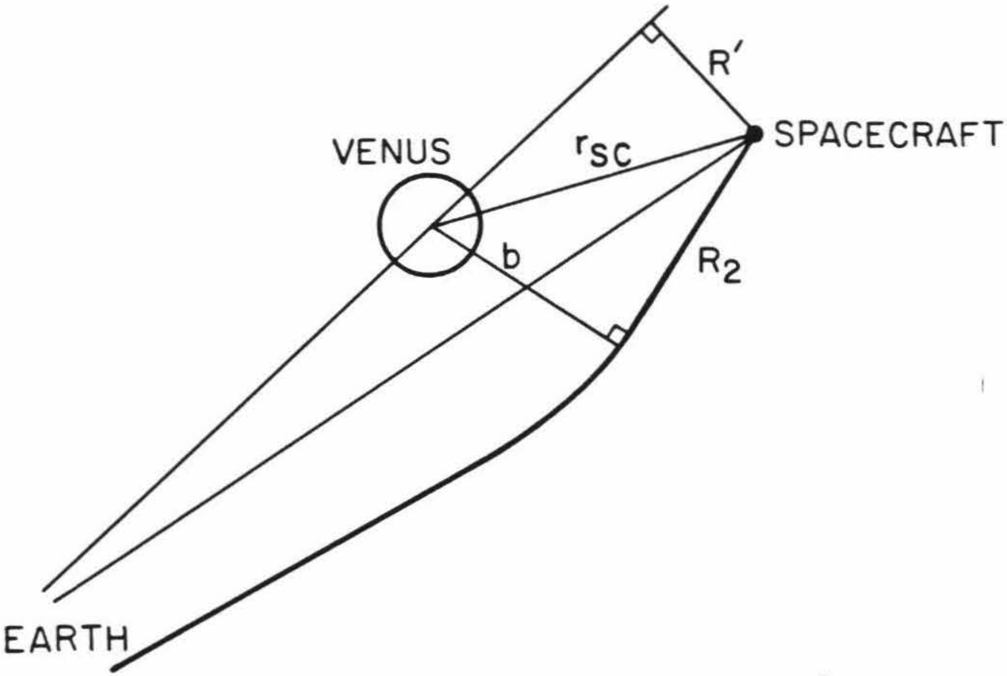
R′
SPACECRAFT
VENUS
r_{SC}
b
R_2
EARTH

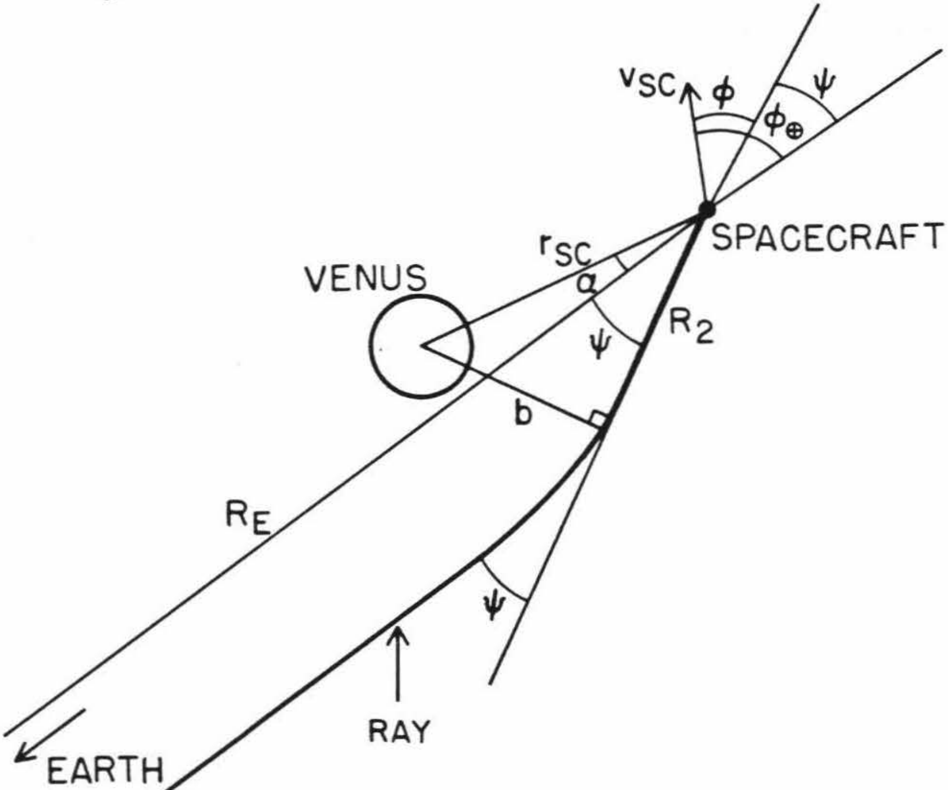
v_{SC}
ϕ
ψ
$\phi_\oplus$
SPACECRAFT
r_{SC}
VENUS
α
ψ
R_2
b
R_E
ψ
RAY
EARTH

$\dot{r}$ the angle φ between $\dot{r}$ and v_{SC} may be calculated:

$$\varphi = \arccos\left[\frac{\dot{r}}{v_{SC}}\right] \tag{16}$$

or, with $\lambda = c/f_o$,

$$\varphi = \arccos\left[\frac{-\lambda f}{2v_{SC}}\right] \tag{17}$$

With $\varphi_\oplus$ known from the trajectory data and φ calculated from the Doppler data, the bending angle, ψ, may be calculated as follows:

$$\psi = \varphi_\oplus - \varphi \tag{18}$$

Once ψ is known, b, the ray asymptote, may be calculated:

$$b = r_{SC}\sin(\psi + \alpha) \quad . \tag{19}$$

Thus from the Doppler and trajectory data, b, the ray asymptote, and ψ, the bending angle can be determined as a function of time throughout the occultation. The index of refraction and radius at any given level in the atmosphere may be calculated using an Abel integral transform as follows (Kliore, 1972)

$$\ln\left[n(r_0)\right] = \frac{1}{\pi}\int_{b(r_0)}^{\infty} \frac{\psi(b)\,db}{\sqrt{b^2 - b^2(r_0)}} \ . \tag{20}$$

As described in Appendix 1, $b(r_0) = r_0 n(r_0)$, thus

$$r_0 = \frac{b(r_0)}{n(r_0)} \tag{21}$$

The result is a profile of the index of refraction as a function of radius.

3. Procedure: Pressure-Temperature Profiles from Refractivity

Once the index of refraction of the atmosphere is known as a function of radius, atmospheric density, pressure and temperature may be calculated. According to the Lorentz-Lorentz law for gases, the atmospheric density is proportional to the refractivity, N:

$$\rho(r) = N(r)\left[\frac{\mu}{RQ}\right] . \tag{22}$$

μ is the molecular weight of the gaseous atmosphere (which can be taken to be CO_2 and N_2 for our purposes here).

$$\mu = f_{CO_2} M_{CO_2} + f_{N_2} M_{N_2} \tag{23}$$

where f_{CO_2} and f_{N_2} are the volume mixing ratios of CO_2 and N_2, respectively, and M_{CO_2} and M_{N_2} are their respective molecular weights. R is the gas constant and

$$Q = 0.269496\left[494.5\, f_{CO_2} + 294.4\, f_{N_2}\right] \tag{24}$$

(Essen and Froome, 1951). Q describes the dependence of the refractivity on the atmospheric density and composition from laboratory measurements (the units of Q are K/mbar).

The pressure may be calculated assuming hydrostatic equilibrium:

$$p(r) = -\int_{r_0}^{r} \rho g dr' + p_0 \tag{25}$$

where

$$p_0 = \rho(r_0)\, \frac{R}{\mu} T_0(r_0) \tag{26}$$

where μ is the molecular weight of the atmosphere, R is the gas constant, and

T_0 is a guessed quantity at r_∞ high in the atmosphere. Pressure profiles for different values of T_0 converge at about 100 mb. The temperature profile may then be calculated from the equation of state assuming the atmosphere is ideal:

$$T(r) = \frac{p(r)}{\rho(r)} \frac{\mu}{R} \quad . \tag{27}$$

The Venus atmosphere is approximately ideal at all altitudes above the critical refraction level.

4. Procedure: Refractive Defocussing Profiles from Bending Angle

The refractive defocussing equation used to compute the loss of power due to spreading of the beam is for a spherically symmetric atmosphere (Eshleman et al., 1980). The derivation of the equation has been described in Chapter II. The equation is

$$I^{-1} = \frac{R'}{b}\left[1 - R_2 \frac{d\psi}{db}\right] \tag{28}$$

where $R_2 = \sqrt{r_{SC}^2 - b^2}$ and R_2, r_{SC}, b and R' are described in Figure 11c. In terms of decibels, the refractive defocussing, A_{REF}, is

$$A_{REF} = 10\log_{10}\left\{\frac{R'}{b}\left[1 - \left[R_{SC}^2 - b^2\right]^{1/2} \frac{d\psi}{db}\right]\right\} \tag{29}$$

5. Errors

Temperature-pressure profiles are calculated from the refractivity profiles derived from the Doppler data as described in the previous section. In order to calculate the refractivity from the Doppler or bending angle data, an Abel integral transform must be used. Due to nonlinearity, errors inherent are not directly calculable; however, the errors may be determined indirectly by recalculating the bending angle from a perturbed refractivity profile. These errors are a result of numerically approximating the Abel integral. Thus a perturbation is a sudden change in the refractivity which introduces an error from the numerical approximation.

The refractivity is perturbed by a known amount, the associated bending angle is calculated from the perturbed refractivity profile and the resulting perturbed bending angle is processed as original data. The integral used in the reverse calculation is:

$$\psi(r_0) = -2\int_{r_0}^{r_\infty} \frac{b(r_0)\dfrac{1}{n}\dfrac{dn}{dr}dr}{\sqrt{r^2n^2 - b(r_0)^2}} \tag{30}$$

In order to change this equation to an integrable form, a method developed by D.O. Muhleman (private communication) is used. A dummy variable, z, is used to simplify the integral as follows:

$$z = rn \tag{31}$$

$$dz = ndr + r\frac{dn}{dr}dr \tag{32}$$

$$\frac{dz}{nr} = \frac{dz}{z} = \frac{dr}{r} + \frac{1}{n}\frac{dn}{dr}dr \tag{33}$$

or

$$\frac{1}{n}\frac{dn}{dr}dr = \frac{dz}{z} - \frac{dr}{r} \ . \tag{34}$$

Substituting the l.h.s. of equation (34) into integral (30) and separating the resulting integral into two parts gives

$$\psi(r_0) = -2b(r_0)\left[\int_{b(r_0)}^{r_\infty} \frac{dz}{z\sqrt{z^2 - b(r_0)^2}} - \int_{r_0}^{r_\infty} \frac{dr}{r\sqrt{r^2n^2 - b(r_0)^2}}\right] . \tag{35}$$

The first integral on the r.h.s. of equation (35) is easily integrated:

$$\int_{b(r_0)}^{r_\infty} \frac{dz}{z\sqrt{z^2 - b(r_0)^2}} = \frac{1}{b(r_0)} \cos^{-1} \frac{b(r_0)}{z} \Big|_{b(r_0)}^{r_\infty}$$

$$= \frac{1}{b(r_0)} \cos^{-1} \frac{b(r_0)}{r_\infty} \tag{36}$$

The second integral on the r.h.s. of equation (35) is just ϑ, the angle between r_0 and r:

$$\vartheta = \int_{r_0}^{r_\infty} \frac{b(r_0)dr}{r\sqrt{r^2n^2 - b(r_0)^2}} \tag{37}$$

The integral equation (35) can be rewritten as:

$$\psi(r_0) = -2b(r_0)\left[\frac{1}{b(r_0)} \cos^{-1} \frac{b(r_0)}{r_\infty} - \frac{\vartheta}{b(r_0)}\right] \tag{38}$$

or

$$\psi(r_0) = -2\left[\cos^{-1} \frac{b(r_0)}{r_\infty} - \vartheta\right] \tag{39}$$

where $b(r_0) = n(r_0)r_0$. This equation may also be derived geometrically from Figure 11b.

The only remaining obstacle to using equation (35) or (39) to calculate the bending angle is the integral ϑ (equation (37)). A mathematical trick is necessary to evaluate the integral. The term $\left(r^2n^2 - b(r_0)^2\right)$ is expanded in a Taylor series around r_0:

$$r^2n^2 - b(r_0)^2 =$$

$$\left(r^2n^2 - b(r_0)^2\right)|_{r=r_0} + \frac{d}{dr}\left(r^2n^2 - b(r_0)^2\right)|_{r=r_0}(r - r_0) + \frac{1}{2}\frac{d^2}{dr^2}\cdots \tag{40}$$

But $r^2n^2|_{r_0} = r_0^2 n(r_0)^2 = b(r_0)^2$ and the first term on the r.h.s. of equation (40) is zero. After differentiating the remaining equation,

$$r^2n^2 - b(r_0)^2 = \left[2rn^2 + 2r^2n\frac{dn}{dr}\right]_{r=r_0}(r - r_0)$$

$$+ \text{ higher order terms } . \tag{41}$$

For purposes of numerical calculations, $c(r_0)$ may be defined as

$$c(r_0) = 2r_0 n(r_0)^2 + 2r_0^2 n(r_0)\left(\frac{dn}{dr}\right)|_{r_0} \ . \tag{42}$$

which simplifies equation (41) to

$$r^2n^2 - b^2(r_0) = c(r_0)(r - r_0) \tag{43}$$

near r_0.

The mathematical trick is to add and subtract

$$\frac{1}{\sqrt{c(r_0)}\sqrt{r - r_0}} \tag{44}$$

as follows

$$\vartheta = b(r_0)\int_{r_0}^{r_\infty} \frac{1}{r}\left[\frac{1}{r^2n^2 - b^2(r_0)} - \frac{1}{\sqrt{c(r_0)}\sqrt{r - r_0}}\right] dr$$

$$+ b(r_0)\int_{r_0}^{r_\infty} \frac{1}{r}\frac{dr}{\sqrt{c(r_0)}\sqrt{r - r_0}} \tag{45}$$

Equation (45) may be divided into two parts — the integral from r_0 to r_0^+ (near r_0) and the integral from r_0^+ to r_∞. The r.h.s. of equation (45) is zero in the region r_0 to r_0^+ because $\sqrt{r^2n^2 - b(r_0)^2} = \sqrt{c(r_0)(r - r_0)^2}$ near r_0. ϑ then becomes

$$\vartheta = b(r_0) \int_{r_0^+}^{r_\infty} \frac{1}{r} \left[\frac{1}{\sqrt{r^2 n^2 - b(r_0)^2}} - \frac{1}{\sqrt{c(r_0)}\sqrt{r - r_0}} \right] dr$$

$$+ b(r_0) \int_{r_0}^{r_\infty} \frac{1}{r} \frac{dr}{\sqrt{c(r_0)}} \tag{46}$$

Simplifying the second integral in equation (46) results in

$$\vartheta = b(r_0) \int_{r_0^+}^{r_\infty} \frac{1}{r} \left[\frac{1}{\sqrt{r^2 n^2 - b(r_0)^2}} - \frac{1}{\sqrt{c(r_0)}\sqrt{r - r_0}} \right] dr$$

$$+ \frac{2b(r_0)}{\sqrt{c(r_0) r_0}} \tan^{-1} \sqrt{\frac{r_\infty - r_0}{r_0}} \tag{47}$$

Summarizing, $\psi(r_0)$ may be calculated from the refractive index, $n(r)$ as follows:

$$\psi(r_0) = 2\left[\vartheta(r_0) - \cos^{-1} \frac{b(r_0)}{r_\infty} \right] \tag{48}$$

where $\vartheta(r_0)$ is given by equation (47) for any $n(r)$.

Figure 12 shows the original bending angle and the bending angle calculated from the refractive index using equation (48). There is essentially no discernible difference between the two curves if no perturbations are introduced.

In order to determine the effect on the pressure-temperature profiles of a perturbation in the refractive index, the procedure outlined in Figure 13 is followed. The original refractive index profile, n_I is perturbed as desired to produce n_p. The bending angle ψ_p corresponding to this perturbed profile is calculated using equation (48). ψ_p is assumed to be the raw data. From ψ_p, a new index of refraction is calculated, n_{pp}. The difference between n_p and n_{pp} represents the additional error to the refractive index introduced by the Abel transform. It is possible the transform may hide or accentuate perturbations in

Figure 12. The original bending angle and the bending angle calculated from the refractive index. There is essentially no discernible difference between the two profiles.

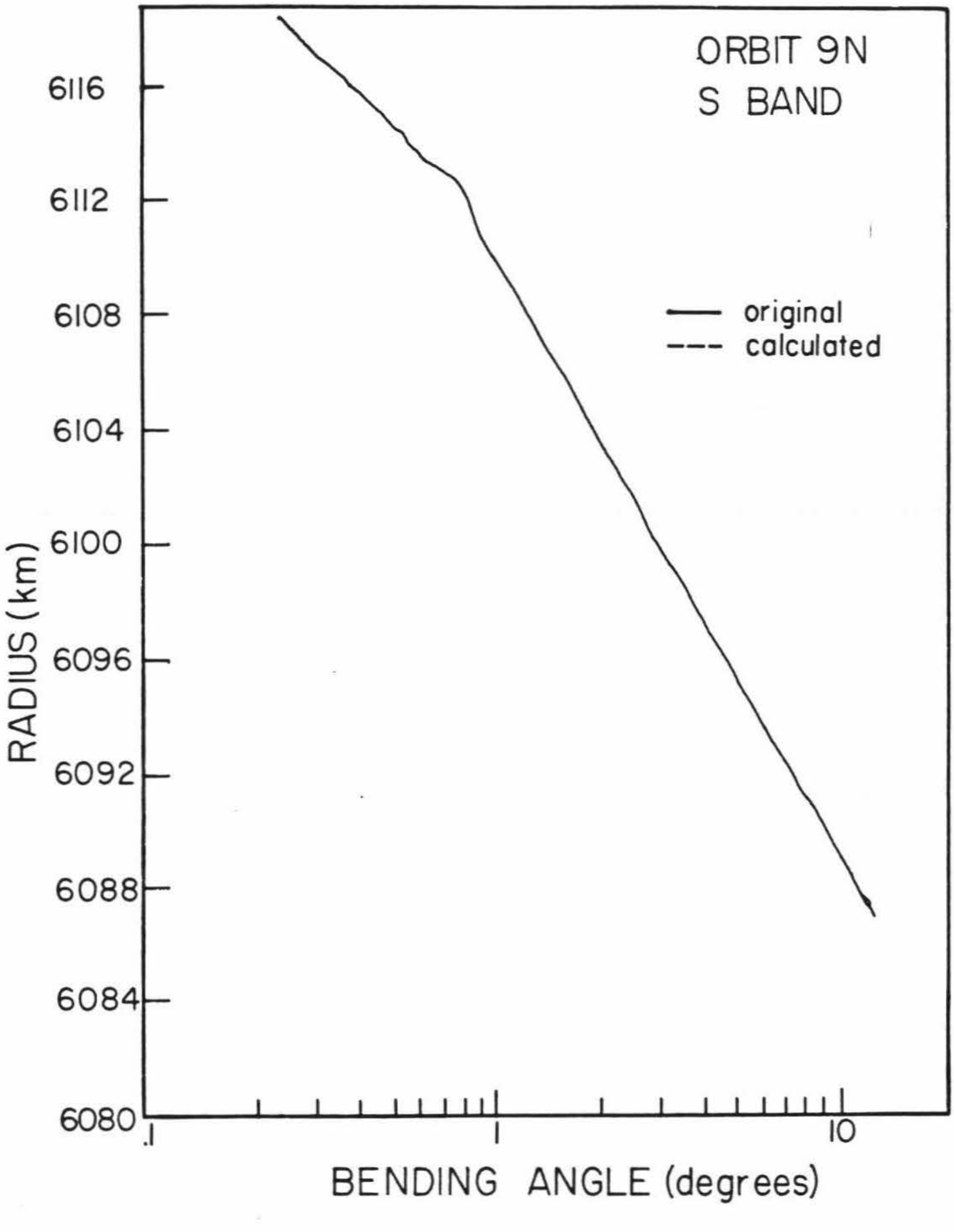
ORBIT 9N
S BAND
original
calculated
RADIUS (km)
6116
6112
6108
6104
6100
6096
6092
6088
6084
6080
.1
1
10
BENDING ANGLE (degrees)

Figure 13. Outline of the proceedure for determining the error resulting from a perturbation in the refractivity profile.

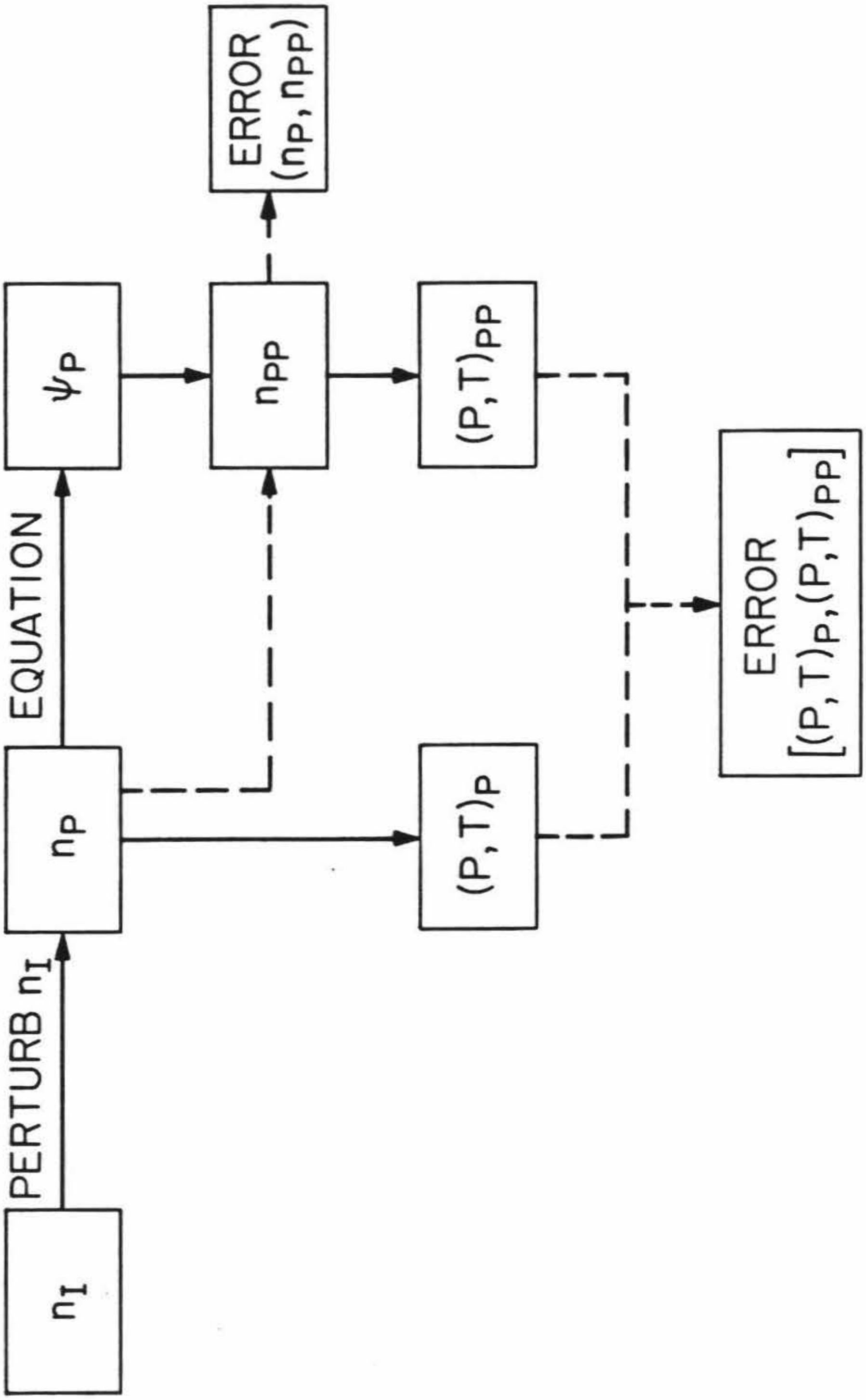
n_I
PERTURB n_I
n_P
EQUATION
ψ_P
n_{PP}
$(P,T)_P$
$(P,T)_{PP}$
ERROR (n_P, n_{PP})
ERROR $[(P,T)_P, (P,T)_{PP}]$

the refractive index. Pressure and temperature profiles are then calculated from n_p and n_{pp} to reveal the final effect of the perturbation.

The kind of perturbations in the index of refraction profile studied here are signatures in the refractive index profile which are not correctly modeled with an assumed CO_2, N_2 atmosphere. These perturbations may result from several atmospheric phenomena including variations in gas composition, contributions from liquid or solid particles and effects due to the oblateness of the atmosphere. The magnitudes of each of these perturbations are estimated individually in the following paragraphs.

The contribution of polar and non-polar atmospheric gases other than CO_2 and N_2 to the refractive index of the atmosphere may be estimated using the following equation (Bean and Dutton, 1966) for the dielectric constant, ε, of the atmosphere:

$$\varepsilon - 1 = \sum_i A_i \frac{P_i}{T} + \sum_j \left[A_j + \frac{B_j}{T} \right] \frac{P_j}{T} . \tag{49}$$

The first term in the summation describes the contribution of non-polar gases and the second term describes the contribution of polar gases to the atmospheric dielectric constant. $A = \frac{4\pi \mathbf{N} \alpha_0}{R} \frac{\text{deg}}{\text{bar}}$ and $B = \frac{4\pi \mathbf{N} \mu^2}{3Rk} \frac{\text{deg}}{\text{bar}}$. P_i and P_j are the partial pressures of non-polar and polar gases, respectively, T is the temperature, α_0 is the average polarizability of the molecules in the liquid state assuming no interaction between molecules, $\mathbf{N}$ is Avagadro's number, k is Boltzmann's constant, R is the gas constant, and μ is the permanent dipole moment. Equation (49) assumes Dalton's law of partial pressure holds thereby allowing the net refractive index to be calculated from the sum of polar and non-polar gases. In terms of the refractivity, equation (49) may be rewritten as

$$N = \frac{10^6\, P}{2T} \left\{ \sum_i A_i \frac{f_i}{T} + \sum_j \left[A_j + \frac{B_j}{T} \right] \frac{f_j}{T} \right\} \tag{50}$$

where $N = (n - 1)10^6$, $n - 1 \simeq \varepsilon - \frac{1}{2}$ assuming the permeability is 1, $f_{i,j}$ are the volume mixing ratios of the non-polar and polar gases respectively, and P is the total pressure. Table IV gives the estimated values of A and B for CO_2, N_2, H_2O, SO_2 and H_2SO_4. A_i are calculated from the dielectric constant:

$$A_i = (\varepsilon_i - 1)\, \frac{T}{P} \ . \tag{51}$$

B_j are calculated from the permanent dipole moments and A_j are calculated from the dielectric constants and B_j:

$$A_j = (\varepsilon_i - 1)\, \frac{T}{P} - \frac{B_j}{T} \ . \tag{52}$$

Values listed in Table IV are for 350 K and 1 bar. ε_i, ε_j and μ_j are from the *Handbook of Chemistry and Physics* (1980). ε_i and ε_j are at temperatures given in Table IV and are not assumed to change significantly at 350 K. The resulting equation for CO_2, N_2, H_2O, CO_2 and H_2SO_4 gases is

$$N = \frac{P}{T} \left\{ 1.4 \times 10^5\, f_{CO_2} + 8.0 \times 10^4\, f_{N_2} + \left[7 \times 10^5 + \frac{3.8 \times 10^8}{T} \right] f_{H_2O} \right.$$

$$\left. + \left[1.3 \times 10^5 + \frac{2.9 \times 10^8}{T} \right] f_{SO_2} + \left[1.2 \times 10^6 + \frac{8 \times 10^8}{T} \right] f_{H_2SO_4} \right\} \tag{53}$$

Table IV

Quantities Required in Estimating the Atmospheric Refractive Index for Polar and Non-Polar Gases

gas	ε_i	ε_j	$T(\varepsilon)$	A_i	μ_j (debyes)	B_j	A_j
CO_2	1.000985		273	0.27			
	1.00922		293				
N_2	1.00580		273	0.16			
	1.000548		293				
H_2O		1.00785	413		1.85	7.5×10^2	1.4
		1.0126	383				
SO_2		1.0075	296		1.63	5.8×10^2	0.26
	1.0093	273					
H_2SO_4		1.02[†]			2.72[•]	1.6×10^3	2.4

[†] estimated from H_2O numbers

[•] from Kuczkowski et al., 1981 other μ's and ε's from CRC

For 350 K, 96% CO_2 and 4% N_2;

$$N = \frac{P}{T}\left\{1.4 \times 10^5 + 1.8 \times 10^6 f_{H_2O} + 9.6 \times 10^5 f_{SO_2} + 3.5 \times 10^6 f_{H_2SO_4}\right\} . \quad (54)$$

Assuming $f_{H_2O} = 2 \times 10^{-4}$, $f_{SO_2} = 2 \times 10^{-4}$ and $f_{H_2SO_4} = 2 \times 10^{-4}$, the difference in N due to the presence of the three gases is about 1%.

The variation in the refractive index of the atmosphere due to the presence of a cloud may be calculated using any one of several theoretical models (Van Beek, 1967). The Maxwell-Garnet equation gives a good estimate of the average dielectric constant, $\overline{\varepsilon}$, of a dilute mixture of spherical particles (ε_s) in a continuous, infinite medium (ε_m);

$$\frac{\overline{\varepsilon} - \varepsilon_m}{\overline{\varepsilon} + 2\varepsilon_m} = \varphi \left[\frac{\varepsilon_s - \varepsilon_m}{\varepsilon_s + 2\varepsilon_m}\right] \quad (55)$$

where φ is the volume fraction of spherical particles to continuous medium. Assuming $\varepsilon_s >> \varepsilon_m$,

$$\frac{\varepsilon_s - \varepsilon_m}{\varepsilon_s + 2\varepsilon_m} \to 1 \tag{56}$$

and

$$\frac{\overline{\varepsilon} - \varepsilon_m}{\overline{\varepsilon} + 2\varepsilon_m} = \varphi \ . \tag{57}$$

Simplifying further

$$\overline{\varepsilon} = \varepsilon_m \frac{(2\varphi + 1)}{1 - \varphi} \tag{58}$$

or, since φ is much less than 1,

$$\overline{\varepsilon} \cong \varepsilon_m (1 + 3\varphi) \ . \tag{59}$$

The index of refraction, n, is

$$n = \sqrt{\varepsilon_m}(1 + 3\varphi)^{1/2} \tag{60}$$

or,

$$n \cong \sqrt{\varepsilon_m}(1 + \frac{3}{2}\varphi) \ . \tag{61}$$

For orbit 9N, the average refractive index is about 1.0015 in the lower cloud region. The maximum expected liquid content is about 1 g/m^3 or a φ of about 5×10^{-7} giving an average index of refraction for the mixture of

$$n = 1.0015(1.00000075) \tag{62}$$

or

$$n = 1.0015008 \ . \tag{63}$$

The effect of a cloud on the atmospheric index of refraction is less than 0.1%.

In light of the above discussion, the atmospheric refractivity profile was perturbed by 0.1%, 1% and 10% (a 10% perturbation is extreme) in a 2 km region from 6090.1 to 6092.1 km. Figure 14 shows the effect of these perturbations on the bending angle. The effect of the perturbations extends above and below the actual level of the perturbation by an additional kilometer in each direction.

Figure 14. Bending angle showing the effect of a 10%, 1% and 0.1% perturbation in the refractive index.

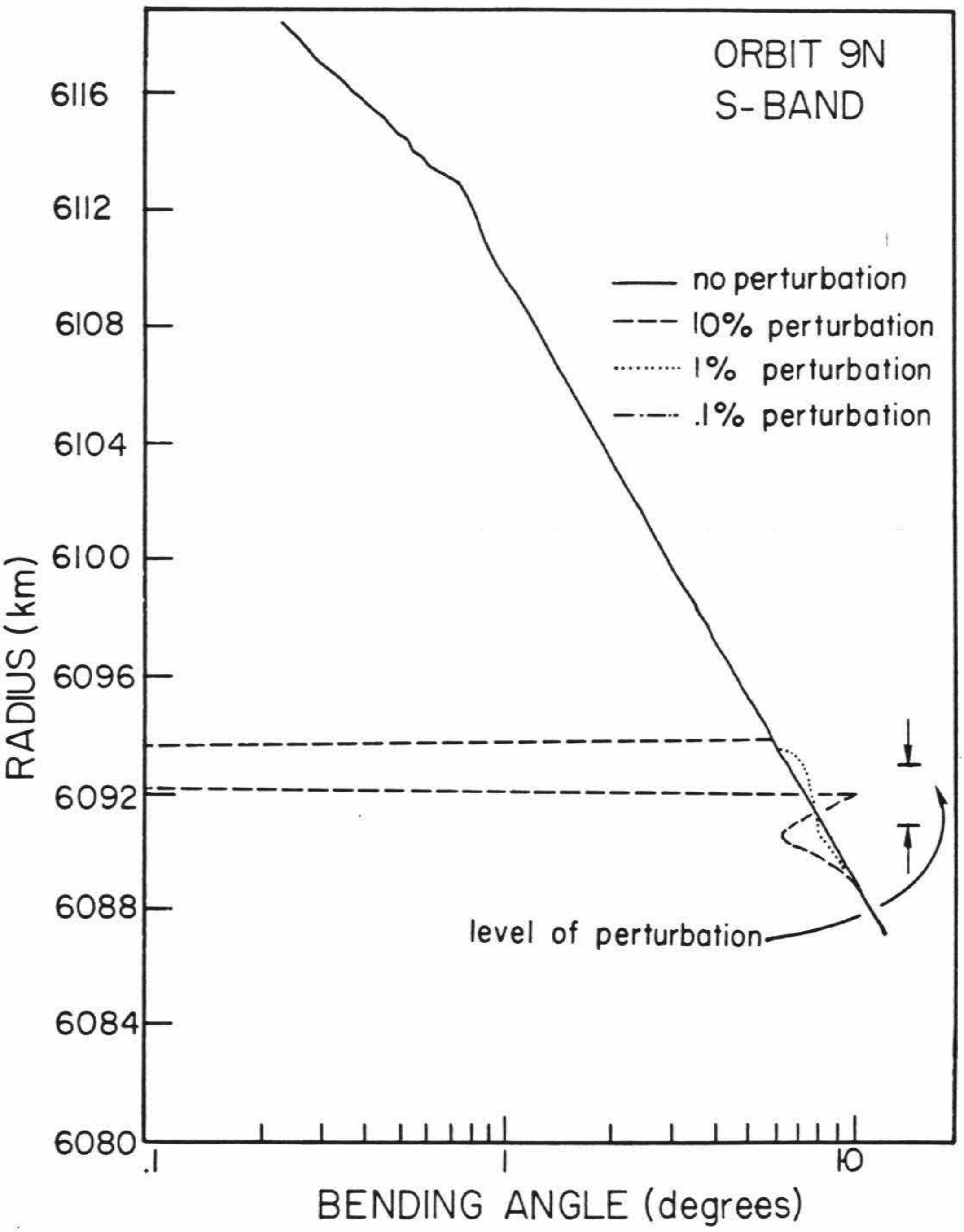
ORBIT 9N
S-BAND
no perturbation
10% perturbation
1% perturbation
.1% perturbation
level of perturbation
RADIUS (km)
6116
6112
6108
6104
6100
6096
6092
6088
6084
6080
.1
1
10
BENDING ANGLE (degrees)

The 0.1% perturbation is not discernible in the figure. Figure 15 shows the original refractive index profile, n, the perturbed refractive index profile, n_p, and the refractive index profile calculated from the perturbed bending angle profiles, n_{pp} for each perturbation. The difference between n_p and n_{pp} is about 0.5% for the 0.1% and 1% perturbations and up to 17% for the 10% perturbation. The Abel transform apparently has little effect on the perturbed refractive index profile for perturbations of 1% or less.

Perturbations in the refractivity profile are best observed by plotting the slope of the refractivity profile. Figure 16 shows the slope of the radius-refractive index curve for the three perturbations. The curve is fairly smooth when no perturbations are applied; however, a 1% perturbation produces approximately a 20-30% perturbation in the dn/dr profile. The deviation in the curve at 6112.4 km may be the result of such a perturbation. In fact, the dn/dr curve is the best method of checking for a perturbation in the actual data. Orbit 9N has no perturbation greater than 0.1% at the levels of the lower cloud deck as evidenced by the smooth dn/dr curve in this lower region.

Finally, the effect of the perturbations on the pressure-temperature profile is shown in Figure 17. A perturbation of 10% is obvious, a perturbation of 1% may be mistaken for a change in lapse rate and a perturbation of 0.1% can not be detected.

The refractive defocussing used in calculating the absorption coefficient is also affected by the refractive index profile. Figure 18 shows the effects of the perturbations on the refractive index calculated from the perturbed bending angle. A comparison of the shape of the perturbed region of the refractive defocussing curve to the fluctuation in the actual data at 6112.4 km suggests there may indeed by an actual perturbation in the atmosphere at this level. It is at this level that Woo et al. (1980) detect the largest turbulent layer. In the region of the lower cloud deck, however, there is no such turbulent layer or

Figure 15. Refractive index profiles including the original refractive index (n), the perturbed index (n_p) and the refractive index calculated from the perturbed bending angle (n_{pp}).

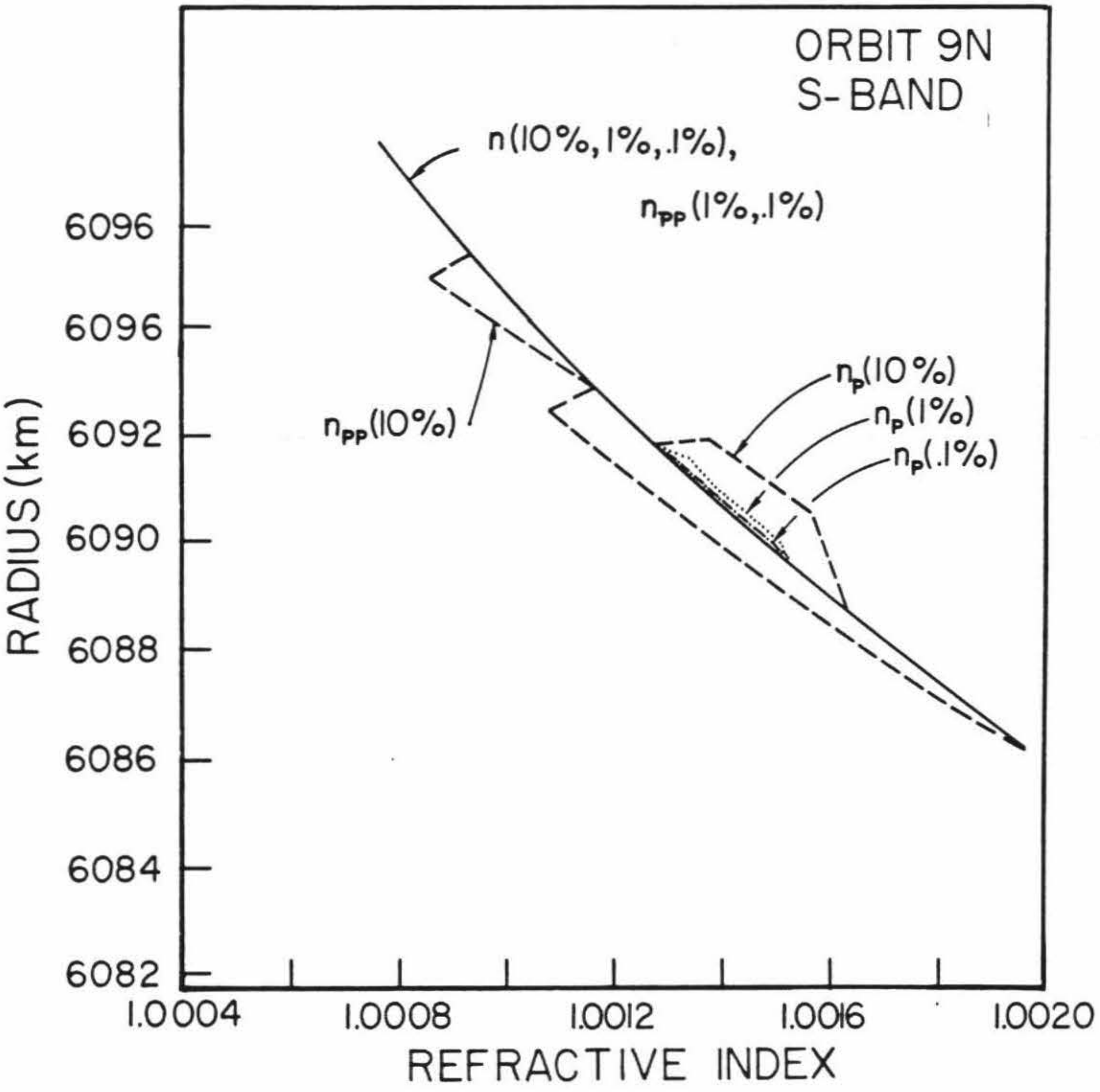
ORBIT 9N
S-BAND
n(10%, 1%, .1%),
n_{pp}(1%, .1%)
n_{pp}(10%)
n_p(10%)
n_p(1%)
n_p(.1%)
RADIUS (km)
6096
6096
6092
6090
6088
6086
6084
6082
1.0004
1.0008
1.0012
1.0016
1.0020
REFRACTIVE INDEX

Figure 16. Profile of $-dn/dr$, the slope of the refractive index profile, for a 10%, 1% and 0.1% perturbation.

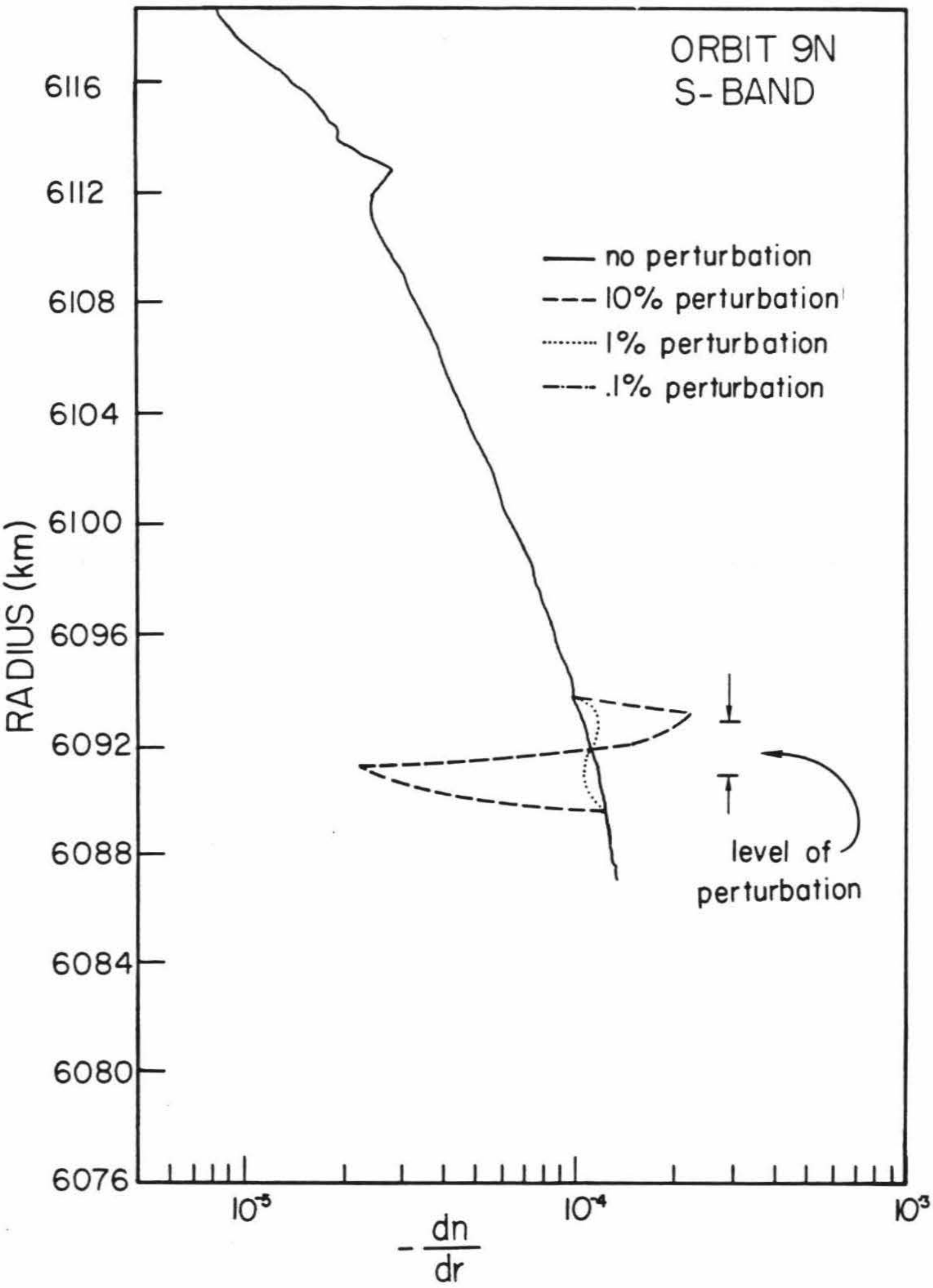
ORBIT 9N
S-BAND
no perturbation
10% perturbation
1% perturbation
.1% perturbation
level of perturbation
RADIUS (km)
6116
6112
6108
6104
6100
6096
6092
6088
6084
6080
6076
10^{-5}
10^{-4}
10^{3}
$-\frac{dn}{dr}$

Figure 17. Temperature profile resulting from a 10%, 1% and 0.1% perturbation in the refractive index profile.

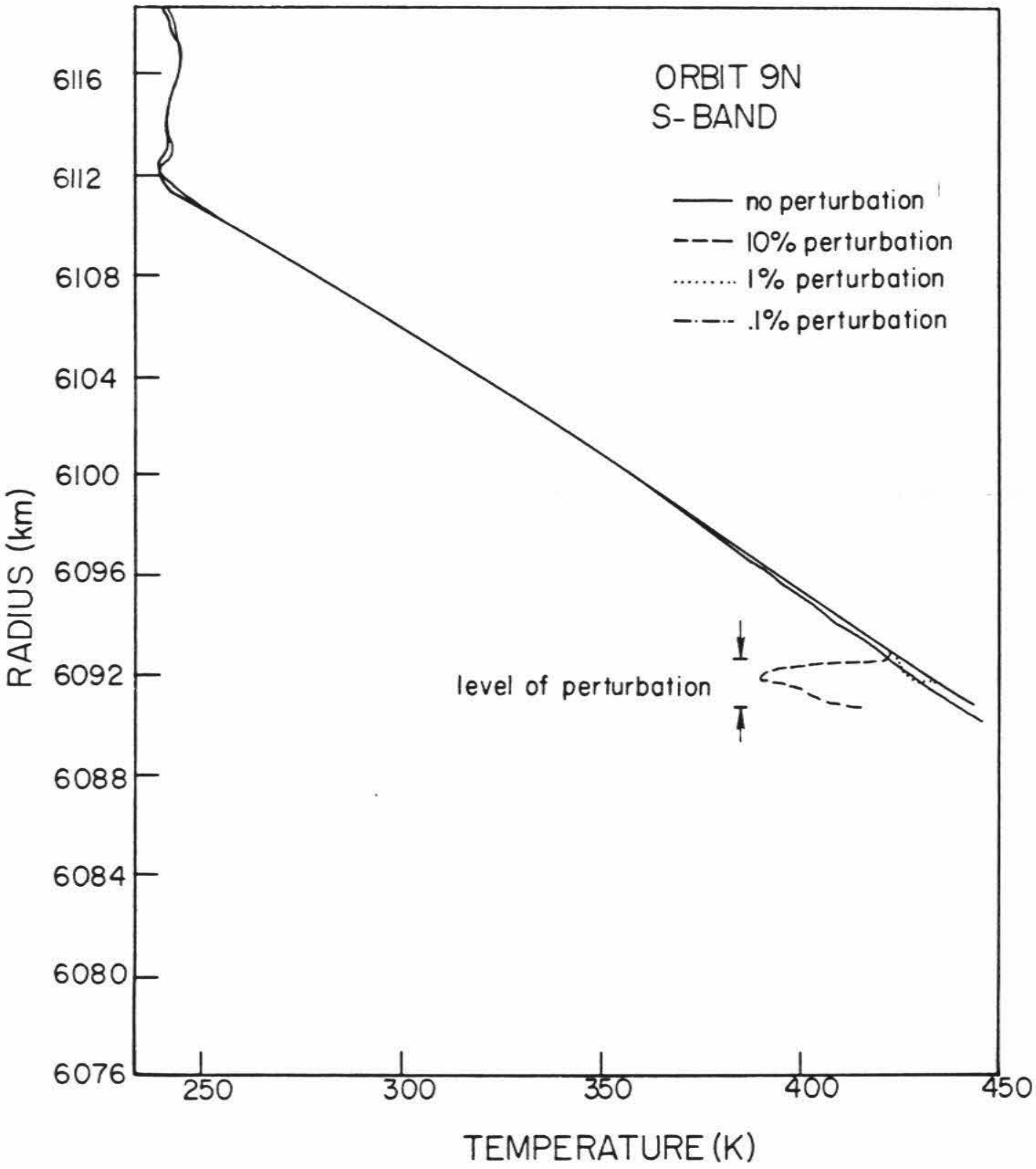
ORBIT 9N
S-BAND
no perturbation
10% perturbation
1% perturbation
.1% perturbation
level of perturbation
RADIUS (km)
6116
6112
6108
6104
6100
6096
6092
6088
6084
6080
6076
250
300
350
400
450
TEMPERATURE (K)

Figure 18. Refractive defocussing resulting from a 10%, 1% and 0.1% perturbation in the refractive index profile.

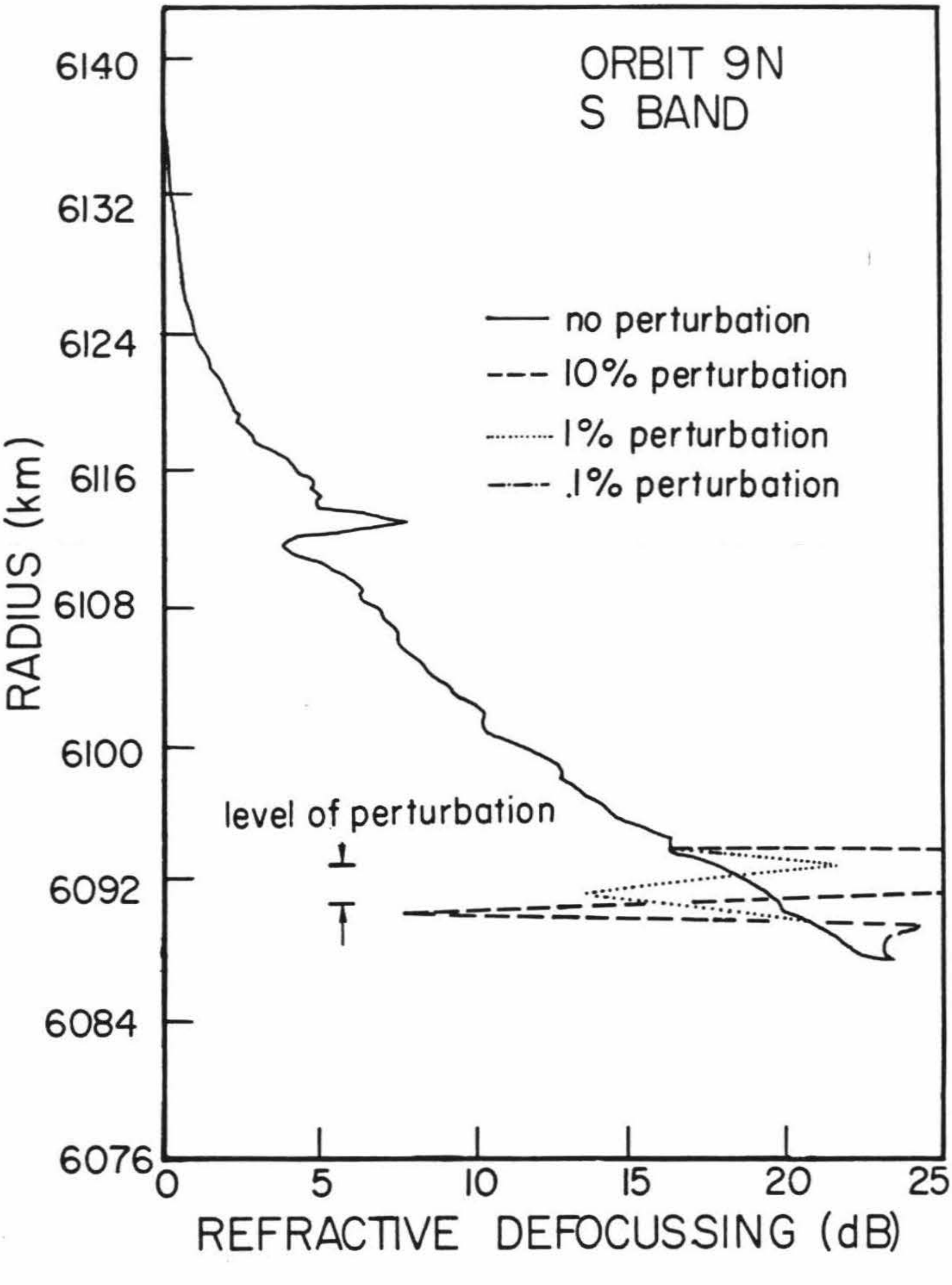
ORBIT 9N
S BAND
no perturbation
10% perturbation
1% perturbation
.1% perturbation
level of perturbation
RADIUS (km)
6140
6132
6124
6116
6108
6100
6092
6084
6076
0
5
10
15
20
25
REFRACTIVE DEFOCUSSING (dB)

associated perturbation as evidenced in the dn/dr curve. The smaller fluctuations in the refractive defocussing curve may indeed be the result of small (0.1%) fluctuations in the refractive index profile. Such fluctuations are included in the final uncertainties calculated for the absorption coefficient profiles.

The results of the investigation of errors resulting from variations in the refractive index profile show perturbations on the order 1% or greater can affect both the pressure-temperature profile and the refractive defocussing profile. Perturbations of such magnitudes are however apparent in the dn/dr curves. These curves are used to determine the existence of any artificially produced fluctuations in the refractive defocussing profile which might be mistaken for cloud layers. In all cases the data were cut off before large fluctuations associated with the lower atmospheric turbulence observed by Woo et al. (1980) were encountered. In several profiles, particularly in the collar region, small fluctuations (much less than what would be produced by a 1% perturbation in the refractive index profile) produced small fluctuations in the final absorption coefficient profile. In all profiles presented in Chapter IV, any small fluctuations in the absorption profiles can be attributed to fluctuations in the refractive index profiles, not layering within the lower cloud deck.

Trajectory uncertainties for all orbits analyzed in this thesis are listed in Table V. The uncertainties are 5 σ values determined from the uncertainty in the x, y, z position of the spacecraft (Kliore, private communication). To determine the effect of the radius uncertainty on the temperature-pressure and refractive defocussing profiles, the radius scale for orbit 9 was artifically shifted by 8 km. The resulting temperature-pressure profile is shown in Figure 19 along with profiles in which no radius shift was applied. There is no discernible difference between the two curves. The refractive defocussing profiles for the shifted and nominal cases are shown in Figure 20 as a function of radius. The only difference between the two profiles is the 8 km radius shift. The final

Figure 19. Temperature profile resulting from a shift of 8 km. There is no discernible difference from the original profile when temperature is plotted as a function of pressure.

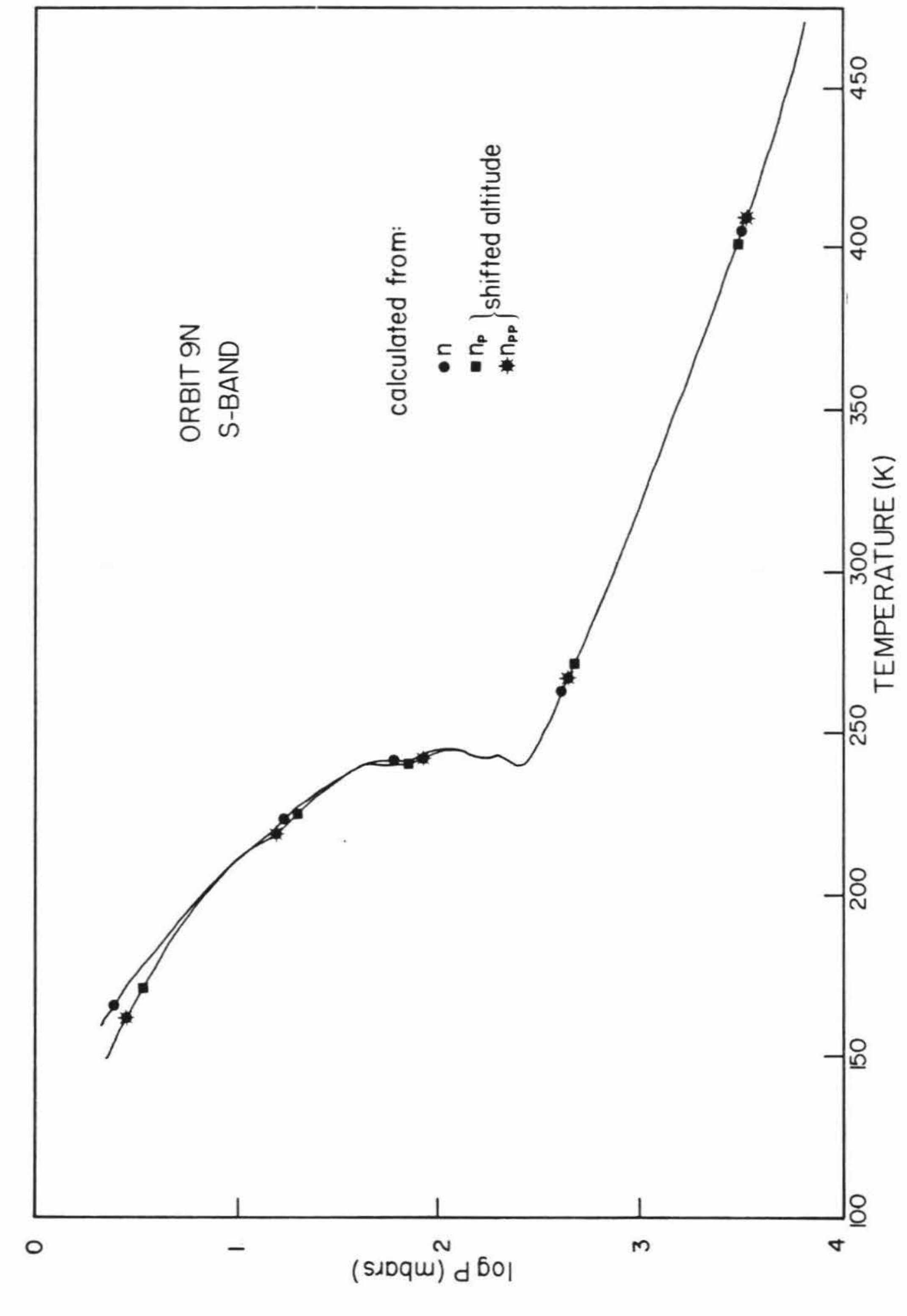
ORBIT 9N
S-BAND
calculated from:
● n
■ n_p
✱ n_{pp}
shifted altitude
TEMPERATURE (K)
100
150
200
250
300
350
400
450
log P (mbars)
0
1
2
3
4

Figure 20. Refractive defocussing determined from the shifted refractivity profile. There is no discernible difference between the two profiles except for the 8 km altitude shift.

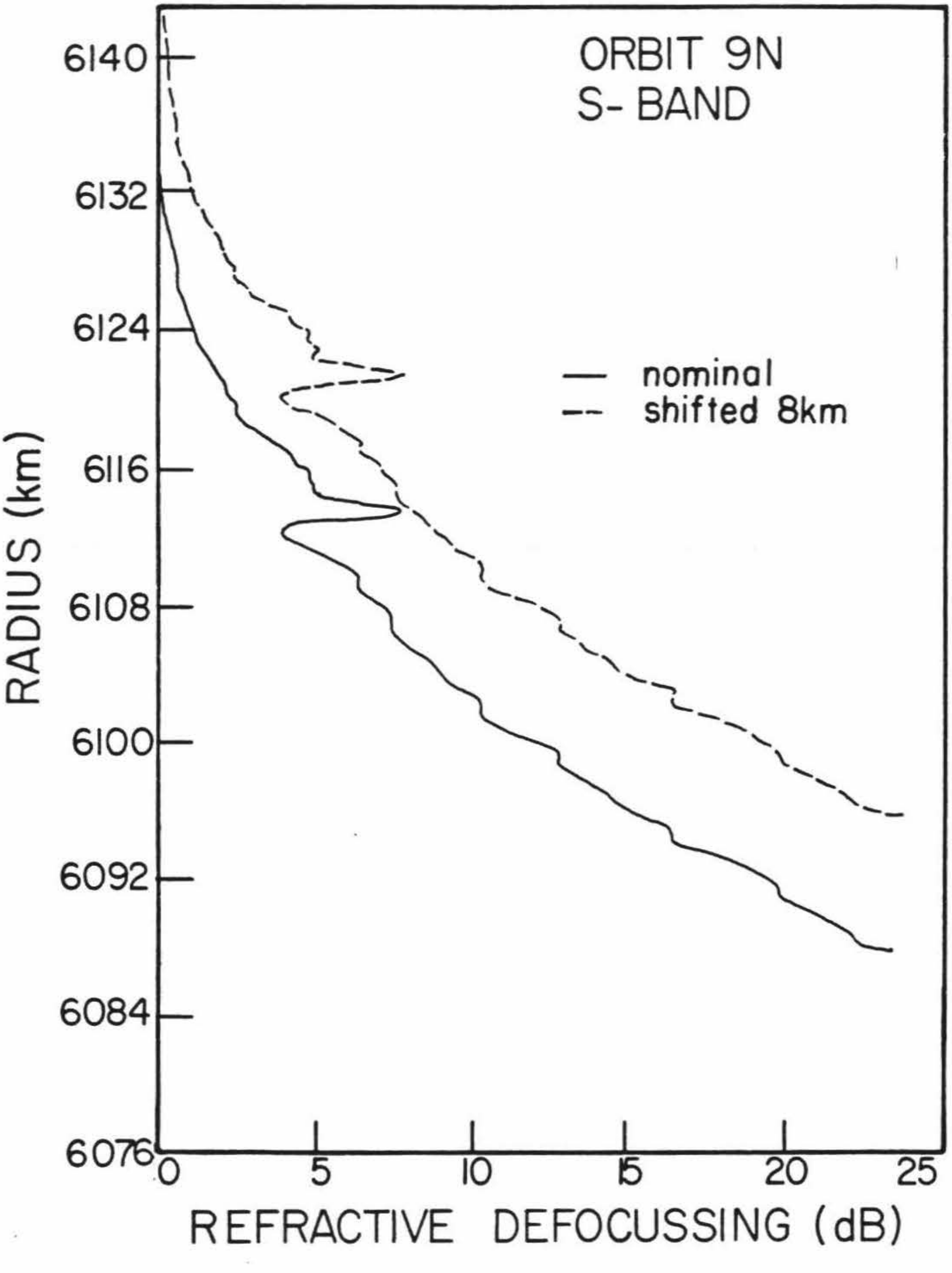
ORBIT 9N
S- BAND
nominal
shifted 8km
RADIUS (km)
6140
6132
6124
6116
6108
6100
6092
6084
6076
0
5
10
15
20
25
REFRACTIVE DEFOCUSSING (dB)

results for all absorption coefficient and temperature profiles will be plotted against pressure to assure a more exact comparison between orbits and eliminate the influence of any trajectory errors.

An oblateness or "expansion" of the atmosphere is caused by the four-day winds on Venus due to the contribution of a centrifugal force from the winds, $\Omega^2 \bar{R}'$, to the Newtonian gravitational force, $\bar{g}_{*}$ · Ω is the angular speed of rotation of the atmosphere at $\bar{R}'$, the position vector from the axis rotation (see Figure 19a). An equipotential surface is described as (Holton, 1979)

Table V

Trajectory errors

Orbit	5 σ Uncertainty (in km)
6	
9	643
18	1.5
19	40.7
21	2.5
29	0.7
30	134.8
45	0.95
69	0.63
338	1.6
339	1.5
340	1.7
342	1.3
347	1.4
350	1.1
352	1.4
358	0.6

$$\Phi_{const} = \Phi_0 k + gz - \frac{1}{2}\Omega^2(z) r^2 \cos^2\lambda \qquad (64)$$

where Φ_0 is the potential in a windless atmosphere at some level r_0, g is the Newtonian gravity at radius r, z is the altitude of the equipotential surface ($z = r - r_{surface}$), and λ is the latitude (see Figure 21). The difference in the level

Figure 21. Geometry used in determining the effect of an oblate atmosphere on the absorption coefficient and temperature data. Figure (d) shows the wind profile used (Counselman,et al., 1980).

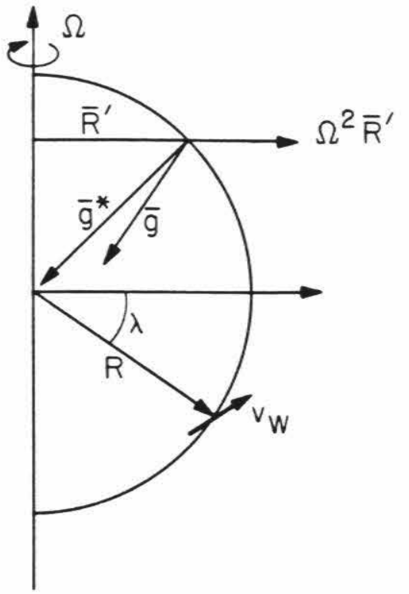

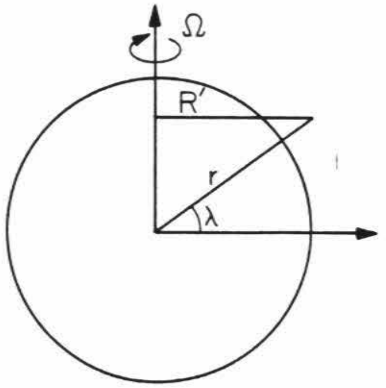

EXAGGERATED
BULGE IN
VENUS
ATMOSPHERE

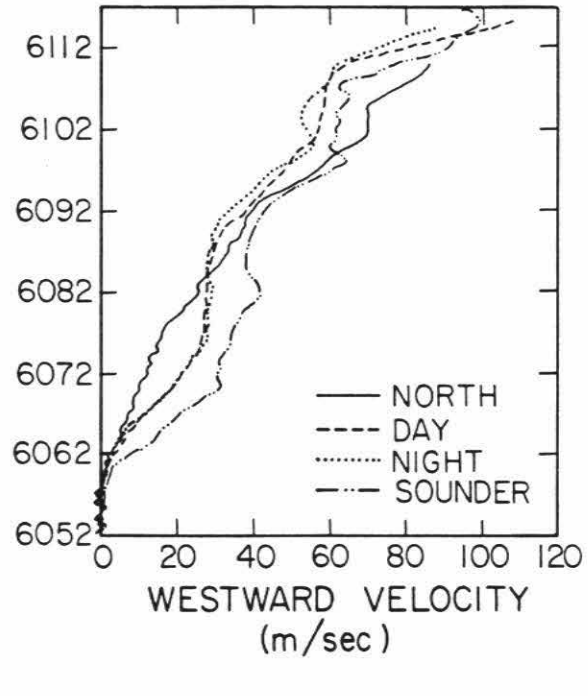

of the equipotential surface for a windy and a windless atmosphere is then

$$\Delta z = \frac{\frac{1}{2}\Omega^2(z)r^2\cos^2\lambda}{g} . \tag{65}$$

On Venus, the four day wind produces a bulge of approximately a kilometer at the 65 km level (Figure 21). The wind profile shown in Figure 21 (Counselman et al., 1980) was used to determine the radial expansion or oblateness resulting from the winds. The resulting pressure-temperature profile for latitudes near the equator is shown in Figure 22. There is approximately a 1% increase in temperature as a result of the oblate atmosphere effect. The effect of the oblate atmosphere on the refractive defocussing profile is negligible in the region of the lower cloud deck as shown in Figure 23.

The above technique investigates the error inherent in an expanded but spherically symmetric pressure profile. The differences will result in errors when latitudinal dependences are investigated. In order to investigate the error resulting from a non-spherical atmosphere as suggested by the oblateness produced by the winds, a technique derived by Kliore (private communication) based in part on the work of Eshleman (1975) and Hubbard et al, (1975) may be used. The difference in temperature, dT, produced by the winds at a latitude λ is

$$\frac{dT}{T} = 2\psi\frac{d}{H}\ \alpha\tan\beta \tag{66}$$

where ψ is the bending angle, d is the distance between the limb and the spacecraft, H is the scale height, β is the angle between the projected velocity vector of the ray and the local vertical and

$$\alpha = \frac{v^2}{gR}\tan A \tag{67}$$

where v is the wind velocity, g is gravity and R is the radius from the planet center to the wind level. Inasmuch as the winds will be a maximum at the equator assuming solid body rotation and tanλ will be a maximum at the pole, a worst case example is assumed to be about 70° latitude. Again the probe wind profile (Counselman et al, 1980) is used and tanβ is assumed to be one. The

Figure 22. Temperature profile resulting from an oblate refractivity profile.

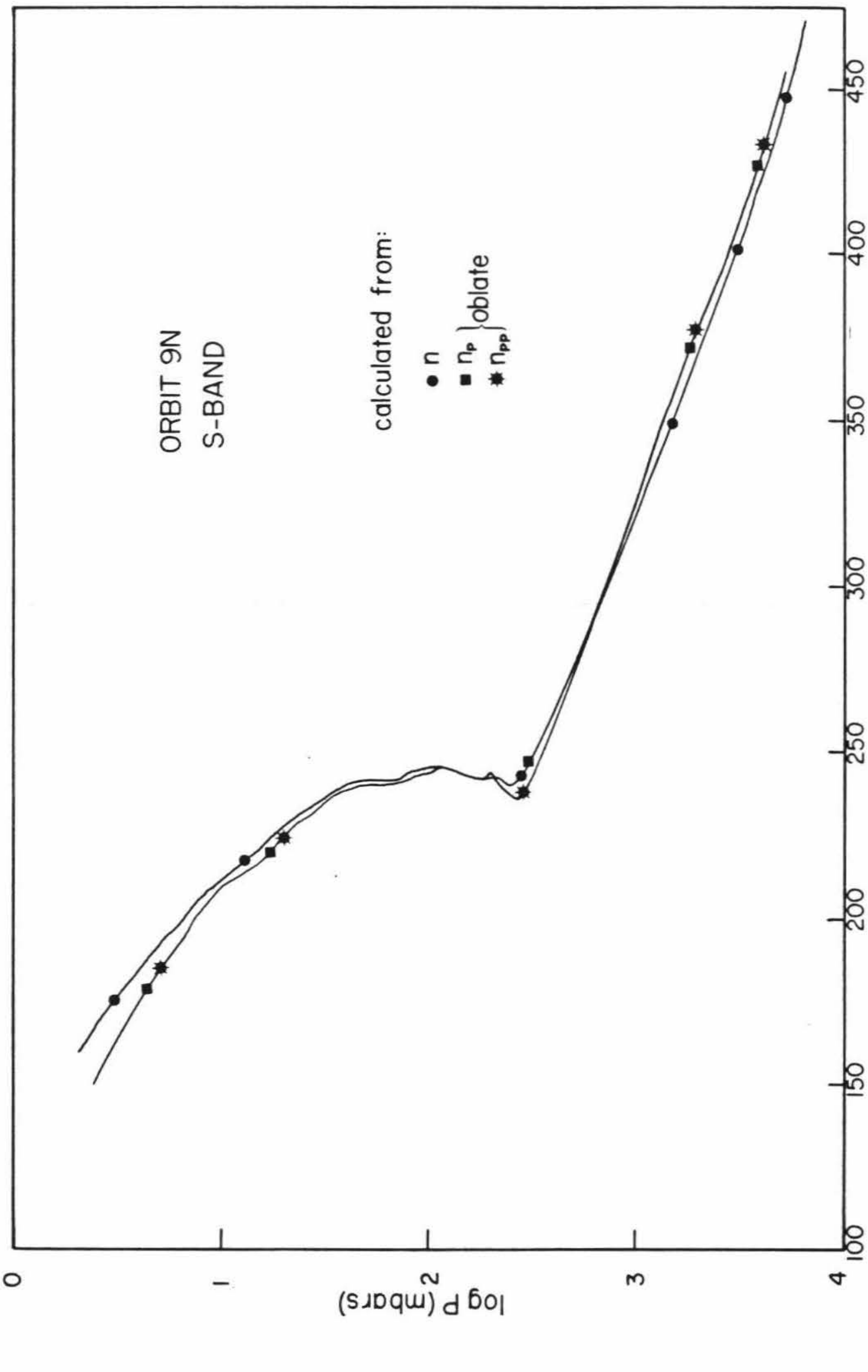
ORBIT 9N
S-BAND
calculated from:
● n
■ n_p }oblate
✱ n_{pp}
TEMPERATURE (K)
100
150
200
250
300
350
400
450
log P (mbars)
0
1
2
3
4

Figure 23. Refractive defocussing profile determined from an oblate refractivity profile.

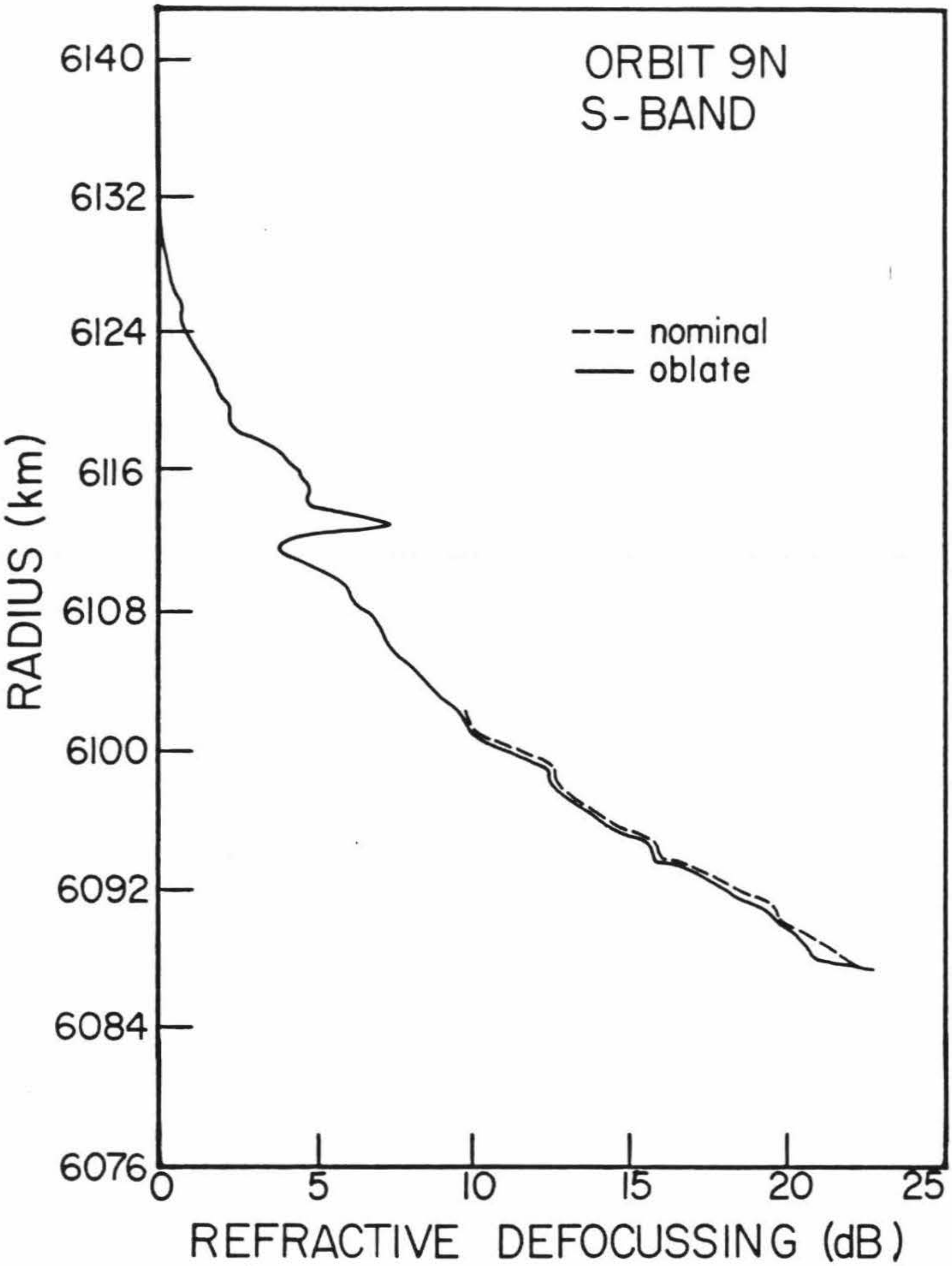
ORBIT 9N
S-BAND
--- nominal
— oblate
RADIUS (km)
6140
6132
6124
6116
6108
6100
6092
6084
6076
0
5
10
15
20
25
REFRACTIVE DEFOCUSSING (dB)

difference in refractivity, N, may be calculated by differentiating the relation $N = PQ/T$. P and Q are assumed to be constant and Q is defined in equation (24). The result is

$$dN = \left[\frac{dT}{T}\right] \frac{TN^2}{PQ} = -\frac{N}{T} dT \ . \tag{68}$$

Table VI lists dT/T, dT and dN as a function of radius for orbit 9N. The difference in temperature at the lower levels of the atmosphere is less than 1%, however this corresponds to a temperature difference of up to 6 K, which is significant. The resulting temperature and refractive defocussing profiles are shown in Figures 24 and 25, respectively. The error in the temperature again is significant however the error in the refractive defocussing is negligible.

6. Pressure Temperature Profiles for All Orbits

Figure 26 describes the temperature-pressure profiles for all orbits for which absorption coefficient data are available. The collection of profiles is divided into four groups according to latitudinal location on the planet. The groups include equatorial, midlatitude (20°-60°), collar and polar regions. The collar is a region of decreased IR brightness temperature and increased turbulence. Within a group or region on Venus, the greatest variation in temperature occurs in the collar region — when the temperature at a given level varies by as much as 30 K. The other three regions show temperature variations of only about 10 K at a given altitude or pressure level.

Figure 27 shows the variation with latitude of the temperature at the 1 bar level. From the pole to about 50° north, there is a rapid increase in temperature of approximately 7° in temperature per ten degrees of latitude. From 50° north to about 30° south, the temperature at the 1 bar level remains fairly constant to within a few degrees. South of 30°S the temperature again begins to decrease. It will be seen later that the latitudinal variations in altitude of the

Figure 24. Temperature profile for an oblate atmosphere.

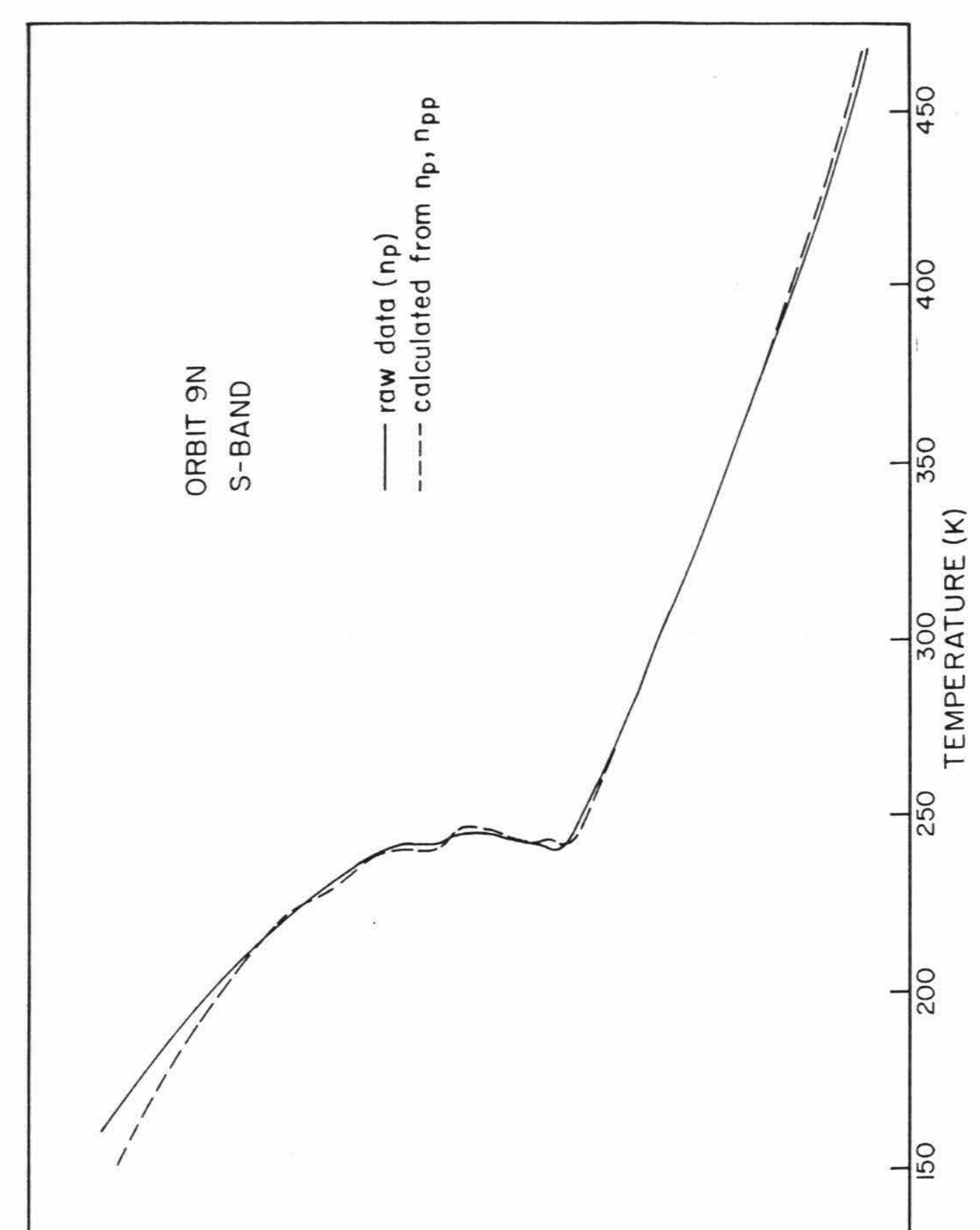
ORBIT 9N
S-BAND
—— raw data (n_p)
- - - - calculated from n_p, n_{pp}
TEMPERATURE (K)
log P (mbars)
100
150
200
250
300
350
400
450
0
1
2
3
4

Figure 25. Refractive defocussing profile for an oblate atmosphere.

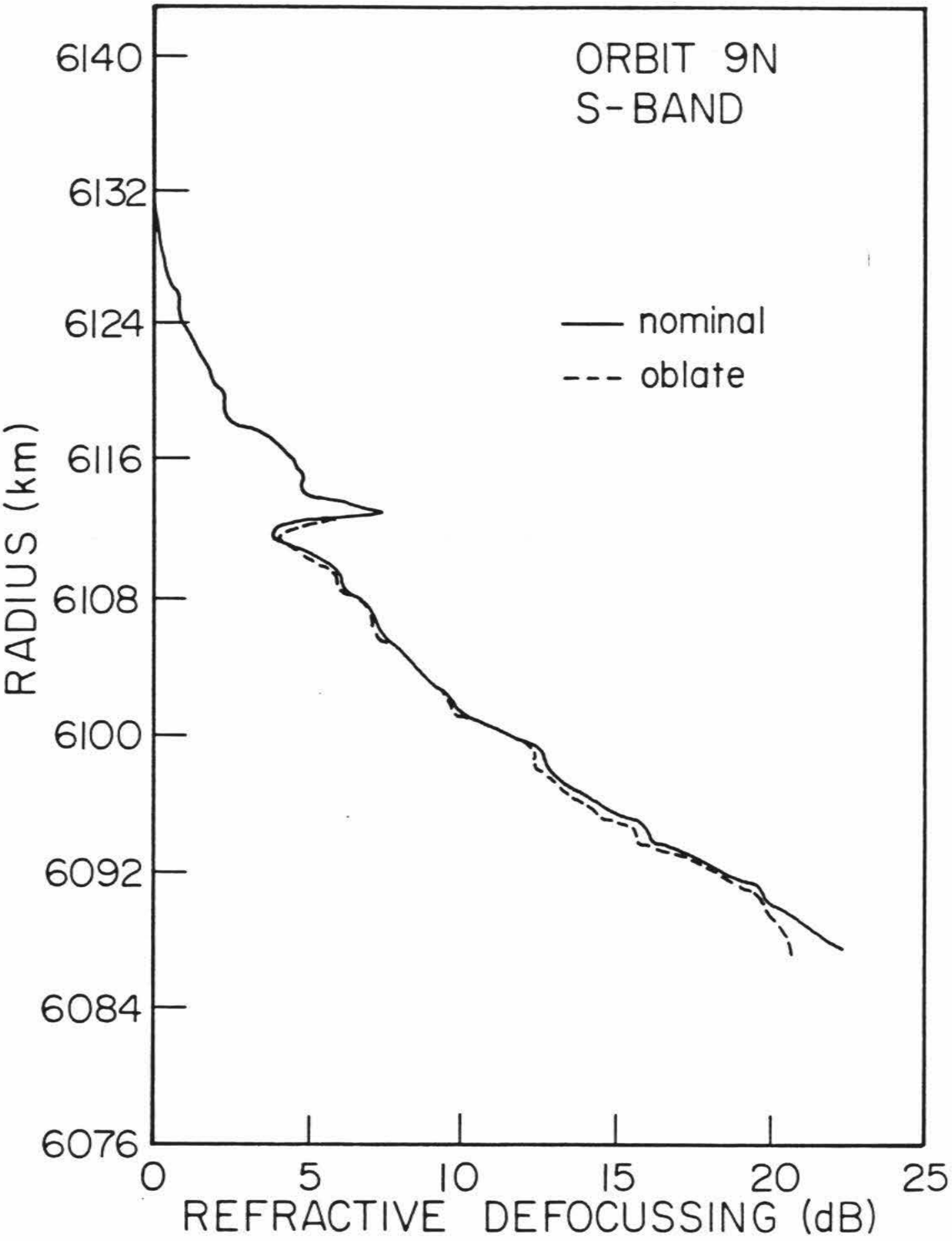
ORBIT 9N
S-BAND
nominal
oblate
RADIUS (km)
6140
6132
6124
6116
6108
6100
6092
6084
6076
0
5
10
15
20
25
REFRACTIVE DEFOCUSSING (dB)

Figure 26. Pressure-temperature profiles for all orbits thus far analyzed for absorption coefficients.

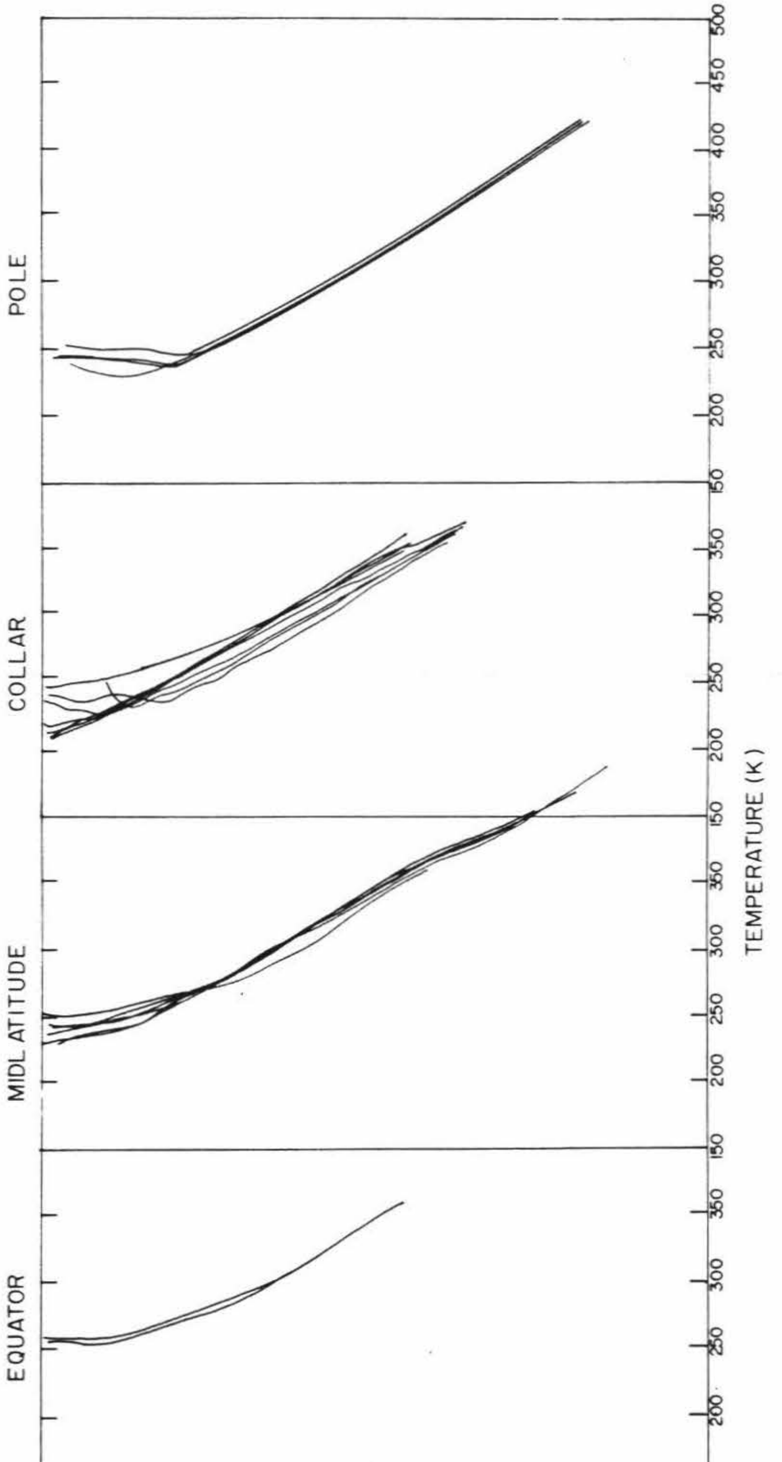
EQUATOR
MIDLATITUDE
COLLAR
POLE
TEMPERATURE (K)
PRESSURE (bars)
1
10
100
150
200
250
300
350
150
200
250
300
350
150
200
250
300
350
150
200
250
300
350
400
450
500

Figure 27. Temperature at the 1 bar level as a function of latitude.

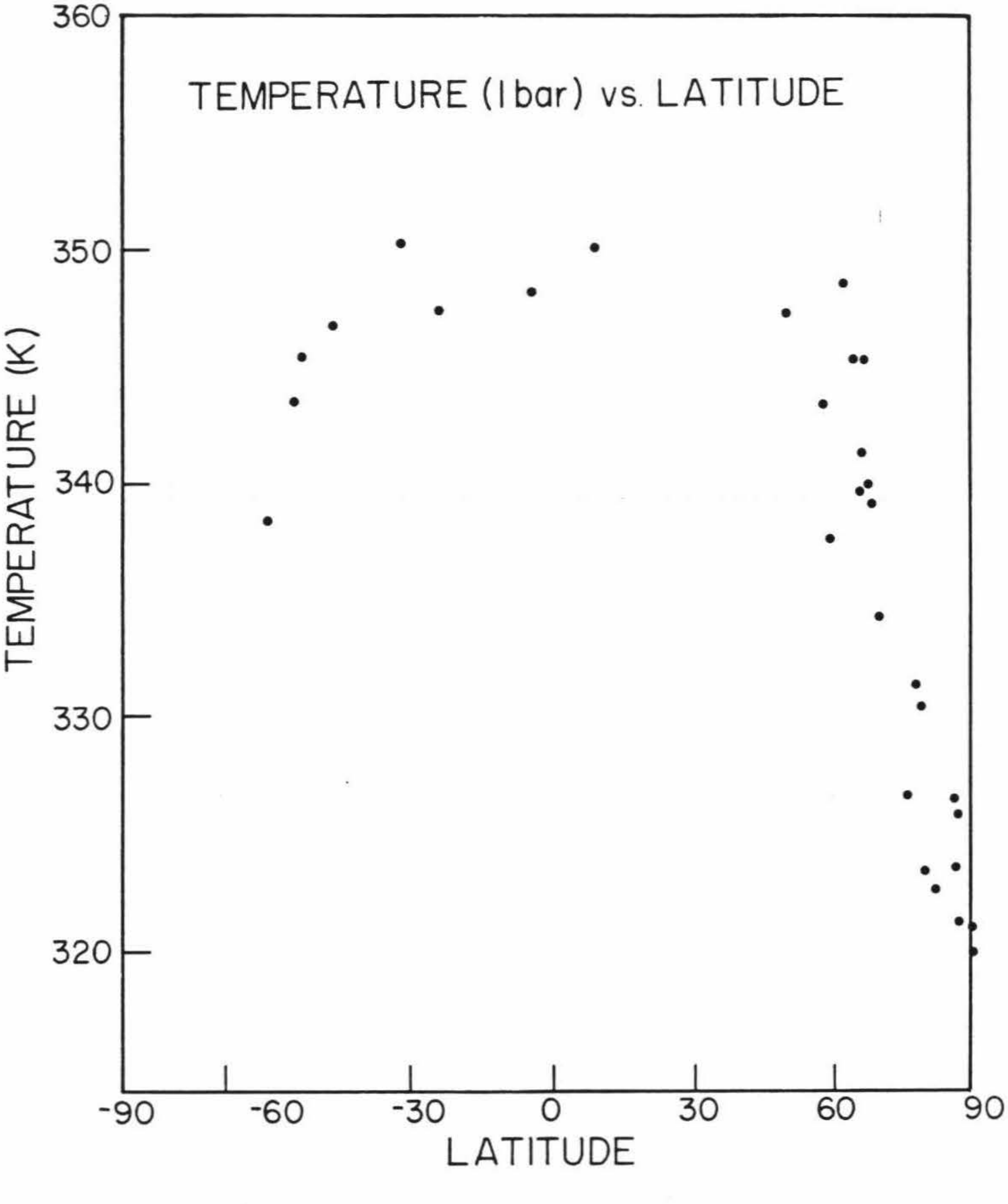
TEMPERATURE (I bar) vs. LATITUDE
TEMPERATURE (K)
360
350
340
330
320
-90
-60
-30
0
30
60
90
LATITUDE

Table VI

Uncertainty due to Oblateness

Radius (km)	dT/T	dT (K)	dN (N-units)
6086.6	0.00977	5.82	-12.6
6087.0	0.00937	5.52	-11.6
6087.1	0.00963	5.65	-11.9
6087.5	0.00898	5.22	-10.7
6088.3	0.00825	4.69	-9.09
6089.1	0.00781	4.34	-7.88
6090.0	0.00756	4.11	-7.01
6090.8	0.00720	3.82	-6.12
6091.4	0.00675	3.53	-5.36
6092.2	0.00629	3.22	-4.58
6092.6	0.00602	3.03	-4.11
6093.3	0.00600	2.98	-3.88
6093.8	0.00608	2.98	-3.70
6094.3	0.00606	2.94	-3.49
6094.8	0.00594	2.84	-3.25
6095.2	0.00591	2.80	-3.07
6095.7	0.00589	2.76	-2.91
6096.2	0.00586	2.71	-2.74
6096.6	0.00586	2.68	-2.61
6097.1	0.00593	2.69	-2.51
6097.4	0.00594	2.67	-2.42
6097.8	0.00602	2.68	-2.34
6098.2	0.00608	2.69	-2.26
6098.6	0.00607	2.66	-2.15
6099.0	0.00602	2.61	-2.03
6099.4	0.00598	2.57	-1.93
6099.8	0.00593	2.53	-1.84
6100.1	0.00591	2.51	-1.76
6100.4	0.00587	2.48	-1.69
6100.0	0.00579	2.42	-1.60
6100.1	0.00571	2.37	-1.52
6101.5	0.00560	2.31	-1.43
6102.0	0.00546	2.23	-1.33
6102.2	0.00533	2.16	-1.25
6102.5	0.00522	2.10	-1.17
6102.8	0.00511	2.05	-1.10
6103.2	0.00499	1.98	-1.04
6103.5	0.00487	1.92	-0.971
6103.8	0.00477	1.87	-0.914
6104.1	0.00465	1.81	-0.859
6104.4	0.00453	1.75	-0.805
6104.7	0.00440	1.69	-0.749
6105.1	0.00425	1.62	-0.693
6105.4	0.00410	1.55	-0.638
6105.8	0.00394	1.48	-0.582
6106.2	0.00377	1.40	-0.530

Table VI (continued)

Radius (km)	dT/T	dT (K)	dN (N-units)
6106.5	0.00361	1.33	-0.483
6106.8	0.00349	1.28	-0.447
6106.1	0.00341	1.24	-0.420
6107.4	0.00331	1.19	-0.389
6107.8	0.00322	1.15	-0.361
6108.1	0.00316	1.12	-0.340
6108.3	0.00312	1.09	-0.319
6108.7	0.00308	1.07	-0.300
6108.9	0.00303	1.05	-0.284
6109.3	0.00301	1.03	-0.267
6109.6	0.00298	1.01	-0.252
6110.0	0.00298	1.00	-0.238
6110.4	0.00299	0.996	-0.224
6110.8	0.00304	1.00	-0.213
6111.4	0.00323	1.05	-0.205
6111.8	0.00334	1.07	-0.195
6112.1	0.00342	1.08	-0.184
6112.4	0.00349	1.09	-0.172
6112.7	0.00329	1.02	-0.148
6113.0	0.00308	0.947	-0.127
6113.3	0.00307	0.932	-0.117
6113.5	0.00298	0.899	-0.108
6113.9	0.00299	0.889	-0.0972
6114.1	0.00287	0.849	-0.0892
6114.6	0.00279	0.811	-0.0770
6114.9	0.00265	0.760	-0.0662
6115.3	0.00254	0.722	-0.0584
6115.5	0.00242	0.680	-0.0515
6116.0	0.00231	0.640	-0.0444
6116.3	0.00217	0.594	-0.0383
6116.8	0.00198	0.533	-0.0311
6117.3	0.00185	0.488	-0.0261
6117.7	0.00177	0.458	-0.0228
6118.0	0.00167	0.425	-0.0199
6118.5	0.00157	0.395	-0.0172
6118.9	0.00148	0.363	-0.0146
6119.2	0.00136	0.332	-0.0125
6119.7	0.00126	0.304	-0.0104
6120.1	0.00115	0.275	-0.00878

level of the lower cloud deck may be associated with the latitudinal variation in temperature shown in Figure 27.

Variations in the temperature profiles are important in calculating the concentration of the sulfuric acid cloud particles from the measured water vapor profiles and sulfuric acid-water saturates vapor pressure data (see section V.4). The dielectric constants of the cloud particles, and therefore their absorption properties, are also temperature dependent. These temperature dependences and their associated effects on the uncertainties of the mass contents will be discussed in later chapters.

7. Lapse Rates

The deviation of the atmospheric lapse rate, Γ, calculated from the occultation temperature profiles from the dry adiabatic lapse rate Γ_d, was calculated for all orbits in order to investigate a possible change in lapse rate due to condensation or evaporation in the cloud region.

To calculate the atmospheric lapse rate, a cubic spline curve was fit to the temperature and radius data points for 5, 7 and 9 consecutive points for orbit 350N. The slope was then calculated at the central point (3rd, 4th and 6th point). The resulting lapse rate differed by less than 1%. Lapse rates for all other orbits were calculated using five consecutive points.

The dry adiabatic lapse rate was estimated from the heat capacity of the atmosphere, assuming the atmosphere is ideal, as:

$$\Gamma_d = -\frac{g}{C_p} \tag{69}$$

where C_p is the heat capacity for 100% CO_2 and varies with temperature and pressure, and g is gravity. The differences in the two lapse rates is

$$\Delta\Gamma = \Gamma - \Gamma_d \ . \tag{70}$$

$\Delta\Gamma$ is shown for orbits 69X (equatorial), 30X (midlatitudinal), 358N (collar) and 9N (polar) in Figure 28 along with the respective absorption coefficient profiles. In all cases $\Delta\Gamma$ is greater than zero in the region of the lower cloud deck. The lapse rate for orbit 358N fluctuates to a much greater extent than in other regions of the atmosphere. This is typical of lapse rate profiles in the collar region and is probably related to greater turbulence in this region.

The lapse rate profiles indicate the atmosphere is very stable throughout the lower cloud region. This was also observed in the temperature profiles determined by the probes (Seiff et al. 1980). The unstable layer above the 0.3 bar pressure level is associated with the middle cloud and may represent a phase change —possibly the freezing of sulfuric acid.

Figure 28. The deviation of the actual lapse rate from the dry adiabatic lapse rate. Also shown are the corresponding absorption coefficient profiles for orbits 69X (equatorial), 30X (midlatitudinal), 358N (collar) and 9N(polar).

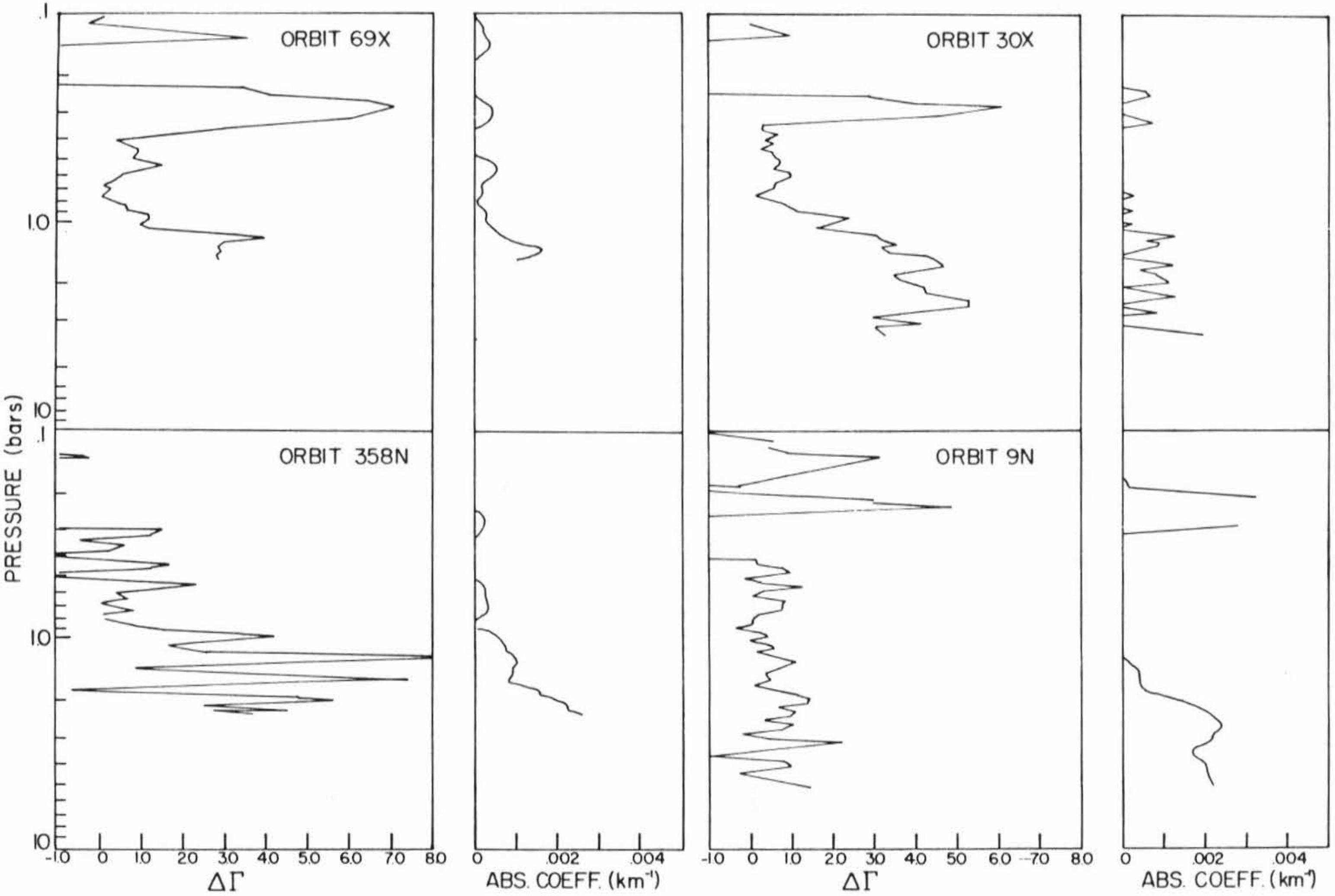
ORBIT 69X
ORBIT 30X
ORBIT 358N
ORBIT 9N
PRESSURE (bars)
.1
1.0
10
-1.0
0
1.0
2.0
3.0
4.0
5.0
6.0
7.0
8.0
ΔΓ
0
.002
.004
ABS. COEFF. (km⁻¹)

CHAPTER IV

ABSORPTION COEFFICIENT PROFILES FROM AMPLITUDE DATA

The amplitude data received from the Pioneer Venus spacecraft are the primary data used to construct the absorption coefficient profiles. These data are affected by three factors:

1. index of refraction gradients in the gaseous atmosphere,
2. attenuation by atmospheric gases and clouds, and
3. deviations of the radio link antenna maximum-gain axis from the refracted direction of the earth.

Deviations of the antenna maximum-gain axis are due to both refraction of the signal by the atmosphere and motion of the antenna due to a predetermined program of antenna slews designed to counteract the refraction effects. In addition, deviations of the spacecraft spin axis from its nominal position due to imbalances and other factors produce gain axis variability. In the particular case of the Pioneer Venus spacecraft, a slight wobble as the spacecraft precessed around its own axis provided sufficient antenna axis motion to render much of the X-band occultation data useless. The effect of errors resulting from the wobble in both S- and X-band power profiles will be discussed.

In order to isolate specifically the excess attenuation or power loss due to atmospheric absorption by gases and clouds, losses due to refractive defocussing and antenna motions must be deleted from the original power profiles. The details and associated errors of the procedure are discussed in this chapter.

1. Calculation of Corrected Power Profile

In order to correct for off-axis pointing of the radio antenna, the difference between the direction of the antenna centerline and the direction of the virtual image of the earth must be determined. Any mispointing will result in a reduction in the power received at earth which must not be confused with power loss due to absorption. Figure 29 shows the antenna power patterns for both S- and X-band wavelengths for the antenna used on Pioneer Venus. The curves were produced in the laboratory before launching Pioneer Venus. As can be seen from the two profiles, a mispointing of a few degrees results in little change in the S-band power; however, a mispointing of only a degree results in a significant drop in X-band power.

To assure the refracted ray is received on earth at all times during an occultation, the antenna must be continually repointed. This is done by moving the antenna in a series of preplanned antenna slews throughout the occultation period. Inasmuch as these slews cannot follow the earth perfectly, the antenna is never pointed directly at Earth. Therefore corrections must be made for any mispointing which occurs during the slews.

Table VII lists the angle between the Earth and the antenna maximum gain axis at the end of each occultation. This angle represents the magnitude of mispointing and can therefore be used to estimate the maximum possible error due to mispointing assuming the antenna offset was not accounted for correctly. From the antenna patterns shown in Figure 29, power loss resulting from antenna mispointings are calculated and listed in Table VII for both S- and X-band wavelengths. As can be seen, a few degrees of mispointing indeed does not affect the S-band power profile; however, it can seriously affect the X-band power profile. As long as the mispointing is corrected, useful X-band data can be

Figure 29. Antenna power patterns for S-and-X band as a function of elevation angle. These profiles were measured in the laboratory.

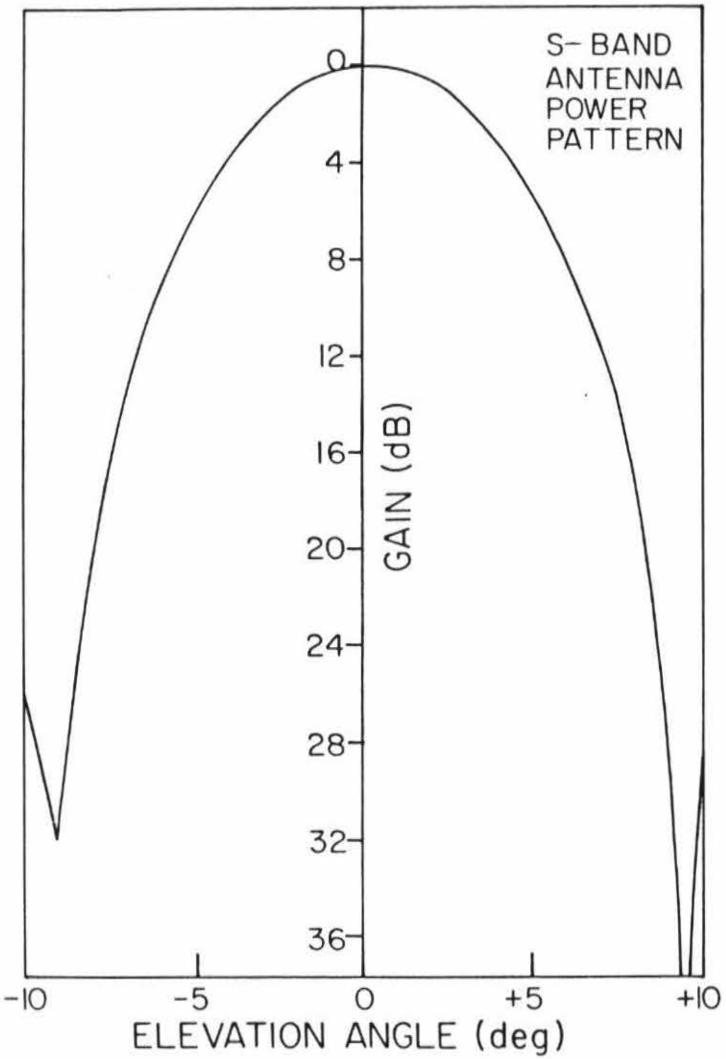
S- BAND
ANTENNA
POWER
PATTERN
GAIN (dB)
0
4
8
12
16
20
24
28
32
36
-10
-5
0
+5
+10
ELEVATION ANGLE (deg)

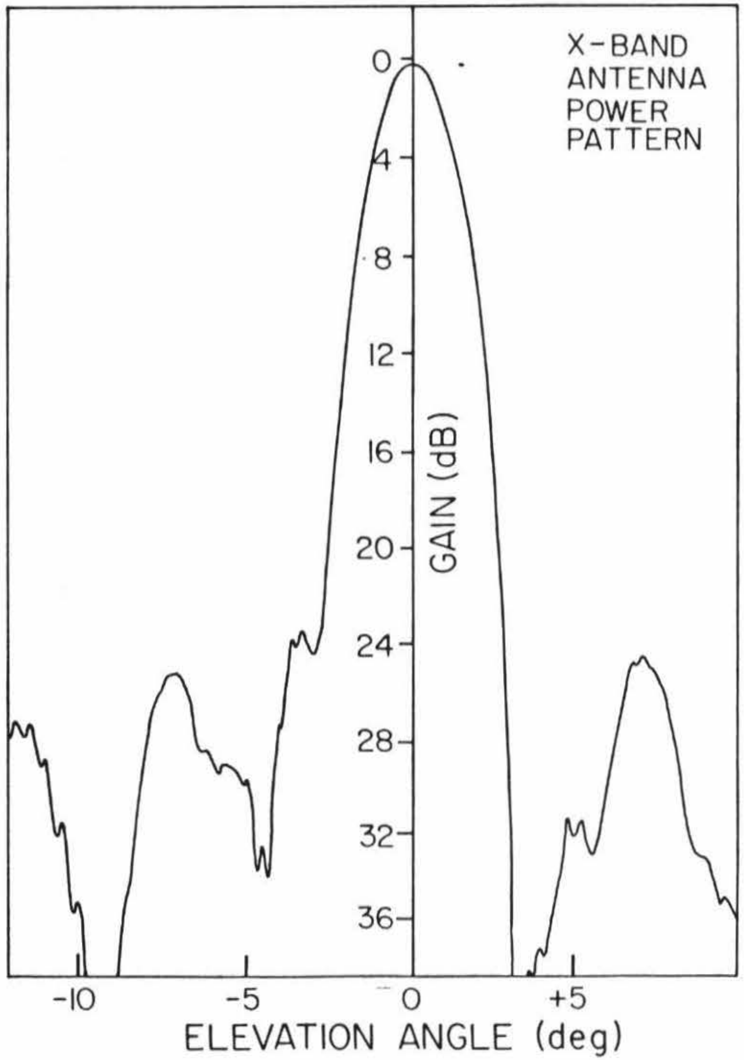
X-BAND
ANTENNA
POWER
PATTERN
GAIN (dB)
0
4
8
12
16
20
24
28
32
36
-10
-5
0
+5
ELEVATION ANGLE (deg)

Table VII

Gain Loss from Angle between Earth and Antenna for S- and X-Band

Orbit	Angle between Earth and Antenna Axis (deg)	dB Loss S-band	dB Loss X-band
6	0.61	0.1	0.9
9	1.37	0.2	3.9
18	0.87	0.1	1.9
19	0.72	0.1	1.0
21	0.17	< 0.1	0.1
29	not available		
30	1.06	0.2	2.9
45	1.21	0.2	3.2
69	no command tables used		
338	0.26	< 0.1	0.1
339	0.33	< 0.1	0.2
340	0.27	< 0.1	0.1
342	0.41	< 0.1	0.2
347	0.23	< 0.1	0.2
350	0.43	< 0.1	0.2
352	0.30	< 0.1	0.15
358	0.33	< 0.1	0.2

expected, however if there are additional uncertainties in the antenna position, such as uncertainties caused by the spacecraft wobble mentioned earlier, the X-band data may be useless.

In order to determine the actual antenna off axis angle, the angle between the beam and the Earth must be determined (Figure 30). Trajectory data and command tables listing the antenna position throughout each occultation are available for each orbit except 69X. These data are used to calculate the angle between the antenna axis and the virtual direction of earth as a function of time as described here.

The occultation location for orbit 69X was near the equator therefore the data were desirable for comparing resulting mass content profiles to those measured by the Sounder Particle Size Spectrometer. The trajectory data for this orbit were determined using a simulated spin period however because the

Figure 30. Geometry used in determining the angle between the antenna beam and the refracted direction of the earth.

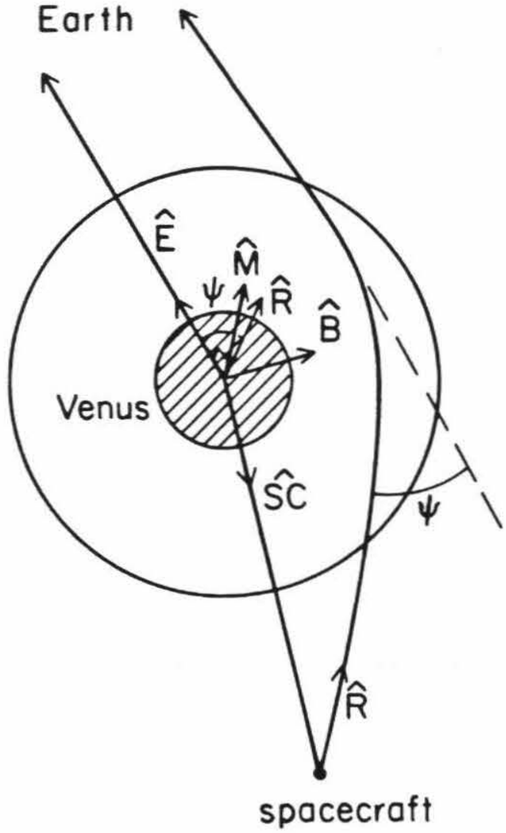
Earth
$\hat{E}$
$\hat{M}$
ψ
$\hat{R}$
$\hat{B}$
Venus
$\hat{SC}$
ψ
$\hat{R}$
spacecraft

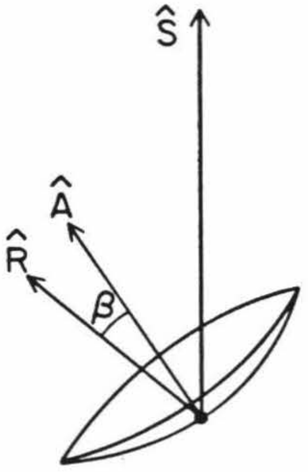
$\hat{S}$
$\hat{A}$
$\hat{R}$
β

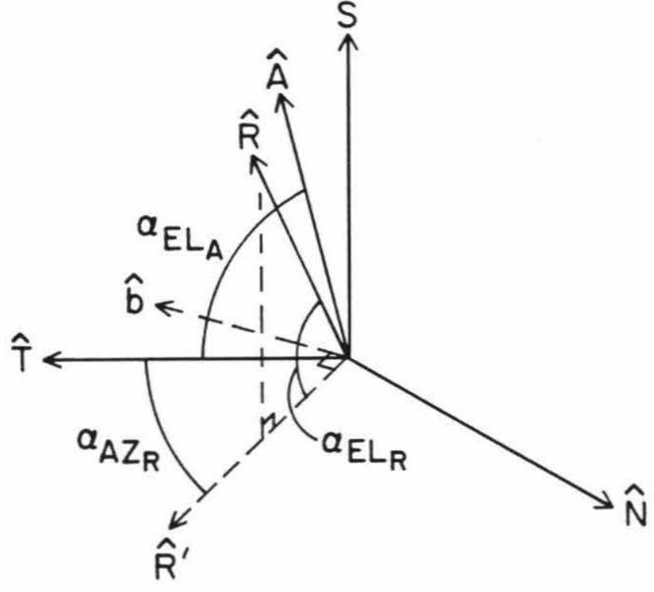
$\hat{S}$
$\hat{A}$
$\hat{R}$
α_{EL_A}
$\hat{b}$
$\hat{T}$
α_{AZ_R}
α_{EL_R}
$\hat{N}$
$\hat{R}'$

sun was eclipsed by Venus relative to the spacecraft during the occultation. This simulated spin period contained a drift which was estimated to give up to a degree of uncertainty in the spacecraft and antenna positions toward the end of the occultation. For this reason no command tables were available. Inasmuch as a one degree uncertainty in the antenna position results in little change in the S-band power, the occultation from orbit 69X was analyzed with no power corrections.

The direction of the refracted ray, $\hat{R}$, is determined from the bending angle, ψ, and the positions of the spacecraft, $\widehat{SC}$, and the earth, $\hat{E}$, relative to Venus as follows (see Figure 30)

$$\hat{R} = \hat{E} \cos\psi + \hat{B} \sin\psi \tag{71}$$

where $\hat{B} = \hat{M} \times \widehat{SC}$, $M = \hat{E} \times \widehat{SC}$, and where $\hat{R}$, $\hat{E}$, $\widehat{SC}$, $\hat{B}$, and $\hat{M}$ are unit vectors. All vectors are in x, y, and z coordinates in an equatorial coordinate system.

The direction of the antenna centerline is determined by setting up a coordinate system using the spacecraft spin axis $\hat{S}$, and the antenna centerline, $\hat{A}$. $\hat{S}$ and $\hat{A}$ are determined from the command tables which give the spacecraft spin vector and antenna centerline in terms of declination and right ascension as a function of time during occultation.

The spacecraft coordinate system is defined by unit vectors $\hat{N}$, $\hat{T}$ and $\hat{S}$ as

$$\hat{N} = \hat{S} \times \hat{A} \tag{72}$$

$$\hat{T} = \hat{N} \times \hat{S} \tag{73}$$

and is shown in Figure 30. The azimuth, elevation and angles, ψ_{AZ} and ψ_{EL}, of $\hat{R}$ and $\hat{A}$ in the $\hat{N}$, $\hat{T}$, $\hat{S}$ coordinate system are calculated as follows:

$$\psi_{EL_R} = \frac{\pi}{2} - \cos^{-1}(\hat{R}\cdot\hat{S}) \ , \tag{74}$$

$$\psi_{AZ_R} = \frac{\pi}{2} - \cos^{-1}(\hat{D}\cdot\hat{T}) \tag{75}$$

where

$$\hat{D} = \hat{R} \times \hat{S} \tag{76}$$

and

$$\psi_{EL_A} = \cos^{-1}(\hat{T}\cdot\hat{A}) \ . \tag{77}$$

Note that in this coordinate system, $\psi_{AZ_A} = 0$. The difference in azimuth between $\hat{A}$ and $\hat{R}$ is then just ψ_{AZ_R} and the difference in elevation is

$$\Delta\psi_{EL} = \psi_{EL_A} - \psi_{EL_R} \ . \tag{78}$$

ψ_{AZ_R} and $\Delta\psi_{EL}$ describe the off-axis angle, or mispointing, in the azimuth and elevation directions, respectively.

Gain tables for the Pioneer Venus antenna are measured in the laboratory for each wavelength, for elevation and azimuth direction, and for nine different dish elevations. The gain at the off axis angle calculated above is determined for each of the nine dish elevations from their associated antenna patterns. Given the azimuth gain, $G(\psi_{AZ})$, and the elevation gain, $G(\Delta\psi_{EL})$, a single gain at the appropriate angle between ψ_{AZ} and $\Delta\psi_{EL}$ is estimated for each of the nine dish elevations. This value is determined by interpolation as described in Figure 31. A constant gain contour as shown in the insert in Figure 31 may be described as an ellipse with axes a and b. The gain, $G(r)$, is equal to $G(a)$ and $G(b)$. Once a (or b) is known, $G(r)$ is known.

The ellipse in the insert in Figure 31 is described by:

Figure 31. Geometry used in interpolating between the azimuth and elevation gain tables.

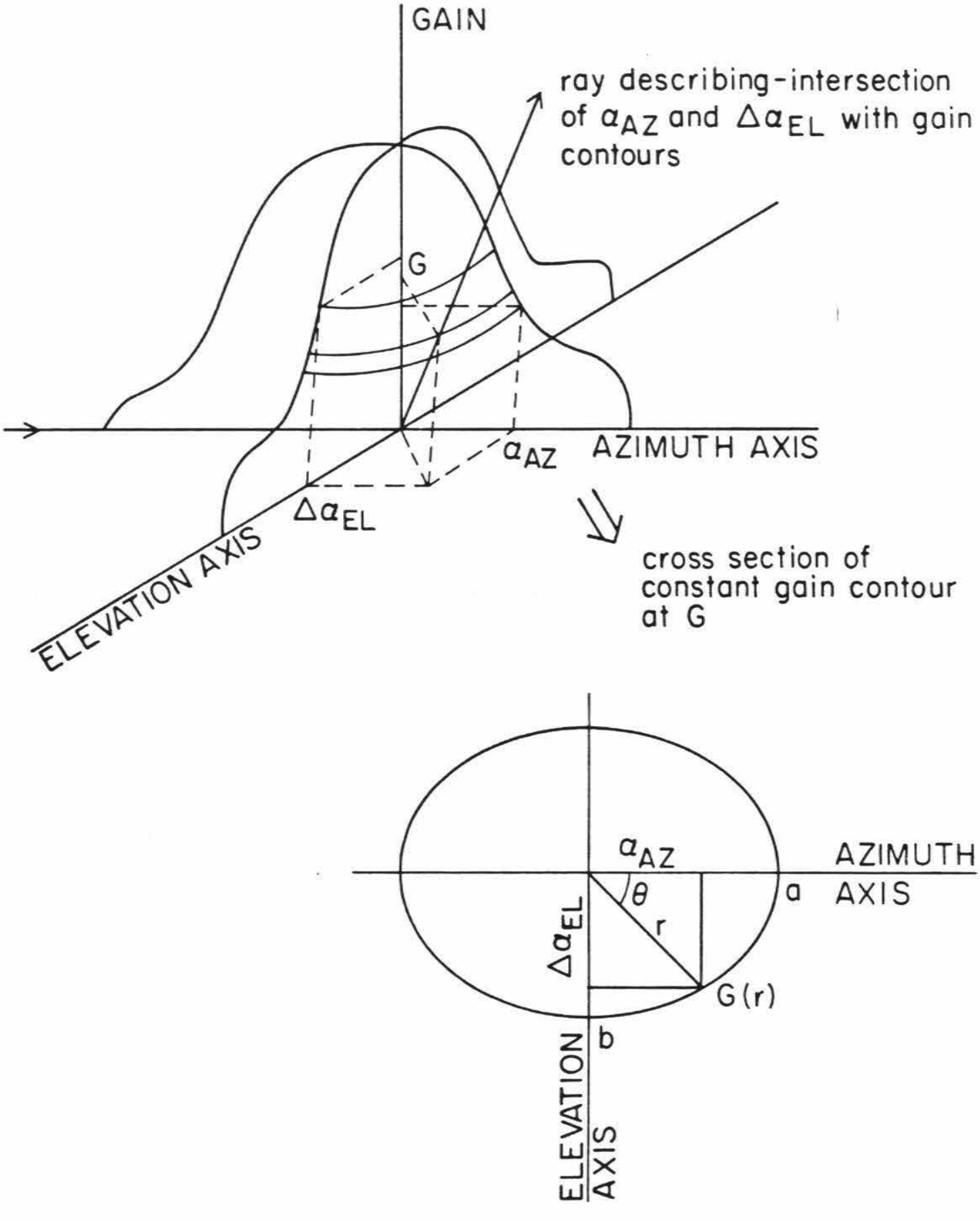
GAIN
ray describing-intersection of α_{AZ} and $\Delta\alpha_{EL}$ with gain contours
G
α_{AZ}
AZIMUTH AXIS
$\Delta\alpha_{EL}$
ELEVATION AXIS
cross section of constant gain contour at G
α_{AZ}
θ
r
a
AZIMUTH AXIS
$\Delta\alpha_{EL}$
G(r)
b
ELEVATION AXIS

$$\frac{x^2}{a^2} + \frac{y^2}{b^2} = 1 \tag{79}$$

where x = azimuth angle and y = elevation angle. Also

$$x = r\cos\vartheta \quad \text{and} \quad y = r\sin\vartheta \tag{80}$$

where

$$\vartheta = \tan^{-1}\left(\frac{\Delta\psi_{EL}}{\psi_{AZ}}\right) \tag{81}$$

Combining Eqs. (79) and (80),

$$\frac{r^2\cos^2\vartheta}{a^2} + \frac{r^2\sin^2\vartheta}{b^2} = 1 \tag{82}$$

or

$$a = \left\{r^2\left[k^2\sin^2\vartheta + \cos^2\vartheta\right]\right\}^{\frac{1}{2}} \tag{83)}$$

where

$$k = \frac{a}{b} = \frac{G_{AZ}(\delta)}{G_{EL}(\psi_{EL_A} + \delta)} \tag{84}$$

and δ is an arbitrary angle (assume 0.5°). The angle r is just

$$r = \cos^{-1}(\hat{R}\cdot\hat{A}) \tag{85}$$

Thus a may be determined from k, r and ϑ, therefore, the gain at angle r is known:

$$G(r) = G(a) \ . \tag{86}$$

$G(r)$ is determined for ψ_{AZ} and $\Delta\psi_{EL}$ as a function of time for each of the nine dish elevations measured in the laboratory. A single gain, P_C, at the off axis angle as a function of time is determined at the dish elevation of the antenna (also listed as a function of time in the command tables) by interpolation from the nine values of gain at the nine dish elevations calculated above. This gain is added to the initial received power, P_I, to obtain the correct power, P_C, as a function of time:

$$P_C = P_I + P_G \tag{87}$$

Figures 32 and 33 (a and b) show the observed power, P_I, and the correct power for orbit 9 (S-band) and orbit 18 (S- and X-band), respectively. Note that the power is relative to free space power, P_0, before any power loss due to absorption or refractive defocussing is detected. The S-band power profiles show no discernible difference between the raw and corrected data, as expected. The X-band power profile shows several decibels of correction due to antenna mispointing. Also shown in the free space power is the effect of the wobble. Each of these effects will be discussed in the section on errors.

Loss of lock is determined by examining the internal frequency of the digital phase lock loop. The internal frequency is the difference between the actual frequency and the reference local oscillator frequency. A sharp deviation in the internal frequency indicates a loss of lock as shown in the inserts in Figures 32 and 33. The arrow in the insert indicates the point in time of loss of lock. In addition, the computed bending angle was examined. An erratic bending angle curve indicates a loss of lock.

As the atmosphere is penetrated by the radio beam, the first disturbances in power at approximately 54825 seconds past midnight for orbit 9 and from 59695 to 59710 seconds past midnight for orbit 18 are introduced by turbulence at the tropopause inversion. This turbulence causes a corresponding disturbance in the attenuation which is not entirely removed when the refractive defocussing attenuation is subtracted. Absorption coefficient profiles were derived from power profiles which contained this turbulent effect and which had the effect removed by artificially smoothing the power profile. No difference was

Figure 32. Superposition of raw and corrected power profiles at S-band for orbit 9N. There is no discernible difference between the raw and corrected profiles. The insert of internal frequency vs. time of reception indicates the time of loss of lock (arrow).

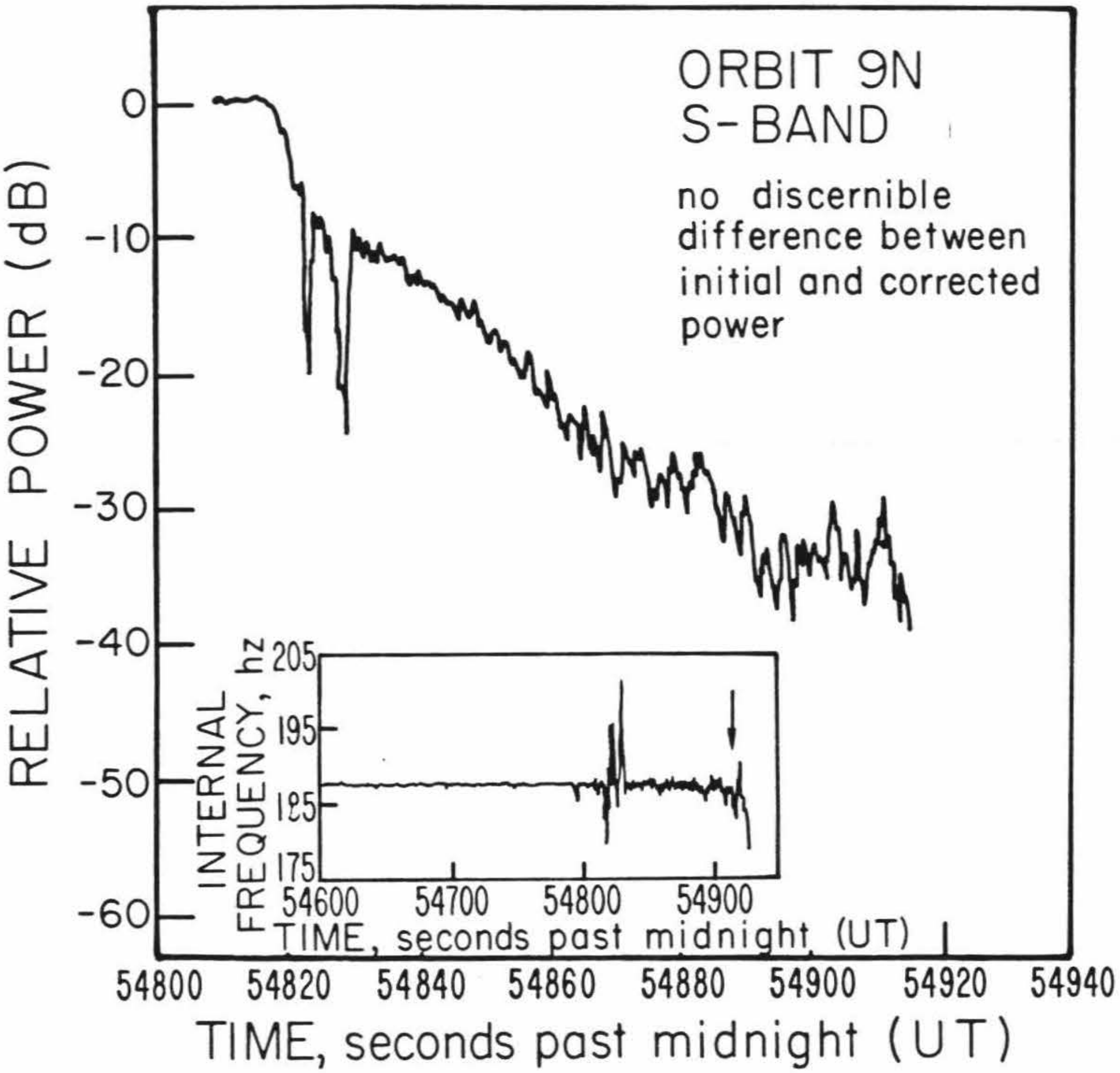
ORBIT 9N
S-BAND
no discernible difference between initial and corrected power
RELATIVE POWER (dB)
0
-10
-20
-30
-40
-50
-60
54800
54820
54840
54860
54880
54900
54920
54940
TIME, seconds past midnight (UT)
INTERNAL FREQUENCY, hz
205
195
185
175
54600
54700
54800
54900
TIME, seconds past midnight (UT)

Figure 33. (a) Superposition of raw and corrected power profiles at S-band for orbit 18N. There is no discernible difference between the raw and corrected profiles. The insert of internal frequency vs. time of reception indicates the time of loss of lock (arrow). (b) Superposition of raw and corrected power profiles at X-band for orbit 18N. profiles. The insert of internal frequency vs. time of reception indicates the time of loss of lock (arrow).

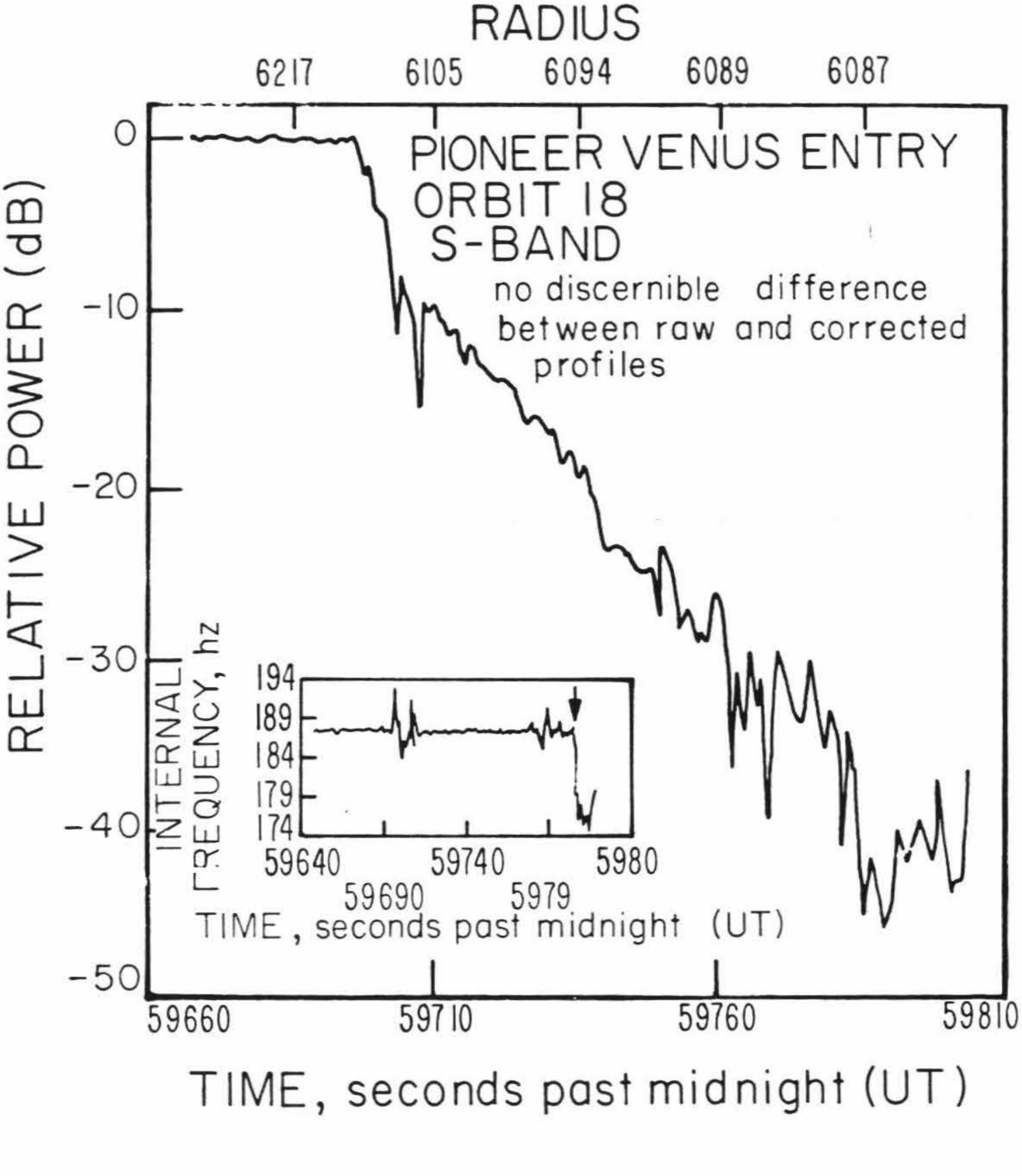
RADIUS
6217
6105
6094
6089
6087
PIONEER VENUS ENTRY
ORBIT 18
S-BAND
no discernible difference
between raw and corrected
profiles
RELATIVE POWER (dB)
0
-10
-20
-30
-40
-50
INTERNAL
FREQUENCY, hz
194
189
184
179
174
59640
59740
5980
59690
5979
TIME, seconds past midnight (UT)
59660
59710
59760
59810
TIME, seconds past midnight (UT)

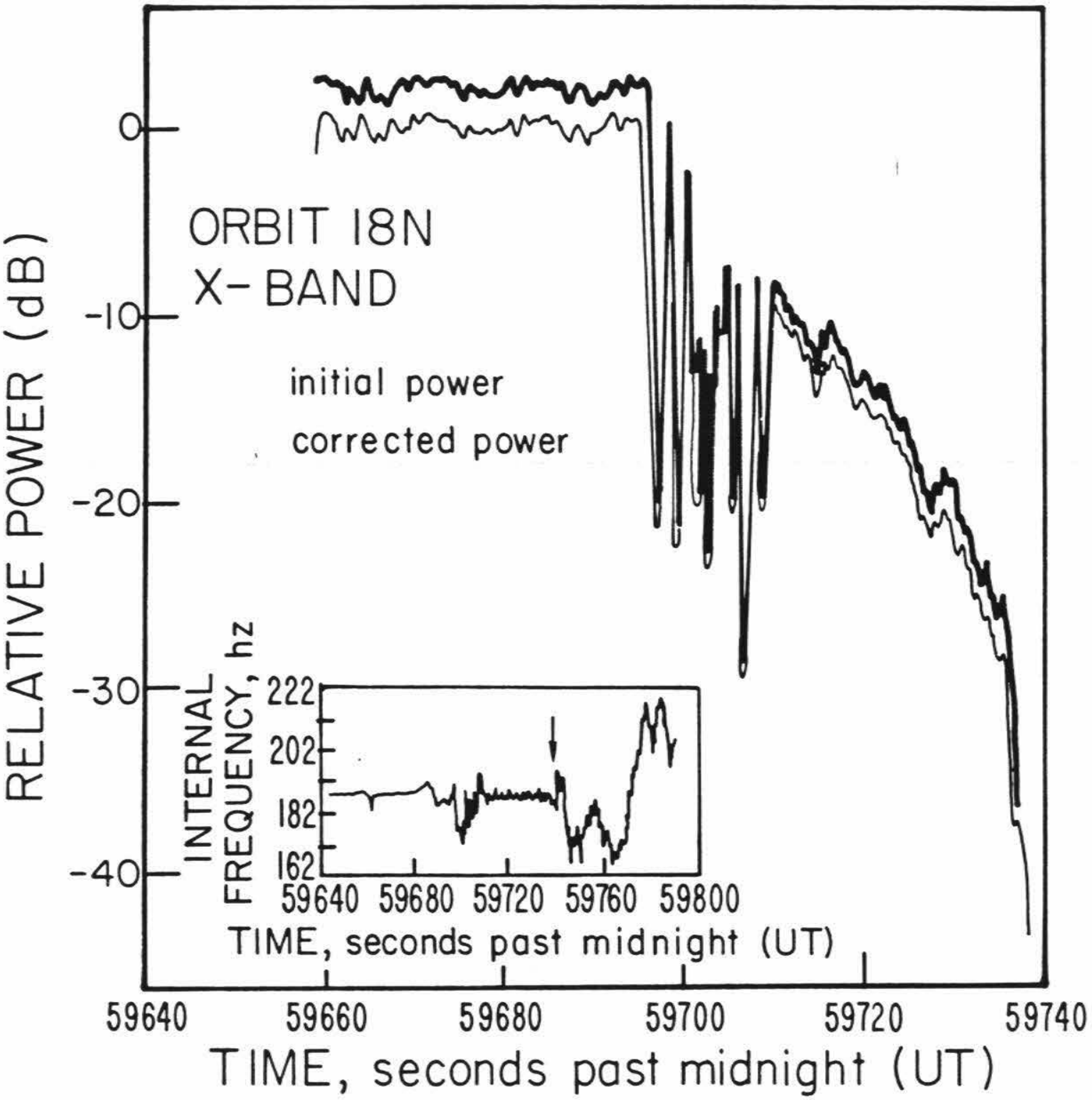
ORBIT 18N
X-BAND
initial power
corrected power
RELATIVE POWER (dB)
0
-10
-20
-30
-40
59640
59660
59680
59700
59720
59740
TIME, seconds past midnight (UT)
INTERNAL FREQUENCY, hz
222
202
182
162
59640
59680
59720
59760
59800
TIME, seconds past midnight (UT)

observed in the absorption coefficient profiles below 57.5 km. This will be discussed in more detail later in this chapter. The question then arises as to whether a similar turbulent layer at the level of the lower cloud is producing artificial attenuation. To investigate this question, plots of bending angle as a function of radius and dn/dr (the slope of the refractive index profile, n, with respect to radius, r) were plotted for orbits 9 and 18 (Figure 34). The orbit 9 profile has been shifted vertically downward in radius by 8.3 km to account for uncertainties in the radius scale described in Table V. The turbulent layer is present in all curves as a deviation from the otherwise smooth curve at about 6112.5 km. There is no evidence of any similar deviation in the lower part of the curve at the altitudes of the lower cloud deck. Below 6090.5 km, the bending angle profile and the dn/dr profile show small fluctuations for the orbit 18 data. This is only the lowest part of the lower cloud deck and probably accounts for the fluctuations in the absorption coefficient profile in this region. These fluctuations have been observed by Woo et al. (1980) and have been attributed to a lower weaker turbulent layer than the one observed at 6112.5 km.

2. Calculation of Excess Attenuation from Power Profiles

The power profiles shown in Figures 33 and 34 (a and b) portray power as a function of time of reception, with measurement points spaced uniformly in time at 0.2 second intervals. These measurements must be transformed to functions of radius in order to deal with vertical profiles of attenuation in the atmosphere. Every measurement point is in one-to-one correspondence with a point of inverted frequency data which is given as a function of the radial distance of the closest approach point of the beam from the center of Venus. However, the radius vs. time function is highly non-linear because of increasing refractive bending in the atmosphere. Hence, a greater number of points are

Figure 34. Bending angle and $-dn/dr$ for orbits 9N and 18N. Any turbulence will show up as fluctuations in these profiles.

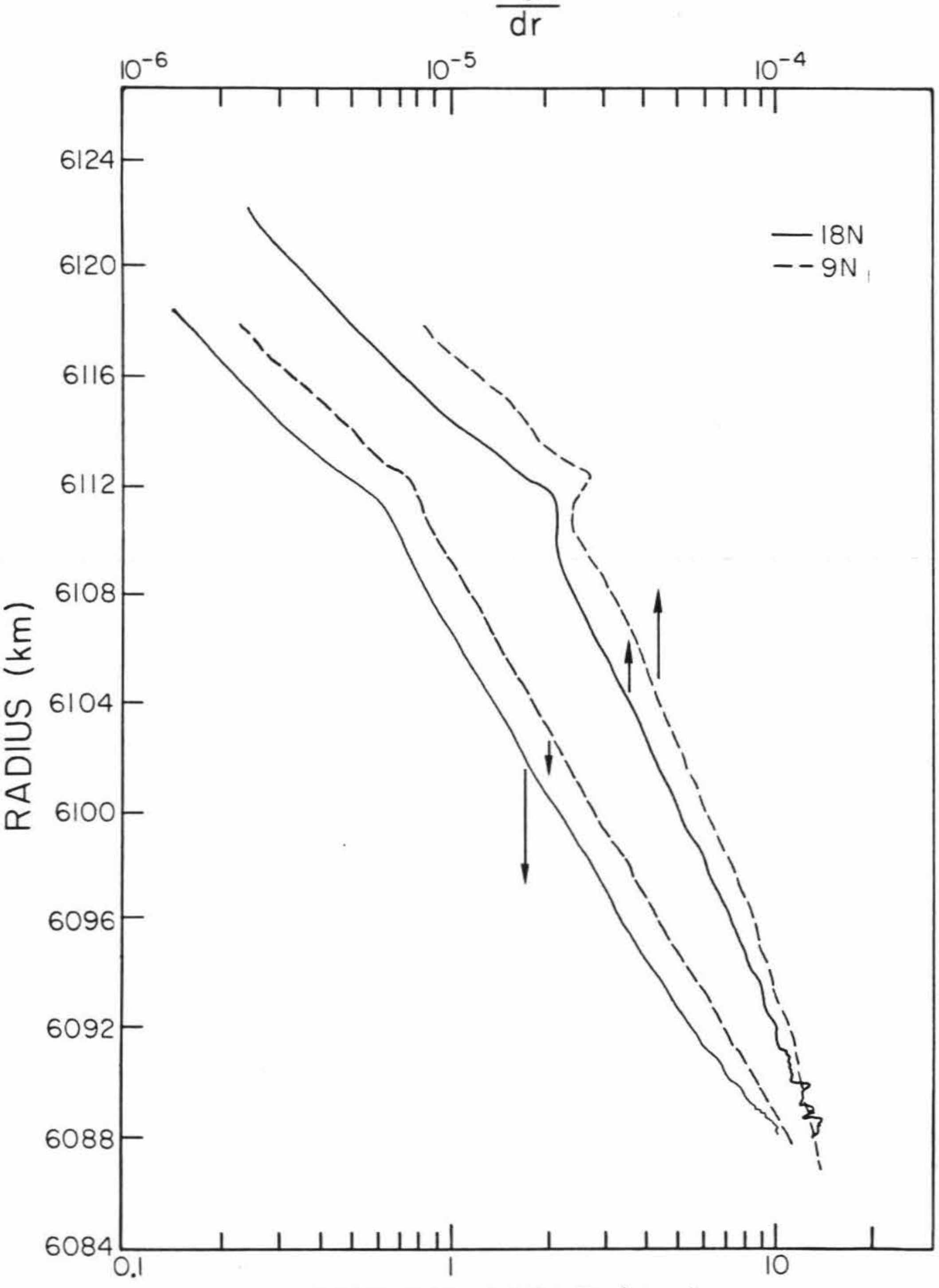
$\frac{-dn}{dr}$
10^{-6}
10^{-5}
10^{-4}
6124
6120
6116
6112
6108
6104
6100
6096
6092
6088
6084
RADIUS (km)
— 18N
-- 9N
0.1
1
10
BENDING ANGLE (deg)

squeezed together in the lower several kilometers of altitude. For this reason, the power vs. radius profiles are averaged in 0.2 km "bins" and tagged with the midpoint of the 0.2 km bin (Kliore, private communication). The error introduced by this averaging is discussed in the errors section.

The total attenuation, A_T, is the difference between the free space power and the corrected power:

$$A_T(r) = P_0 - P_C(r) \tag{88}$$

where P_0 is the free space power prior to the onset of atmospheric occultation effects, and $P_C(r)$ is the corrected power as a function of radius in dB. P_0 values are chosen by averaging a short interval immediately preceeding the power loss. In the Mariner 10 power profiles a drift in the antenna centerline was evidenced by a sloping free space power profile. Thus far all Pioneer Venus occultation profiles have shown a flat free space power profile.

In order to obtain the attenuation due only to atmospheric absorption effects, the power loss due to refractive defocussing must be subtracted from the total attenuation. This refractive defocussing A_{REF} was derived previously and is

$$A_{REF}^{(r)} = 10\log_{10}\left\{\frac{R'}{b}\left[1 - \left(R_{sc}^2 - b^2\right)^{1/2}\frac{d\psi}{db}\right]\right\} \tag{89}$$

where R_{sc} is the distance of the spacecraft from the center of Venus, b is the ray asymptote distance, ψ is the bending angle and R' describes the position of the spacecraft and the earth relative to Venus. The greatest error inherent in the refractive defocussing equation itself results from the calculation of $d\psi/db$. The magnitude of this error is discussed in the errors section. Other errors were discussed in Chapter III.

The excess attenuation, A_{EX}, is then the difference between the total attenuation and the refractive defocussing attenuation:

$$A_{EX}(r) = A_T(r) - A_{REF}(r) \tag{90}$$

Profiles of the total attenuation, the refractive defocussing and the excess attenuation are shown for orbit 9N (S-band) and 18N (S- and X-band) in Figures 35 and 36 (a and b), respectively.

In the region of the lower cloud deck (below 6092.5 km for orbits 9 and 18 in the north polar region) the excess attenuation makes up a significant fraction of the total attenuation. Above 6092.5 km, where the cloud becomes less dense, the excess attenuation decreases to a small fraction of the total attenuation. Above 6102.5 km, the excess attenuation is nearly zero with the refractive defocussing accounting for nearly all of the total attenuation. It should be mentioned that the refractive defocussing is the same for S- and X-band wavelengths. In the lower part of the X-band profiles (Fig. 36b), the excess attenuation is equivalent to the refractive defocussing. These comparisons were made to demonstrate that the excess attenuation is of the same magnitude as the total attenuation and the refractive defocussing (and not the result of subtracting two large numbers!).

3. Calculation of Absorption Coefficient Profiles from Excess Attenuation

The path length or optical depth, τ, at r_0 is equal to the integral of the absorption coefficient, α, from r_0 to the top of the atmosphere (Kliore et al, 1971):

$$\tau(r_0) = 2 \int_{r_0}^{R} \alpha(r)\, ds \ . \tag{91}$$

The optical depth profiles may be computed from the excess attenuation profiles as follows:

Figure 35. Total attenuation, excess attenuation and refractive defocussing for orbit 9N S-band.

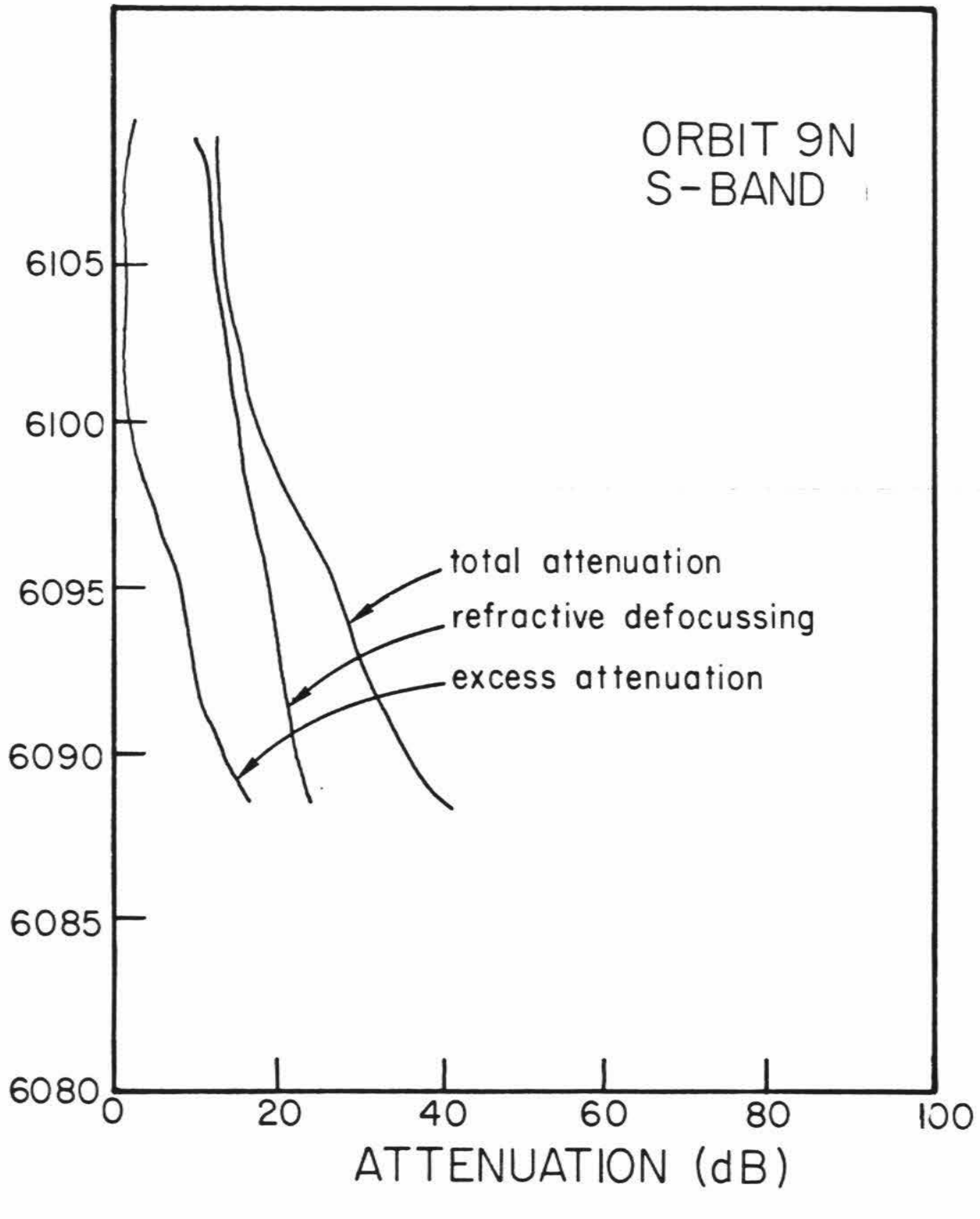
ORBIT 9N
S-BAND
RADIUS (km)
6080
6085
6090
6095
6100
6105
ATTENUATION (dB)
0
20
40
60
80
100
total attenuation
refractive defocussing
excess attenuation

Figure 36. Total attenuation, excess attenuation and refractive defocussing for orbit 18N S-and X-band.

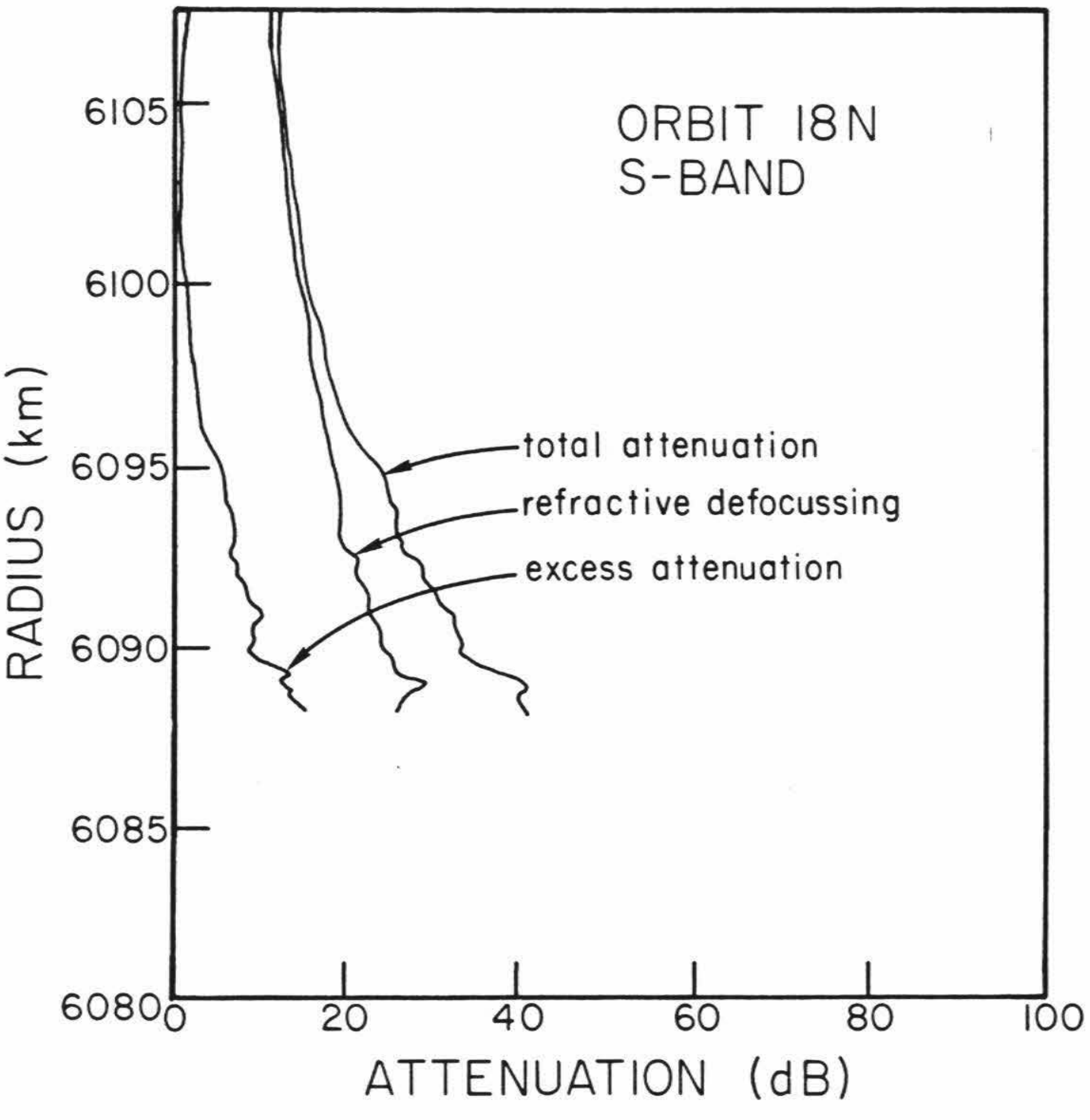
ORBIT 18N
S-BAND
total attenuation
refractive defocussing
excess attenuation
RADIUS (km)
6105
6100
6095
6090
6085
6080
0
20
40
60
80
100
ATTENUATION (dB)

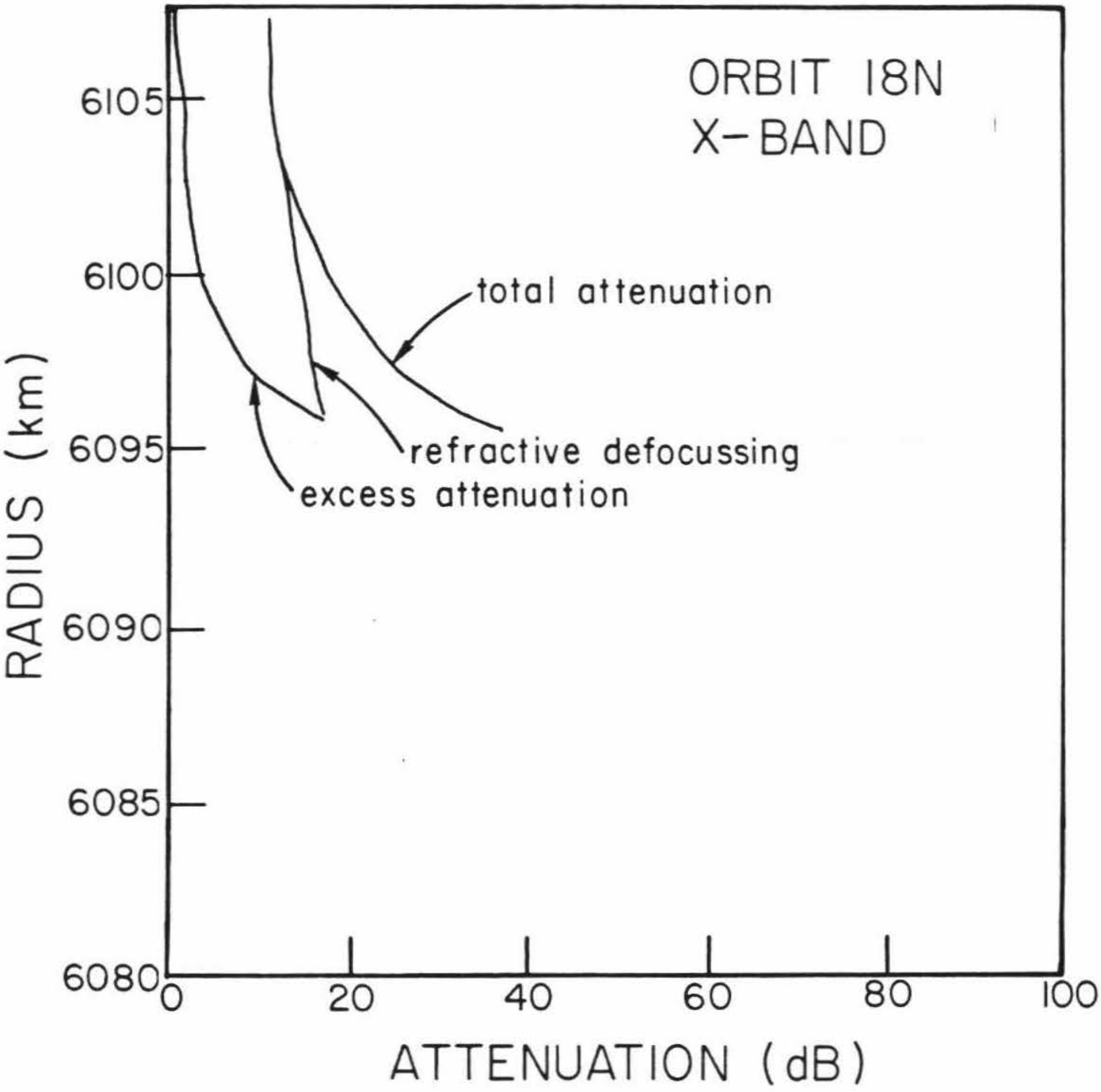
ORBIT 18N
X-BAND
total attenuation
refractive defocussing
excess attenuation
RADIUS (km)
6105
6100
6095
6090
6085
6080
0
20
40
60
80
100
ATTENUATION (dB)

$$\tau = \frac{A_{EX}}{10\log_{10}e} \quad . \tag{92}$$

Equation (92) may be rewritten in terms of measurable quantities by rewriting ds in terms of r, $n(r)$ and $b(r_o)$ (see Fjeldbo and Eshleman, 1968 and Kliore, 1972):

$$\tau(r_0) = 2\int_{r_0}^{R} \frac{\alpha(r)\ r\ n(r)\ dr}{\sqrt{r^2n^2(r) - b(ro)^2}} \tag{93}$$

Thus absorption coefficient profiles may be calculated from the excess attenuation using the integral equation (93) and the Abel transform (Spiro and Lass, private communication, 1973).

Absorption coefficient profiles are shown in Figure 37 for orbits 9N (S-band) and 18N (S- and X-band). The S-band absorption coefficient reaches its maximum of about 0.002 km^{-1} at about 2.5 bars, steadily increasing from minimal absorption at 1.0 bar. The absorption remains fairly constant down to about 4.7 bars where the profile is cut-off due to large fluctuations in the refractivity due to turbulence. The X-band profile also increases with increasing pressure from a low absorption due mostly to gaseous absorption at about the 1 bar level to its cut off value at critical refraction of about 0.005 km^{-1} at about 1.5 bars. As expected, the X-band absorption coefficient is significantly greater than the S-band absorption coefficient. The actual wavelength dependence will be discussed in later chapters in connection with the interpretation of the data.

The remainder of this chapter is devoted to the error analysis of the absorption coefficient profiles due to uncertainties in the received power.

4. Errors

In the preceeding sections, the equations used to derive the excess attenuation A_{EX} from the initial power profile were described. These equations

Figure 37. Absorption coefficient profiles for orbits 9N (S-band) and 18N (S-and X-band).

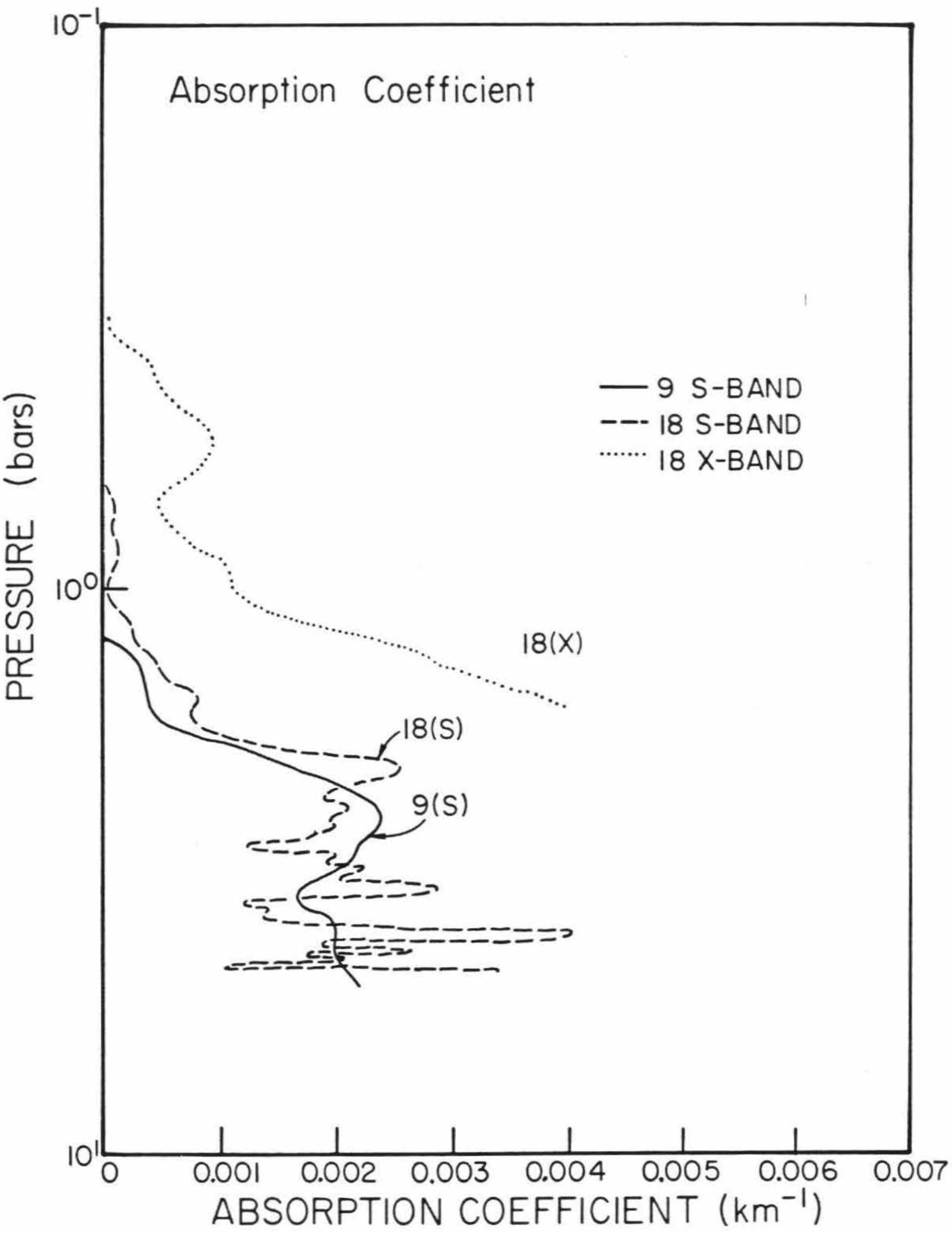
Absorption Coefficient
— 9 S-BAND
--- 18 S-BAND
····· 18 X-BAND
18(X)
18(S)
9(S)
PRESSURE (bars)
10^{-1}
10^{0}
10^{1}
0
0.001
0.002
0.003
0.004
0.005
0.006
0.007
ABSORPTION COEFFICIENT (km^{-1})

may be summed up into a single equation for purposes of determining contributing uncertainties:

$$A_{EX} = P_0 - P_I + P_G - 10\log_{10}\left[\frac{R'}{b}\left[1 - (R_{sc}^2 - b^2)^{1/2}\,\frac{d\psi}{db}\right]\right] \tag{94}$$

where P_0 is the free space power, P_I is the initial uncorrected power, P_G is the gain due to antenna motions, $d\psi/db$ is the slope of the bending angle vs. impact parameter curve, R' and R_{sc} describe the position of the spacecraft and Earth relative to Venus, and b is the impact parameter. Errors in R', R_{sc} and b result from trajectory errors and contribute only to the radius scale. The errors in P_0 and P_I result from power fluctuations and antenna wobble. Errors in P_G result from uncertainties in the antenna position caused by refractive defocussing effects and antenna slews. Finally, errors in $d\psi/db$ are included in the error analysis of the refractive defocussing equation. In addition, averaging of the power-radius profile may introduce uncertainties in A_{EX}.

The errors that will be discussed are the following:

1. fluctuations in the power profile and averaging errors,
2. errors due to spacecraft wobble;
3. errors due to antenna gain calculations, and
4. refractive defocussing errors,

Fluctuations in the power profile contribute the greatest to errors in the S-band absorption coefficients. Errors due to spacecraft wobble and fluctuations in the power profile contribute an equal amount to the error in the orbit 18N X-band profile.

Each of the above mentioned sources of error will be discussed separately. The results of the error analysis will then be used to put error bars on the resulting absorption coefficient profiles.

4.1 Errors Due to Power Fluctuations and Averaging of Power vs. Radius Data

The dashed and dotted lines in the power profiles for orbits 9N (S-band) and 18N (S- and X-band) shown in Figures 38 and 39 (a and b), respectively, represent the maximum and minimum possible errors expected due to received power fluctuations. The maximum and minimum curves are extreme and are intended to represent very conservative error estimates. These new power profiles are then used to calculate total attenuation, excess attenuation, and, finally, absorption coefficients. Figures 40 and 41 (a and b) show the results for attenuation for orbit 9 (S-band) and orbit 18 (S- and X-band) wavelengths, respectively. Also represented in the figures are curves derived using 0.1, 0.2 and 0.3 km averaging of the power vs. radius data. Power fluctuations result in a significantly greater uncertainty in the total and excess attenuation than averaging uncertainties. The uncertainty due to power fluctuations is much less for the X-band data than for the S-band data because the total power loss at X-band is greater.

Figures 42 and 43 (a and b) show the absorption coefficient profiles for the minimum and maximum power profiles described in Figures 38 and 39, and for 0.1, 0.2 and 0.3 km averaged power profiles for orbit 9 (S-band) and 18 (S- and X-band). Again the power fluctuations contribute most to the absorption coefficient uncertainty and the S-band power fluctuations produce greater uncertainty than the X-band power fluctuations. Below 6097.5 km, the X-band absorption coefficient has an extremely large uncertainty due to the steepness

Figure 38. Power profile for orbit 9N (S-band) showing minimum and maximum power.

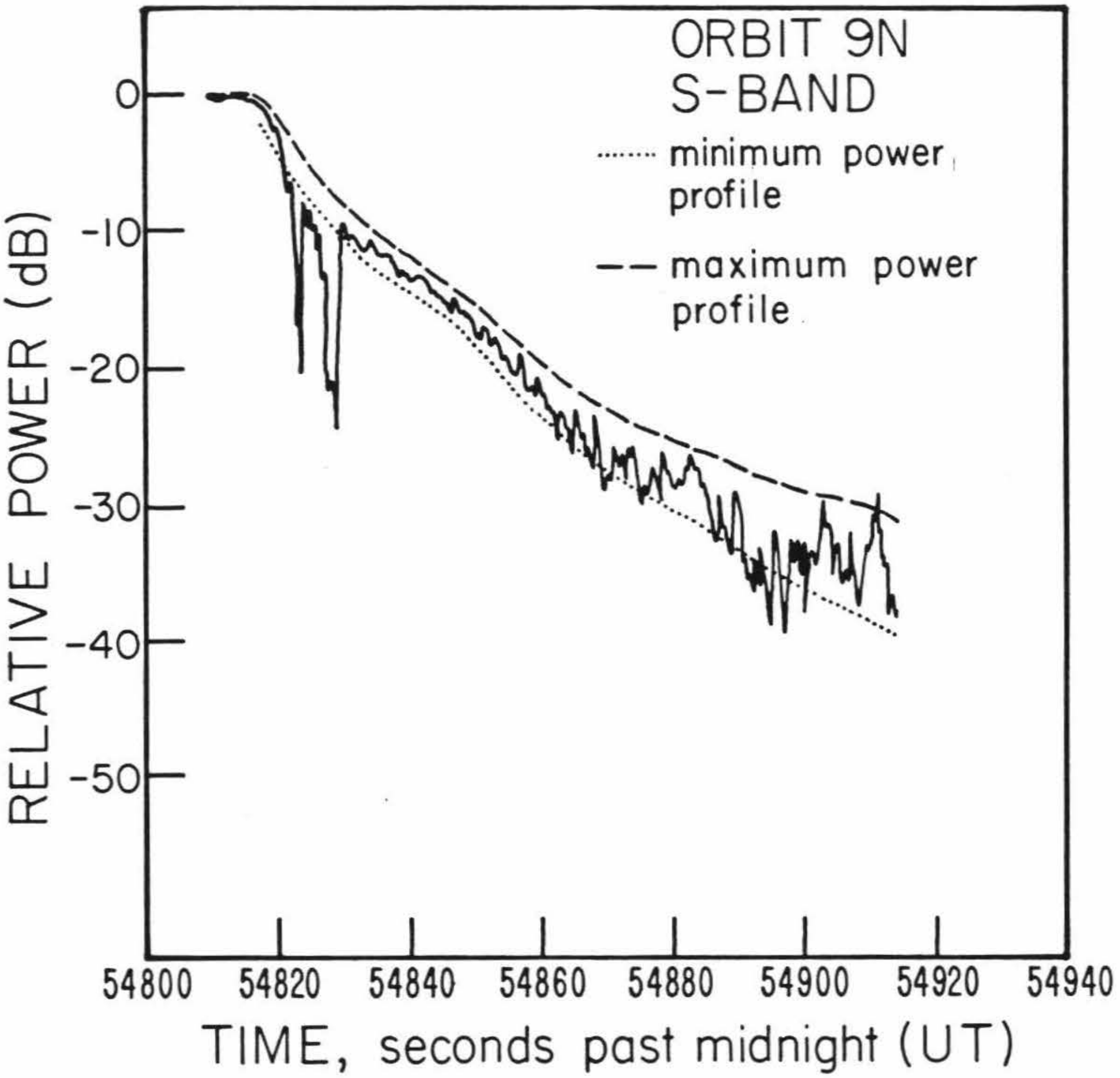
ORBIT 9N
S-BAND
minimum power profile
maximum power profile
RELATIVE POWER (dB)
0
-10
-20
-30
-40
-50
54800
54820
54840
54860
54880
54900
54920
54940
TIME, seconds past midnight (UT)

Figure 39. Power profile for orbit 18N (S-and X-band) showing minimum and maximum power.

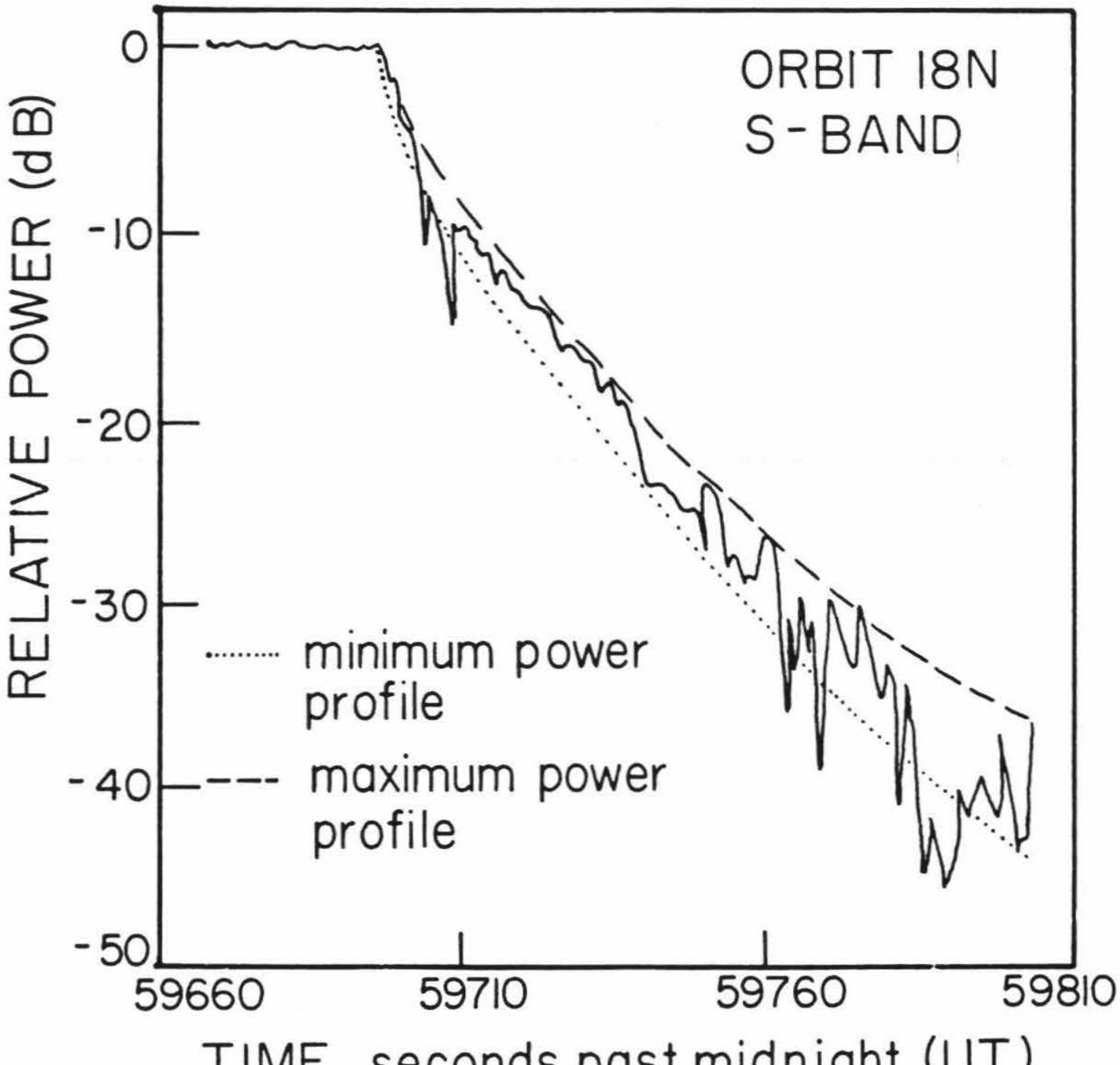
ORBIT 18N
S-BAND
RELATIVE POWER (dB)
0
-10
-20
-30
-40
-50
minimum power profile
maximum power profile
59660
59710
59760
59810
TIME, seconds past midnight (UT)

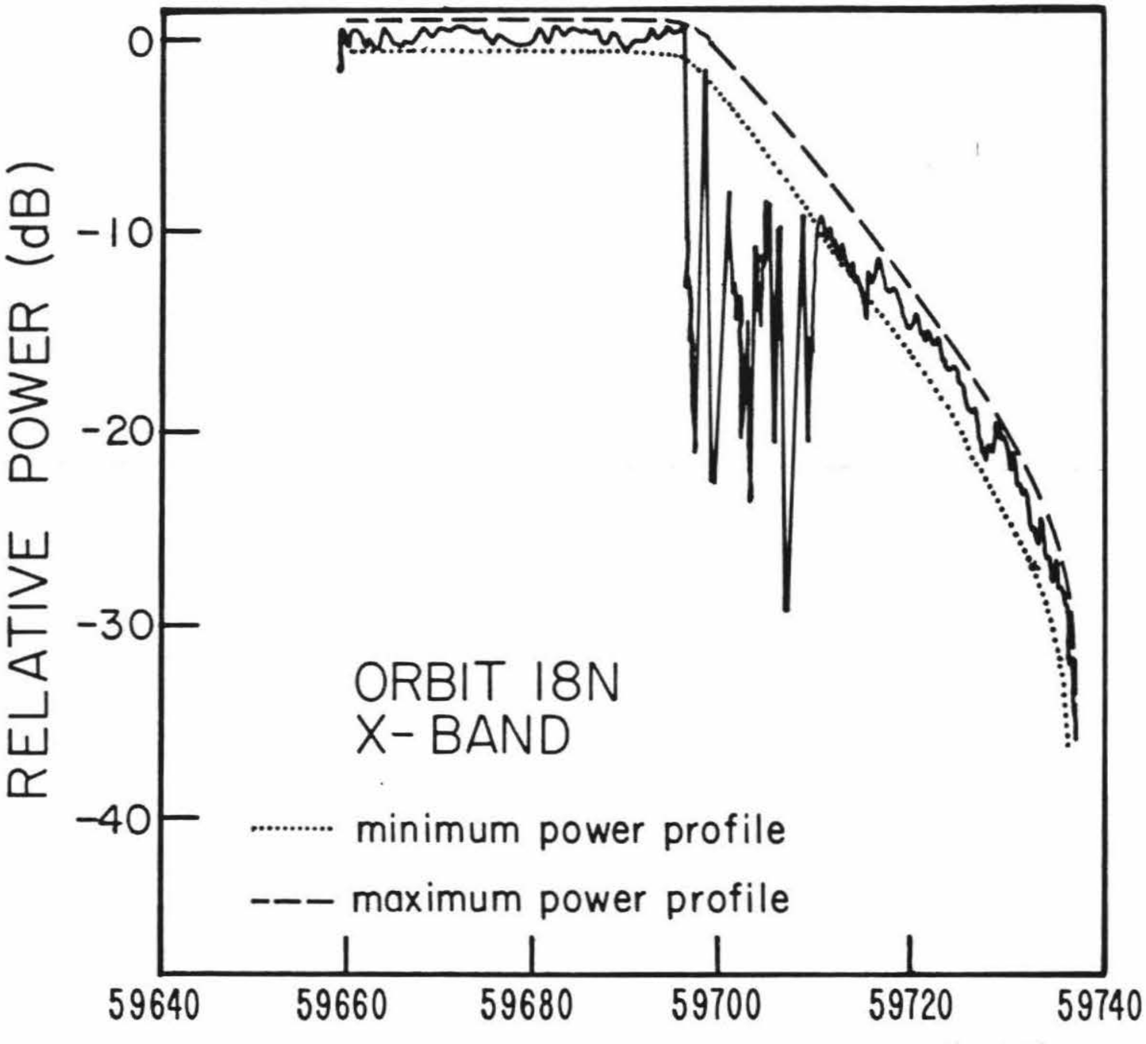
RELATIVE POWER (dB)
0
-10
-20
-30
-40
ORBIT 18N
X- BAND
minimum power profile
maximum power profile
59640
59660
59680
59700
59720
59740
TIME, seconds past midnight (UT)

Figure 40. Total and excess attenuation profiles for orbit 9N (S-band) showing profiles determined from minimum and maximum power.

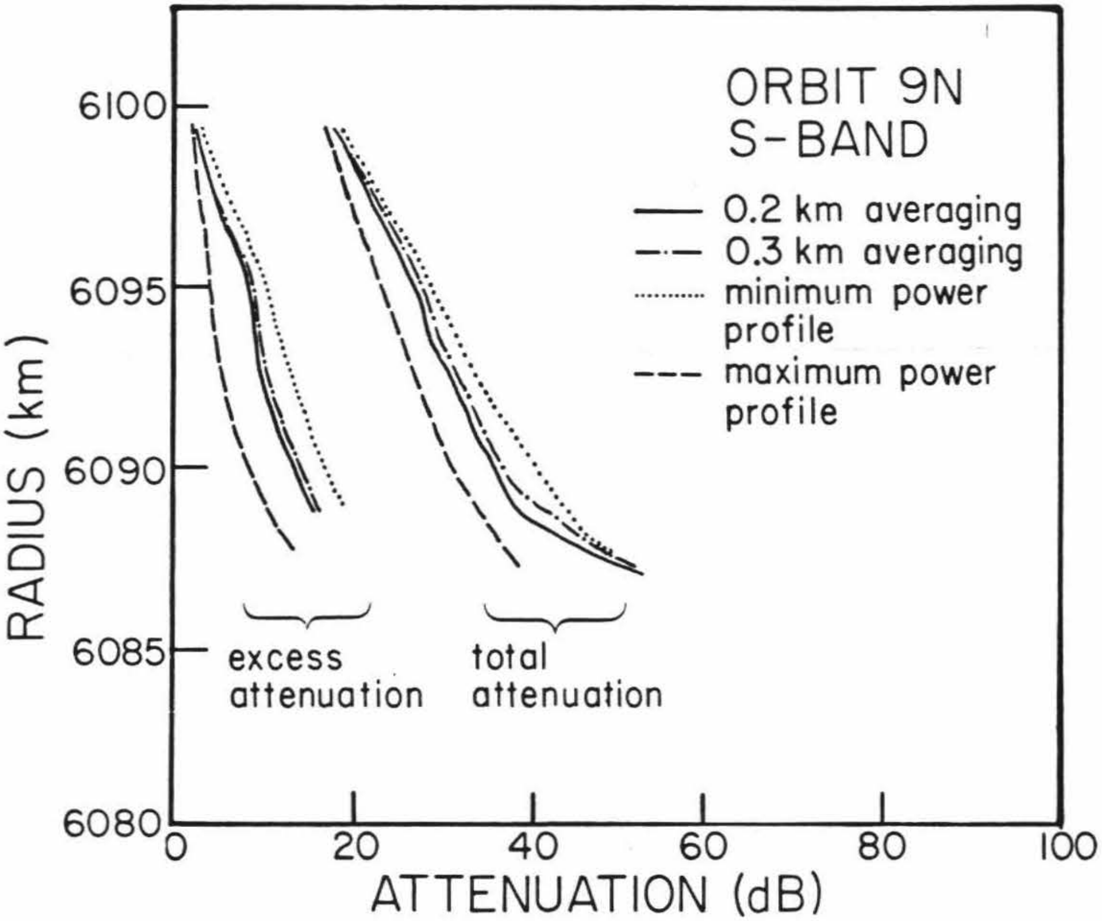
ORBIT 9N
S-BAND
0.2 km averaging
0.3 km averaging
minimum power profile
maximum power profile
excess attenuation
total attenuation
RADIUS (km)
6100
6095
6090
6085
6080
0
20
40
60
80
100
ATTENUATION (dB)

Figure 41. Total and excess attenuation profiles for orbit 18N (S- and X-band) showing profiles determined from minimum and maximum power.

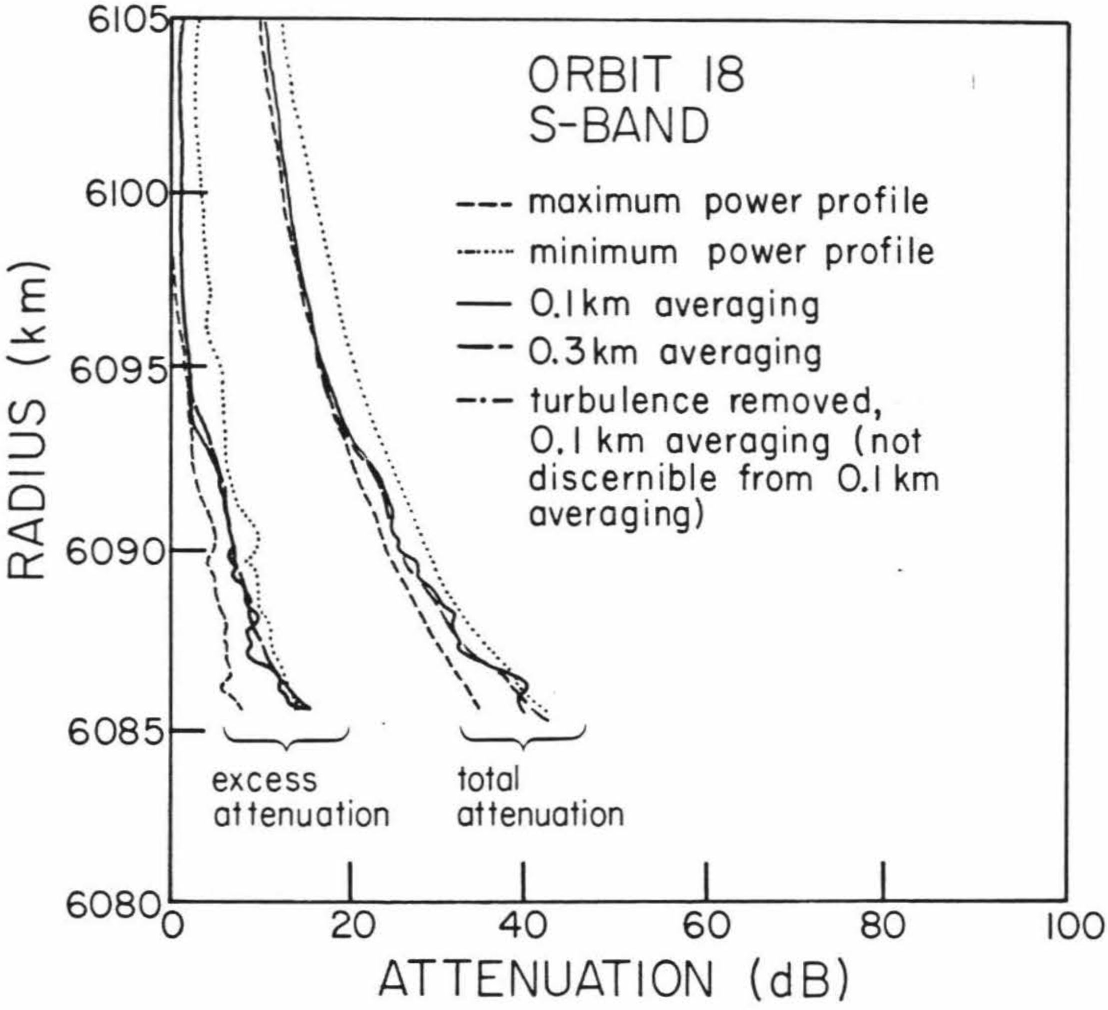
ORBIT 18
S-BAND
--- maximum power profile
······ minimum power profile
— 0.1km averaging
—- 0.3km averaging
-·- turbulence removed, 0.1 km averaging (not discernible from 0.1 km averaging)
excess attenuation
total attenuation
RADIUS (km)
6105
6100
6095
6090
6085
6080
0
20
40
60
80
100
ATTENUATION (dB)

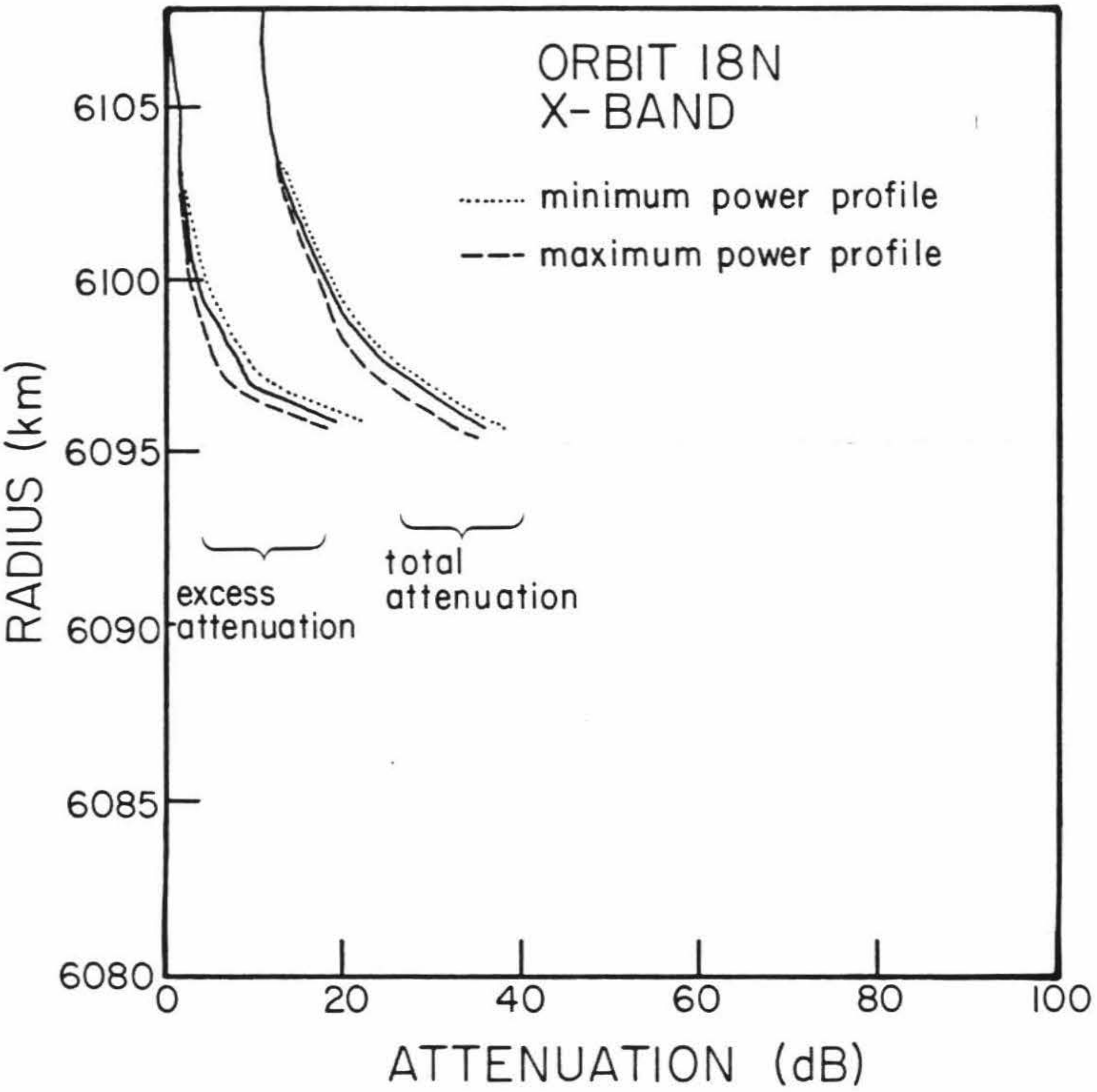
ORBIT 18N
X-BAND
minimum power profile
maximum power profile
excess attenuation
total attenuation
RADIUS (km)
6105
6100
6095
6090
6085
6080
0
20
40
60
80
100
ATTENUATION (dB)

Figure 42. Absorption coefficient profiles for orbit 9N (S-band) calculated from the minimum and maximum power profiles. Also shown are profiles determined using different averagings.

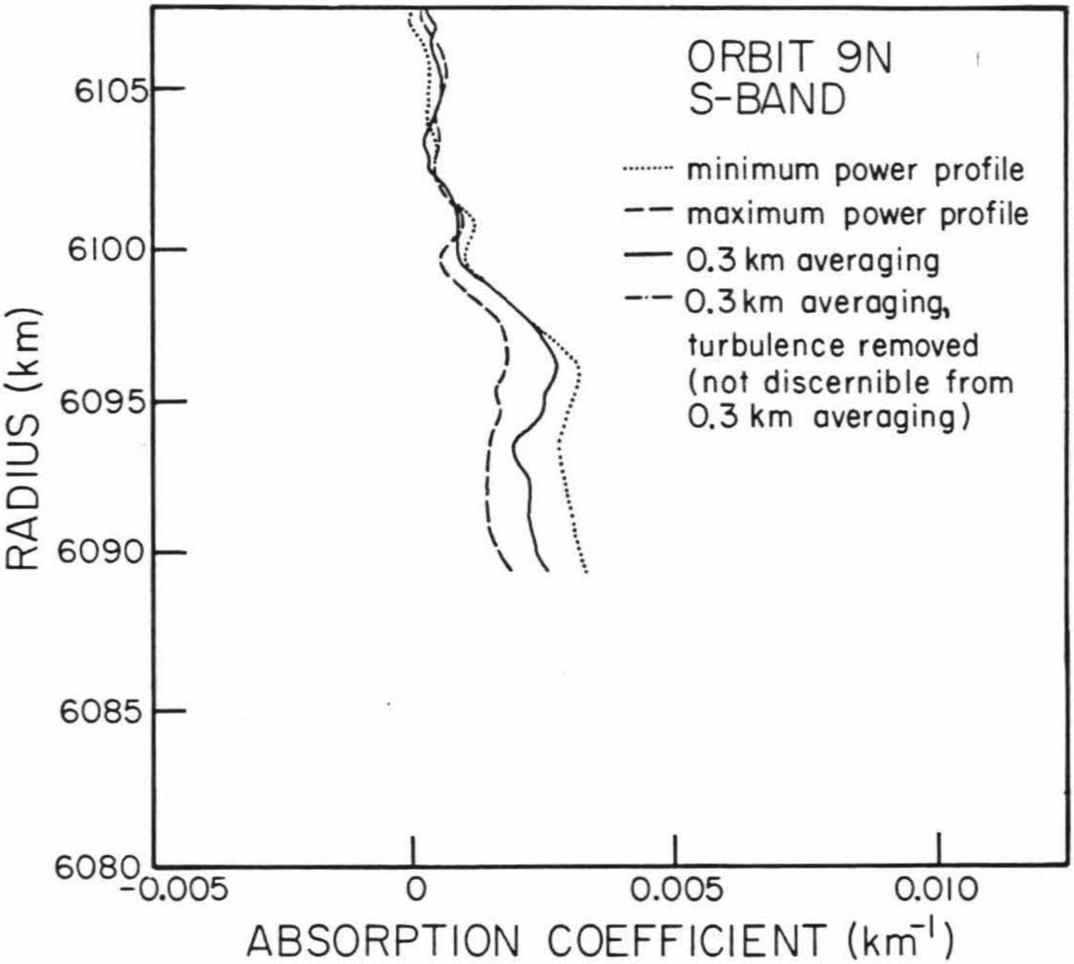
ORBIT 9N
S-BAND
minimum power profile
maximum power profile
0.3 km averaging
0.3 km averaging, turbulence removed (not discernible from 0.3 km averaging)
RADIUS (km)
6105
6100
6095
6090
6085
6080
-0.005
0
0.005
0.010
ABSORPTION COEFFICIENT (km^{-1})

Figure 43. Absorption coefficient profiles for orbit 18N (S-and X-band) calculated from the minimum and maximum power profiles. Also shown are profiles determined using different averagings. In (b) is shown the uncertainty resulting from spacecraft wobble.

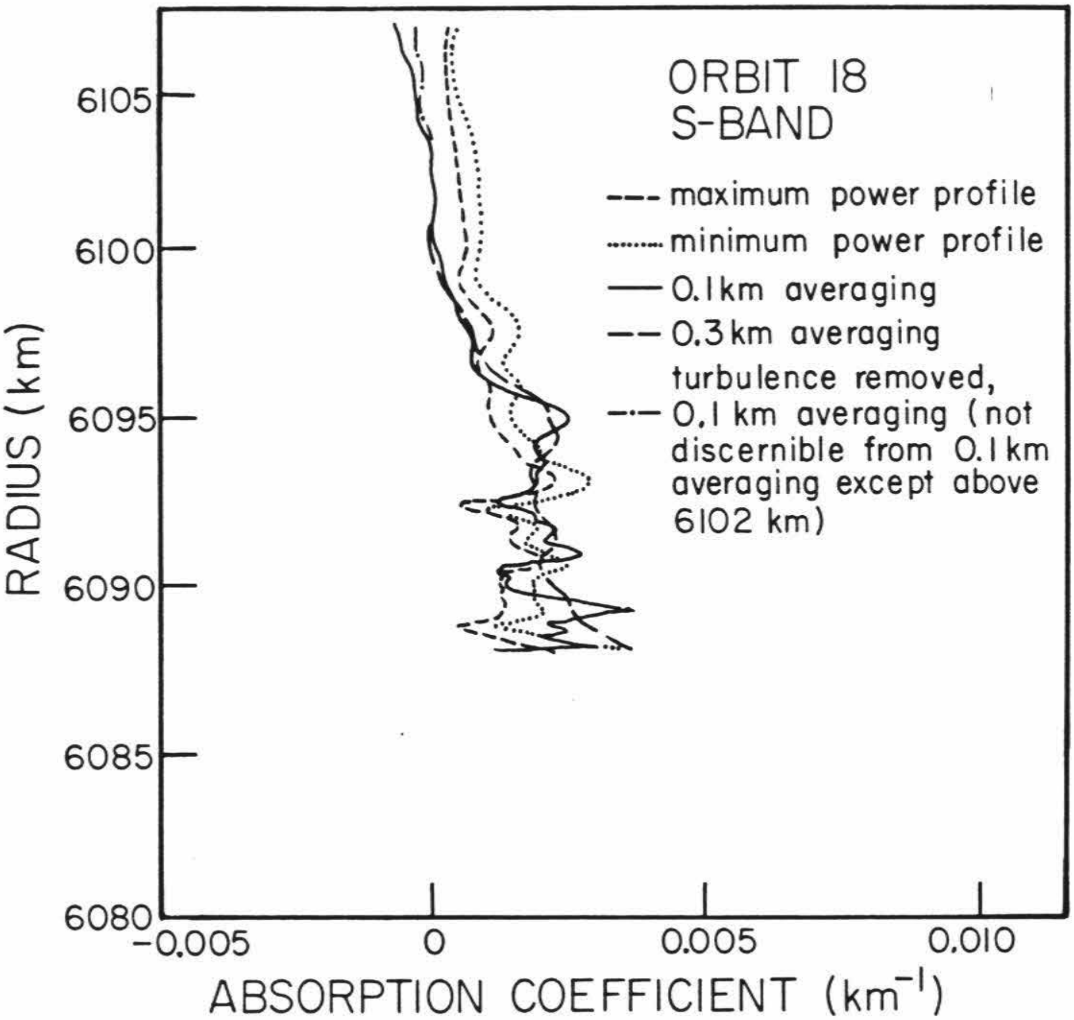
ORBIT 18
S-BAND
maximum power profile
minimum power profile
0.1km averaging
0.3km averaging
turbulence removed, 0.1 km averaging (not discernible from 0.1km averaging except above 6102 km)
RADIUS (km)
6105
6100
6095
6090
6085
6080
-0.005
0
0.005
0.010
ABSORPTION COEFFICIENT (km^{-1})

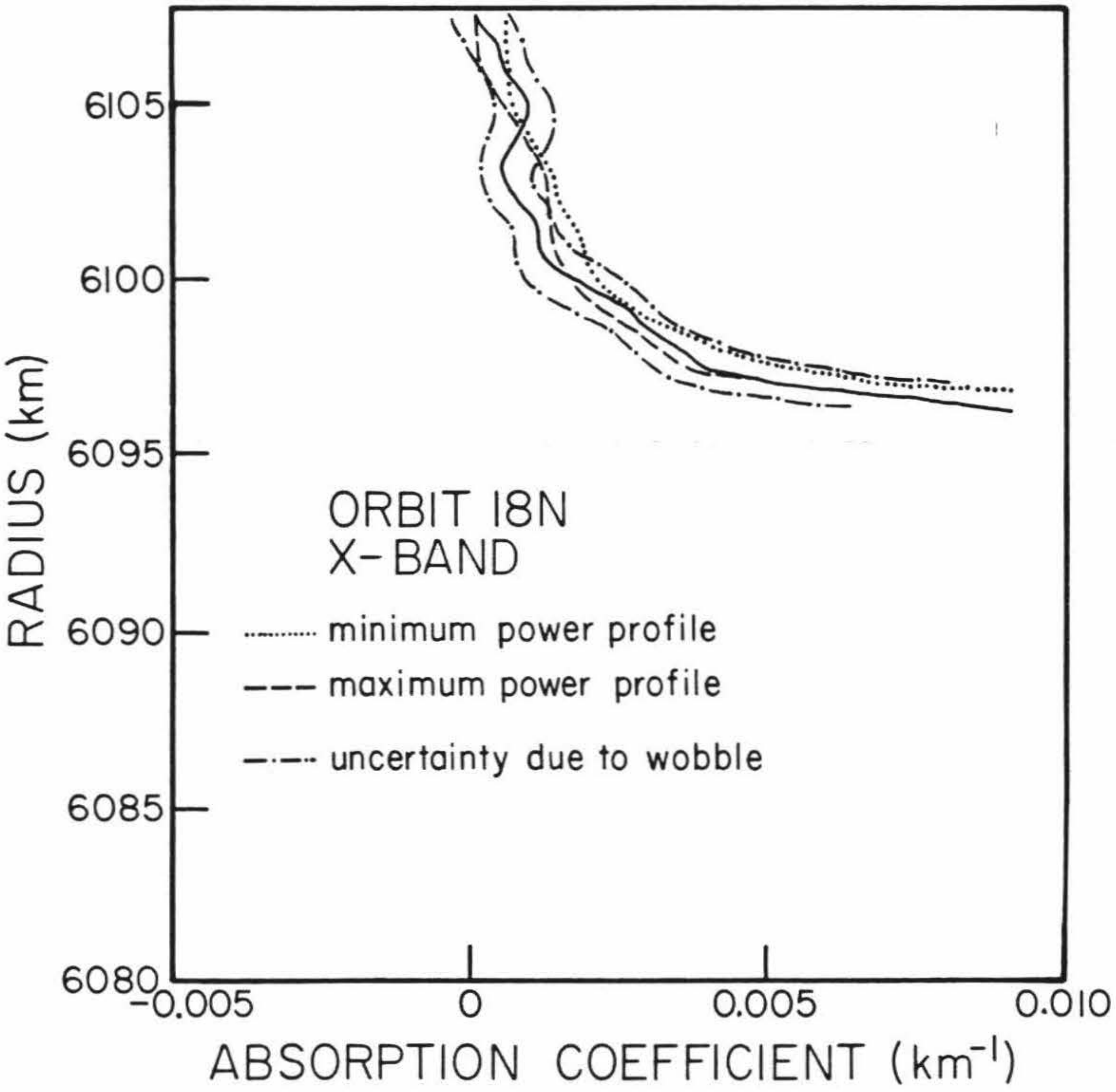
6105
6100
6095
6090
6085
6080
RADIUS (km)
-0.005
0
0.005
0.010
ABSORPTION COEFFICIENT (km⁻¹)
ORBIT 18N
X-BAND
minimum power profile
maximum power profile
uncertainty due to wobble

of the power vs. time profile at this level in the atmosphere.

4.2 Errors due to Spacecraft Wobble

The error due to spacecraft wobble will be considered separately for S- and X-band wavelengths inasmuch as the wobble is expected to produce more uncertainties in the X-band power profile than in the S-band power profile.

The error due to wobble in the S-band power profile can be estimated from Figures 38 and 39. The free space relative power varies by less than ± 0.5 dB. This corresponds to an angular variation of less than 2° as observed in the S-band gain pattern (Figure 29). A 0.5 dB uncertainty is insignificant compared to uncertainties due to power fluctuations calculated earlier.

The corresponding error in the X-band power profile due to spacecraft wobble is demonstrated in Figure 44. The wobble is observed to fluctuate by approximately 0.8 dB. The effect of this wobble on the power uncertainty is demonstrated in Figure 45. The maximum off axis angle is 0.87° (see Table VII) for orbit 18N. A gain variation of 0.8 dB due to spacecraft wobble corresponds to an additional 4° off axis angle uncertainty as shown in the figure as "expected angular variation due to antenna wobble." This additional angular variation results in a gain uncertainty at the maximum off axis angle of ± 1.8 dB. Figure 46 shows the effect of a ± 1.8 dB gain uncertainty on the power profile. The error is of the same magnitude (in fact is approximately equal to) the error calculated due to power fluctuations. The result for orbit 18N is to double the uncertainty in the absorption coefficient profile shown earlier in Figure 43.

4.3 Errors due to Antenna Gain Calculations

The maximum error due to antenna gain calculations was determined earlier for all orbits in Table VII. These errors are significantly less than errors due to power fluctuations and, in the case of X-band gain, spacecraft wobble.

Figure 44. Initial power in free space showing the effect of the wobble on the X-band power profile.

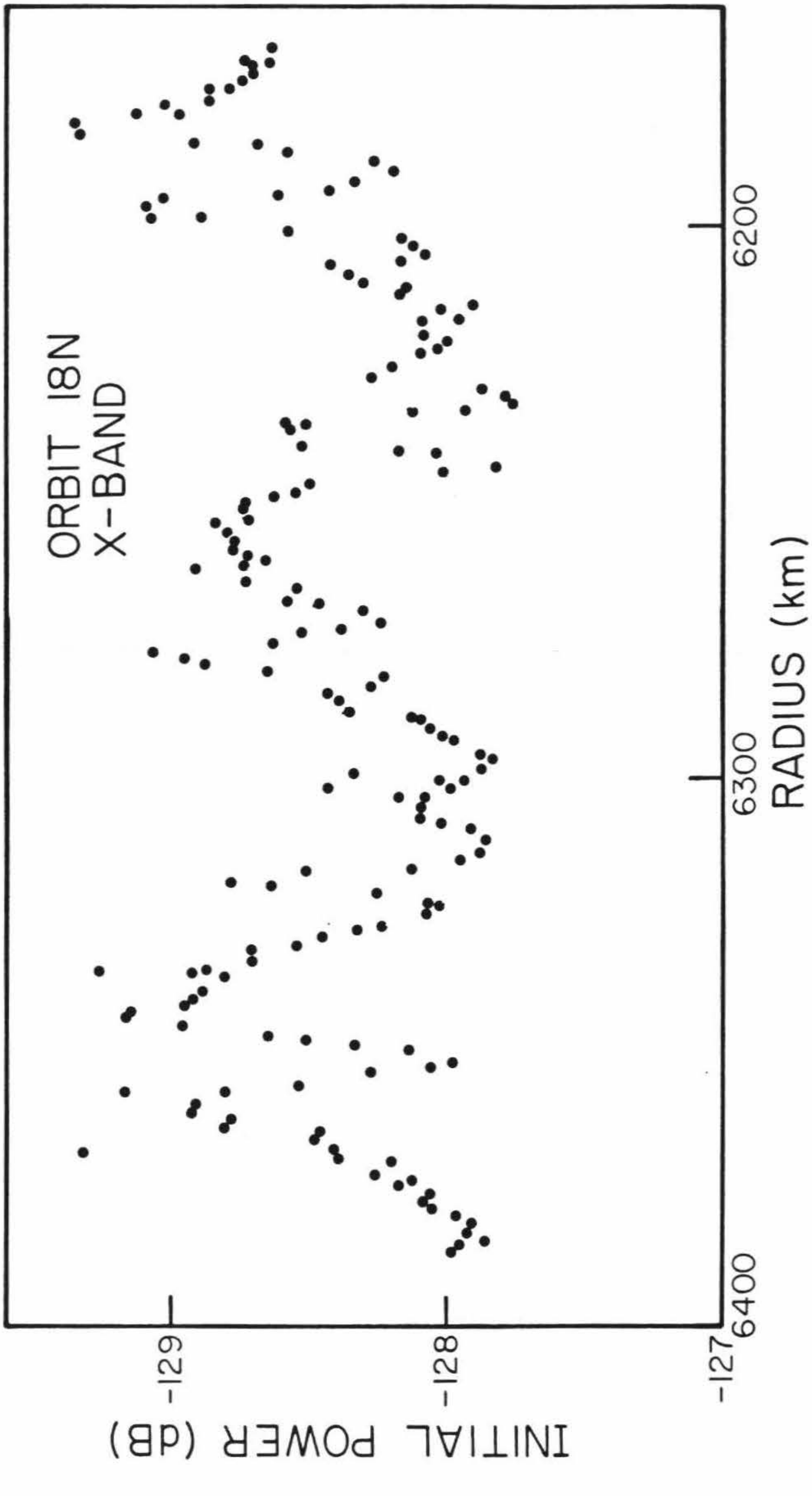
ORBIT 18N
X-BAND
RADIUS (km)
6200
6300
6400
INITIAL POWER (dB)
-129
-128
-127

Figure 45. The effect of the angular variation of the antenna due to spacecraft wobble on the antenna gain is shown at the maximum off axis angle due to antenna mispointing.

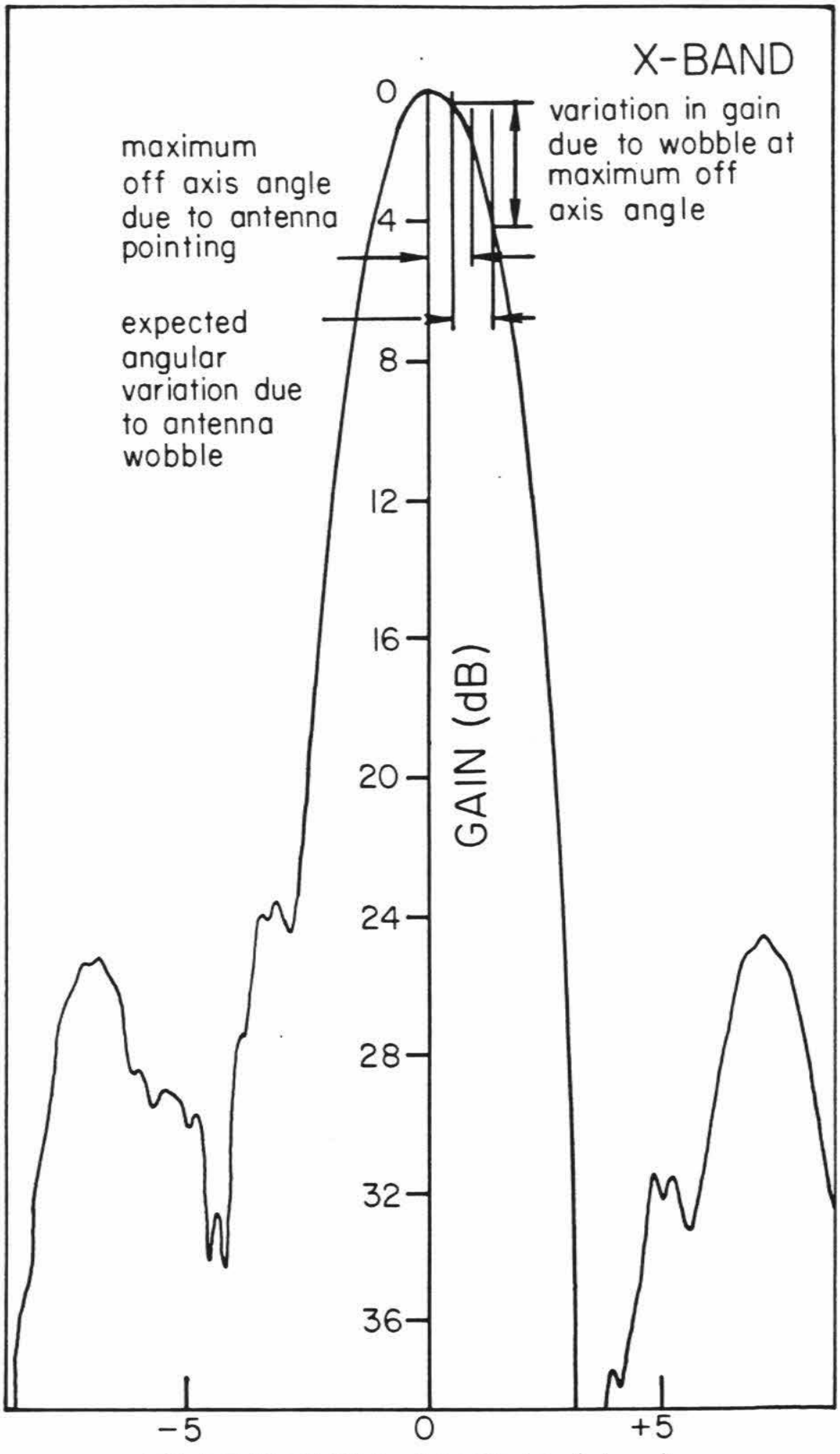
X-BAND
maximum off axis angle due to antenna pointing
expected angular variation due to antenna wobble
variation in gain due to wobble at maximum off axis angle
0
4
8
12
16
20
24
28
32
36
GAIN (dB)
−5
0
+5
ELEVATION ANGLE (deg)

Figure 46. Effect of 1.8 dB gain error resulting from spacecraft wobble on the power profile.

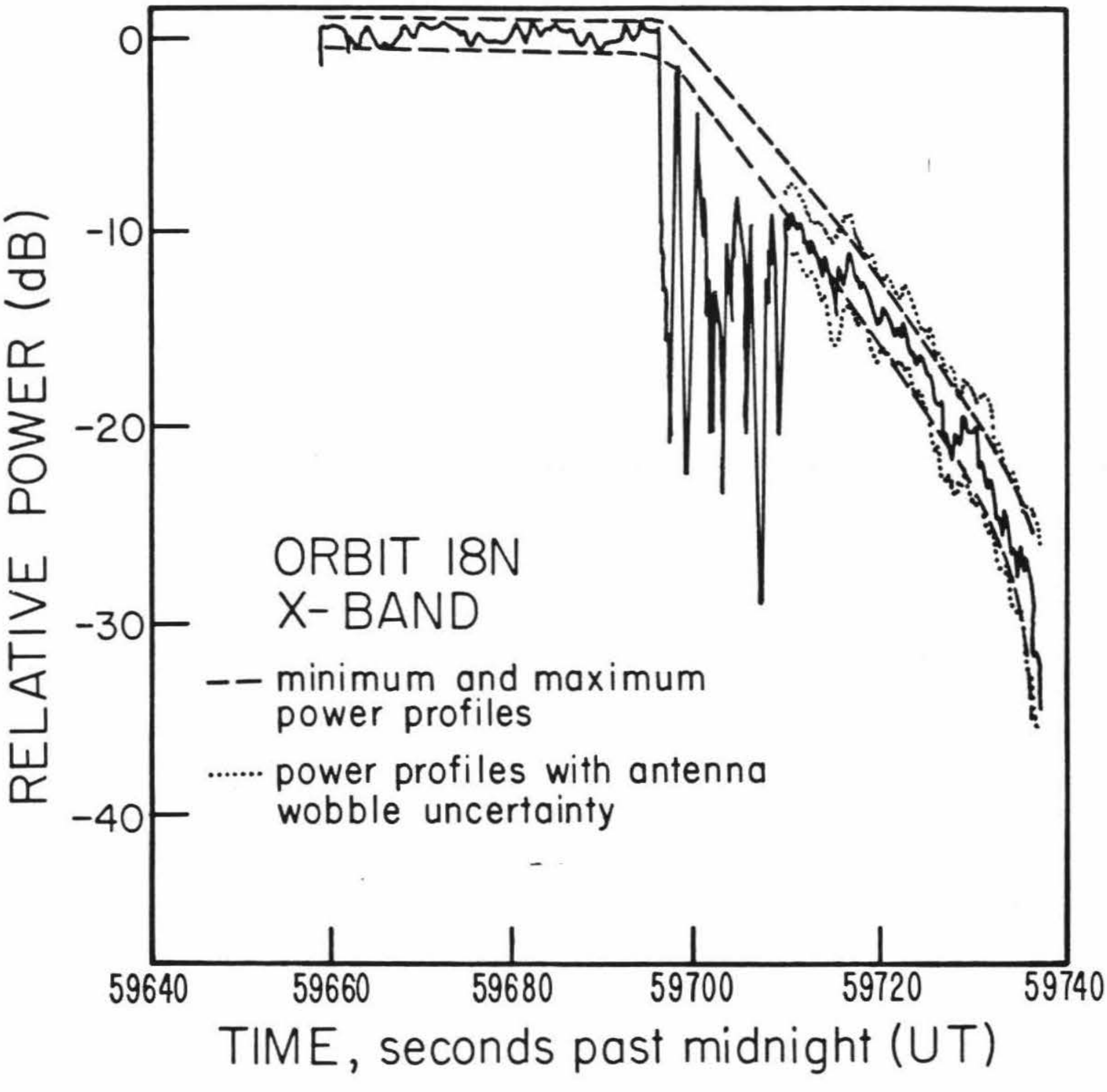
RELATIVE POWER (dB)
0
-10
-20
-30
-40
ORBIT 18N
X-BAND
— — minimum and maximum power profiles
······ power profiles with antenna wobble uncertainty
59640
59660
59680
59700
59720
59740
TIME, seconds past midnight (UT)

A more detailed plot of the antenna corrections for the S-band power profile is shown in Figure 47 where $(P_I - P_C)$ is plotted as a function of ray asymptote in the region of the lower cloud deck. The maximum correction is 0.13 dB — significantly less than any other uncertainty thus far examined.

4.4 Refractive Defocussing Errors

Errors resulting from the calculation of the refractive defocussing are due primarily to the calculation of $d\psi/db$ (the slope of the bending angle vs. ray asymptote curve). Table VIII lists the values of $d\psi/db$ calculated using four different methods as a function of radius for orbit 9N (S-band). The methods include the following:

A. The slope at point i is determined by differentiating the equation at i determined by a quadratic fit of points $i + 1$, i and $i - 1$.

B. The slope at point i is determined by calculating the linear slope for points $i + 1$ and $i - 1$.

C. and D. The slopes at i are calculated by differentiating Lagrange's polynomials. (C) is determined using Lagrange's five-point formula (five points used to determine the polynomial including $i + 2$, $i + 1$, i, $i - 1$, $i - 2$) and (D) is determined using Lagrange's three point formula ($i + 1$, i, and $i - 1$).

Also listed in Table VIII are the average and standard deviations calculated at each radius for $d\psi/db$ and the resulting standard deviation in the refractive defocussing equation. A maximum standard deviation in the refractive defocussing of 2 dB occurs at radii below 6095.5 km. Above this radius, the standard deviation is less than 0.6 dB and in most cases is less than 0.2 dB. This again is an insignificant error compared to power fluctuations for both S- and X-band wavelengths. Figure 48 shows the refractive

Figure 47. S-band antenna corrections for orbit 9N.

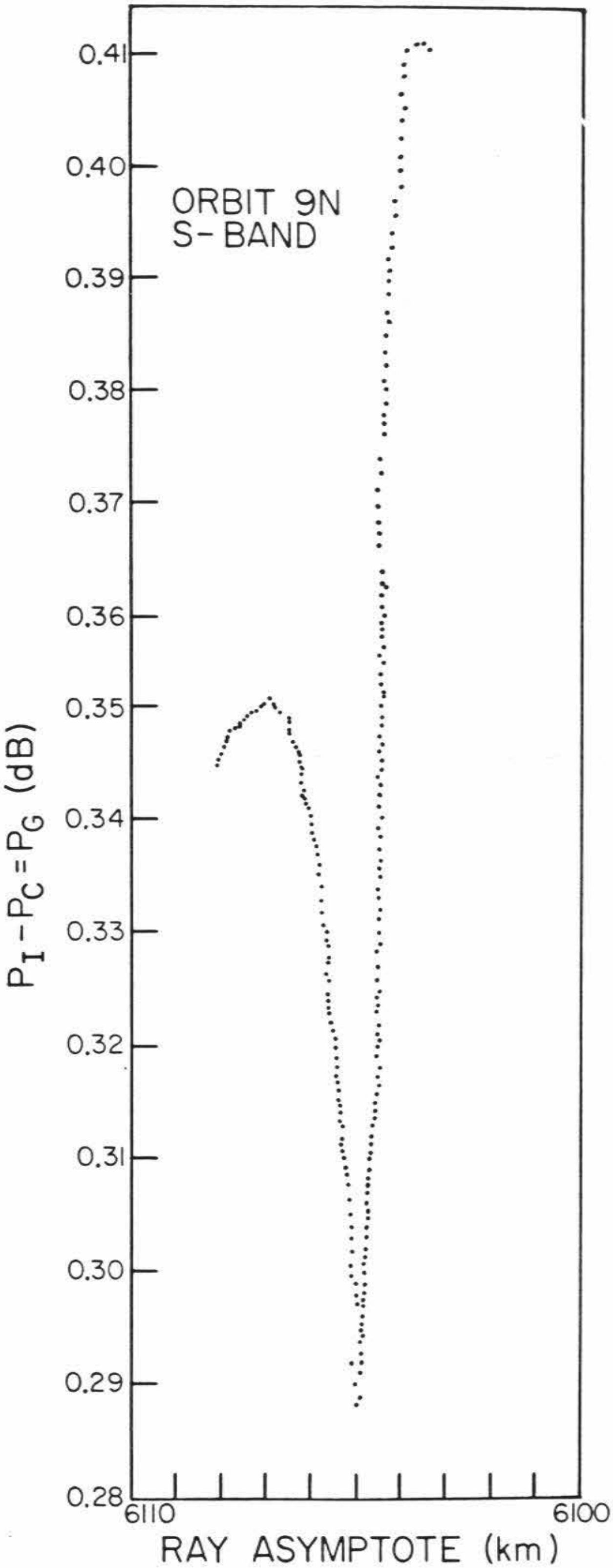
ORBIT 9N
S-BAND
0.41
0.40
0.39
0.38
0.37
0.36
0.35
0.34
0.33
0.32
0.31
0.30
0.29
0.28
$P_I - P_C = P_G$ (dB)
6110
6100
RAY ASYMPTOTE (km)

Table VIII

Error in Calculating $d\psi/db$

Radius	$d\psi/db$ dP/dB (A)	$d\psi/db$ dP/db (B)	$d\psi/db$ dp/db (C)	$d\psi/db$ (D)	$d\psi/db$ (average)	Standard Deviation in $d\psi/db$	Refractive Defocussing Standard Deviation (db)
6084.3	-5.05×10^{-2}	-1.28×10^{-1}	-1.28×10^{-1}	-8.38×10^{-2}	-9.76×10^{-2}	3.77×10^{-2}	1.90
6084.4	-6.36×10^{-2}	-1.11×10^{-1}	-4.50×10^{-2}	-4.32×10^{-2}	-6.57×10^{-2}	3.16×10^{-2}	1.86
6084.6	-6.54×10^{-2}	-9.39×10^{-2}	-9.77×10^{-2}	-1.23×10^{-1}	-9.50×10^{-2}	2.36×10^{-2}	1.12
6085.6	-8.51×10^{-2}	-8.59×10^{-2}	-1.02×10^{-1}	-1.12×10^{-1}	-9.62×10^{-2}	1.31×10^{-2}	0.57
6086.4	-7.17×10^{-2}	-7.11×10^{-2}	-7.47×10^{-2}	-7.60×10^{-2}	-7.34×10^{-2}	2.35×10^{-3}	0.134
6087.3	-5.78×10^{-2}	-5.77×10^{-2}	-6.14×10^{-2}	-5.96×10^{-2}	-5.91×10^{-2}	1.75×10^{-3}	0.123
6088.1	-5.40×10^{-2}	-5.50×10^{-2}	-5.03×10^{-2}	-5.10×10^{-2}	-5.26×10^{-2}	2.28×10^{-3}	0.189
6088.7	-4.76×10^{-2}	-4.81×10^{-2}	-4.92×10^{-2}	-4.91×10^{-2}	-4.85×10^{-2}	7.79×10^{-4}	0.068
6089.5	-3.95×10^{-2}	-4.10×10^{-2}	-4.62×10^{-2}	-4.59×10^{-2}	-4.32×10^{-2}	3.41×10^{-3}	0.34
6090.1	-3.43×10^{-2}	-3.45×10^{-2}	-3.05×10^{-2}	-3.05×10^{-2}	-3.24×10^{-2}	2.25×10^{-4}	0.295
6090.6	-2.72×10^{-2}	-2.71×10^{-2}	-2.07×10^{-2}	-2.58×10^{-2}	-2.52×10^{-2}	3.07×10^{-3}	0.125
6091.1	-2.60×10^{-2}	-2.70×10^{-2}	-2.70×10^{-2}	-2.69×10^{-2}	-2.27×10^{-2}	8.48×10^{-3}	0.008
6091.6	-2.77×10^{-2}	-2.77×10^{-2}	-2.64×10^{-2}	-2.74×10^{-2}	-2.73×10^{-2}	6.16×10^{-4}	0.090
6092.1	-2.30×10^{-2}	-2.20×10^{-2}	-2.34×10^{-2}	-2.34×10^{-2}	-2.315×10^{-2}	3.00×10^{-4}	0.054
6092.5	-1.89×10^{-2}	-1.89×10^{-2}	-1.86×10^{-2}	-1.81×10^{-2}	-1.86×10^{-2}	3.77×10^{-2}	0.085
6093.0	-1.80×10^{-2}	-1.80×10^{-2}	-1.81×10^{-2}	-1.81×10^{-2}	-1.80×10^{-2}	5.77×10^{-5}	0.006
6093.6	-1.70×10^{-2}	-1.70×10^{-2}	-1.73×10^{-2}	-1.75×10^{-2}	-1.72×10^{-2}	2.45×10^{-4}	0.575
6093.9	-1.49×10^{-2}	-1.49×10^{-2}	-1.59×10^{-2}	-1.57×10^{-2}	-1.54×10^{-2}	5.26×10^{-4}	0.137
6094.4	-1.37×10^{-2}	-1.41×10^{-2}	-1.32×10^{-2}	-1.32×10^{-2}	-1.36×10^{-2}	4.36×10^{-4}	0.121
6094.7	-1.31×10^{-2}	-1.32×10^{-2}	-1.23×10^{-2}	-1.23×10^{-2}	-1.27×10^{-2}	4.92×10^{-4}	0.150
6095.1	-1.22×10^{-2}	-1.22×10^{-2}	-1.28×10^{-2}	-1.26×10^{-2}	-1.24×10^{-2}	3.00×10^{-4}	0.093
6095.5	-1.26×10^{-2}	-1.26×10^{-2}	-1.20×10^{-2}	-1.22×10^{-2}	-1.24×10^{-2}	3.00×10^{-4}	0.093
6095.9	-1.23×10^{-2}	-1.23×10^{-2}	-1.24×10^{-2}	-1.27×10^{-2}	-1.24×10^{-2}	1.89×10^{-7}	0.054
6096.3	-1.11×10^{-2}	-1.10×10^{-2}	-1.22×10^{-2}	-1.21×10^{-2}	-1.16×10^{-2}	6.38×10^{-5}	0.222
6096.7	-9.68×10^{-3}	-9.99×10^{-3}	-1.00×10^{-2}	-1.00×10^{-2}	-9.92×10^{-3}	1.58×10^{-4}	0.068
6097.1	-8.86×10^{-3}	-8.83×10^{-3}	-7.99×10^{-3}	-7.98×10^{-3}	-8.41×10^{-3}	4.97×10^{-4}	0.228
6097.4	-7.70×10^{-3}	-7.69×10^{-3}	-7.62×10^{-3}	-7.53×10^{-3}	-7.64×10^{-3}	7.85×10^{-5}	0.038
6097.7	-7.22×10^{-3}	-7.22×10^{-3}	-7.52×10^{-3}	-7.47×10^{-3}	-7.36×10^{-3}	1.60×10^{-4}	0.085
6098.1	-7.07×10^{-3}	-7.10×10^{-3}	-6.96×10^{-3}	-6.93×10^{-3}	-7.02×10^{-3}	8.27×10^{-5}	0.042
6098.4	-7.15×10^{-3}	-7.17×10^{-3}	-6.76×10^{-3}	-6.75×10^{-3}	-6.96×10^{-3}	2.34×10^{-4}	0.127

defocussing calculated using the four methods for calculating $d\psi/db$.

4.5 Summary of Errors

Table IX lists the parameters for which uncertainties have been calculated along with the associated uncertainties for S- and X-band wavelengths. The parameter producing the greatest uncertainty in the S-band excess attenuation is power fluctuation. Two parameters contribute to the X-band uncertainty; power fluctuations and spacecraft wobble. Uncertainty in antenna position can also contribute significantly to the X-band excess attenuation.

Figure 49 (a and b) show the absorption coefficient profiles for orbits 9N (S-bnd) and 18N (S- and X-band) with associated error bars as calculated in this chapter. Although small fluctuations in the absorption coefficient profiles cannot be attributed to cloud layers within the lower cloud deck, the estimated uncertainties in no way preclude the existence of a highly absorbing lower cloud layer.

Table IX

Summary of Errors

Parameter	S-band Uncertainty in Excess Attenuation	X-band Uncertainty in Excess Attenuation
Power fluctuations	4 dB	2 dB
Averaging	0.5 dB	--
Spacecraft wobble	0.5 dB	2 dB
Antenna position	0.2 dB	0.6 dB
Refractive defocussing	$\lesssim$ 0.2 dB	$\lesssim$ 0.2 dB

5. Resulting Absorption Coefficient Profiles for All Orbits

Figure 50 shows the absorption coefficient profiles for all orbits thus far analyzed. The profiles are divided into four groups representing four different

Figure 48. Refractive defocussing calculated using four methods of determining $d\psi/db$.

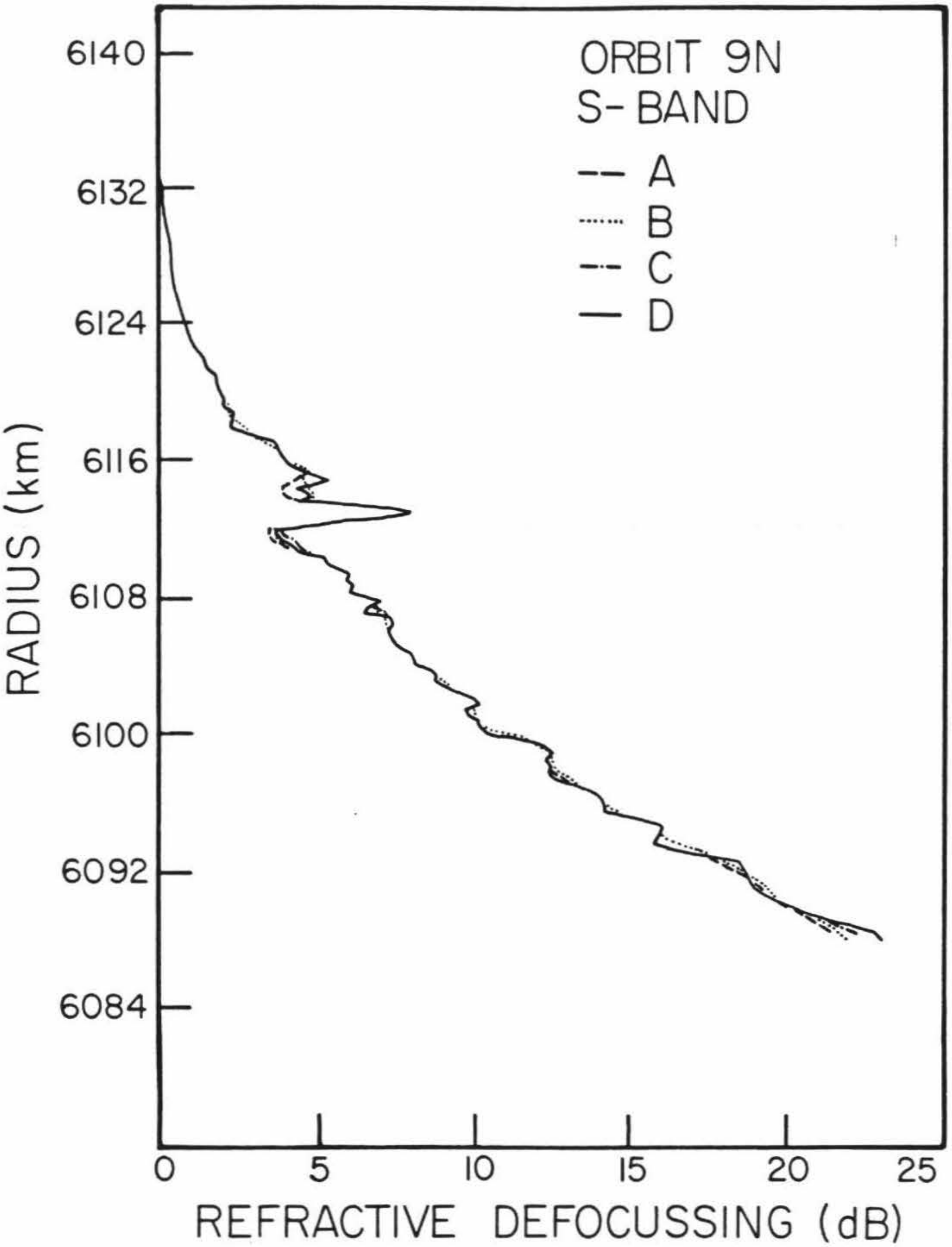
ORBIT 9N
S- BAND
A
B
C
D
RADIUS (km)
6140
6132
6124
6116
6108
6100
6092
6084
0
5
10
15
20
25
REFRACTIVE DEFOCUSSING (dB)

Figure 49. Absorption coefficient profile for orbit 9N and 18N (S- and X-band) showing error bars resulting from all error calculations.

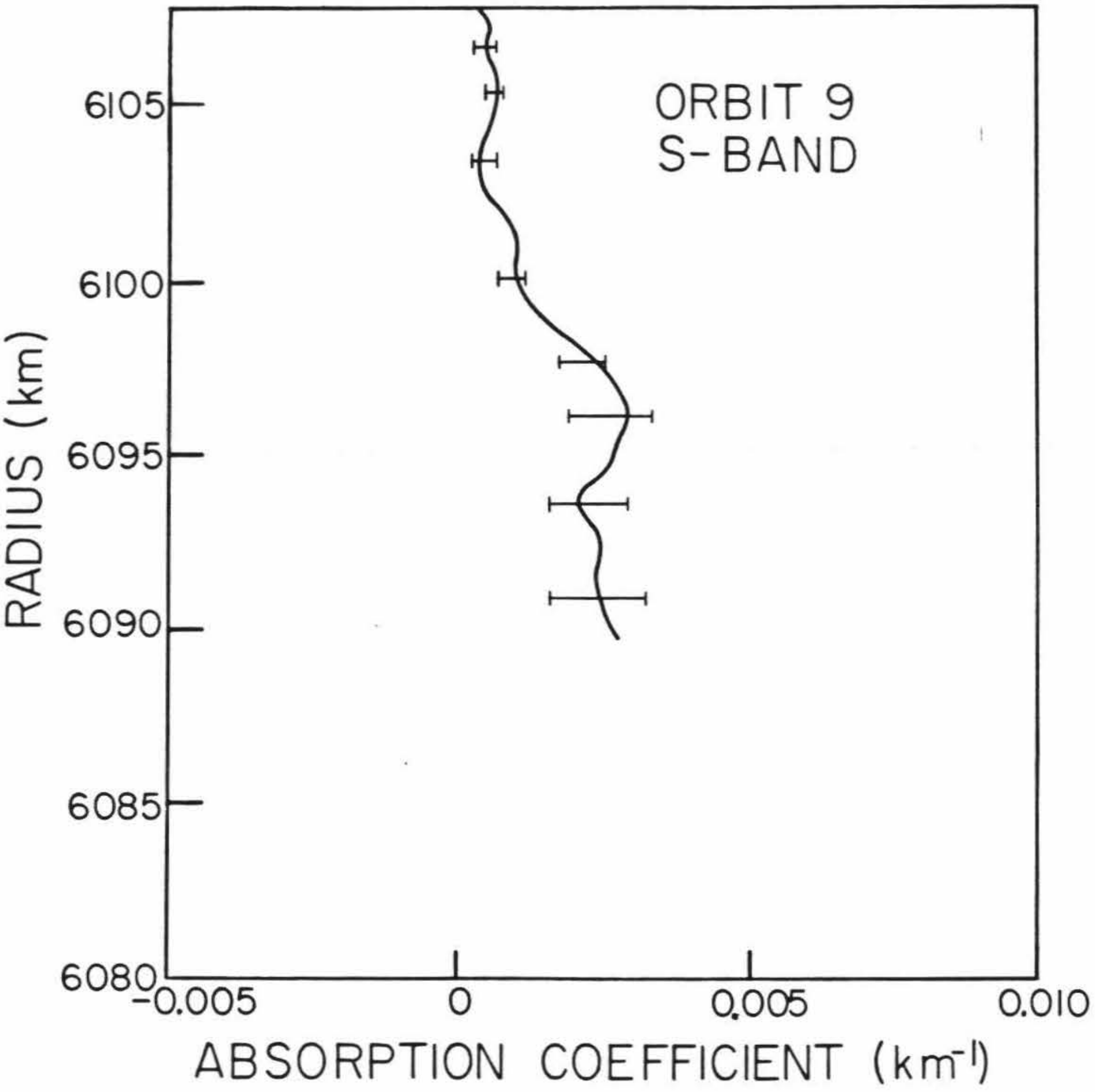
ORBIT 9
S-BAND
RADIUS (km)
6105
6100
6095
6090
6085
6080
-0.005
0
0.005
0.010
ABSORPTION COEFFICIENT (km^{-1})

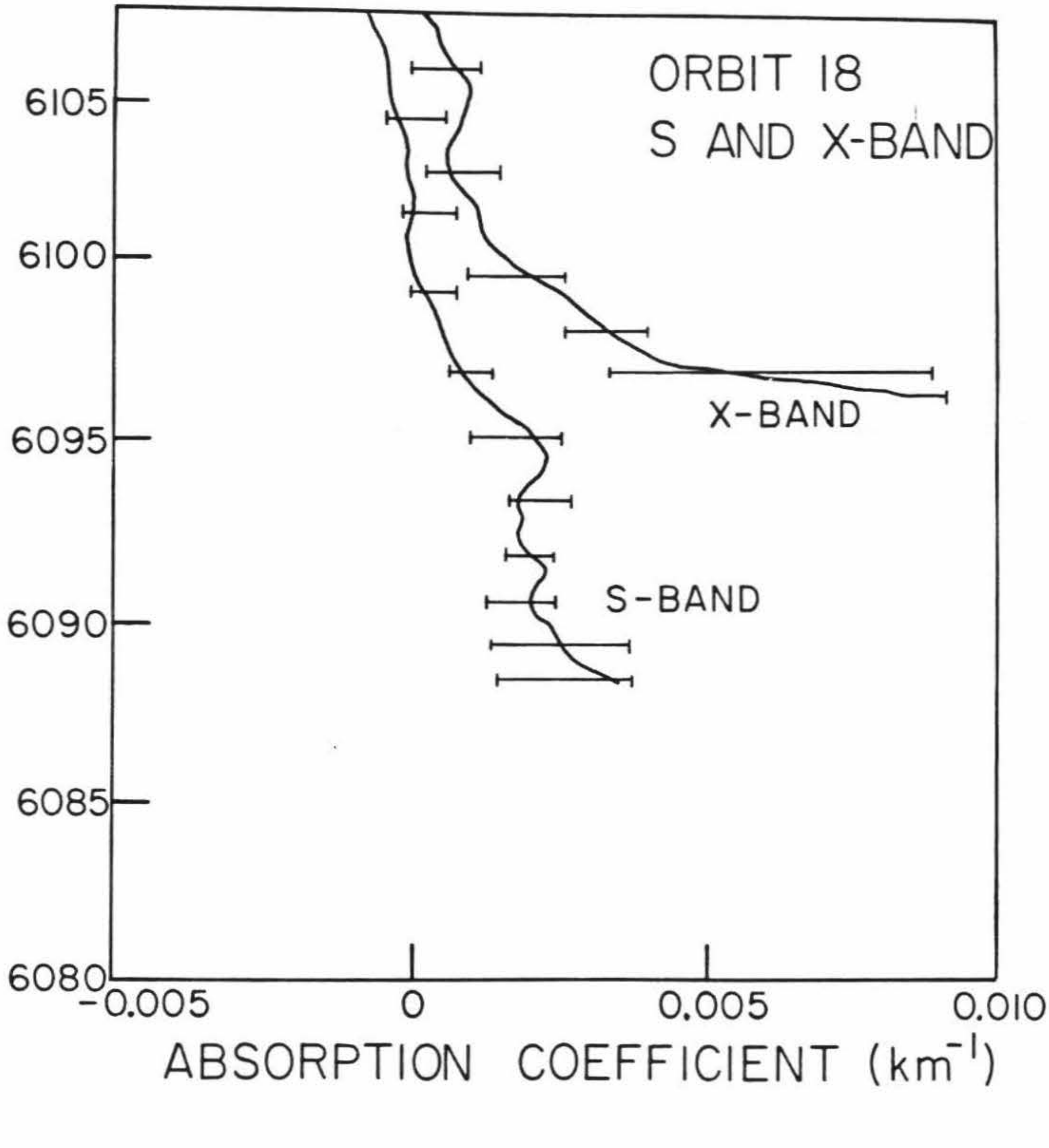
ORBIT 18
S AND X-BAND
X-BAND
S-BAND
RADIUS (km)
6105
6100
6095
6090
6085
6080
-0.005
0
0.005
0.010
ABSORPTION COEFFICIENT (km^{-1})

latitudinal regions of the Venus atmosphere. These groups include the equatorial, the midlatitudinal, the collar and the polar regions. Substantial variability in these absorption coefficient profiles is apparent. The midlatitude absorption coefficients are in general much less than in the other three regions and remain fairly constant from 1 bar to about 3 bars (7 bars in the case of Mariner 5). Farther north in the collar region, the absorption coefficient increases by about a factor of four or possibly more. The bottom of the absorbing region, or a leveling off was not detected. In the polar region, the absorption coefficients are of approximately the same magnitude as in the collar region but reach their maximum at a lower altitude than in the collar region. The profiles in the equatorial region suggest the absorption is approximately twice that in the midlatitude regions but the bulk of the absorption is contained in a fairly well defined layer between about 0.9 bars and 1.5 bars. This layering phenomena was also observed by the Particle Size Spectrometer and the Sounder nephelometer.

Figure 50. S-band absorption coefficient profiles for all orbits thus far analyzed.

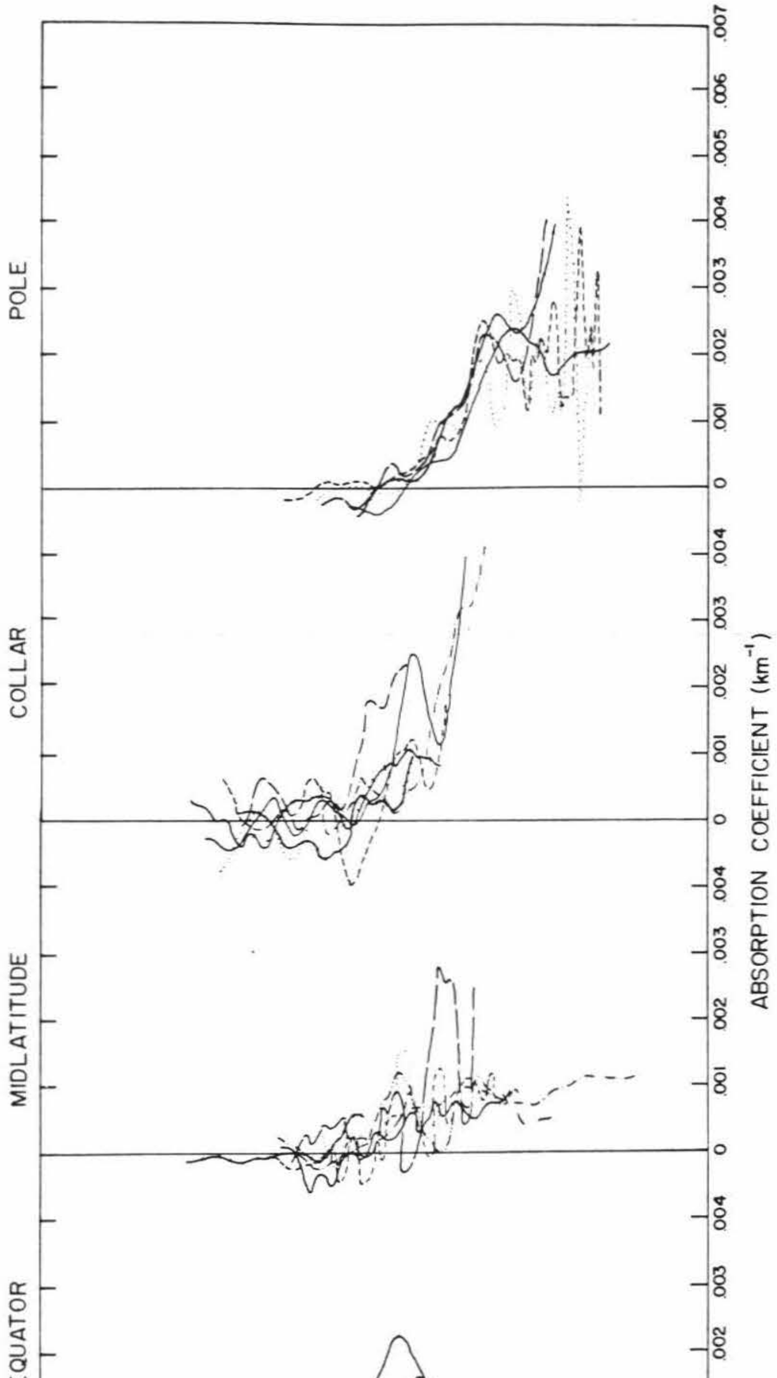
EQUATOR
MIDLATITUDE
COLLAR
POLE
PRESSURE (bars)
1
10
10
ABSORPTION COEFFICIENT (km^{-1})
0
.001
.002
.003
.004
0
.001
.002
.003
.004
0
.001
.002
.003
.004
0
.001
.002
.003
.004
.005
.006
.007

CHAPTER V

LIQUID CONTENT CALCULATIONS

The primary goal of this thesis is to determine the composition and global variability of the lower cloud deck on Venus using the absorption coefficient profiles obtained from the Pioneer Venus radio occultation experiment. In order to accomplish this goal, a cloud composition must be proposed, its dielectric properties measured or calculated, and a mass content determined. If the wavelength dependence of the dielectric properties of the proposed material match those determined by the S- and X- band absorption coefficient measurements, and the mass content derived near the equator matches that determined by the Particle Size Spectrometer, it is likely the correct cloud composition has been chosen. Thus the main goal of the following chapters is to determine the composition of the clouds.

A number of authors have concluded that the upper and middle atmospheric regions of Venus are made up of concentrated sulfuric acid-water clouds. Hansen and Hovenier (1974) determined using polarimetry that the upper clouds are monodispersed spherical droplets with an index of refraction of 1.44 ± 0.01 and a radius of 1.05 μ. Sill (1972), Pollack et al (1974) and Young (1973) proposed a concentrated sulfuric acid-water solution as the only plausible cloud component which matched Hansen and Hovenier's measurements and in addition had a very low water vapor pressure. The proposed composition was supported by data from the Venera 9 and 10 spacecraft to several optical depths by in situ measurements of Venusian clouds. Pollack et al (1978) determined through modeling that the clouds are 85% sulfuric acid (by weight) down to an optical depth of at least 25 at 1.2 to 4.0 μ wavelengths. This includes the upper and middle cloud decks.

More recently, modeling has been done using the backscatter cross-sections measured by the Pioneer Venus nephelometers (Ragent and Blamont, 1980) and the size and number distributions measured by the Pioneer Venus Particle Size Spectrometer (LCPS) (Knollenberg and Hunten, 1980) aboard the Sounder probe. The size and number distributions are used along with a suggested index of refraction to produce a backscatter cross-section. The backscatter cross-sections measured by the nephelometers can be matched when indices corresponding to concentrated sulfuric acid are chosen — except in the lower cloud deck for the largest particle size mode (mode 3). The calculated mode 3 index is 1.2-1.3 assuming spherical liquid cloud particles. This index does not correspond to any known material capable of composing the clouds of Venus. In order to explain this unusually low index of refraction, several cloud particle models may be invoked including absorbing particles, irregularly shaped particles, composite particles (several smaller particles clumped together) and particles with entrained smaller particles (Knollenberg et al., 1980). Blamont and Ragent (1980) favor absorbing particles to explain the low refractive index. Knollenberg and Hunten (1980) favor irregularly shaped particles and make a strong argument for solid mode 3 particles. As will be seen in Chapter VI, this author favors the entrained particle model.

As a first attempt at determining the mass content of the lower cloud deck using the radio occultation absorption coefficient data, it will be assumed that the lower cloud deck is composed of a liquid concentrated sulfuric acid-water solution. Excluding the evidence provided by the LCPS and nephelometer against purely liquid cloud particles, this is the most probable and simplest model for the cloud particles. In addition, conclusions about the lower cloud deck based on the probe results represent one pass through the atmosphere on one day in one part of a cloud deck which is known to be variable (Blamont and

Ragent, 1980). Based on this limited evidence, it is important to investigate all plausible cloud models before any firm conclusions may be reached.

Occultation data from orbit 69 exit (69X) will be used as an example inasmuch as it was located closest to the equator and can therefore be compared to the probe results. Data from orbit 18N, 338N and 30X will also be shown to provide a comparison between polar, collar, midlatitudinal and equatorial regions of the Venus atmosphere.

1. Subtraction of Gaseous Absorbers

In order to use the absorption coefficient profiles derived in the previous chapter to calculate the mass content of the clouds, absorption due to all gaseous species in the Venus atmosphere must be subtracted out. Gases that are known to be present in significant abundances are CO_2, N_2, H_2O, SO_2 and H_2SO_4. Other trace gases were detected by the probe gas chromatograph (Oyama et al., 1980) and mass spectrometer (Hoffman et al., 1980a) aboard the Pioneer Venus probes, however, the mixing ratios are small and therefore they are not expected to contribute to the atmospheric absorption. Figure 51 shows the mixing ratios (in ppm) of these gases for orbits 69X (equatorial), orbit 30X (midlatitudinal), orbit 338N (collar) and 18N (polar), respectively. The N_2, SO_2 and H_2O profiles are the same for orbits 69X and 18N; however, the SO_3 and H_2SO_4 profiles are different due to differences in the temperature profiles in the two regions. The profile for N_2 was derived from nitrogen mixing ratios estimated by Hoffman et al. (1980a). The CO_2 profile is just the difference between the nitrogen profile and 100%. The SO_2 profile was derived from the measurements of several authors (Hoffman et al., 1980a; Moroz et al., 1979 a and b; Stewart et al., 1979; and Oyama et al., 1980) and includes results from the Pioneer Venus mission as well as Veneras 11 and 12. The profile describing the H_2O mixing ratio is

Figure 51. Mixing ratio of gaseous components of the atmosphere for orbits 69X (equatorial), 30X (midlatitudinal), 338N (collar) and 18N (polar).

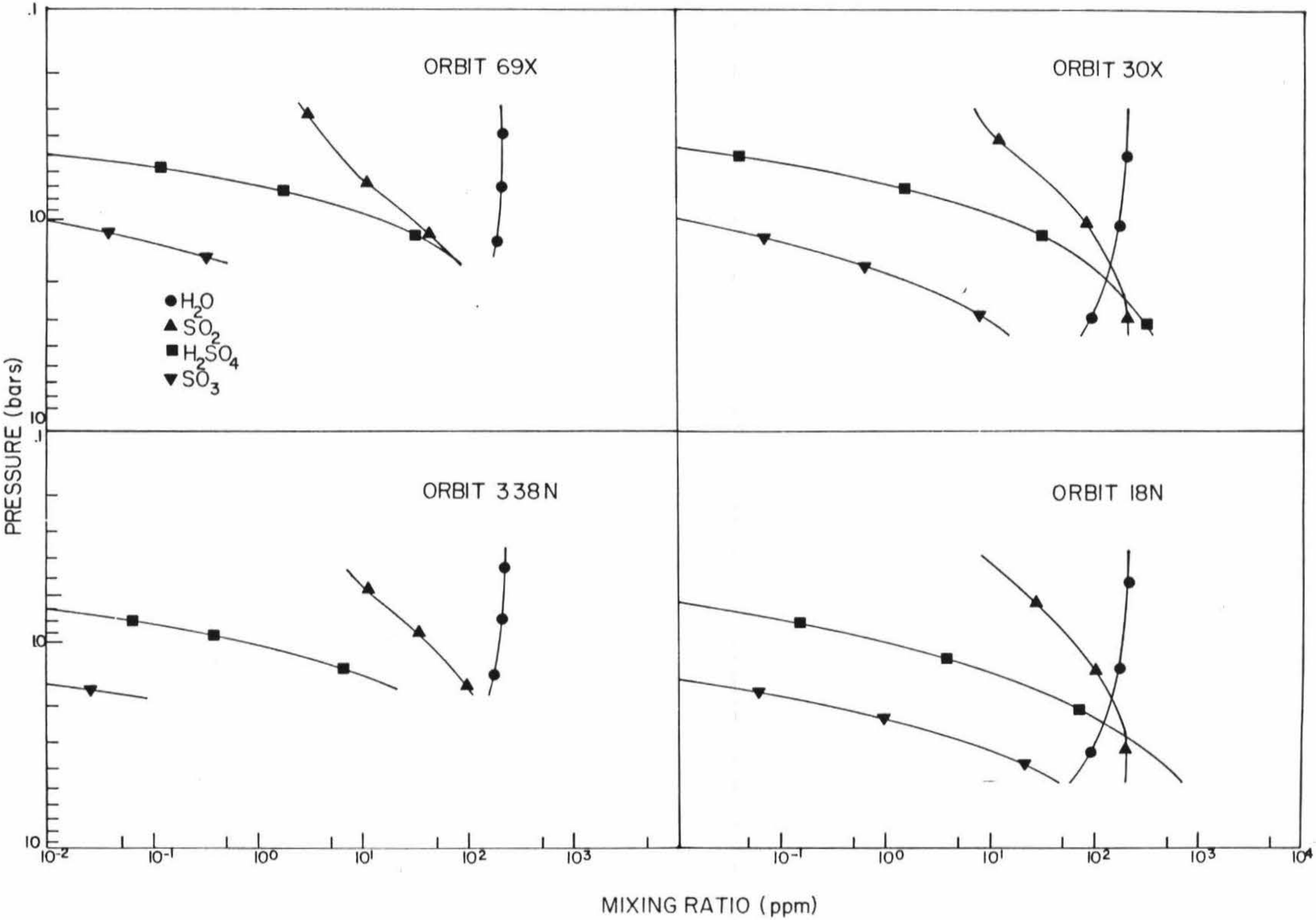
ORBIT 69X
ORBIT 30X
ORBIT 338N
ORBIT 18N
● H_2O
▲ SO_2
■ H_2SO_4
▼ SO_3
PRESSURE (bars)
.1
1.0
10
.1
1.0
10
MIXING RATIO (ppm)
10^{-2}
10^{-1}
10^{0}
10^{1}
10^{2}
10^{3}
10^{-1}
10^{0}
10^{1}
10^{2}
10^{3}
10^{4}

that which was measured spectrophotometrically aboard Veneras 11 and 12 (Moroz et al., 1979 a and b). The H_2SO_4 profile is the equilibrium sulfuric acid vapor pressure above a solution of liquid sulfuric acid-water at the temperature and composition of the lower cloud (see section on cloud concentration calculations). These profiles are correct to within a factor of two.

The absorption properties of CO_2 and N_2, including pressure broadening effects, are very well understood and have been measured in the laboratory (Ho et al., 1966). The absorption is due to quadrupole-induced dipole transitions which become important at high pressure and is

$$\alpha_{CO_2} = 2.65 \times 10^7 \left[f^2_{CO_2} + 0.25 f_{CO_2} f_{N_2} + 0.0054 f^2_{N_2}\right] \frac{\nu^2 P^2}{T^5} \text{ km}^{-1} \qquad (95)$$

where α is the absorption coefficient in km^{-1}, f is the volume mixing ratio, P is the pressure in atmospheres, ν is the frequency in GHz and T is the temperature in K.

The absorption coefficient of SO_2 was determined theoretically by Janssen and Poynter (1981) using the Van Vleck-Weisskopf theory. Later laboratory measurements of the SO_2 absorption were made by Steffes and Eshleman (1981) resulting in the following expression

$$\alpha_{SO_2} = 5.76\, \nu^2\, P^{1.20}\, T^{-3.1}\, f_{SO_2} \text{ km}^{-1} \qquad (96)$$

where f is now in ppm.

The absorption coefficient equation for water vapor is taken from Janssen (1972) and includes Earth atmospheric water vapor absorption (Barrett and Chung, 1962) along with high pressure effects as determined by Ho et al. (1966)

$$\alpha_{H_2O} = 7.535 \times 10^7 f_{H_2O}\, \nu^2 \left[\exp\left(-\frac{644}{T}\right)\right] \frac{P}{T^{3.5}}$$

$$\times \left[\frac{\Delta\nu}{(\nu - \nu_0)^2 + \Delta\nu^2} + \frac{\Delta\nu}{(\nu + \nu_0)^2 + \Delta\nu^2}\right]$$

$$+ 3.80 \times 10^9 f_{H_2O}\, \nu^2 \frac{bP^2}{T^{5.1}} \text{ km}^{-1} \tag{97}$$

where

$$b = f_{N_2} + 1.62 f_{CO_2} + 4.6 f_{H_2O} \tag{98}$$

$$\nu_0 = 22.235 \text{ GHz} \tag{99}$$

$$\Delta\nu = 95.64 \frac{bP}{T^{0.625}} \text{GHz} \tag{100}$$

and f is the volume mixing ratio.

The absorption coefficient for sulfuric acid vapor was calculated from the sulfuric acid vapor spectrum measured by Kuczkowski et al. (1981). Allen (private communication) determined the lines and corresponding intensities between 311 MHz and 244 GHz at 300 K (Figure 52). The maximum absorption coefficient per mixing ratio of H_2SO_4 was then determined for each line from Allen's calculated intensities assuming a linewidth parameter of 7.2 MHz/Torr — the linewidth parameter of SO_2 in CO_2. The Van Vleck-Weiskopf function was used to determine the pressure broadening effects which are important in the region of the lower cloud deck. The result of summing all contributing lines at S- and X-band frequencies is an absorption coefficient per unit volume mixing ratio which is greater than SO_2. In light of these preliminary results, Janssen and Poynter (private communication) determined the absorption coefficient at several pressures and temperatures appropriate to the lower cloud region. The results of their calculations are shown in Figure 52 for 180 ppm H_2SO_4. The

Figure 52. (a) Intensity as a function of frequency for the lines in the sulfuric acid vapor spectrum. (b) Absorption coefficient for sulfuric acid vapor at 10, 3, 2 and 1 bar and for 180 ppm of the vapor.

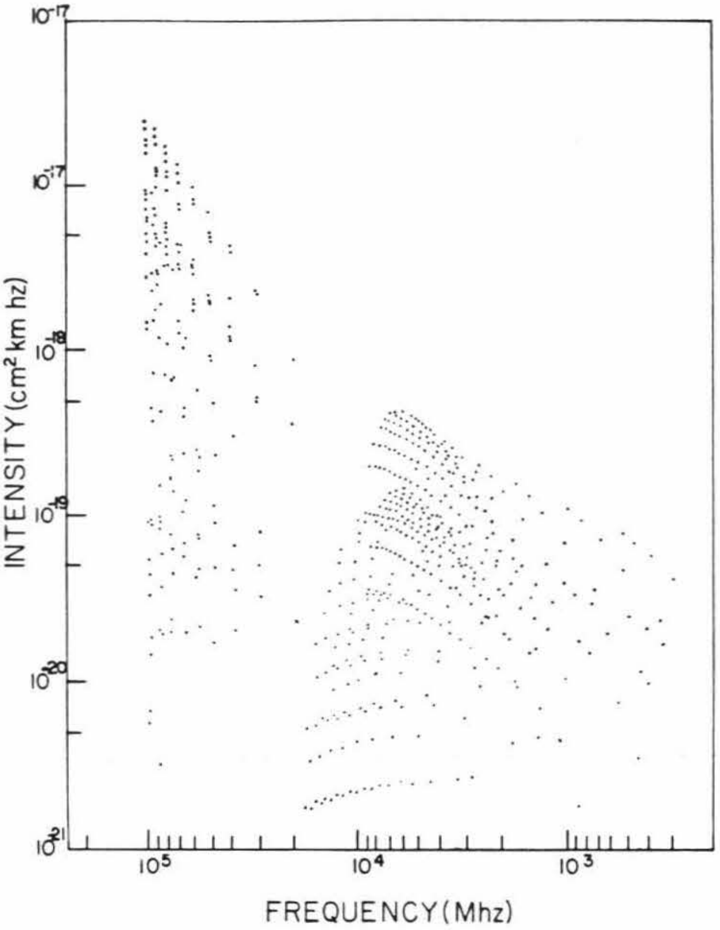
10^{-17}
10^{-17}
10^{-18}
10^{-19}
10^{-20}
10^{-21}
INTENSITY (cm^2 km hz)
10^5
10^4
10^3
FREQUENCY (Mhz)

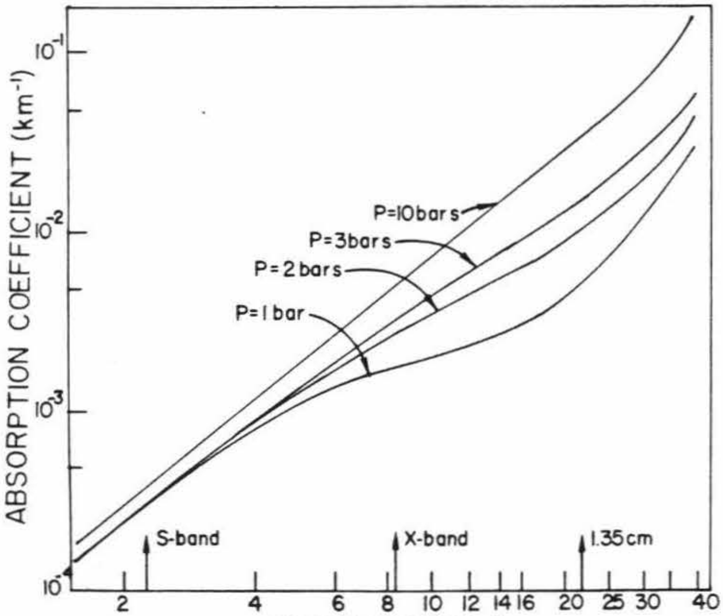
10^{-1}
10^{-2}
10^{-3}
10^{-4}
ABSORPTION COEFFICIENT (km^{-1})
P=10bars
P=3bars
P=2bars
P=1bar
S-band
X-band
1.35cm
2
4
6
8
10
12
14
16
20
25
30
40
FREQUENCY (Ghz)

primary source of error in the absorption coefficient estimates is the choice of the linewidth parameter. The uncertainty in this parameter is expected to be less than a factor of two, however.

Sulfuric acid vapor absorption coefficients used in subtracting out the absorption due to gases were determined from Figure 52 and were corrected for the appropriate vapor mixing ratios

Note that the wavelength dependence of all the above gases is exactly $1/\lambda^2$, except for sulfuric acid. This dependence will be important later when the wavelength dependence of the X- and S-band absorption profiles is discussed.

Figure 53 (a,b and c) shows the absorption coefficient profiles for CO_2, H_2O, H_2SO_4 and SO_2 as well as the absorption coefficient profile derived from orbits 69X, 30X, 338N, 347N, (S-band) and 18N (S- and X-band) radio occultation experiment both before and after the gaseous absorptions have been subtracted out. Gaseous absorption contributes significantly to the total atmospheric absorption only in the lowest regions of the lower cloud deck where SO_2 and H_2SO_4 absorption is appreciable. H_2SO_4 absorption contributes the most to the total absorption coefficient; however, it is significantly less than the absorption due to cloud material except at the lowest levels of the lower cloud deck. H_2O vapor absorption is insignificant at all levels of the lower cloud deck.

2. The Liquid Content Equation

Now that the absorption coefficient profiles due only to absorption by cloud material have been derived, the liquid content of the clouds may be calculated. The equation used in this calculation was originally derived by Mie(1908) and is described in detail and in English by Van de Hulst (1957) and Hasted (1973). When an electromagnetic wave propagates through a cloud, it is scattered and absorbed by the cloud particles. The cross-sections depend on the

Figure 53. All absorption coefficient profiles for orbits (a) 69X (equatorial) and 30X (midlatitudinal); (b) 338N (collar) and 347N (collar-warmer); and (c) 18N (polar), for S-and X-band.

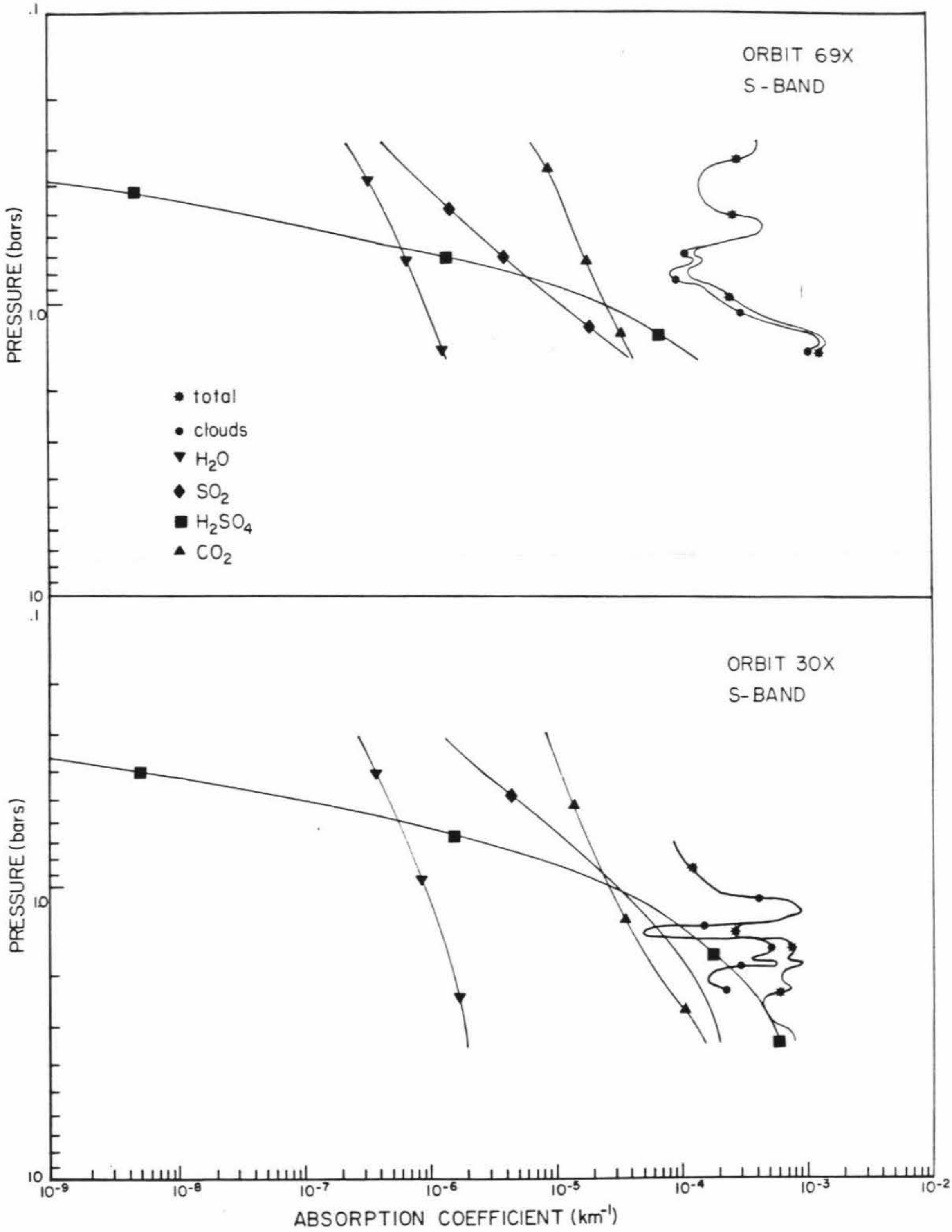
ORBIT 69X
S-BAND
ORBIT 30X
S-BAND
✱ total
● clouds
▼ H_2O
◆ SO_2
■ H_2SO_4
▲ CO_2
PRESSURE (bars)
.1
1.0
10
ABSORPTION COEFFICIENT (km^{-1})
10^{-9}
10^{-8}
10^{-7}
10^{-6}
10^{-5}
10^{-4}
10^{-3}
10^{-2}

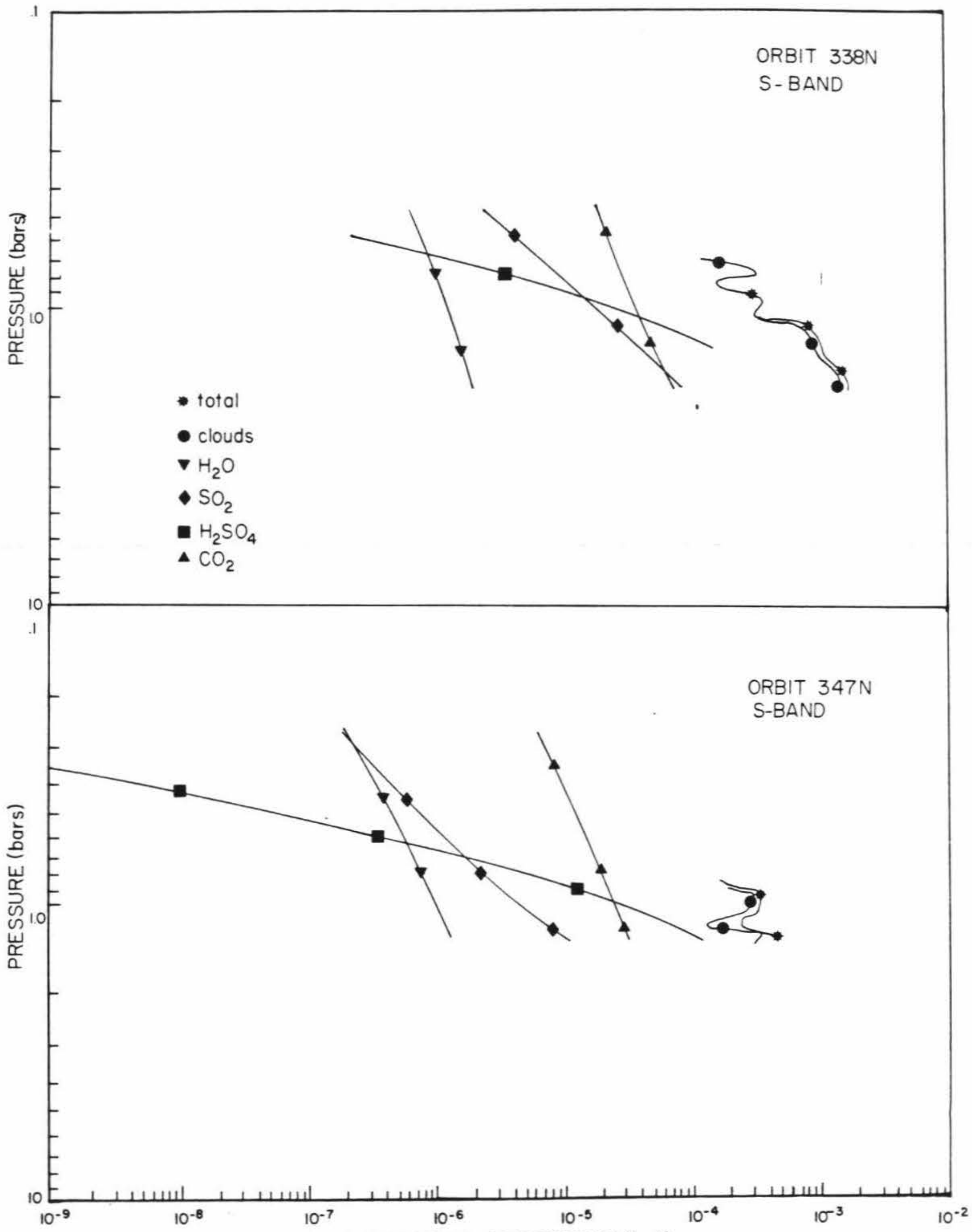
ORBIT 338N
S-BAND
ORBIT 347N
S-BAND
PRESSURE (bars)
PRESSURE (bars)
.1
1.0
10
.1
1.0
10
* total
● clouds
▼ H_2O
◆ SO_2
■ H_2SO_4
▲ CO_2
10^{-9}
10^{-8}
10^{-7}
10^{-6}
10^{-5}
10^{-4}
10^{-3}
10^{-2}
ABSORPTION COEFFICIENT (km^{-1})

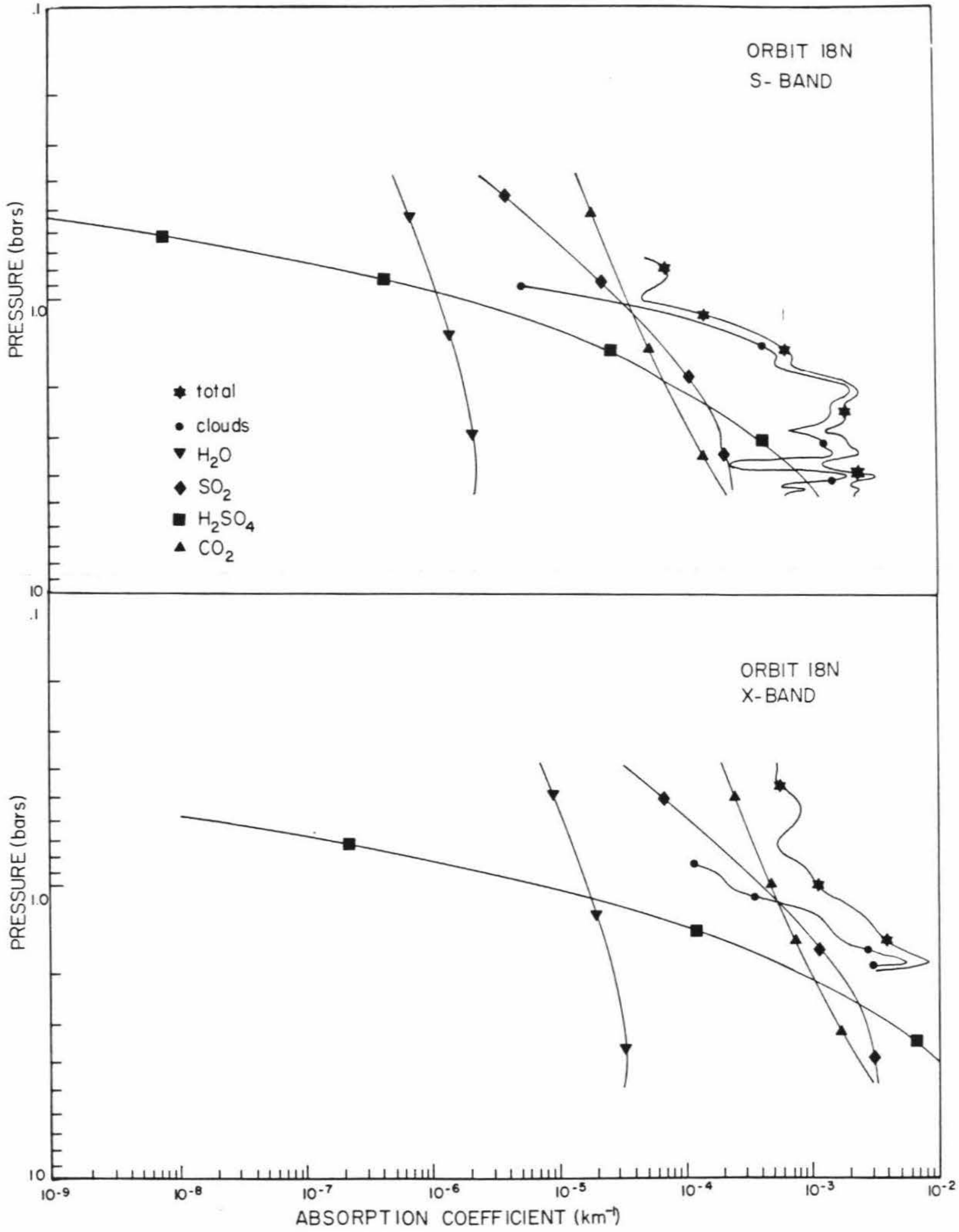
.1
1.0
10
PRESSURE (bars)
ORBIT 18N
S- BAND
✱ total
● clouds
▼ H_2O
◆ SO_2
■ H_2SO_4
▲ CO_2
.1
1.0
10
PRESSURE (bars)
ORBIT 18N
X- BAND
10^{-9}
10^{-8}
10^{-7}
10^{-6}
10^{-5}
10^{-4}
10^{-3}
10^{-2}
ABSORPTION COEFFICIENT (km^{-1})

size, shape and electromagnetic properties of the particles. For a plane wave of wavelength λ incident on a single spherical particle of radius a, the scattering cross-section, C_s, is given by:

$$C_s = \frac{\lambda^2}{2\pi} \sum_{n=1}^{\infty} (2n + 1)(c_n^2 - b_n^2) \tag{101}$$

and the absorption cross-section by:

$$C_a = \frac{\lambda^2}{2\pi}(-Re) \sum_{n=1}^{\infty} (2n + 1)(c_n - b_n) \tag{102}$$

where c_n and b_n are Mie coefficients which are functions of $\alpha_0 = 2\pi a/\lambda$ and the complex dielectric constant. If $\alpha_0 << 1$ as is the case for spherical particles of radii much less than the wavelength, all powers higher than the sixth can be neglected. The resulting cross-sections are:

$$C_s = \frac{128\pi^5 a^6}{3\lambda^4} \left| \frac{\varepsilon - 1}{\varepsilon + 2} \right|^2 \tag{103}$$

$$C_a = \frac{8\pi^2 a^3}{\lambda} \mathrm{Im} \left[\frac{\varepsilon - 1}{\varepsilon + 2} \right] \tag{104}$$

where $\left[\frac{\varepsilon - 1}{\varepsilon + 2} \right]$ describes the polarization for a spherical particle of complex dielectric constant ε.

Figure 54 shows the $\lambda = 13.06$ cm absorption and scattering cross-sections for a 10 μ radius particle at 350 K as a function of sulfuric acid concentration. Figure 54 shows the cross-sections for a 10 μ particle and $\lambda = 13.06$ cm as a function of temperature for several concentrations. The plots demonstrate the absorption cross-section is many orders of magnitude greater than the scattering and reflection cross-sections for 10 μ particles at the temperatures and compositions relevant to the lower cloud deck of Venus. Figure 54c (i,ii and iii) show the scattering and absorption cross-sections as a function of radius at

Figure 54. (a) Absorption and scattering as a function of sulfuric acid concentration; (b) absorption and scattering as a function of temperature; and (c) absorption and scattering as a function of sphere radius.

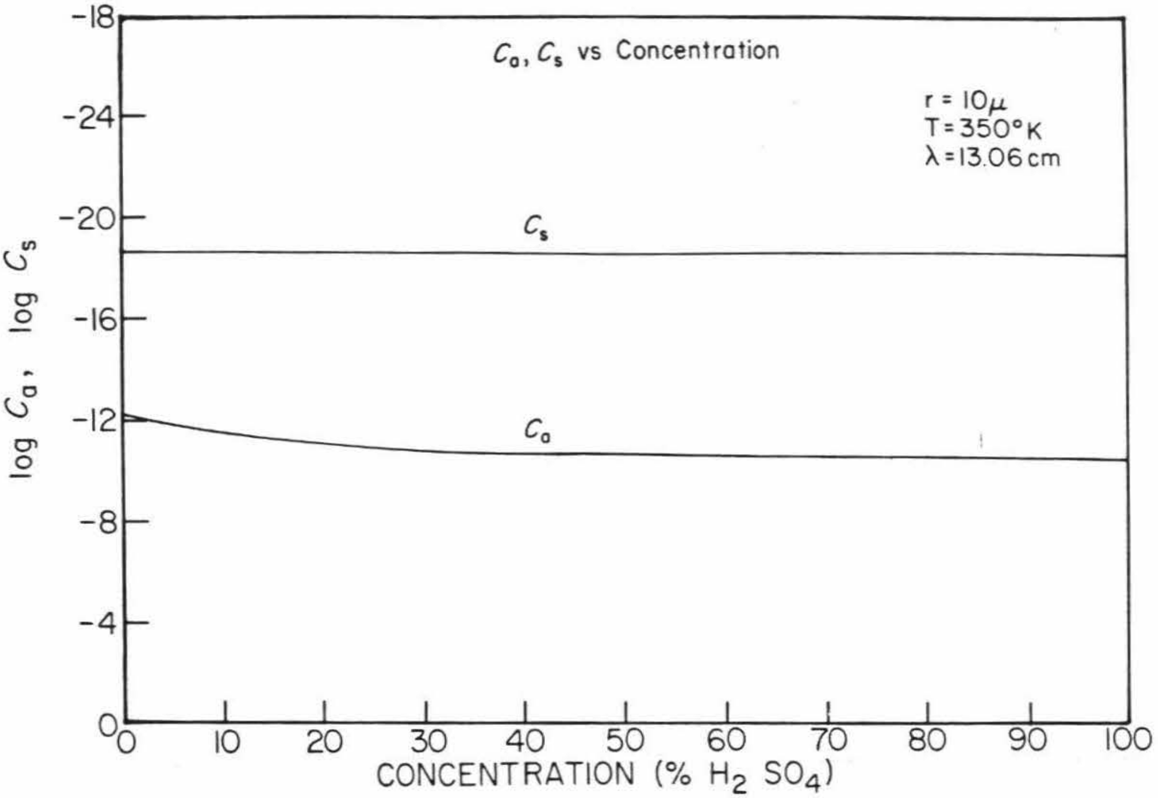
C_a, C_s vs Concentration
r = 10μ
T = 350°K
λ = 13.06 cm
C_s
C_a
log C_a, log C_s
-18
-24
-20
-16
-12
-8
-4
0
0
10
20
30
40
50
60
70
80
90
100
CONCENTRATION (% H_2SO_4)

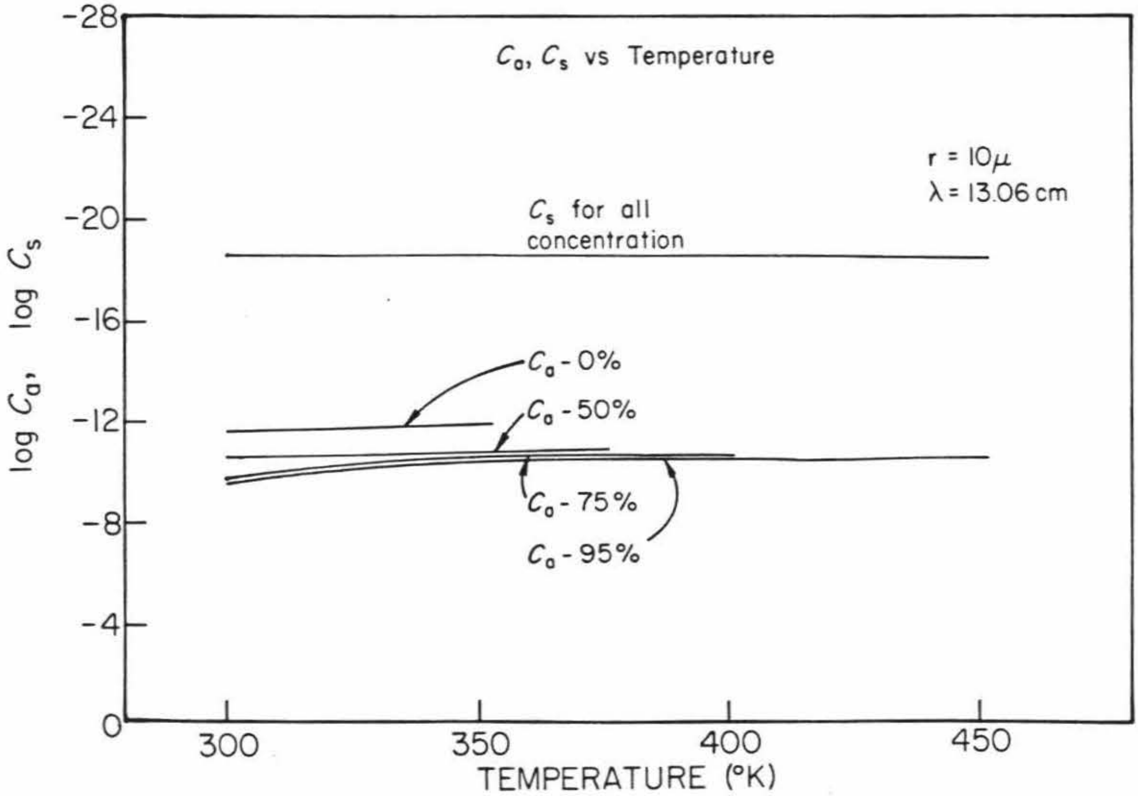
C_a, C_s vs Temperature
r = 10μ
λ = 13.06 cm
C_s for all concentration
C_a - 0%
C_a - 50%
C_a - 75%
C_a - 95%
log C_a, log C_s
-28
-24
-20
-16
-12
-8
-4
0
300
350
400
450
TEMPERATURE (°K)

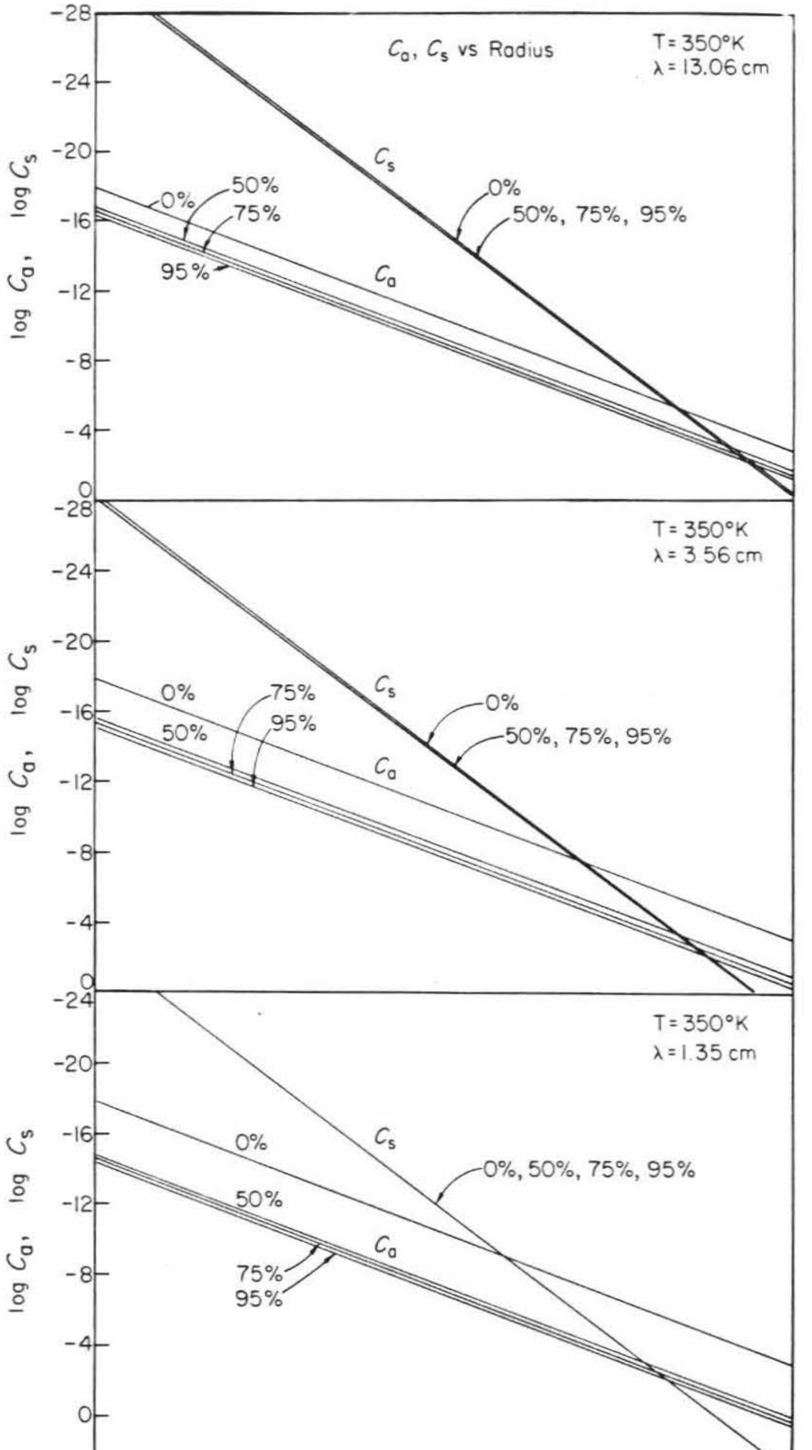
C_a, C_s vs Radius
T = 350°K
λ = 13.06 cm
C_s
0%
50%, 75%, 95%
0%
50%
75%
95%
C_a
T = 350°K
λ = 3.56 cm
C_s
0%
50%, 75%, 95%
0%
75%
95%
50%
C_a
T = 350°K
λ = 1.35 cm
C_s
0%, 50%, 75%, 95%
0%
50%
C_a
75%
95%
log C_a, log C_s
-28
-24
-20
-16
-12
-8
-4
0
4
10^{-5}
10^{-4}
10^{-3}
10^{-2}
10^{-1}
10^{0}
RADIUS (cm)

350 K for 13.06 cm, 3.56 cm and 1.35 cm, respectively. Absorption dominates the total attenuation for all particles with radii less than about 2000 μ at S-band, 1000 μ for X-band (except at 0% H_2SO_4 where $C_a \approx C_s$ at a radius of 200 μ), and 500 μ at 1.35 cm (except for 0% H_2SO_4 where $C_a \approx C_s$ at 50 μ).

Therefore, for particles of radii up to about 1000 μ S- and X- band wavelength attenuation may be assumed to be due entirely to absorption. Knollenberg and Hunten (1980) detected particles with a maximum size of only about 40 μ with the Particle Size Spectrometer.

Equation (101) may be expanded for a complex dielectric constant of $\varepsilon = \varepsilon' - i\varepsilon''$, where ε' is the real part and ε'' is the imaginary part of the dielectric constant. The equation (101) becomes

$$C_a = \frac{8\pi^2 a^3}{\lambda}\left[\frac{3\varepsilon''}{(\varepsilon' + 2)^2 + \varepsilon''^2}\right] \qquad (105)$$

for a single spherical particles of radius a.

For the case of a cloud containing N droplets per cubic centimeter, the total cross-section per cubic centimeter of atmosphere, or total absorption coefficient, α, is

$$\alpha\left[\frac{\mathrm{cm}^2}{\mathrm{cm}^3}\right] = \frac{\sum_N C_a}{\mathrm{cm}^3} = \frac{8\pi^2 \sum_N a^3}{\lambda}\left[\frac{3\varepsilon''}{(\varepsilon' + 2)^2 + \varepsilon''^2}\right] \mathrm{cm}^{-1} \qquad (106)$$

In terms of mass of cloud per cubic centimeter of atmosphere, $M' = \frac{4}{3}\pi\rho\sum_N a^3$, where ρ is the density of the drops in $\mathrm{g/cm}^3$,

$$\alpha = \frac{18\pi M'}{\lambda\rho}\left[\frac{\varepsilon''}{(\varepsilon' + 2)^2 + \varepsilon''^2}\right] \mathrm{cm}^{-1} \qquad (107)$$

or with the mass content, M, in $\mathrm{g/m}^3$ and α in km^{-1},

$$\alpha = \frac{1.8\pi M}{\lambda\rho}\left[\frac{\varepsilon''}{(\varepsilon' + 2)^2 + \varepsilon''^2}\right] \mathrm{km}^{-1} \ . \tag{108}$$

This equation can be used to calculate the liquid content profiles, M, from the measured radio occultation absorption coefficient profiles, α using measured values of ε' and ε'' for sulfuric acid-water solutions.

3. Dielectric Constant Measurements

Measurements of the dielectric constants of sulfuric acid-water solutions as a function of concentration and temperature at microwave frequencies were found to be non-existent in the literature. The only measurements available are for pure water at a wide range of temperatures and frequencies (see Hasted, 1973 for a summary), pure sulfuric acid at 20°C and six frequencies (Brand et al., 1953) and pure and 99.856% sulfuric acid at 25°C and several frequencies (Hall and Cole, 1978). These measurements are shown as a function of wavelength for several temperatures in Figure 55. Note the scale difference for ε' and ε''.

An anomalous dispersion (decrease in the real part of the dielectric constant with increasing frequency or decreasing wavelength) occurs for both liquids in the wavelength range of interest. Anomalous dispersions occur in liquids comprised of polar molecules with OH or NH_2 groups which can hydrogen bond and therefore are expected phenomena for both water and sulfuric acid. The real part of the dielectric constant at low frequencies represents a distortion and a transition of molecular orientation. The additional influence of hydrogen bonding produces the high dielectric constants observed at low frequencies.

At high frequencies, only distortion of the molecules occurs resulting in the low dielectric constants. The transition occurs at an approximate frequency

Figure 55. Real and imaginary dielectric constants as a function of wavelength for pure water and pure sulfuric acid.

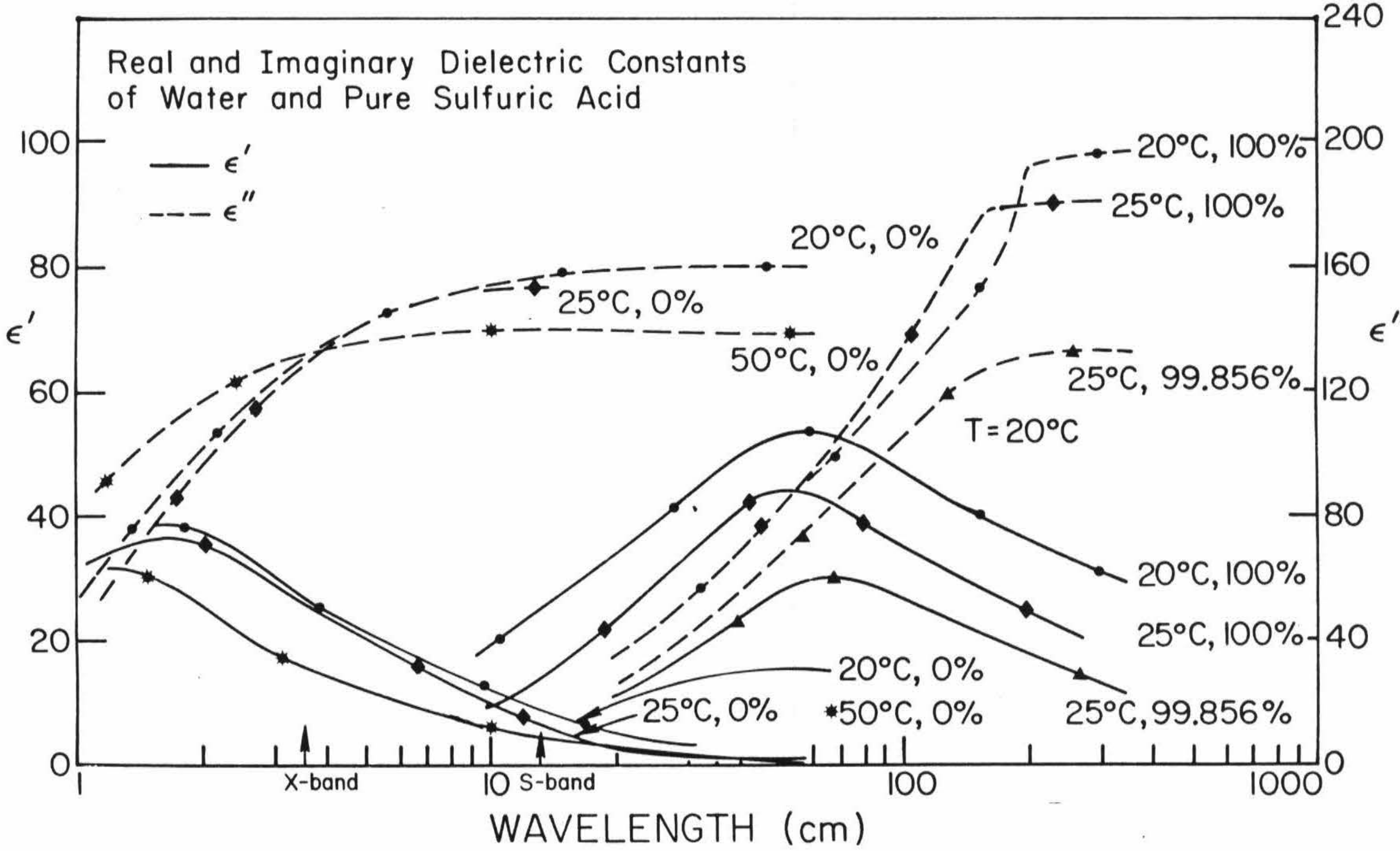
Real and Imaginary Dielectric Constants
of Water and Pure Sulfuric Acid
ε′
ε″
ε′
ε″
100
80
60
40
20
0
240
200
160
120
80
40
0
1
10
100
1000
X-band
S-band
WAVELENGTH (cm)
20°C, 100%
25°C, 100%
20°C, 0%
25°C, 0%
50°C, 0%
25°C, 99.856%
T=20°C
20°C, 100%
25°C, 100%
20°C, 0%
25°C, 0%
50°C, 0%
25°C, 99.856%

of $\nu_0 = \frac{1}{\tau}$, where τ is the relaxation time or time required for the molecules to return to a random distribution once an applied direct current electric filled is removed. For $\nu < \nu_0$, the molecules can rotate with the slowly oscillating, field producing high dielectric constants. But, for $\nu > \nu_0$, the molecules cannot respond rapidly enough and essentially are rotating randomly, leaving only electronic polarization as a source of the dielectric constant.

In view of the above discussion on the properties of an anomalously dispersive liquid, it is clear interpolation for sulfuric acid-water concentrations between 0 and 100% are not straightforward. The addition of only 0.144% by weight H_2O to a pure sulfuric acid solution results in a substantial drop in the real and imaginary parts of the dielectric constant, as seen by comparison the 100% and 99.856% sulfuric acid curves in Figure 55. Obviously the introduction of "foreign" molecules into the structure of a pure liquid results in a substantial change in the polarization of the liquid. In addition, the polarization is further complicated by the formation of increasingly higher concentrations of ions as the fractions of sulfuric acid and water in the solution become more equal.

While there are several theoretical equations which describe the dielectric properties of combined polar liquids, they are good only for very low concentrations. It is essential therefore to measure the real and imaginary dielectric constants at all concentrations and temperatures applicable to the Venus middle atmosphere at both S- and X-band wavelengths in the laboratory.

Measurements of the real and imaginary parts of the dielectric constant of the sulfuric acid-water system were done at Rockwell Science Center under the direction of William Ho and William Hall. The cavity perturbation technique using a high Q cavity was used for both S- and X-band measurements. The real part of the dielectric constant is determined by measuring the shift in cavity resonance caused by inserting a dielectric sample, and the imaginary part is determined by measuring the change in the quality factor, Q, of the high Q cavity. The technique is described in detail by Ho and Hall (1973) and is summarized here.

A right circular reflection-type cavity was used in this experiment, as shown in Figure 56a. The sample tube size is greatly exaggerated for illustration purposes; in reality, its inner diameter was between 0.0027 cm and 0.0062 cm. The oscillating electric field is axially symmetric and is a maximum and most stable along the axis at the location of the sample tube. The insert in Figure 56a describes the electric field intensity in the tube cavity and sample. With the geometry described above, the only parameters that enter into the calculations are the ratios of the diameters of the cavity, and the inner and outer walls of the capillary. It is essential that the sample tube be small enough that the electric field is not totally attenuated at the center of the tube.

The resonance frequency shift, δ', for this cavity geometry can be calculated using perturbation techniques as described by Hidy et al. (1972):

$$\delta' = \left[\frac{\nu_0}{2J_1^2(x_0)}\right]\left\{\left[\frac{\varepsilon_3'}{\varepsilon_0} - 1\right]\left(\frac{r_1}{r_3}\right)^2 + \left[\frac{\varepsilon_2'}{\varepsilon_0} - 1\right]\left(\frac{r_2^2 - r_1^2}{r_3^3}\right)\right\} \tag{109}$$

where ε_3', ε_2' and ε_0 are the real parts of the dielectric constant for the sample, the sample tube and the air, respectively, r_1, r_2 and r_3 are the inner and outer radii of the sample tube and the cavity radius, respectively, and $J_1(x_0)$ is the value of the Bessel function $J_1(x)$ at the first zero of $J_0(x)$. The first term describes the frequency shift produced by the sample material and the second term that produced by the empty tube. If ε_0 is one and the frequency shift is measured from the resonant frequency with the tube inserted, ν_0', the second term in the above equation disappears and the equation reduces to:

Figure 56. (a) Reflection cavity used in S-and X-band dielectric constant measurements. The insert describes the electric field in the sample tube and cavity. (b) Describes the parameters used in calculating the real and imaginary dielectric constants.

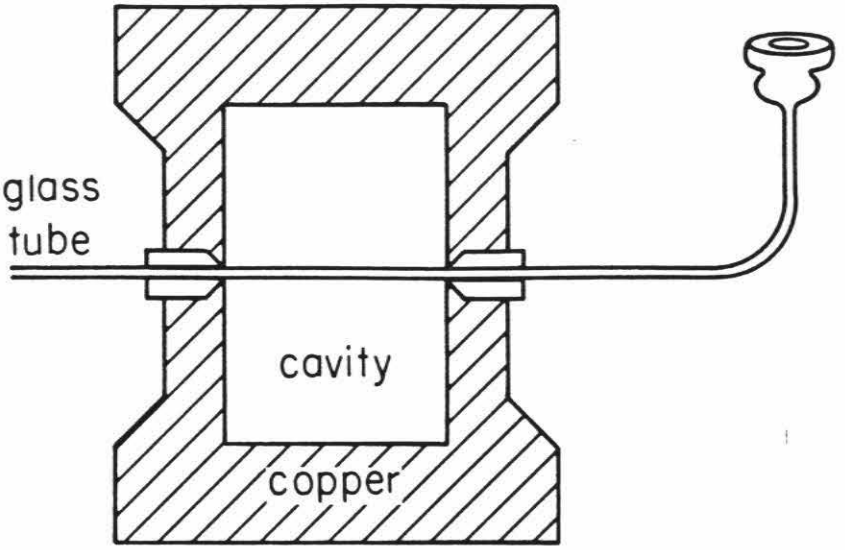
glass
tube
cavity
copper

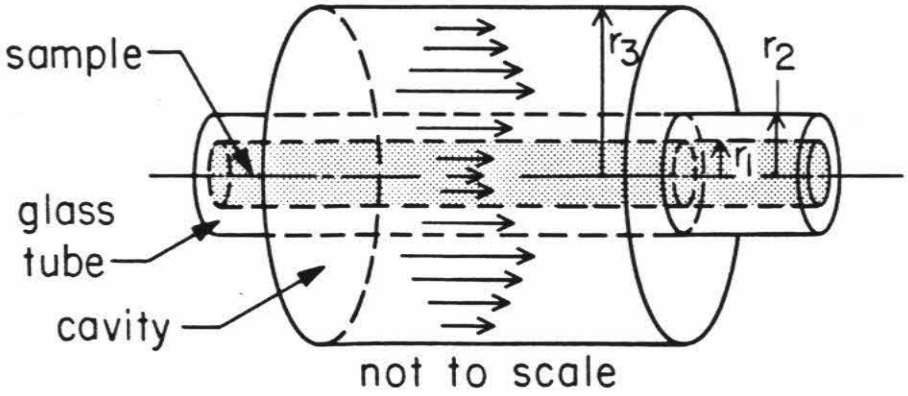
sample
glass
tube
cavity
r_3
r_2
r_1
not to scale

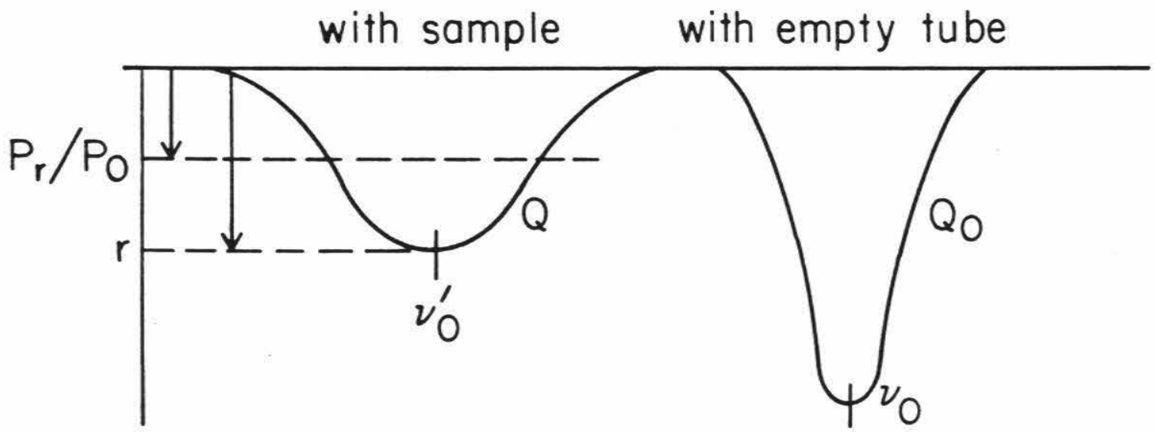
with sample
with empty tube
P_r/P_0
r
Q
ν_0'
Q_0
ν_0

$$\delta = \left[\frac{\nu_0'}{2J_1^2(x_0)}\right](\varepsilon_3' - 1)\left[\frac{r_1}{r_3}\right]^2 \tag{110}$$

Since ν_0', $J_1^2(x_0)$, r_1 and r_3 are constant for any sample as long as the sample tube remains the same, the shift due to water may be used along with the known dielectric constant of water to determine ε' for H_2SO_4 solutions as follows:

$$\frac{\delta_{H_2SO_4}}{\delta_{H_2O}} = \frac{(\varepsilon_3' - 1)_{H_2SO_4}}{(\varepsilon_3' - 1)_{H_2O}} \tag{111}$$

and

$$\varepsilon_{H_2SO_4}' - 1 = \frac{\delta_{sample}}{\delta_{water}}(\varepsilon_{water}' - 1) \ . \tag{112}$$

The equation describing the Q of a reflection cavity in terms of measurable quantities is obtained from the equation for the relation between the reflected power (P_r) and the incident power (P_0) in terms of Q_0, the cavity quality factor, Q_c, the coupling quality factor, ν_0, the resonant frequency, and ν, the actual frequency (Montgomery, 1947; Ho and Hall, 1973)

$$\frac{P_r}{P_0} = \frac{\frac{1}{4}\left[\left(\frac{1}{Q_0}\right) - \left(\frac{1}{Q_c}\right)\right]^2 + \left(\nu - \nu_0\right)^2/\nu_0^2}{\frac{1}{4}\left[\left(\frac{1}{Q_0}\right) + \left(\frac{1}{Q_c}\right)\right]^2 + \left(\nu - \nu_0\right)^2/\nu_0^2} \ . \tag{113}$$

At the resonant frequency, equation (110) reduces to:

$$\left(\frac{P_r}{P_0}\right)_{\nu=\nu_0} = r = \frac{\left(Q_c - Q\right)^2}{\left(Q_c + Q\right)^2} \tag{114}$$

Combining the above two equations gives

$$Q = \frac{\nu_0}{\left[(\nu - \nu_0)(1 + r^{1/2})\right]} \left\{ \frac{\frac{P_r}{P_0} - r}{1 \ \frac{P_r}{P_0}} \right\}^{1/2} \tag{115}$$

Q may be determined by measuring r, ν_0, ν and $\frac{P_r}{P_0}$. Therefore, measuring r, ν_0, ν and $\frac{P_r}{P_0}$ gives Q. Q must be measured for the empty cavity (Q_0) and for the filled cavity (Q_{total}) in order to separate the losses of the cavity itself from those of the dielectric. Since it is the attenuation factors (attenuation $\alpha \tan\delta \alpha \frac{1}{Q}$ which add,

$$\tan\delta_{dielectric} = \tan\delta_{cavity+dielectric} - \tan\delta_{cavity} \quad , \tag{116}$$

$$\left[\frac{1}{Q}\right]_{dielectric} = \frac{1}{Q_{total}} - \frac{1}{Q_0} \tag{117}$$

For a sample tube material with negligible dielectric loss,

$$\Delta\left[\frac{1}{Q}\right] = \frac{J_1^2(X_0)}{\varepsilon_3'' \left[\frac{r_1}{r_3}\right]^2} \ . \tag{118}$$

Combining equations (107) and (115) gives

$$\frac{\varepsilon_3''}{\varepsilon_3' - 1} = \frac{\nu_0'}{2\delta} \Delta\left[\frac{1}{Q}\right] \tag{119}$$

which is the equation used to determined ε''.

Summarizing, r, $\frac{P_r}{P_0}$, ν_0' and ν_0 are measured (see Figure 56b) for a given sample to determine Q. r, $\frac{P_r}{P_0}$, ν_0' and ν_0 are measured for an empty cavity to determine Q_0. Then

$$\Delta\left[\frac{1}{Q}\right] = \left[\frac{1}{Q}\right]_{sample} - \frac{1}{Q_0} \tag{120}$$

δ is calculated from the resonant frequency of the empty sample tube, ν_0, and the resonant frequency of the filled sample tube, ν_0' ($\delta = \nu'_0 - \nu_0$). The real dielectric constant is then calculated from equation (109) and ε'' is calculated from equation (116).

The results of the measurements of the real and imaginary parts of the dielectric constants at S- and X-band are shown in Figures 57 (a and b), 58 (a and b) as functions of concentration and at all measured temperatures. The results are presented numerically in Appendix II. These results will be published in a forthcoming paper by Cimino, Ho and Hall. The exact wavelengths are 3.56 cm for X-band and 11.32 cm for S-band. The occultation wavelengths are 3.57 cm and 13.08 cm, therefore the data were extrapolated to the appropriate S-band wavelength before the dielectric terms were calculated.

The real dielectric constants for both wavelengths show approximately the same structure as a function of concentration. The X-band values are in general slightly less than the S-band values as is expected since the sulfuric acid dipole is strongest at S-band wavelengths (see Figure 55). At 0% sulfuric acid (i.e., water), the dielectric constant is high due to the strong hydrogen bonding structure effects in water. When small amounts of sulfuric acid are added, the uniform structure is disrupted and the dielectric constant rapidly decreases with increasing sulfuric acid concentration. Between 30 and 70% sulfuric acid, the 11.32 cm dielectric constant remains fairly constant while there is a dip in the X-band dielectric constant. We have no explanations for this phenomenon. At about 70-80%, the ratio of water molecules to sulfuric acid molecules has decreased to about 1:1. At this point the sulfuric acid system probably begins to dominate. At both S- and X-band, the frequency is sufficiently high (the sulfuric

Figure 57. Real dielectric constant measurements as a function of concentration for all measured temperatures. (a) 11.32 cm. (b) 3.56cm.

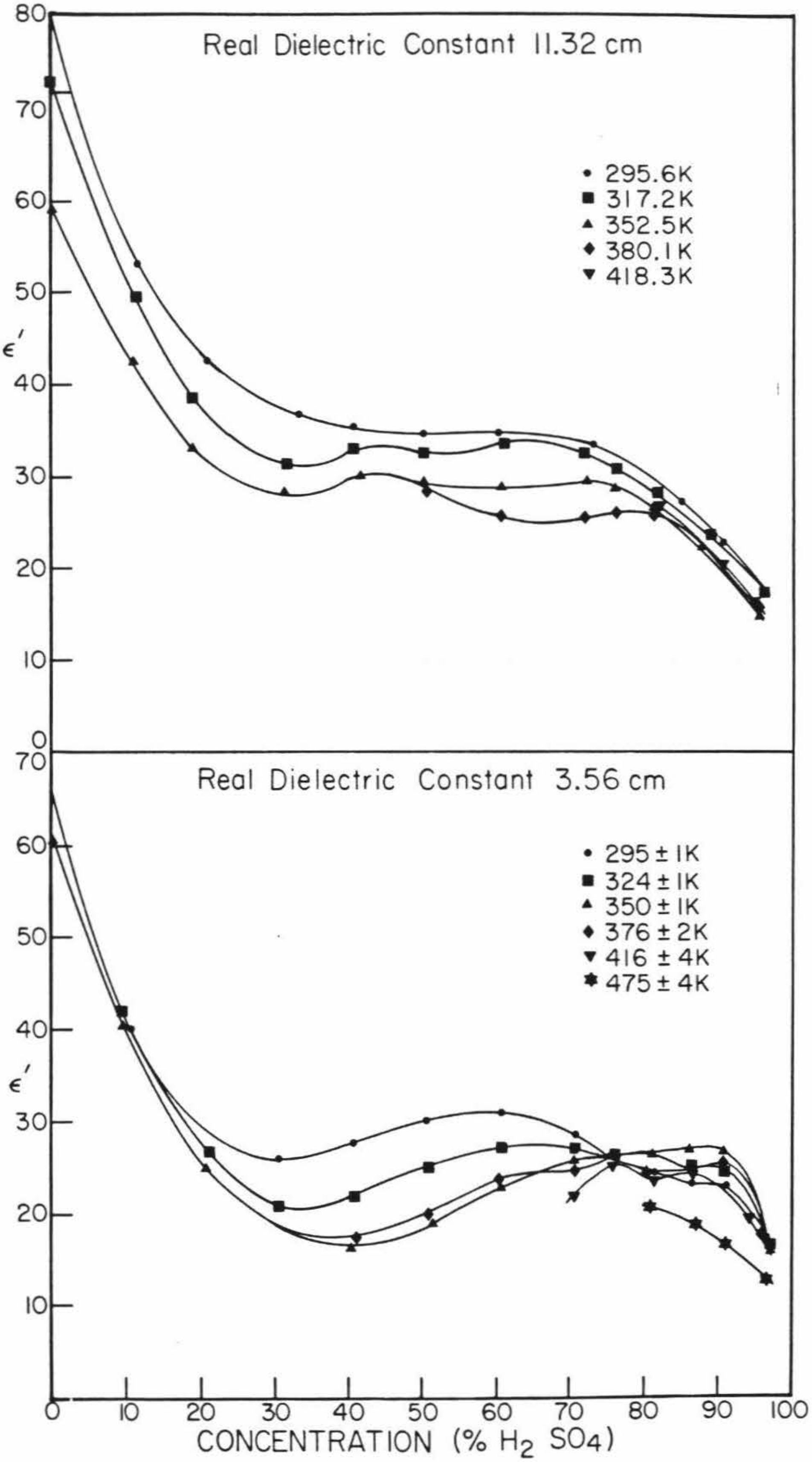
Real Dielectric Constant 11.32 cm
• 295.6K
■ 317.2K
▲ 352.5K
◆ 380.1K
▼ 418.3K
ε'
80
70
60
50
40
30
20
10
0
Real Dielectric Constant 3.56 cm
• 295 ± 1K
■ 324 ± 1K
▲ 350 ± 1K
◆ 376 ± 2K
▼ 416 ± 4K
✱ 475 ± 4K
ε'
70
60
50
40
30
20
10
0
10
20
30
40
50
60
70
80
90
100
CONCENTRATION (% H2 SO4)

Figure 58. Imaginary dielectric constant measurements as a function of concentration for all measured temperatures. (a) 11.32 cm. (b) 3.56cm.

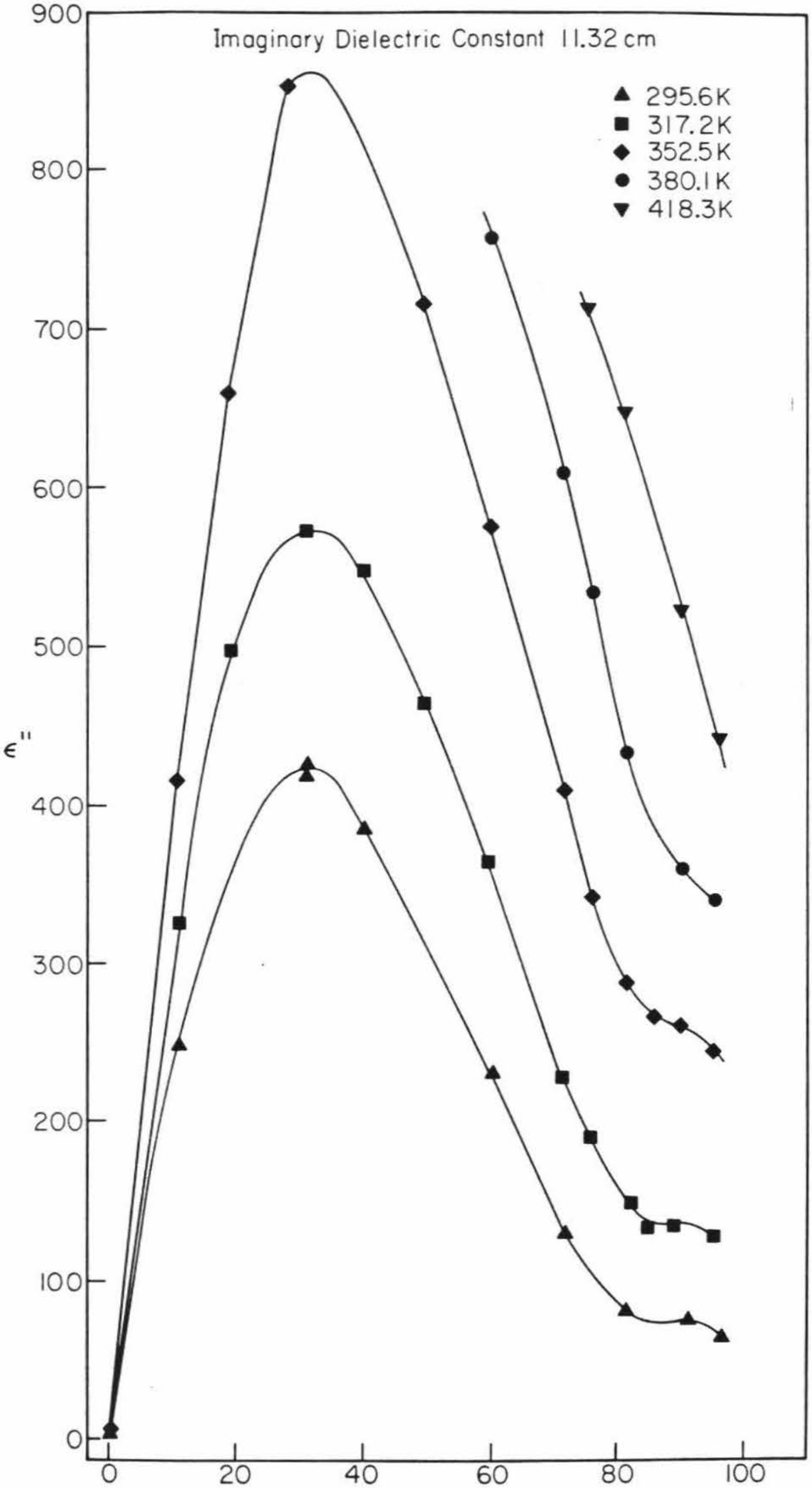
Imaginary Dielectric Constant 11.32 cm
▲ 295.6K
■ 317.2K
◆ 352.5K
● 380.1K
▼ 418.3K
ε''
900
800
700
600
500
400
300
200
100
0
0
20
40
60
80
100
CONCENTRATION (% H_2SO_4)

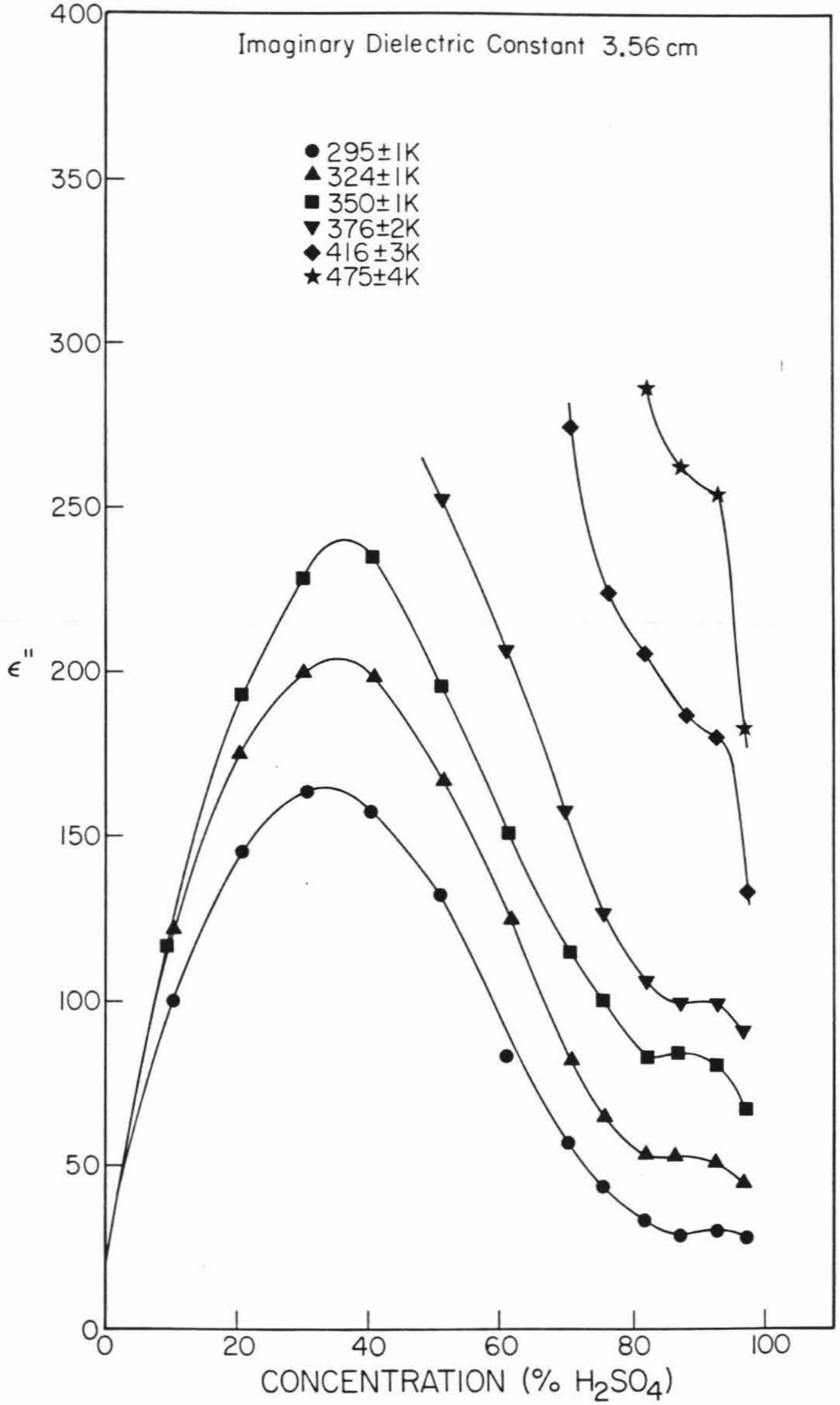
Imaginary Dielectric Constant 3.56 cm
● 295±1K
▲ 324±1K
■ 350±1K
▼ 376±2K
◆ 416±3K
★ 475±4K
ε''
400
350
300
250
200
150
100
50
0
0
20
40
60
80
100
CONCENTRATION (% H_2SO_4)

acid relaxation time is sufficiently low) that the sulfuric acid molecules cannot respond rapidly enough to the alternating field and the dielectric constant decreases. At all concentrations, the real part of the dielectric constant decreases with increasing temperature. At the higher temperatures the more energetic molecules have difficulty aligning themselves with the electric field.

The imaginary part of the dielectric constant also shows similar trends for both S- and X-band wavelengths; however, the dielectric constant is much greater at S-band than at X-band at all concentrations. The imaginary part of the dielectric constant is composed of two parts — one due to the static diffusional conductivity and one due to rotation of the polar molecules in an alternating field. The static or direct current (dc) conductivity of sulfuric acid as a function of concentration and temperature is shown in Figure 59 (Timmermans, 1960). This conductivity can be converted to a dc imaginary dielectric constant, ε''_{dc}, as follows

$$\varepsilon''_{dc} = \sigma \; \varepsilon_0 \; \omega \tag{121}$$

where σ is the conductivity in mho/cm, $\varepsilon_0 = 8.854 \times 10^{-14}$ and ω is the angular frequency in rad/sec. The results are shown in Table X for 22.5°C and 44.1°C. Also included in this table are the imaginary dielectric constants at S- and X-band frequencies and the difference $\Delta\varepsilon$ where

$$\Delta\varepsilon = \varepsilon'' - \varepsilon''_{dc} \quad . \tag{122}$$

At S-band frequencies, $\Delta\varepsilon$ is negative and at X-band frequencies $\Delta\varepsilon$ is small at high concentrations and lower temperatures but also becomes negative with decreasing concentration and increasing temperature. The small negative $\Delta\varepsilon$'s indicate that most of the imaginary part of the dielectric constant is due to dc conductivity, however, the dc conductivity itself is somewhat frequency dependent and this has not been accounted for in ε''_{dc}.

Figure 59. Static conductivity of sulfuric acid-water mixtures for several temperatures.

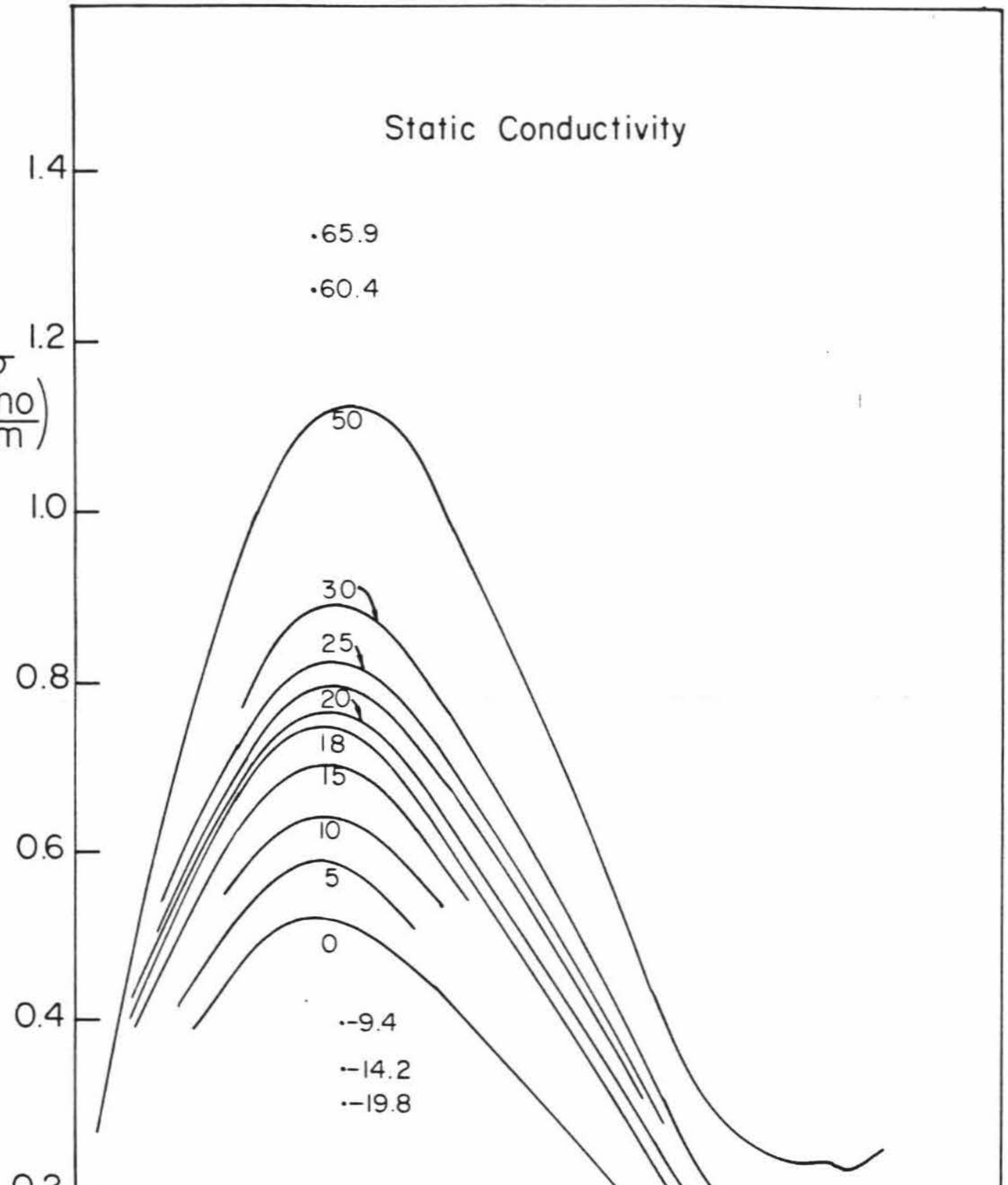
Static Conductivity
σ (mho/cm)
1.4
1.2
1.0
0.8
0.6
0.4
0.2
0
•65.9
•60.4
50
30
25
20
18
15
10
5
0
•-9.4
•-14.2
•-19.8
•-34.1
•-44.8
0
20
40
60
80
100
CONCENTRATION (% H_2SO_4)

Table X
Contribution of Conductivity to the Imaginary Part of the Dielectric Constant

Conductivity S-Band

Temperature	Concentration (%H_2SO_4)	ε''	σ_{dc} (mho/cm)	ε^{-}_{dc}	$\Delta\varepsilon$ ($\varepsilon''-\varepsilon^{-}_{dc}$)
22.5°C	95	68	0.125	85	-17
295.6 K	90	74	0.125	85	-11
	85	76	0.11	74.8	1.2
	80	86	0.13	88.4	-2.4
	75	112	0.175	119	-7
	70	140	0.25	170	-30
	60	238	0.44	299	-61
	50	310	0.61	415	-105
	40	388	0.74	503	-115
	30	418	0.79	537	-119
	20	365	0.68	462	-97
	10	228	0.42	285	-57
44.1°C	95	126	0.20	136	-10
317.2 K	90	134	0.21	143	-9
	85	132	0.21	143	-11
	80	162	0.24	163	-1
	75	195	0.30	204	-9
	70	242	0.39	265	-23
	60	360	0.64	425	-75
	50	462	0.86	585	-123
	40	550	1.05	714	-164
	30	568	1.08	734	-166
	20	500	0.91	619	-119
	10	295	0.55	374	-76

Conductivity X-Band

Temperature	Concentration (%H_2SO_4)	ε''	σ_{dc} (mho/cm)	ε^{-}_{dc}	$\Delta\varepsilon$ ($\varepsilon''-\varepsilon^{-}_{dc}$)
22.2°C	95	31	0.125	26.6	4.4
295.3 K	90	30	0.125	26.6	3.4
	85	31	0.11	23.4	7.6
	80	36	0.13	27.7	8.3
	75	45	0.175	37.3	7.7
	70	58	0.25	53.2	4.8
	60	95	0.44	93.7	1.3
	50	135	0.61	130	5
	40	158	0.74	158	0
	30	163	0.79	168	-5
	20	143	0.68	145	-2
	10	100	0.42	89	11
50.3°C	95	48	0.24	51	-3
323.5 K	90	53	0.23	49	4
	85	53	0.23	49	4
	80	55	0.26	55	0
	75	67	0.32	68	-1
	70	85	0.42	89	-4
	60	130	0.66	140	-10
	50	170	0.89	189	-19
	40	200	1.08	230	-30
	30	200	1.11	236	-36
	20	171	0.93	198	-27
	10	132	0.55	117	18

No conductivity data for temperatures greater than 68°C.

Equation (118) suggests the wavelength dependence of the S- and X-band imaginary dielectric constants is just $\frac{1}{\lambda}$. This wavelength dependence is used to calculate the 13.08 cm dielectric constants from the 11.32 and 3.56 cm data. The variation with concentration of ε'' at S- and X-band, which is directly related to the variation of the dc conductivity with concentration, can be explained by a combination of two factors which contribute to diffusional conductivity. Actually at very concentrated and very dilute concentrations of sulfuric acid, the conductivity is that of proton-transfer by $H_3SO_4^+$ HSO_4^-, H_3O^+ and OH^- ions. The proton transfer method involves successive transfer of protons along hydrogen bonds which results in the effective movement of the $H_3^+SO_4$ and HSO_4^- ions through the solution without need for actual diffusion of individual ions. This is explained in detail in Flowers et al., 1960. As the concentration of the solute (whether H_2O in H_2SO_4 at concentrated solutions or H_2SO_4 in H_2O at dilute solution) increases, diffusional conductivity dominates over proton-transfer conductivity.

The contribution of the two factors contributing to the variation of ε'' with concentration, and their relation to the conductivity, is illustrated in Figure 60. The first is one of available free ions and the second is viscosity inasmuch as the position of the dipole relative to its nearest neighbors is maintained by viscous forces. As the concentration of sulfuric acid increases from 0%, the concentration of free ions increases (a) due to the formation of H_3O^+ and HSO_4^-. From 0 to 30%, the diffusional conductivity and therefore the imaginary part of the dielectric constant increase simply because the ionic concentration increases. At about 30% sulfuric acid, the viscosity begins to increase as ionic interactions begin to dominate the motion of the molecules thus making it more difficult for diffusional conduction to occur. The conductivity and ε'' decrease (b). The maximum in ε'' at about 30% shifts toward higher sulfuric

Figure 60. Viscosity and imaginary dielectric constant shown as a function of concentration.

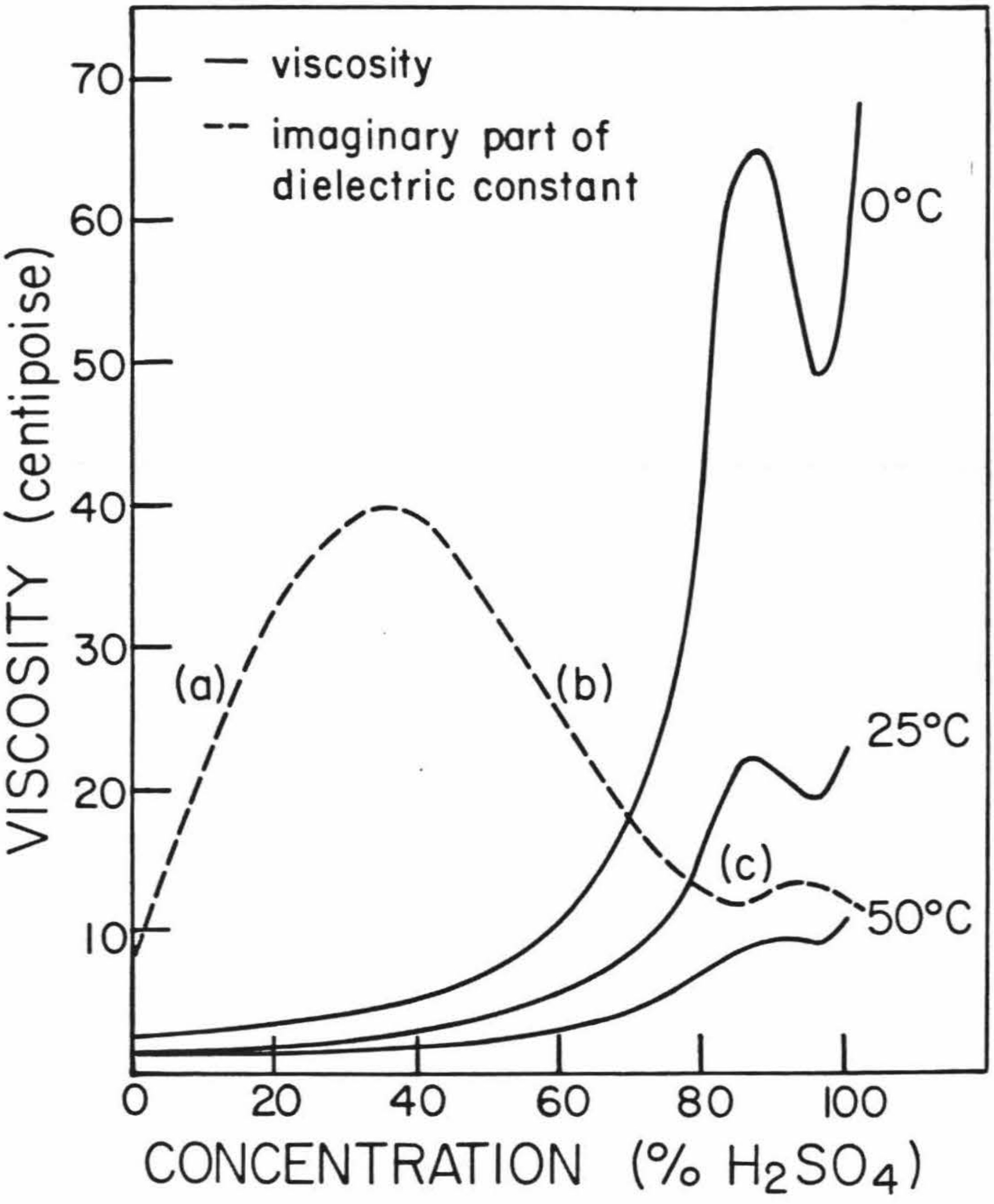
— viscosity
-- imaginary part of dielectric constant
0°C
25°C
50°C
(a)
(b)
(c)
70
60
50
40
30
20
10
VISCOSITY (centipoise)
0
20
40
60
80
100
CONCENTRATION (% H_2SO_4)

concentrations with increasing temperature due to the decrease in viscosity with increasing temperature.

At about 83% sulfuric acid, the viscosity is a maximum and the imaginary part of the dielectric constant is a minimum (c). From 83% to 95%, the viscosity again decreases due to the formation of the monohydrate, and ε'' increases to a peak at about 92%. This peak broadens with increasing temperature until it disappears at about 100°C. Correspondingly, the viscosity curve also loses its minimum at higher temperatures.

At concentrations greater than 92%, ε'' again decreases due to rapidly increasing conductivity until at very high concentrations no diffusional conduction occurs. At this point proton-transfer conduction, which is not affected by viscosity, dominates.

At all concentrations, ε'' increases with temperature as a result of increasing free ion concentration and decreasing viscosity with increasing temperature. The results of the measurements of the real and imaginary dielectric constants will be used to determine the dielectric constant term in equation (108). It will then be possible to determine the mass content of the clouds from the absorption coefficient profiles.

4. Concentration Profile

In order to determine the concentration of the proposed liquid sulfuric acid clouds, certain constraints must be put into effect. One of two possible assumptions may be made:

1. It may be assumed that the Venera 11 and 12 (Moroz, private communication) water vapor measurements are correct over the entire planet. In order to determine the concentration of the cloud

detected by the occultation experiment, a constraint is made that the vapor pressure must equal saturated water vapor pressure over the sulfuric acid-water cloud (a strong function of acid concentration and temperature). In making the constraint as a means of determining cloud concentration, equilibrium between the cloud and vapor is required. If the cloud is condensing this is a good assumption. Once the cloud concentration is known the liquid content may be calculated from equation (108). When this is done for both X- and S-band, the two resulting liquid contents should be equal assuming the correct composition has been chosen.

2. If X-band data are available, they can be used in combination with the S-band data to determine cloud composition. This technique requires the liquid contents, M, determined from the absorption coefficient data be equivalent at both wavelengths if the correct dielectric constant values, and thereby the correct concentrations are chosen:

$$M_X = M_S \tag{123}$$

or

$$\frac{\alpha_X \lambda_X}{\mathbf{D}_X} = \frac{\alpha_S \lambda_S}{\mathbf{D}_S} \tag{124}$$

or

$$\frac{\mathbf{D}_S}{\mathbf{D}_X} = \frac{\alpha_S \lambda_S}{\alpha_X \lambda_X} \tag{125}$$

where M is the liquid content, α is the absorption coefficient, λ is the wavelength, and $\mathbf{D}$ is the dielectric constant term $\left[\mathbf{D} = \frac{\varepsilon''}{(\varepsilon' + 2)^2 + \varepsilon''^2}\right]$. The dielectric constant term, $\mathbf{D}$, is a function of temperature and acid concentration, therefore at each level the concentration is chosen such that the ratio is $\mathbf{D}_S/\mathbf{D}_X$ is equal to $\alpha_S\lambda_S/\alpha_X\lambda_X$. Unfortunately, this ratio does not vary strongly with concentration. Pure water, 99% sulfuric acid and a H_2SO_4-H_2O solution may be distinguished; however, the exact value of the solution is difficult to determine using this technique. It is fortunate, however, in that when only S-band data are available, it is not necessary to know the exact cloud composition in order to derive reliable liquid content profiles.

Due to the lack of available X-band absorption coefficient profiles, and the insensitivity of the ratio of the dielectric terms to H_2SO_4 concentration, the cloud composition will be determined using the water vapor profile constraint. The liquid content will then be calculated from the resulting composition profile and, when X-band data are available, the ratio M_S/M_X will be calculated as a check on the proposed concentration.

Laboratory measurements of the H_2O, SO_3 and H_2SO_4 vapor pressures in equilibrium with concentrations of sulfuric acid-water solutions ranging from 0 to 100% and at temperatures ranging from less than 0°C to boiling temperatures were made by Gmitro and Vermeulen (1963). The vapor pressures resulting from their work were used to determine the concentration of the clouds as a function of temperature and water vapor content.

Figure 61 shows typical concentration profiles for orbit 69X in the equatorial region and 18N in the polar region. Variations from orbit to orbit within a

Figure 61. Concentration of sulfuric acid-water clouds shown as a function of pressure in the Venus atmosphere for orbits 69X (equatorial) and 18N (polar).

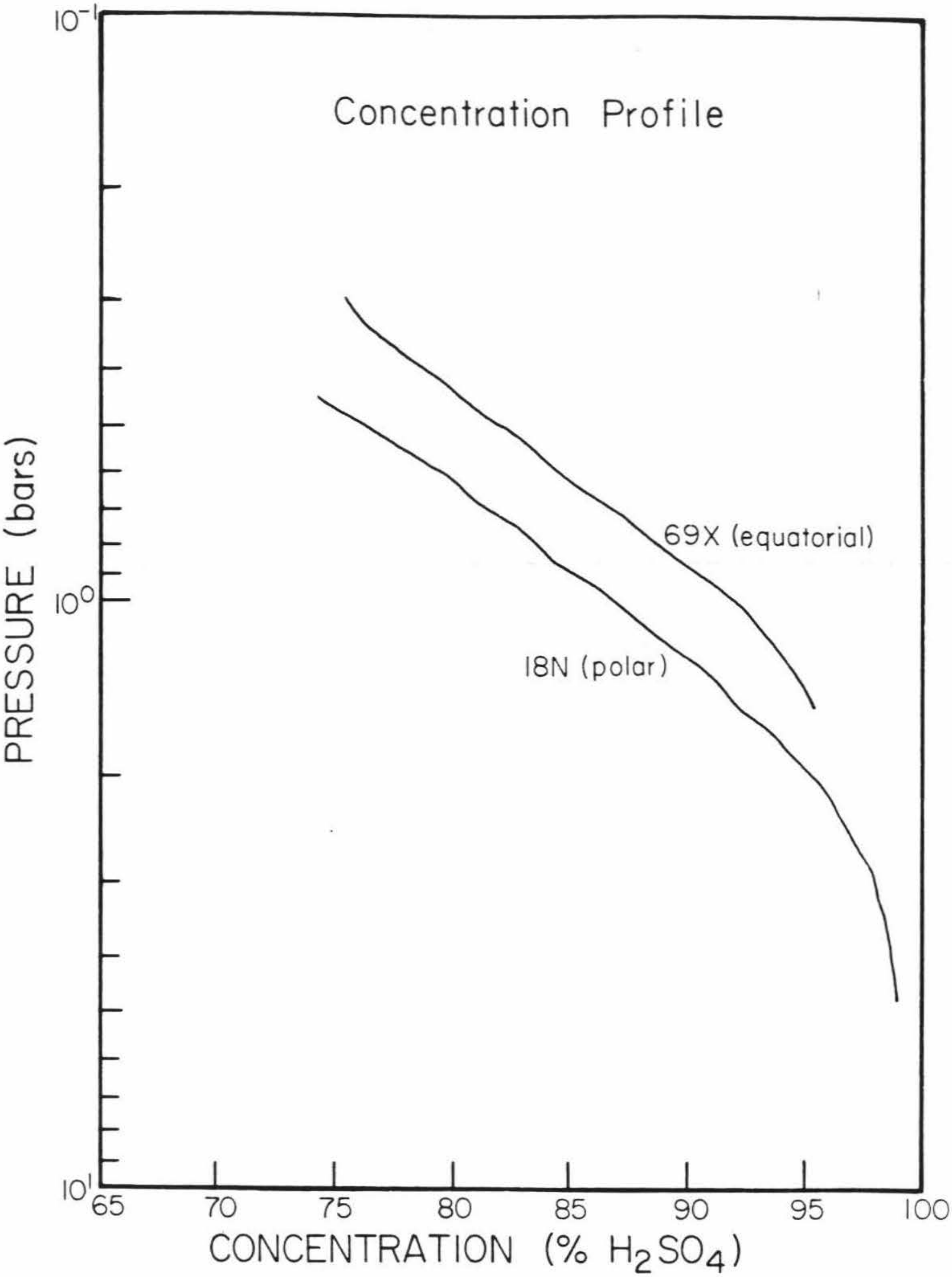
Concentration Profile
PRESSURE (bars)
10^{-1}
10^{0}
10^{1}
69X (equatorial)
18N (polar)
65
70
75
80
85
90
95
100
CONCENTRATION (% H_2SO_4)

latitude region are slight and result from variations in the temperature profiles.

5. Results of Liquid Content Profiles

Figure 62 shows the liquid content profiles derived assuming the cloud particles consist of concentrated liquid sulfuric acid water solutions of concentrations consistent with the measured water vapor profile. The profiles shown in the figure are for orbits 69X at the equator, 30X in the midlatitude regions, 338N in the collar and 18N in the polar regions of Venus. The mass contents derived with this assumption are on the order of several g/m^3 — more than an order of magnitude greater than mass contents determined by the Pioneer probe Particle Size Spectrometer (LCPS). The peak Particle Size Spectrometer mass content is 0.08 g/m^3. The level in the atmosphere of the orbit 69X cloud, located at the same latitude as the Sounder probe, is the same as the level of the LCPS cloud layer.

The wavelength dependence of the absorption coefficient data for orbit 18N (S- and X-band) is from $1/\lambda$ to $1/\lambda^{1.4}$. The wavelength dependence of liquid sulfuric acid is $1/\lambda^2$ (see Figure 64) — significantly different from the measured wavelength dependence.

In light of the discrepancies in total mass content and wavelength dependence for clouds composed of liquid sulfuric acid droplets, an attempt will be made to determine a cloud component which has a higher absorptivity and $1/\lambda^{1.2}$ wavelength dependence.

Figure 62. Mass content profiles derived assuming liquid sulfuric acid-water clouds for orbits 69X (equatorial), 30X (midlatitudinal),338N (collar) and 18N (polar).

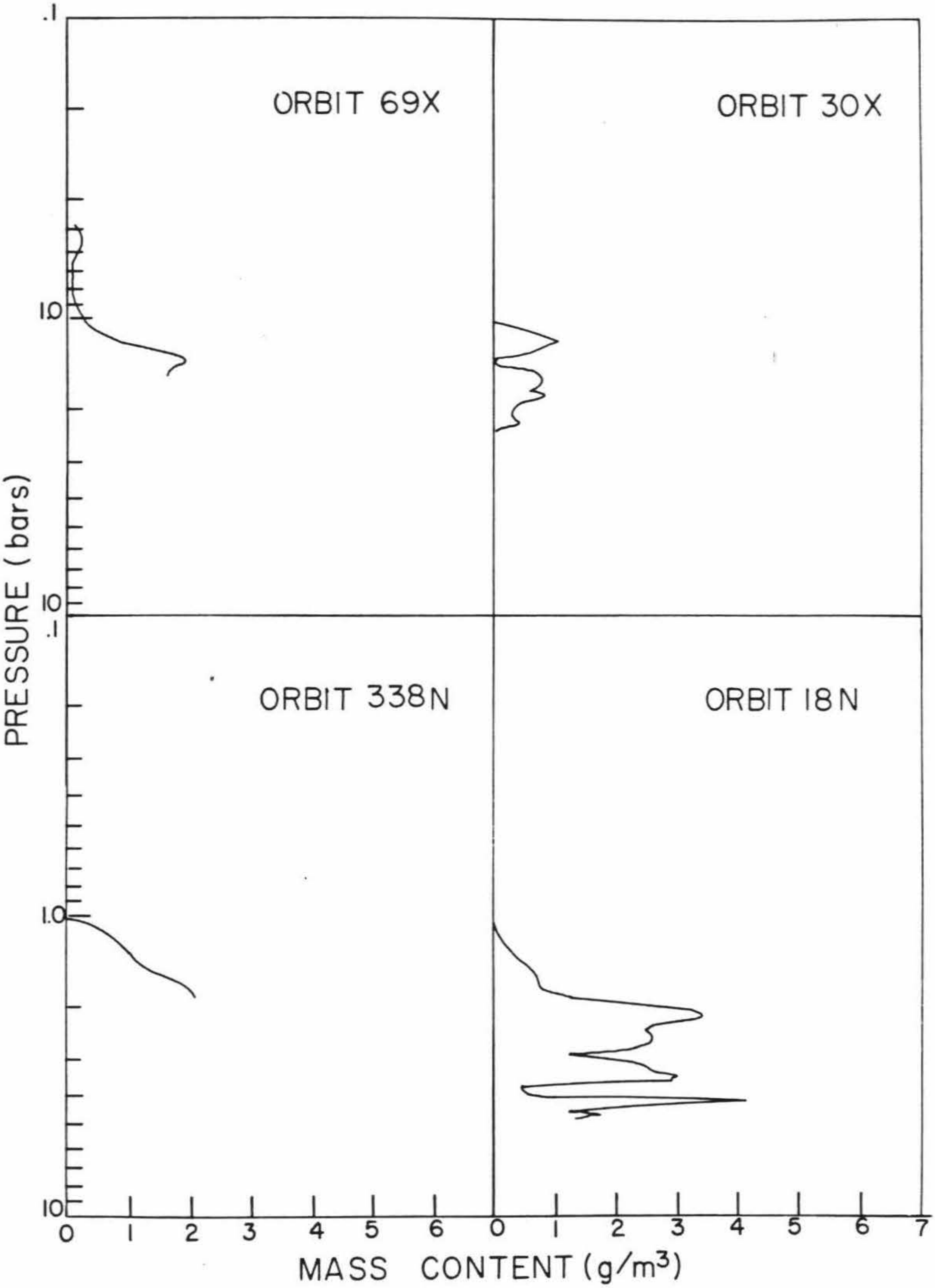
ORBIT 69X
ORBIT 30X
ORBIT 338N
ORBIT 18N
PRESSURE (bars)
.1
1.0
10
.1
1.0
10
0
1
2
3
4
5
6
0
1
2
3
4
5
6
7
MASS CONTENT (g/m3)

CHAPTER VI

THE SPHERICAL SHELL MODEL

Inasmuch as the mass contents derived from the absorption coefficient data assuming liquid sulfuric acid-water droplets are about an order of magnitude greater than those measured by the particle size spectrometer aboard the Sounder probe, an attempt was made to devise an alternate cloud model. The only cloud particle model found that is capable of increasing the absorption of the cloud material and thereby reducing the calculated mass content of the cloud is that of a dielectric, nonabsorbing core with an outer shell of sulfuric acid solution (Figure 63).

Such a particle may be produced in the atmosphere by at least two methods. It may form from a liquid in which a solid is precipitating to form the core or it may form from a solid spherical particle onto which the liquid is precipitating from the atmosphere (heterogeneous condensation). The second type of formation is the common method of cloud formation in the Earth's atmosphere since supersaturations required for condensation are usually less than a few percent. The first type of formation is typical of the sulfuric system on Earth (Seinfeld, 1975). In this system, SO_3 is formed from SO_2 and reacts immediately with H_2O to form H_2SO_4. The H_2SO_4 readily combines with water droplets to give an H_2SO_4 solution. If NH_3 or NaCl particles are present, $(NH_4)_2SO_4$ or Na_2SO_4 (and HCl), both sulfate salts, are formed.

1. Derivation of the Polarization Equation for the Spherical Shell Model

The polarization term in equation (104) is for spheres of a single dielectric material. If the sphere is instead covered with a concentric spherical shell with a different dielectric constant, the polarization changes. Van de Hulst (1957) gives the equation for the shell model but does not derive the equation.

Figure 63. Cloud particle model showing definitions of the parameters used.

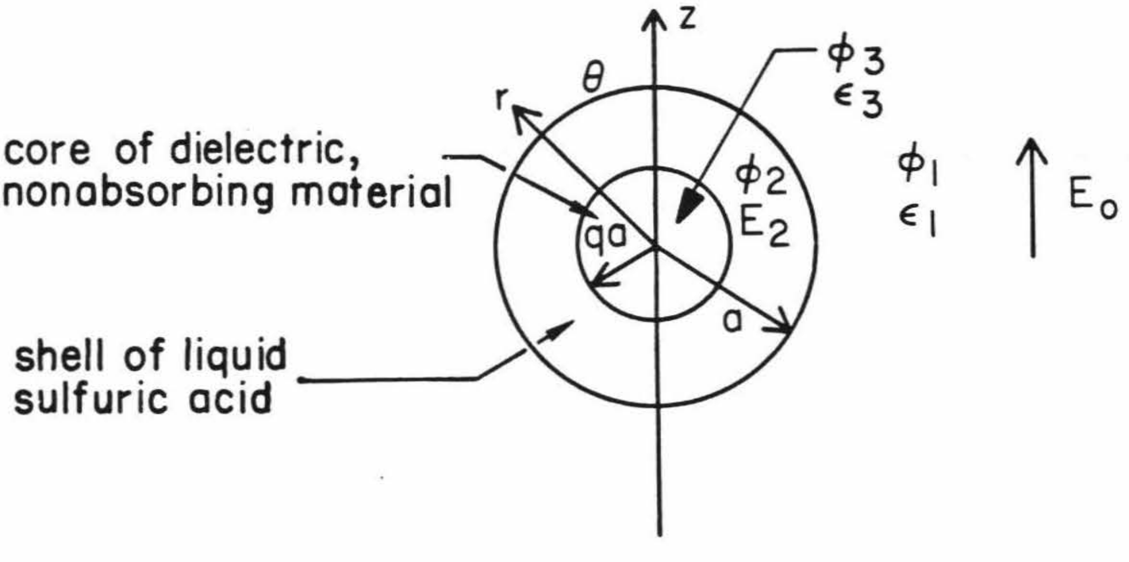
z
θ
r
ϕ_3
ϵ_3
core of dielectric, nonabsorbing material
ϕ_2
E_2
ϕ_1
ϵ_1
E_0
qa
a
shell of liquid sulfuric acid

The following derivation results in the same equation presented by Van de Hulst.

In order to calculate the polarization of the spherical shell model, the potential, φ, outside the sphere must be calculated. The potential at any point in a system consisting of a sphere, or several concentric spheres, embedded in a homogeneous isotropic dielectric is given by Stratton (1941):

$$\varphi = \sum_{l=0}^{\infty} \left[A_l r^l + \frac{B_l}{r^{l+1}} \right] P_l(\cos\vartheta) \tag{126}$$

where A_l and B_l are arbitrary constants, r is the radial distance from the center of the sphere, and $P_l(\cos\vartheta)$ are the Legendre functions for systems which are symmetric about the z-axis. The applied electric field, E_o, is parallel to the z-axis as shown in Figure 60b. For the system considered here, ε_3, ε_2 and ε_1 are the dielectric constants of the core, the shell and the atmosphere, respectively, and φ_3, φ_2 and φ_1 are the potentials in the core, shell and atmosphere, respectively. There are six boundary conditions that must be satisfied by equation (126). φ_1 must equal $-E_o z$ at $r = \infty$ where the sphere no longer influences the electric field or potential in the atmosphere. The potential and the displacement at the boundaries between the air and the shell, and the shell and the core must be equal and at $r = 0$, the potential φ_3 must not be singular. The boundary conditions are as follows:

$$1.\ (\varphi_1)_{r\to\infty} = -E_o z = -E_o r\cos\vartheta \tag{127}$$

$$2.\ (\varphi_1)_{r=a} = (\varphi_2)_{r=a} \tag{128}$$

$$3.\ (\varphi_2)_{r=qa} = (\varphi_3)_{r\ qa} \tag{129}$$

$$4.\ \varepsilon_1 \left[\frac{\delta\varphi_1}{\delta r} \right]_{r=qa} = \varepsilon_2 \left[\frac{\delta\varphi_2}{\delta r} \right]_{r=a} \tag{130}$$

$$5.\ \varepsilon_2\left(\frac{\delta\varphi_2}{\delta r}\right)_{r=qa} = \varepsilon_3\left(\frac{\delta\varphi_3}{\delta r}\right)_{r=qa} \tag{131}$$

6. at r = 0, φ_3 is not singular. (132)

where q is the ratio of the core radius to the total radius of the sphere.

Note that in this derivation, the electric field is considered to be constant. In the case of an alternating electric field,

$$\vec{E} = \vec{E}_o\ e^{-i\omega t} \tag{133}$$

where ω is the frequency of oscillation. The displacement which is connected with the polarization of the molecules shows some inertia and therefore lags E by a phase constant Φ:

$$\vec{D} = \vec{D}_o\ e^{-i(\omega t - \Phi)}\ . \tag{134}$$

If the dielectric constant is complex,

$$\varepsilon = \varepsilon' - \varepsilon''\ , \tag{135}$$

the relation

$$\vec{D} = \varepsilon\vec{E} \tag{136}$$

still holds for the alternating field case. The boundary conditions are the same as for $\vec{E} = \vec{E}_o$ (Frohlich, 1949).

Equation (126) may be simplified by using the boundary conditions. From the first boundary condition, $A_l = 0$ for φ_1 except at $l = 1$, in which case $A_l = -E_o\varphi_1$. The equation reduces to:

$$\varphi_1 = \sum_{l=0}^{\infty} \frac{B_l}{r^{l+1}} P_l(\cos\vartheta) - E_o r \cos\vartheta \tag{137}$$

From the sixth boundary condition, $B_l = 0$ for all l for φ_3, thus reducing φ_3 to:

$$\varphi_3 = \sum_{l=0}^{\infty} A_l\, r^l\, P_l(\cos\vartheta) \tag{138}$$

The potential equations for the three regions are now:

$$\varphi_1 = \sum_{l=0}^{\infty} \frac{B_l}{r^{l+1}} P_l(\cos\vartheta) - E_o r \cos\vartheta \tag{139}$$

$$\varphi_2 = \sum_{l=0}^{\infty} \left[C_l\, r^l + \frac{D_l}{r^{l+1}} \right] P_l(\cos\vartheta) \tag{140}$$

$$\varphi_3 = \sum_{l=0}^{\infty} A_l\, r^l\, P_l(\cos\vartheta) \tag{141}$$

where B, C, D and A are constants. The boundary conditions 2-5 may then be used to solve equations (139) to (141) as follows.

From boundary conditions 2 and 3 for the flux at the sphere boundaries the following simplifications may be made.

$$(\varphi_1)_{r=a} = (\varphi_2)_{r=a} \tag{142}$$

$$\frac{B_l}{a^{l+1}} P_l(\cos\vartheta) = \left[C_l a^l + \frac{D_l}{a^{l+1}} \right] P_l(\cos\vartheta) \tag{143}$$

$$\frac{B_l}{a^{l+1}} = C_l\, a^l + \frac{D_l}{a^{l+1}}\, . \tag{144}$$

For the second boundary condition.

$$(\varphi_2)_{r=qa} = (\varphi_3)_{r=qa} \tag{145}$$

$$\left[C_l q^l a^l + \frac{D_l}{a^{l+1} q^{l+1}} \right] = A_l\, a^l\, q^l \tag{146}$$

for the third boundary condition.

The fourth and fifth boundary conditions require the differentiation of the flux with respect to r resulting in the following equations:

$$\frac{\delta\varphi_1}{\delta r} = \sum_{l=0}^{\infty} -(l+1)\frac{B_l}{r^{l+2}}P_l(\cos\vartheta) - E_o\cos\vartheta \tag{147}$$

$$\frac{\delta\varphi_2}{\delta r} = \sum_{l=0}^{\infty}\left[lC_l\, r^{l-1} - \frac{(l+1)D_l}{r^{l-2}}\right]P_l(\cos\vartheta) \tag{148}$$

$$\frac{\delta\varphi_3}{\delta r} = \sum_{l=0}^{\infty} lA_l\, r^{l-1}\, P_l(\cos\vartheta) \tag{149}$$

Then from the fourth boundary condition,

$$\varepsilon_1\left[\frac{-(l+1)B_l}{a^{l+2}}\right] = \varepsilon_2\left[lC_l\, a^{l-1} - \frac{(l+1)D_l}{a^{l-2}}\right] \tag{150}$$

and from the fifth boundary condition,

$$\varepsilon_2\left[-lC_l\ \frac{a^{l-1}\, q^{l-1}\,(l+1)}{a^{l-2}\, q^{l-2}}\right]D_l = \varepsilon_3\left[lA_l\, a^{l-1}\, q^{l-1}\right] \tag{151}$$

Equations (144), (146), (150) and (151) may now be solved for A_l, B_l, C_l and D_l in terms of a, q, ε_1, ε_2 and ε_3 as illustrated in the following equations:

From (144),

$$B_l = C_l\, a^{2l+1} + D_l\ . \tag{152}$$

Substitution of (152) into (150) gives

$$\varepsilon_1\left[\frac{-(l+1)(C_l\, a^{2l+1} + D_l)}{a^{l+2}}\right] = \varepsilon_2\left[lC_l\, a^{l-1} - \frac{(l-1)\, D_l}{a^{l-2}}\right] \tag{153}$$

Equation (153) is true for $l \neq 1$ only if

$$C_l = 0 \quad \text{and} \quad D_l = 0 \tag{154}$$

From (146),

$$A_l = C_l + \frac{D_l}{a^{2l+1}\, q^{2l+1}} \tag{155}$$

Therefore

$$A_l = 0 \tag{156}$$

and from (152),

$$B_l = 0 \tag{157}$$

Thus A_l, B_l, C_l and D_l are 0 for all values of l except $l = 1$. For the case of $l = 1$ (subscripts will now be dropped and $P_1(\cos\vartheta) = \cos\vartheta$),

$$\varphi_1 = \frac{B}{r^2}\cos\vartheta - E_o\, r\cos\vartheta \tag{158}$$

$$\varphi_2 = \left[Cr + \frac{D}{r^2}\right]\cos\vartheta \tag{159}$$

$$\varphi_3 = Ar\ \cos\vartheta \tag{160}$$

$$\frac{\delta\varphi_1}{\delta r} = \frac{-2B\cos\vartheta}{r^3} - E_o\cos\vartheta \tag{161}$$

$$\frac{\delta\varphi_2}{\delta r} = \left[C - \frac{2D}{r^3}\right]\cos\vartheta \tag{162}$$

$$\frac{\delta\varphi_3}{\delta r} = A\ \cos\vartheta \tag{163}$$

To satisfy boundary conditions 2-5, the $\cos\vartheta$ term always cancels out, therefore for simplification, $\varphi' = \varphi/\cos\vartheta$ will be used:

$$\varphi_1' = \frac{B}{r^2} - E_o r \qquad \frac{\delta\varphi_1'}{\delta r} = \frac{-2B}{r^3} - E_o \tag{164}$$

$$\varphi_2' = Cr + \frac{D}{r^2} \qquad \frac{\delta\varphi_2'}{\delta r} = C - \frac{2D}{r^3} \tag{165}$$

$$\varphi_3' = Ar \qquad \frac{\delta\varphi_3'}{\delta r} = A \tag{166}$$

Solving for A, B, C and D as for the $l \neq 1$ case, results in the following:

$$A = \frac{-3E_o\ \varepsilon_1(2\varepsilon_3 + \varepsilon_2)}{Q} \tag{167}$$

$$B = \frac{-3E_o\ \varepsilon_1\ a^3(\varepsilon_3 + 2\varepsilon_2 + q^3\varepsilon_2 - q^3\varepsilon_3)}{Q} + E_o\ a^3 \tag{168}$$

$$C = \frac{-3E_o\varepsilon_1\ (\varepsilon_3 + 2\varepsilon_2)}{Q} \tag{169}$$

$$D = \frac{-3E_o\ \varepsilon_1\ q^3\ a^3\ (\varepsilon_2 - \varepsilon_3)}{Q} \tag{170}$$

where $Q = (\varepsilon_3 + 2\varepsilon_2)(2\varepsilon_1 + \varepsilon_2) + q^3(2\varepsilon_2 - 2\varepsilon_1)(\varepsilon_3 - \varepsilon_2)$. The equations for the potentials in the air, in the liquid shell and in the dielectric core are, respectively:

$$\varphi_1 = \left[\frac{-3E_o\varepsilon_1 a^3(\varepsilon_3 + 2\varepsilon_2 + q^3\varepsilon_2 - q^3\varepsilon_3)}{Qr^2} + \frac{E_o a^3}{r^2} - E_o r\right]\cos\vartheta \tag{171}$$

$$\varphi_2 = \left[\frac{-3E_o\varepsilon_1(\varepsilon_3 + 2\varepsilon_2)r}{3} - \frac{3E_o\varepsilon_1 q^3 a^3(\varepsilon_2 - \varepsilon_3)}{Qr^2}\right]\cos\vartheta \tag{172}$$

$$\varphi_3 = \frac{-3E_o\varepsilon_1(2\varepsilon_2 + \varepsilon_3)r}{Q}\cos\vartheta \tag{173}$$

The only equation required to calculate the potential due to the spherical shell system is φ_1. φ_1 is the potential due to the external field E_o $(-E_o z)$ plus the potential due to the dielectric sphere. The potential due only to the dielectric sphere (φ_1') is Consider the potential along the z axis, $r = z$, and consider $\varepsilon_1 = 1$; thus

$$\varphi_1' = \frac{-3E_o a^3(\varepsilon_3 + 2\varepsilon_2 + q^3\varepsilon_2 - q^3\varepsilon_3)}{Qr^2} + \frac{E_o a^3}{r^2} \tag{174}$$

The polarizability, P, is the dipole moment, p, per electric field, E_o. The potential for a dipole along the z axis is

$$\varphi = p/r^2 \tag{175}$$

Thus $P = \varphi r^2/E_o$ and

$$P = \frac{-3a^3(\varepsilon_3 + 2\varepsilon_2 + q^3\varepsilon_2 - q^3\varepsilon_3) + a^3}{Q} \tag{176}$$

which simplifies to:

$$\frac{P}{a^3} = \frac{(\varepsilon_2-1)(2\varepsilon_2+\varepsilon_3)+q^3(2\varepsilon_2+1)(\varepsilon_3-\varepsilon_2)}{(\varepsilon_3+2\varepsilon_2)(2+\varepsilon_2)+q^3(2\varepsilon_2-2)(\varepsilon_3-\varepsilon_2)} \tag{177}$$

The absorption in the dielectric sphere system is proportional to the imaginary part of the polarization, P (see equation (104)). Consider $\varepsilon_2 = \varepsilon' - i\varepsilon''$ (for liquid sulfuric acid-water solutions) and $\varepsilon_3 = \varepsilon$ (core with no absorption). Equation (179) then becomes:

$$\frac{P}{a^3} = \frac{(\varepsilon'-i\varepsilon''-1)(\varepsilon+2\varepsilon'-2i\varepsilon'')+q^3(2\varepsilon'-2i\varepsilon''+1)(\varepsilon-\varepsilon'+i\varepsilon'')}{(\varepsilon'-i\varepsilon''+2)(\varepsilon+2\varepsilon'-2i\varepsilon'')+q^3(2\varepsilon'-2i\varepsilon''-2)(\varepsilon-\varepsilon'+i\varepsilon'')} \tag{178}$$

The imaginary part of this polarization is

$$\mathrm{Im}\left(\frac{P}{a^3}\right) = \frac{(E+q^3F)(C+q^3D) - (A+q^3B)(G+q^3H)}{(E+q^3F)^2 + (G+q^3H)^2} \tag{179}$$

where

$$A = \varepsilon'\varepsilon + 2\varepsilon'^2 - 2\varepsilon''^2 - \varepsilon - 2\varepsilon' \tag{180}$$

$$B = 2\varepsilon'\varepsilon - 2\varepsilon'^2 + 2\varepsilon''^2 + \varepsilon - \varepsilon' \tag{181}$$

$$C = -4\varepsilon''\varepsilon' - \varepsilon''\varepsilon + 2\varepsilon'' \tag{182}$$

$$D = 4\varepsilon'\varepsilon'' - 2\varepsilon''\varepsilon + \varepsilon'' \tag{183}$$

$$E = \varepsilon'\varepsilon + 2\varepsilon'^2 - 2\varepsilon''^2 + 2\varepsilon + 4\varepsilon' \tag{184}$$

$$F = 2\varepsilon'\varepsilon - 2\varepsilon'^2 + 2\varepsilon''^2 - 2\varepsilon + 2\varepsilon' \tag{185}$$

$$G = -4\varepsilon''\varepsilon' - \varepsilon''\varepsilon - 4\varepsilon'' \tag{186}$$

$$H = 4\varepsilon'\varepsilon'' - 2\varepsilon''\varepsilon - 2\varepsilon'' \tag{187}$$

For $q = 0$, equation (181) simplifies to the pure liquid equation and for $q = 1$, equation (181) is 0 (no absorption). Also the absorption equals zero if $\varepsilon'' = 0$.

The imaginary part of the polarization is related to the absorption coefficient and mass content in the same way as for a pure liquid, with slight adjustments which are necessary due to differences in the densities of the core and liquid. The polarization is proportional to the absorption coefficient and inversely proportional to the mass content of the clouds. The details of the absorption equation for the spherical shell case will be worked out in the next section.

Several properties of the spherical shell dielectric term, **D**, (equation (181)) will be studied before it is used to compute the mass content of the Venus clouds. These properties include the wavelength dependence, the variation of the absorption with ε, the dielectric constant of the core, the temperature dependence, the dependence on concentration of sulfuric acid and the dependence on q, the ratio of the core radius to the total radius.

The wavelength dependence of the dielectric term for the spherical shell model was calculated using the following equation

$$n = \frac{\ln\left(\mathrm{Im}(P/a)s/\mathrm{Im}(P/a)x\right)}{\ln(\lambda_S/\lambda_X)} = \frac{\ln\left(\mathbf{D}_S/\mathbf{D}_X\right)}{\ln\left(\lambda_S/\lambda_X\right)} \tag{188}$$

where $\frac{\mathrm{Im}(P/a)s}{\mathrm{Im}(P/a)x} = \left(\frac{\lambda_S}{\lambda_X}\right)^n$ and n is the wavelength dependence. The dependence of the absorption coefficient on wavelength is equal to the wavelength dependence of the dielectric term minus one since the absorption coefficient is inversely proportionally to the wavelength and proportional to the dielectric term (see equation (101)). The results for (90% H_2SO_4, 375 K), (85% H_2SO_4, 375 K) and (90% H_2SO_4, 400 K) as a function of q are shown in Figure 64. For q ranging from 0 to about 0.9, the wavelength dependence is nearly independent of the value of q and is approximately −1.0. At values of q greater than 0.9, the dependence becomes a strong function of q ranging from −0.9 at $q = 0.9$ to greater than +1.1 at $q = 0.998$. This dependence decreases slightly with decreasing sulfuric acid concentration and increasing temperature. The variation with temperature and pressure are more exaggerated for higher values of q.

The dependence of the dielectric term on ε, the dielectric constant of the core, is shown in Figure 65 for S- and X-band wavelengths at a concentration of 90% sulfuric acid and a temperature of 375 K. As would be expected, the ratio of the two dielectric terms diverges from one at large values of q. The ratio deviates from 1 at lower values of q for X-band than S-band. For values of q greater than 0.9, it is important that a good estimate of ε be made. This will be discussed in a later section.

The variation of the dielectric term with temperature at S- and X-band wavelengths for 90% sulfuric acid and $\varepsilon = 2.9$ is shown in Figure 66. The S-band dielectric term increases with decreasing temperatures. This increase is greatest for $q = 0$ and least for high values of q. The X-band dielectric term dependence on temperature is more complex. For $q = 0$, the dependence is similar to S-band — increasing with decreasing temperatures. At $q = 0.90$, the shape of the curve is inverted and at $q = 0.98$, the dielectric term increases with increasing temperature.

The variation of the dielectric term with concentration is shown in Figure 67 for a temperature of 375 K and several values of q (0, 0.9 and 0.98). Both S- and X-band dependences are shown. For $q = 0$, there is very little dependence

Figure 64. Wavelength dependence of the dielectric term as a function of q.

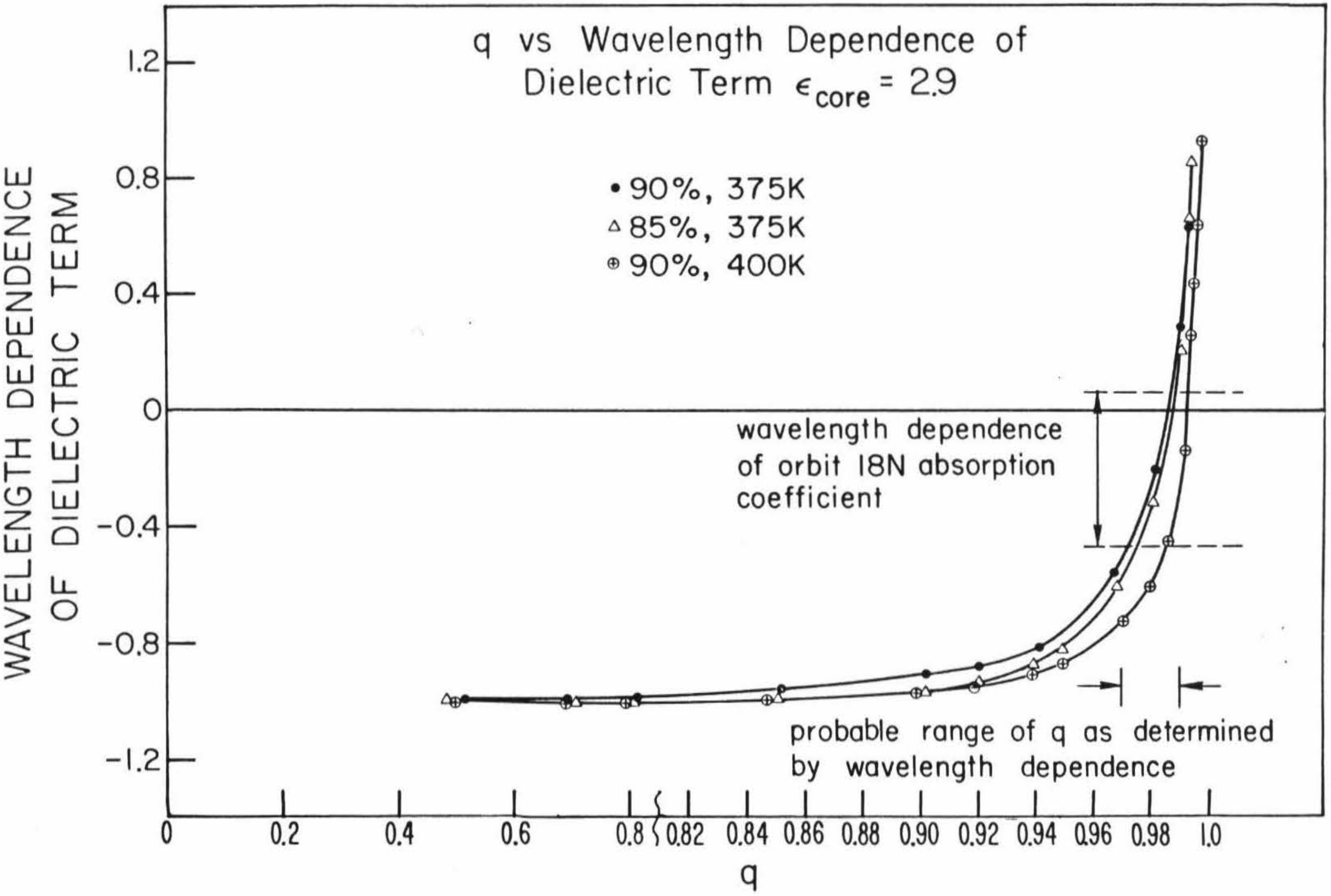
q vs Wavelength Dependence of Dielectric Term $\epsilon_{core} = 2.9$
• 90%, 375K
△ 85%, 375K
⊕ 90%, 400K
wavelength dependence of orbit 18N absorption coefficient
probable range of q as determined by wavelength dependence
WAVELENGTH DEPENDENCE OF DIELECTRIC TERM
1.2
0.8
0.4
0
-0.4
-0.8
-1.2
0
0.2
0.4
0.6
0.8
0.82
0.84
0.86
0.88
0.90
0.92
0.94
0.96
0.98
1.0
q

Figure 65. Variation of the dielectric term with the dielectric constant of the core.

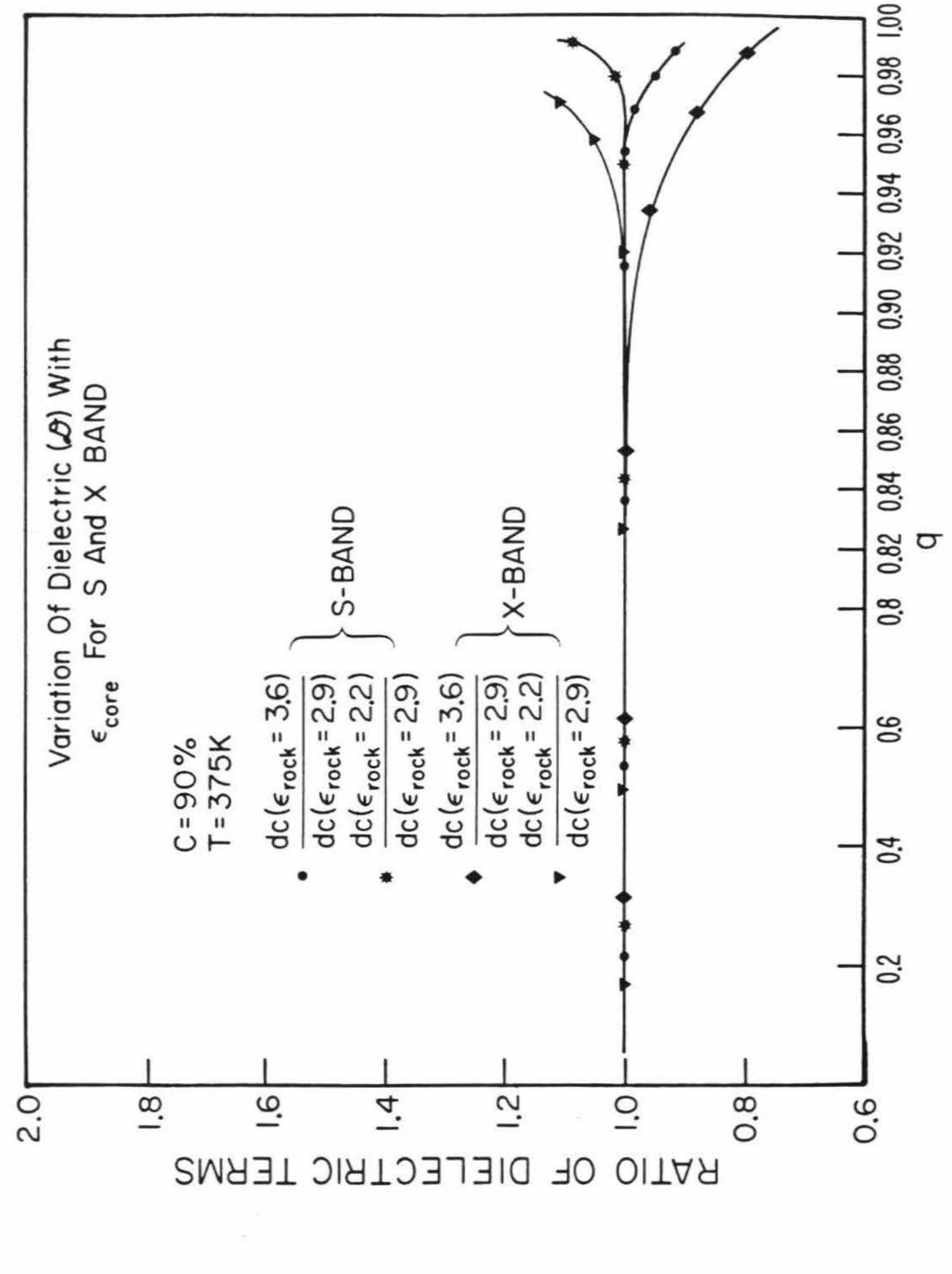
Variation Of Dielectric ($\mathcal{B}$) With
ϵ_{core} For S And X BAND
C = 90%
T = 375K
● $\frac{dc(\epsilon_{rock} = 3.6)}{dc(\epsilon_{rock} = 2.9)}$
✱ $\frac{dc(\epsilon_{rock} = 2.2)}{dc(\epsilon_{rock} = 2.9)}$
S-BAND
◆ $\frac{dc(\epsilon_{rock} = 3.6)}{dc(\epsilon_{rock} = 2.9)}$
▼ $\frac{dc(\epsilon_{rock} = 2.2)}{dc(\epsilon_{rock} = 2.9)}$
X-BAND
RATIO OF DIELECTRIC TERMS
2.0
1.8
1.6
1.4
1.2
1.0
0.8
0.6
q
0.2
0.4
0.6
0.8
0.82
0.84
0.86
0.88
0.90
0.92
0.94
0.96
0.98
1.00

Figure 66. Variation of the dielectric term with temperature.

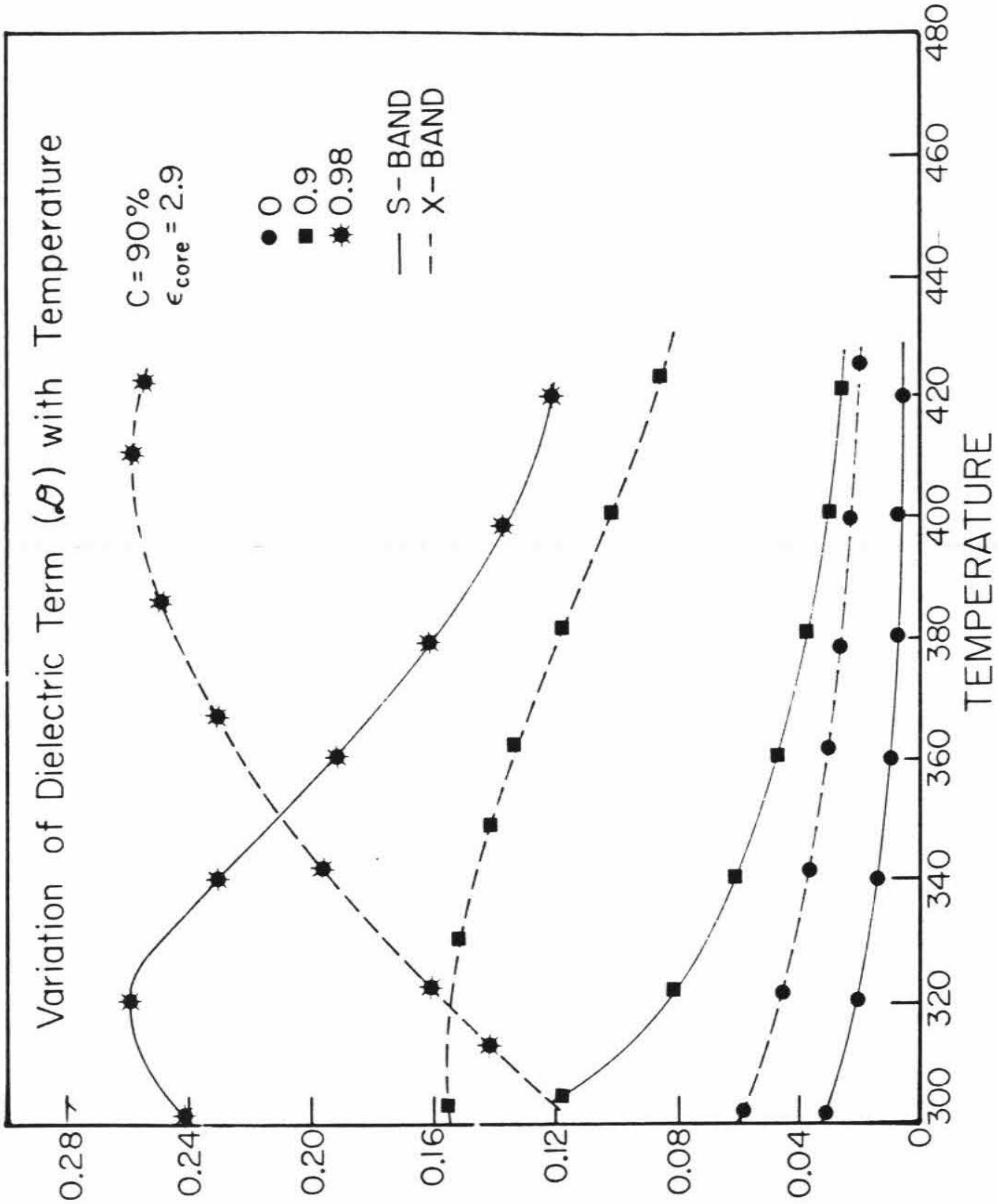
Variation of Dielectric Term ($\mathcal{B}$) with Temperature
C = 90%
ϵ_{core} = 2.9
● 0
■ 0.9
✸ 0.98
— S-BAND
-- X-BAND
DIELECTRIC TERM
0
0.04
0.08
0.12
0.16
0.20
0.24
0.28
TEMPERATURE
300
320
340
360
380
400
420
440
460
480

Figure 67. Variation of the dielectric term with concentration of sulfuric acid.

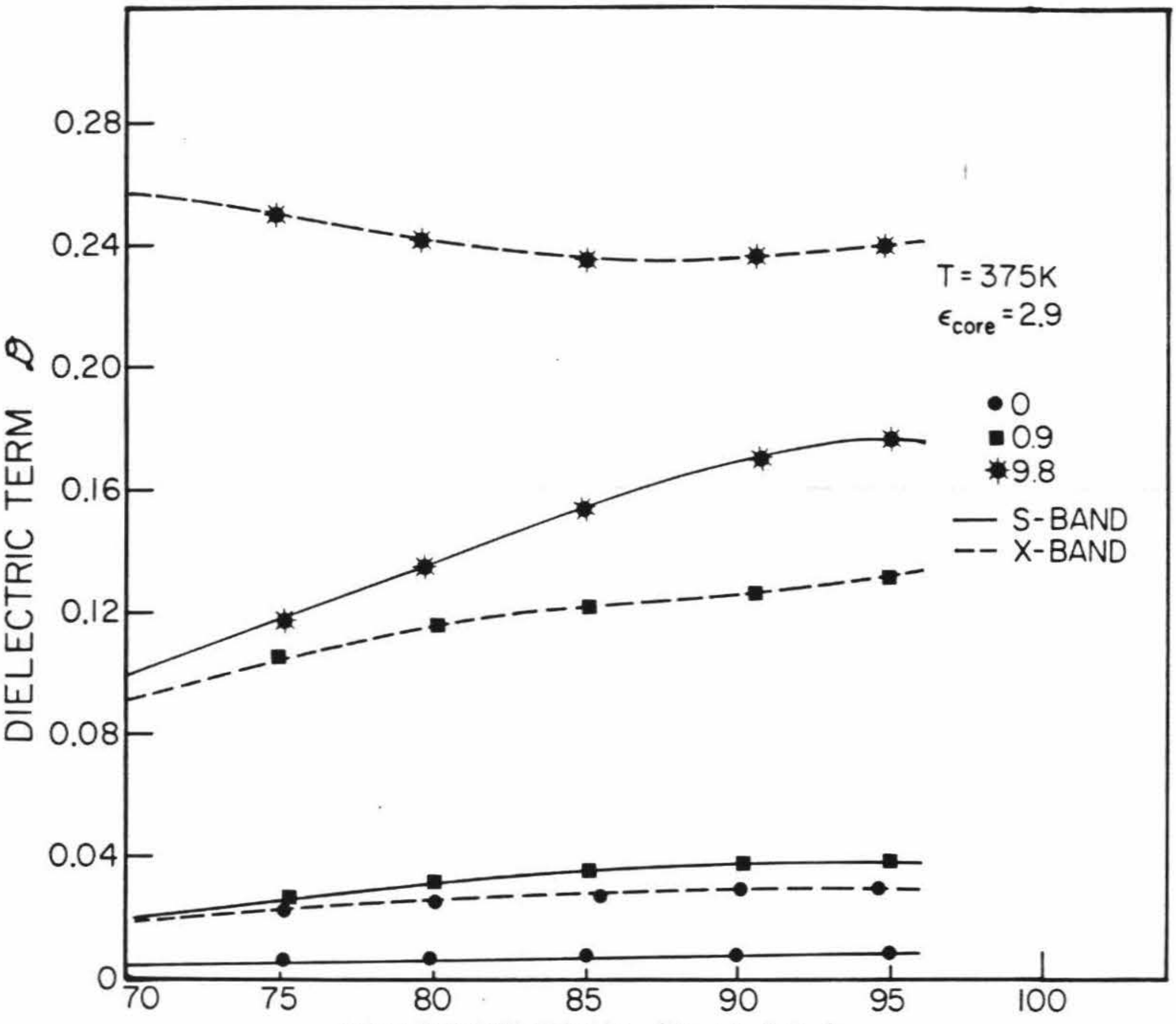
0.28
0.24
0.20
0.16
0.12
0.08
0.04
0
70
75
80
85
90
95
100
DIELECTRIC TERM $\mathcal{D}$
CONCENTRATION (% H_2SO_4)
T = 375K
ϵ_{core} = 2.9
● 0
■ 0.9
✸ 9.8
— S-BAND
-- X-BAND

of the dielectric term on concentration as was discussed in the analysis assuming pure liquid clouds. For $q = 0.90$, again there is very little dependence on concentration at S-band but the X-band dielectric term begins to show some dependence at concentrations greater than 70%. For $q = 0.98$, both wavelengths are concentration dependent throughout the range shown; however, the S-band dielectric term increases with increasing concentration and the X-band term decreases with increasing concentration (opposite to its direction for $q = 0.9$). Inasmuch as the concentration of the sulfuric acid is fairly well known due to its dependence on water vapor pressure (which is known from Moroz) and temperature, the concentration and temperature dependences described in Figures 66 and 67 are not significant sources of error in calculating the dielectric term and thus the cloud mass contents. A maximum uncertainty of a factor of 2 is possible if the assumed core composition and sulfuric acid concentration are wrong.

The dielectric term varies most substantially with q, as seen in Figure 68. The dielectric term is plotted as a function of q for several concentrations and several temperatures. For values of q greater than about 0.6, for X-band and 0.85 for S-band, the dielectric term increases nearly exponentially with q to a maximum which is nearly an order of magnitude greater than for small values of q. This maximum occurs for q at about 0.975 for S-band and 0.994 for X-band. Past these maxima, the dielectric term drops rapidly to 0 for a q close to 1 as is expected since the core is non-absorbing.

In summary, the most pronounced variation in the dielectric term for a spherical shell model is due to q, the ratio of the core radius to the total radius. As the shell becomes thinner, the dielectric term increases and thus the absorptivity of the droplet per unit volume of material increases. An increase in the absorptivity decreases the mass content for a given absorption coefficient profile. By varying the thickness of the shell, the mass content can be reduced

Figure 68. Variation of the dielecrtic term with q, the ratio of the inner core to the outer radius.

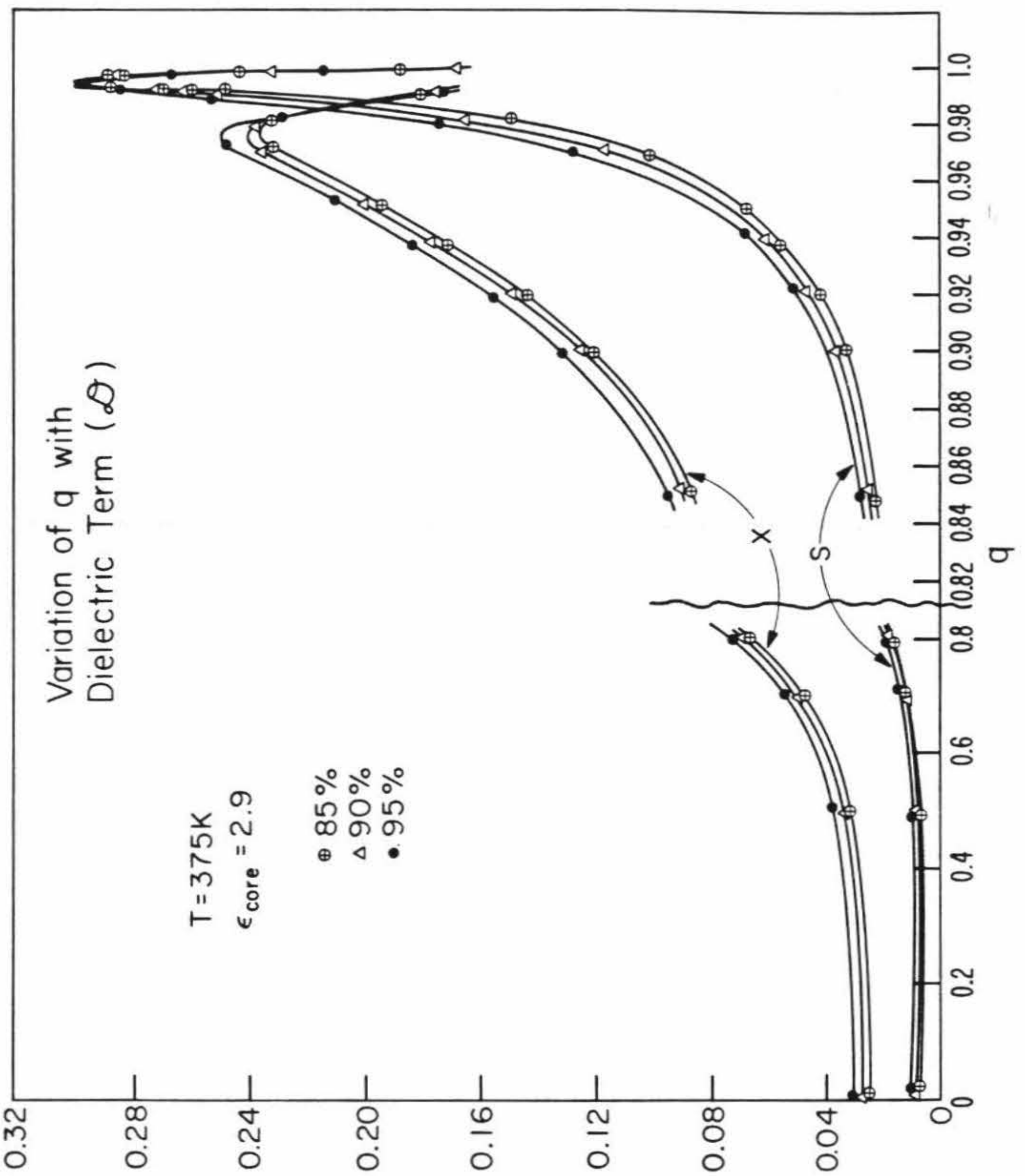
Variation of q with
Dielectric Term (𝒟)
T = 375K
ε_core = 2.9
⊕ 85%
△ 90%
● 95%
X
S
DIELECTRIC TERM, 𝒟
0.32
0.28
0.24
0.20
0.16
0.12
0.08
0.04
0
q
0
0.2
0.4
0.6
0.8
0.82
0.84
0.86
0.88
0.90
0.92
0.94
0.96
0.98
1.0

by more than an order of magnitude from that calculated assuming the cloud is made up of pure liquid droplets.

The absorptivity of a particle is proportional to the electric field which penetrates that particle. In the case of a pure liquid sulfuric acid droplet, the conductivity is sufficiently high that some of the field is excluded from the interior of the drop thereby reducing the absorption. The exclusion of the electric field occurs because free charges of opposite sign collect at opposite sides of the droplet in the presence of an electric field (see Figure 69a for illustration). In the case of a pure conductor, the surface charge is so great that the electric field is totally excluded and no absorption occurs. When a dielectric core of non-absorbing material is introduced in a particle of the same total volume as in the pure liquid case, two effects occur which contribute to the increase in electric field which penetrates the drop and therefore the increase in absorption. First, the volume filled by sulfuric acid in the spherical shell case is less than in the pure liquid case therefore the number of available free conducting charges available to exclude the electric field decreases. Second, the dielectric core, which is also polarized in the presence of the electric field, affects the arrangement of the free charges in two ways. First, its own polarization attracts some of the free charges to the surface of the core rather than the exterior surface. Second, it acts as a sort of barrier which divides the free charges into two regions on either side of the core. In the presence of a rapidly alternating field, the free charges have a more difficult time getting around the barrier than they would if there were no central core (Figure 69b). As the core size increases, fewer charges can get around the barrier until it becomes so large that the total number of free charges available is divided in half with half on each side of the barrier (see Figure 69c).

Figure 69. Variation of the conductivity with different particle models: (a) no core, (b) dielectric core and (c) large dielectric core.

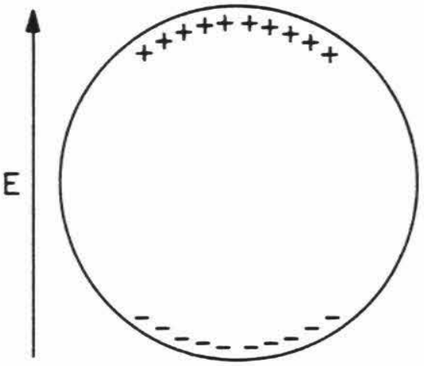
E
no core,
10 available
free charges

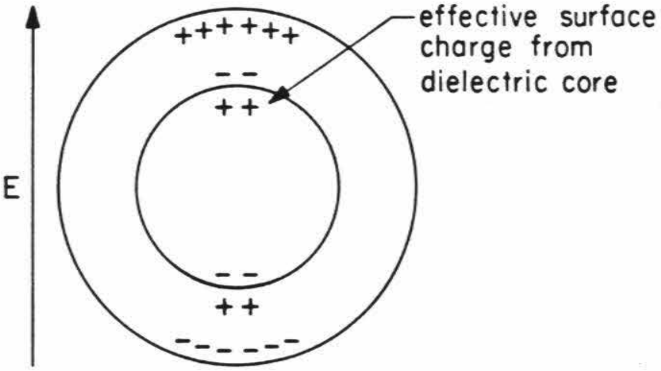
E
effective surface
charge from
dielectric core
small core,
only 8
available
free charges

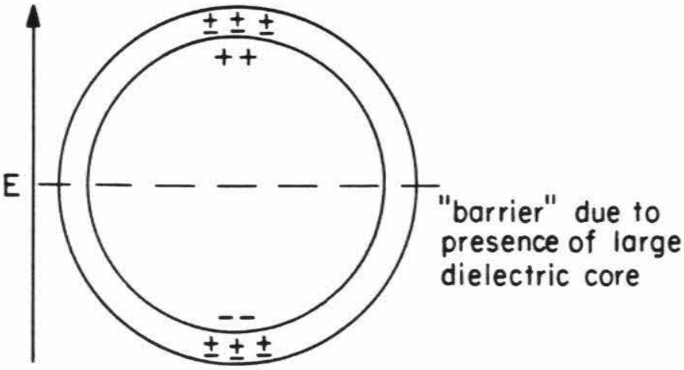
E
"barrier" due to
presence of large
dielectric core
large core,
only 6
available
free charges

2. Application to Absorption Coefficient Profiles

Apparently the spherical shell model for cloud particles is capable of producing mass content profiles from the absorption coefficient profiles which are comparable in magnitude to the mass content profiles determined by the Sounder Particle Size Spectrometer. In order to use the spherical shell model to calculate mass contents, it is first necessary to revise equation (105) slightly. From equation (101)

$$\alpha(\mathrm{km}^{-1}) = \frac{0.8\pi^2}{\lambda}\left[\sum_{vol} a^3\right] \mathrm{Im}(P) \tag{189}$$

where α is the absorption coefficient, P is the polarization, and a is the particle radius. For the spherical shell model,

$$\alpha(\mathrm{km}^{-1}) = \frac{0.8\pi^2}{\lambda}\left[\sum_{vol-core} a^3 + \sum_{vol-shell} a^3\right] \mathrm{Im}(P) \tag{190}$$

Since $M = \frac{4}{3}\pi\rho\sum a^3$, the above equation can be written as

$$\alpha(\mathrm{km}^{-1}) = \frac{0.6\pi}{\lambda}\left[\frac{M_{core}}{\rho_{core}} + \frac{M_{shell}}{\rho_{shell}}\right] \mathrm{Im}(P) \tag{191}$$

In terms of q (the ratio of the core radius to the total radius), the mass contents calculated from the absorption coefficient profiles are

$$M_{core} = \frac{\alpha\lambda\rho_{core} q^3}{0.6\pi\ \mathrm{Im}(P)} \tag{192}$$

$$M_{shell} = \frac{\alpha\lambda\rho_{liquid}(1 - q^3)}{0.6\pi\ \mathrm{Im}(P)} \tag{193}$$

$$M_{total} = M_{core} + M_{shell} \tag{194}$$

Table XI lists the densities of the solid species suggested by Knollenberg and Hunten (1980) along with those for solid sulfur, SiO_2 and Al_2O_3 (the main components of rocks). An average core density of 2.5 g/cm^3 will be used in all cloud profile calculations. Depending on the exact composition of the core material, the mass content profiles could vary by as much as a factor of 1.6 due to the density factor alone.

Table XI.

Suggested Dielectric Constants for the Core Material

	ε' (S)	ε' (X)	ρ (g/cm^3)	n	n^2
Sulfur	3.62*	3.58*	2.07†	1.957†	3.83
Sandy Soil	2.5*	2.5*			
Clay Soil	2.38*	2.27*			
NH_4Cl			1.527†	1.642†	2.7
$FeCl_3$			2.898†		
$AlCl_3$			2.44†		
SiO_2 (average rock)			2.26†	1.47†	2.16
Al_2O_3 (average rock)			3.965†	1.76†	3.10

*From Von Hipple (1954b).
†From *CRC*.

The density of the cloud material also affects the mass content profiles derived from Particle Size Spectrometer measurements. The experiment measured the number and the size of the particles and therefore the resulting volume of cloud material must be multiplied by a density. Kollenberg assumes the cloud is concentrated sulfuric acid and therefore uses a density of 2.0 g/cm^3. The cloud profiles used for comparison with the radio occultation results have been multiplied by a factor of (2.5/2.0) to compensate for the differences in density between solids and sulfuric acid since the bulk of the cloud mass is core material as will be shown later.

As was shown in Figure 65, the dielectric term, and therefore the calculated mass content of the clouds, varies with the dielectric constant of the core. Table XI also lists the dielectric constant (or n^2, when the dielectric constant is not available) for the suggested core materials. The average core dielectric constant is 2.9; however, it can be as large as 3.6 or as small as about 2.2. The uncertainty in the dielectric constant can cause the mass content of the clouds to change by as much as about 30%. Obviously the identification of the core material would be of great assistance in analyzing the absorption coefficient profiles in terms of its effect on the mass content due to density and dielectric constant. Until a probe once again penetrates the Venus atmosphere, the best that can be done is assume some "average" core material and remember that the calculated mass contents can vary by as much as a factor of nearly 2 depending on the composition of the core material.

The next step in the analysis of the absorption coefficient profiles is to use the occultation profiles which are nearest to the location of the Sounder probe to determine a value for q. Table XII lists the latitudes and solar zenith angles (SZA) for the Pioneer Venus probes (at 65 km altitude) (Colin, 1981) along with those for the occultations which are located in the equatorial region. According to the location and SZA, it would be most appropriate to use mass content profiles from the night probe to compare with orbits 30X and 45X, the north probe to compare with orbit 18X (assuming Venus is symmetric about the equator in terms of cloud morphology), the day probe to compare with orbit 352X and the Sounder probe to compare with orbit 69X. However, mass content data are not available except for the Sounder probe. Backscatter profiles from the nephelometer (Ragent and Blamont, 1980) are available for all four probes and can be used to estimate the mass content profiles at all probe locations. Since the backscatter cross section is proportional to the area of the particle and the mass content is proportional to the volume, the mass content at the small probe locations may be calculated using the following:

$$M_{smallprobe} = M_{Sounder}\left(\frac{\sigma_{smallprobe}}{\sigma_{Sounder}}\right)^{2/3} \tag{195}$$

where σ is the backscatter cross section. The day probe has essentially no lower cloud detectable by the nephelometer. The mass contents calculated assume a cloud particle density of 2.0 g/cm^3. These are multiplied by a factor of 2.5/2.0 before comparison to the radio occultation mass contents.

As described earlier, the sulfuric acid concentration is determined by the H_2O vapor pressure and absorption due to H_2O, SO_2, H_2SO_4 and CO_2 is subtracted from the absorption coefficient profile before the mass content profiles are calculated.

Table XII.

Locations of Probes and Occultations in Equatorial and Midlatitudinal Regions

Probe	Latitude	Solar Zenith Angle
Sounder	4.0N	65.7 (day)
Night	28.7N	150.7 (night)
North	60.2N	108.0 (night)
Day	31.3S	79.9 (day)
Orbit 78X	54.3S	89.9 (terminator)
Orbit 21X	52.2S	122.9 (night)
Orbit 30X	45.5S	130.8 (night)
Orbit 45X	31.2S	146.4 (night)
Orbit 69X	5.4S	165.4 (night)
Orbit 352X	22.3S	61.2 (day)

Figures 70 (a-f) show the mass contents for orbits 69X, 352X, 30X, 45X, 18X and 21X, respectively calculated using a q of 0.98. Mass contents calculated using many values of q were used; however, in all cases a q of 0.98 fit the radio occultation mass content profiles to the probe profiles. Also shown in Figure 70 are the mass content profiles of the Sounder, Night and North probes determined assuming $\rho = 2.5$ g/cm^3.

The mass content profiles derived from the radio occultation data for orbits 69X and Mariner 10 at the equator fit the Sounder mass content profiles best for a q of 0.98. The mass content profiles for orbits 30X, 45X, 18X and 21X in the latitude range of 30 to 55°S fit the north and night probe mass content

Figure 70 Mass contents derived assuming the spherical shell cloud particle model with a q of 0.98. (a) and (b) are 69X and Mariner 10-both equatorial occultations which should be compared with the Sounder profile. (c)-(f) are 30X, 45X, 18X and 21X-all midlatitudinal and should be compared with the Night and North probe profiles.

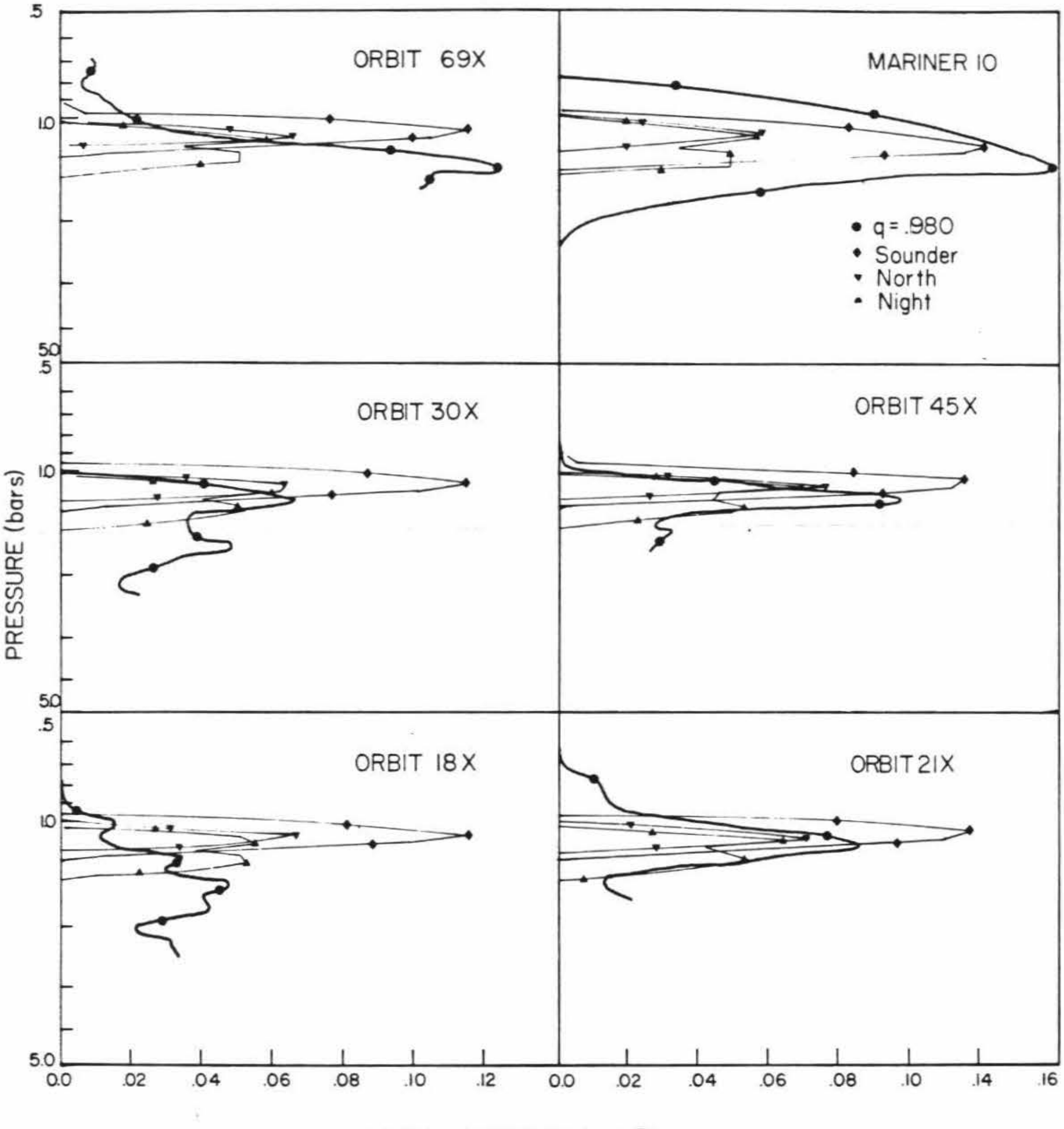
ORBIT 69X
MARINER 10
ORBIT 30X
ORBIT 45X
ORBIT 18X
ORBIT 21X
● q = .980
♦ Sounder
▾ North
▴ Night
PRESSURE (bars)
.5
1.0
5.0
0.0
.02
.04
.06
.08
.10
.12
.14
.16
MASS CONTENT (g/m^3)

profiles best for a q of from 0.97 to 0.992 with an average of about 0.982. thus the radio occultation mass content profiles fit the mass content profiles determined by the probe Particle Size Spectrometer and nephelometers if a cloud particle model consisting of a dielectric core with a liquid sulfuric acid coating is chosen with the ratio of core radius to the droplet radius is 0.98. This ratio may also be determined by examining the wavelength dependence of the S- and X-band absorption data.

As was observed in Figure 64 there is a strong wavelength dependence for high values of q. Thus far the only occultation which has produced a reliable X-band absorption coefficient profile is orbit 18N in the north polar region of Venus. Figure 64 shows the wavelength dependence calculated for orbit 18N which ranges from 0.46 at 6093.5 km to 0.92 at 6094.9 km. This wavelength dependence corresponds to a q of from 0.97 to 0.99. Table XIII lists the ratio of the mass content calculated at S-band to that calculated at X-band in the region of the lower cloud deck where X-band data are available. Six values of q are considered. The ratio approaches 1 for a q of from 0.97 to 0.98.

Table XIII.

Ratio of M_S/M_X for Various Values of q

(M_S/M_X)

R	q = 0.95	q = 0.96	q = 0.97	q = 0.98	q = 0.990	q = 0.992
6094.9	2.28	2.00	1.63	1.14	0.60	0.51
6094.6	2.20	1.93	1.56	1.08	0.56	0.47
6094.3	1.71	1.50	1.21	0.83	0.42	0.35
6094.0	1.30	1.14	1.92	0.63	0.32	0.26
6093.8	1.20	1.05	0.85	0.58	0.29	0.24
6093.5	1.32	1.16	0.93	0.64	0.31	0.26

The wavelength dependence may also be compared to microwave brightness temperature results. Janssen and Klein (1981) derive an upper limit for the opacity of a cloud in the region of 50 km at a wavelength of 1.35 cm. Their upper limit is 0.17. Muhleman et al. (1979) observe that the extra opacity source in the Venus atmosphere required to explain radar and radio observations must be located below 30 km if a $1/\lambda^2$ wavelength dependence is assumed. Figure 71 compares the 1.35 cm optical depth with that calculated by integrating the total absorption coefficient profiles obtained from the radio occultation experiment at S-band. The X-band optical depths are determined assuming the $1/\lambda^{1.2}$ wavelength dependence determined from the orbit 18 S- and X-band absorption coefficient profiles. Also shown are the optical depths at 1.35 cm determined from the S-band optical depths again, assuming a wavelength dependence of $1/\lambda^{1.2}$. The two data sets are consistent assuming the $1/\lambda^{1.2}$ dependence which offers additional support to the spherical shell model for cloud particles.

For the analysis of the remainder of the occultation absorption coefficient profiles, a value of $q = 0.98$ will be used in light of the above comparisons with probe data and the wavelength dependence considerations. In reality, there is probably a distribution of q's in the cloud which have an effective q of 0.98 ± 0.01.

3. Mass Content Profiles for All Orbits

Figure 72 shows the mass contents for all occultation orbits thus far analyzed. The results are divided into four regions of the atmosphere — the equator, midlatitudes, the collar and the pole. Mass contents are largest in the collar and the polar region. The maximum mass content in the collar region has not been reached for any of the occultations due to increased turbulence effects

Figure 71. Opacity as a function of wavelength as determined from the absorption coefficient profiles and the 1.35cm brightness temperatures.

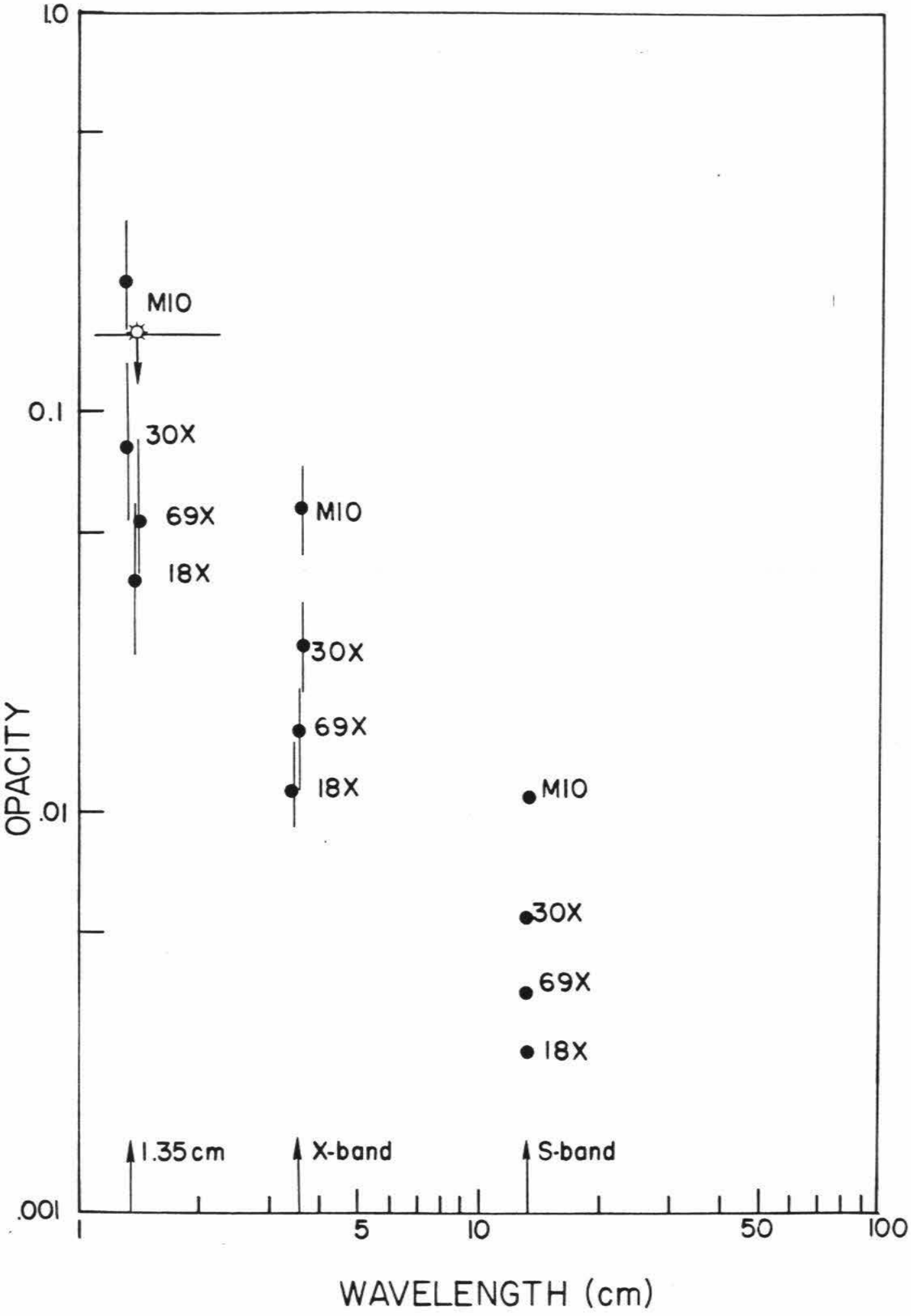
OPACITY
1.0
0.1
.01
.001
WAVELENGTH (cm)
1
5
10
50
100
M10
30X
69X
18X
M10
30X
69X
18X
M10
30X
69X
18X
1.35 cm
X-band
S-band

Figure 72. Mass contents for all orbits thus far analyzed. A q of 0.98 was used for all occultations.

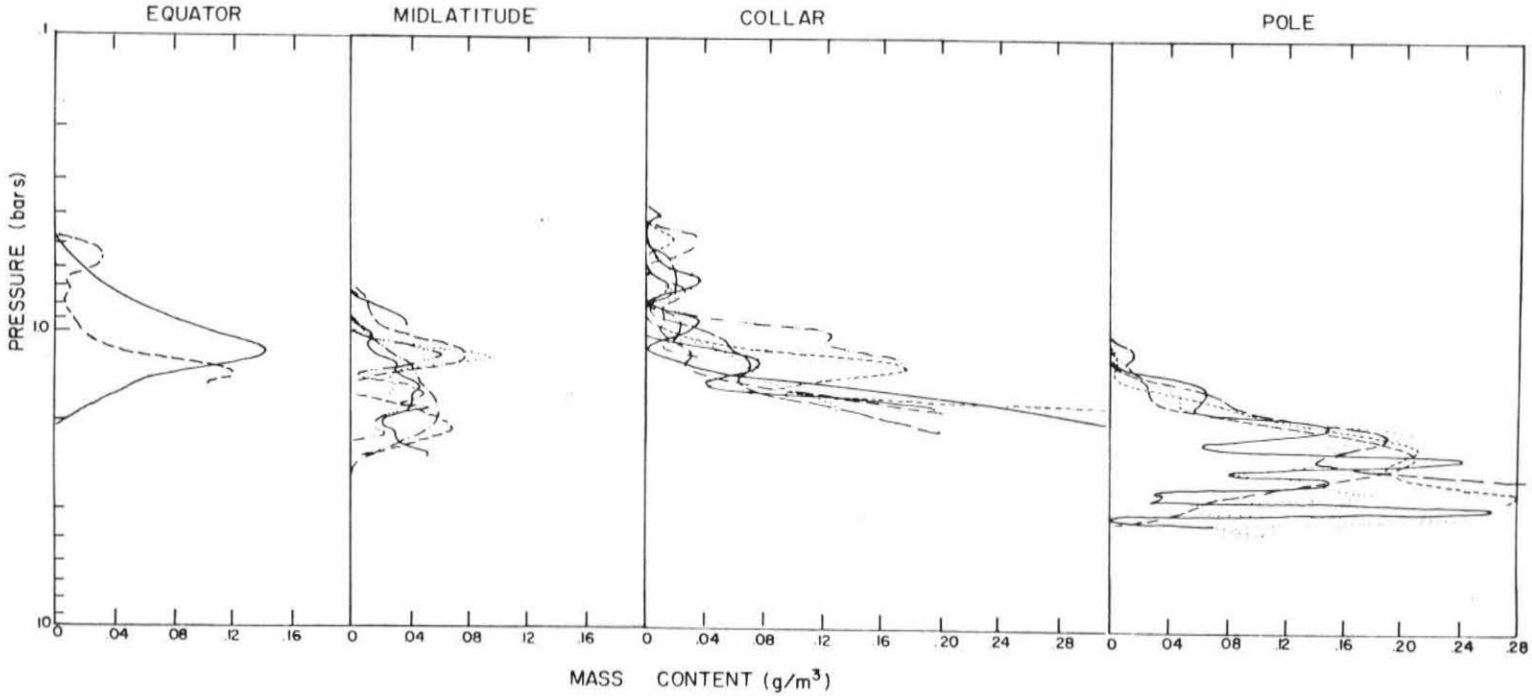
EQUATOR
MIDLATITUDE
COLLAR
POLE
PRESSURE (bars)
.1
1.0
10
0
.04
.08
.12
.16
.20
.24
.28
MASS CONTENT (g/m³)

below the 2 bar level rendering the lower absorption data useless. It is believed layering such as that observed in orbit 350N (1.5 bar level) is a result of refractivity fluctuations, not actual cloud layering.

The mass contents are least in the midlatitude regions. At the equator, a very pronounced cloud bottom is observed in the Mariner 10 profile and suggested in the orbit 69X profile.

Variation in the level in the atmosphere of the cloud layer is consistent with variations in the latitudinal variation of the temperature profile. At a given pressure level, the temperature is coolest in the pole and warmest at the equator. Cloud levels are lower in altitude at the pole (below the 2 bar level) than at the equator (at the 1 to 2 bar level). This is consistent with condensation occurring at a lower level in the atmosphere for a cooler temperature profile.

The only occultation profile which does not fit into the above mentioned pattern is orbit 352X in the midlatitude region. This is the only occultation in this region which occurred during the day. This suggests the mass content in the midlatitude regions is greater during the day than at night. Additional daytime occultations in the midlatitude regions are desirable before any conclusions can be reached.

CHAPTER VII

CONCLUSION

Absorption coefficient and temperature profiles used to derive the mass content profiles were analyzed in detail for all known uncertainties including averaging effects, power fluctuations, spacecraft wobble, turbulence, trajectory errors, perturbations in the refractivity profile and atmospheric oblateness due to winds. Inasmuch as the power loss due to refractive defocussing is determined from the Doppler data, uncertainties in the refractivity as well as the received power were considered. Power fluctuations were found to produce the greatest uncertainty in the S-band absorption coefficient profiles. Power fluctuations and spacecraft wobble contribute the greatest uncertainty in the X-band data. In fact, in many cases the spacecraft wobble has rendered the X-band data useless.

Absorption due to gaseous components of the atmosphere were determined and were subtracted from the measured profiles to produce absorption coefficient profiles resulting only from cloud material. The H_2O mixing ratio profile used was that measured by the Venera 11 and 12 spectrophotometers. The SO_2 profile was determined from the Venera 11 and 12 and Pioneer probe gas chromatographs and mass spectrometer results. The H_2SO_4 vapor mixing ratio profile used is the equilibrium saturation vapor pressure above a concentrated sulfuric acid-water solution at the temperatures of the lower cloud deck.

The absorption due to the gaseous components represents a small part of the total absorption. In the main cloud deck, gaseous absorption contributes 10 to 20% and at the bottom of the detected absorption layer, the sulfuric acid vapor contributes 60 to 100% to the absorption due to increased vapor pressure resulting from higher temperatures in this region. The clouds are the primary contributing absorbers in the 1 to 3 bar level of the Venus atmosphere. Below about 3 bars, absorption due to sulfuric acid vapor dominates.

As a first attempt, mass content profiles were produced from the absorption data assuming the clouds were composed of concentrated sulfuric acid resulting in mass contents on the order of several grams per cubic meter. Although planetwide variability in the lower cloud deck may account for differences in these radio occultation mass contents and those determined by the Pioneer probes, a second factor discounting purely liquid sulfuric acid clouds has arisen. The dielectric constants of liquid sulfuric acid were measured in the laboratory at S- and X-band wavelength and the results suggest the wavelength dependence for absorption by the liquid is $1/\lambda^2$. The wavelength dependence measured by the radio occultation experiment is about $1/\lambda^{1.2}$. In addition, the wavelength dependence required to fit the opacity determined from the 1.35 cm microwave emission data is $1/\lambda^{1.5}$ to. $1/\lambda^{1.2}$ Apparently the liquid sulfuric acid droplet model does not satisfy the observed wavelength dependence.

If, however, a cloud particle model consisting of a solid non-absorbing dielectric sphere with a concentric liquid sulfuric acid coating is invoked, the absorptivity of the particles increases and the mass content derived from the absorption coefficient profiles decreases. As the ratio of the core radius to total radius (q) increases, absorption increases by more than a factor of 10 for high values of q. In the case of pure sulfuric acid droplets, the conductivity is sufficiently high that some of the field is excluded from the interior of the droplet thereby reducing the absorption. When a dielectric core of non-absorbing material is introduced, two effects occur which contribute to the increase in the electric field which penetrates the drop. First, the volume filled by sulfuric acid decreases and the number of available free charges decreases. Second, the dielectric core, which is also polarized in the presence of the electric field, affects the arrangement of the free charges by attracting them to the inner surface and by acting as a barrier in the presence of the rapidly alternating electric field.

The mass contents of all orbits in the equatorial region of Venus were calculated using values of q of from 0 to 1. The resulting profiles match the probe mass content profiles at similar locations when a q of 0.98 ± 0.01 is chosen. Values of q of 0.97 and 0.99 change the absorptivity of the cloud particles by about 50%.

The wavelength dependence of the absorption for the spherical shell model varies with q from $1/\lambda^2$ for pure liquid to $\lambda^{0.2}$ for a large core. A q of 0.98 ± 0.01 results in a wavelength dependence of $1/\lambda^{1.0}$ to $1/\lambda^{1.4}$ which makes the radio occultation absorption coefficient data consistent with ± 1.35 cm opacity.

Mass content profiles using a q of 0.98 were determined for occultations in the polar, collar, midlatitudinal and equatorial regions assuming q remains fairly constant over the planet. The results show considerable variability in both the level and the magnitude of the lower cloud deck The cloud layer is lowest in altitude in the polar region. This might be expected as the temperature profile is cooler in the polar region than over the rest of the planet. The mass content is greatest in the polar and collar regions; however, many of the collar profiles were cut off due to fluctuations resulting from the increased turbulence in the collar region. The mass contents are least dense in the midlatitude regions and and are confined to a relatively thin layer at the equator.

The mass content profiles and cloud particle composition derived from the radio occultation absorption coefficient data are the primary results of this work. By invoking a cloud particle model consisting of a solid spherical dielectric core coated with a concentric spherical shell of a liquid sulfuric acid-water solution, the mass content profiles derived using the radio occultation data in the equatorial region match those measured by the probe Particle Size Spectrometer and estimated from the small probe nephelometers. The ratio of the inner core radius to the total droplet radius (q), which provides the best fit of the two data sets is 0.98 ± 0.01. In addition, the wavelength dependence of the S- and X-band absorption coefficient data is satisfied with the proposed spherical shell cloud particle model, again with an inner core to outer core radius ratio of 0.98 ± 0.01.

Future work in this field of research will include laboratory measurements of the sulfuric acid vapor absorption coefficient and the effect of the dielectric properties from absorption into liquid sulfuric acid of atmospheric gases (CO_2, SO_2, etc.). Accurate pointing of the X-band antenna before the onset of atmospheric attenuation must be accomplished if good X-band absorption profiles are to be obtained. The wavelength dependence measured in the one available occultation is unique and add considerable insight to the properties of the lower cloud. Finally, the processing and analysis of mass content profiles for many orbits is the primary goal in the near future. More detailed latitude, solar zenith angle and temporal variations will be studied. The radio occultation technique indeed provides a valuable method of determining the spatial and temporal variability of the cloud structure and composition on the planet Venus.

APPENDIX 1

DERIVATION OF $b = nr$

Essential to the radio occultation experiment is the equality

$$b = nr \tag{A1}$$

where b is the ray asymptote, n is the index of refraction at r and r is the radius, or point of closest approach of the radio beam as it is refracted by the atmosphere. The derivation of this equation is based on the geometry in Figure A1. From this geometry,

$$\sin i = \frac{r\,d\vartheta}{\sqrt{dr^2 + r^2 d\vartheta^2}} \tag{A2}$$

or

$$\sin i = \frac{r\frac{d\vartheta}{dr}}{\sqrt{1 + r^2 l(\frac{d\vartheta}{dr}r)^2}} \,. \tag{A3}$$

From Fermat's principle, $d\vartheta/dr$ may be calculated as:

$$\frac{d\vartheta}{dr} = \frac{b}{r\sqrt{r^2 n^2 - b^2}} \tag{A4}$$

resulting, after substitution, in

$$\sin i = \frac{b}{rn(r)} \,. \tag{A5}$$

or

$$rn(r)\sin i = b \tag{A6}$$

Equation (A6) is Bouger's law. It applies to each layer in the atmosphere traversed by the ray, as shown in Figure A2. At the point of closest approach, $i = \frac{\pi}{2}$ and Bouger's law simplifies to:

$$rn(r) = b \,. \tag{A7}$$

Figure A1: Geometry used in deriving the quantity $B = nr$.

Figuure A2: Path of ray in refractive atmosphere — shows relation to the incident angle of each layer.

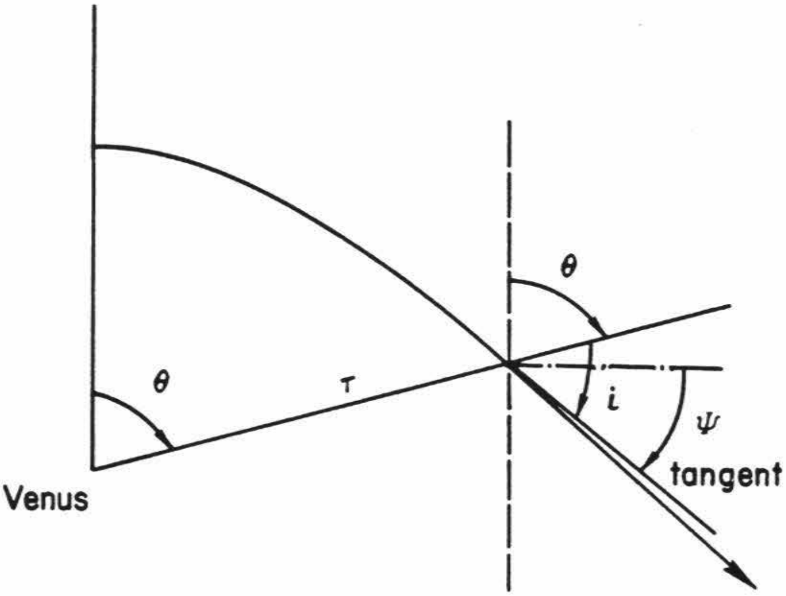
θ
θ
τ
i
Ψ
tangent
Venus

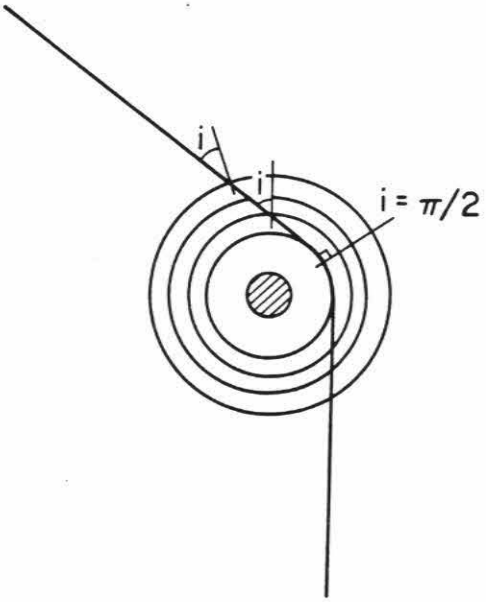
i
i
i = π/2

APPENDIX 2

PREPARATION OF SULFURIC ACID SOLUTIONS

Correct concentrations of (H_2O-H_2SO_4) solutions were prepared from reagent grade sulfuric acid (95-98% by weight) according to the following scheme:

A = % H_2SO_4 (by weight) wanted

B = ml H_2SO_4 (reagent grade) used

$\rho_{H_2SO_4}$ = density of reagent grade H_2SO_4 (g/ml)

$g_T = B \times \rho_{H_2SO_4}$ = total grams of solution in B ml reagent grade H_2SO_4

$g_{H_2SO_4} = g_r \times$ (% reagent grade) = grams of H_2SO_4 in B ml reagent grade H_2SO_4

$g_{H_2O} = g_T - g_{H_2SO_4}$ = grams of H_2O in B ml reagent grade H_2SO_4

$S = \dfrac{g_{H_2SO_4} \times 100}{A}$ = grams total solution wanted after adding H_2O

$S - g_T$ = grams H_2O added to B ml H_2SO_4 (reagent grade) in order to have a solution of A% H_2SO_4.

S ml (= S grams) of water were placed in a 250 ml flask. B ml of reagent grade H_2SOS_4 were added slowly and the flask was cooled in a water-ice bath under the fume hood. After the samples were cooled they were titrated using a 2 N NaOH solution and Bromthymol Blue as an indicator. The exact concentration of the sulfuric acid solutions was calculated using the following equation:

$$\%\ H_2SO_4 = \frac{(98.08)(\frac{1}{2})(10^{-3})(N_{NaOH})(V_{NaOH})(100)}{(w_{H_2SO_4})} \qquad \text{(A1)}$$

where N_{NaOH} is the exact normality of the NaOH solution, V_{NaOH} is the volume of the NaOH used in the titration and $w_{H_2SO_4}$ is the weight of sulfuric acid solution being titrated.

The resulting concentrations of sulfuric acid solutions are given in Appendix 3. All solutions were retitrated after the dielectric constant measurements were done. The concentrations were found to change by less than 2% in all cases.

APPENDIX 3

Raw Data-11.32 cm, 2.64 Ghz

Temperature (°C)	Temperature (K)	Concentration (% wt)	ε'	ε''
21.0	294.2	0	78.2	11.0
22.8	295.0	11.16	52.9	250
22.4	295.6	31.57	37.2	418
23.2	296.4	40.61	35.5	390
23.6	296.8	50.16	34.4	350
23.5	296.7	60.75	34.5	234
21.2	294.4	72.00	33.8	126
21.8	295.0	81.20	29.0	78.1
24.2	297.4	85.46		
23.0	296.2	91.10	23.1	75.1
24.2	297.4	96.65	16.1	67.1
22.8 average	296.0			
50.0	323.2	0	70.0	5.2
42.6	315.8	11.16	50.0	327
41.9	315.1	19.68	38.0	497
43.7	316.9	31.57	31.7	572
44.5	317.7	40.61	33.2	545
43.8	317.0	50.16	32.4	464
44.6	317.8	60.75	34.0	363
44.5	317.7	72.01	32.1	227
45.2	318.4	76.32	30.3	190
44.8	318.0	82.47	28.0	150
45.4	318.6	84.95	27.1	134
44.4	317.6	89.30	34.1	133
44.6	317.8	95.93	15.9	128
44.6 average	317.8			

Temperature (°C)	Temperature (K)	Concentration (% wt)	ε'	ε''
80.0	353.2	0	59.0	2.8
78.1	351.3	11.16	42.5	414
80.4	353.6	19.68	32.6	660
80.2	353.4	31.57	28.3	847
80.1	353.3	40.61	29.9	811
78.6	351.8	50.16	28.7	715
79.6	352.8	60.75	29.2	575
77.6	350.8	72.01	29.6	409
79.0	352.2	76.32	28.6	341
78.9	352.1	81.78	26.4	286
79.5	352.7	86.08	24.4	265
79.5	352.7	90.35	23.1	254
79.8	353.0	95.93	14.7	245
79.4 average	352.5			
108.3	381.5	50.16	27.9	971
108.2	381.4	60.75	25.9	760
106.8	379.9	72.01	25.7	610
106.8	379.9	76.32	26.3	535
104.4	377.6	81.75	25.8	426
106.8	380.1	90.35	22.9	359
107.2	380.4	95.93	18.9	338
106.9 average	380.1			
144.8	418.0	76.0	22.5	712
145.6	418.8	81.78	26.1	646
145.1	418.3	90.35	20.7	524
145.0	418.2	96.65	15.6	441
145.2 average	418.3			

Raw Data (X-Band) — 3.56 cm, 8.42 GHz

	Concentration (%)*	ε'	ε''
$T = 22 \pm 1$°C (295 ± 1 K) $\varepsilon' \pm 7\%$ $\varepsilon'' \pm 5\%$	0	65.7	28.5
	10.0	41.8	97.4
	21.1	28.8	147
	30.6	26.2	163
	40.8	27.3	155
	51.0	29.5	129
	60.8	31.0	89.2
	70.5	28.5	57.3
	75.9	26.0	44.0
	81.3	24.2	33.0
	86.4	23.1	29.9
	90.9	23.1	31.6
	97.1	17.3	28.7
$T = 51 \pm 1$°C (324 ± 1 K) $\varepsilon' \pm 7\%$ $\varepsilon'' \pm 5\%$	0	64.9	15.5
	10.0	40.3	123
	21.1	26.7	178
	30.6	20.3	203
	40.8	22.1	202
	51.0	24.5	167
	60.8	27.2	127
	70.5	27.1	83.7
	75.9	26.5	66.0
	81.3	24.2	53.4
	86.4	25.1	54.6
	90.9	25.0	52.9
	97.1	17.2	46.8

*Concentration uncertainty of 1%.

	Concentration (%)*	ε'	ε''
	0	60.1	9.2
	10.0	41.7	118.3
	21.1	25.0	196
	30.6	20.3	230
T = 77 ± 1°C	30.6	20.3	230
(350 ± 1 K)	40.8	15.4	235
ε' ± 7%	51.0	19.0	199
ε'' ± 5%	60.8	22.5	152
	70.5	26.2	116
	75.9	26.0	101
	81.3	26.4	83.6
	86.4	27.2	85.9
	90.9	27.0	81.5
	97.1	17.4	66.6
	30.6	(18.3)	(259)
	40.8	16.6	295
	51.0	19.3	255
T = 103 ± 2°C	60.8	23.7	208
(376 ± 1 K)	70.5	24.7	158
ε' ± 10%	75.9	25.8	139
ε'' ± 10%	81.3	26.5	114
	86.4	24.8	110
	90.9	25.8	108
	97.1	16.6	98.3

*Concentration uncertainty of 1%.

	Concentration (%)*	ε'	ε''
	70.5	21.7	277
= 143 ± 3°	75.9	25.5	227
(416 ± 3 K)	81.3	23.7	209
ε' ± 10%	86.4	24.4	177
ε'' ± 5%	90.9	22.6	182
	97.1	15.7	133
= 202 ± 4°C	81.3	20.9	282
(475 ± 4 K)	86.4	18.8	261
ϵ' ± 10-15%	90.9	17.4	256
ε'' ± 5%	97.1	12.2	182

BIBLIOGRAPHY

Barrett, A.H. and V.K. Chung (1962). A method for the determination of high altitude water vapor abundance from ground based microwave observations, *J. Geophys. Res.* **67**, 4259-4266

Battan, L.J. (1959). *Radar Meteorology*. University of Chicgo Press, Chicago, Illinois.

Battan, L.J. (1973). *Radar Observation of the Atmosphere*. University of Chicago Press, Chicago, Illinois.

Bean, B.R. and E.J. Dutton (1966). *Radio Meteorology*. National Bureau of Standards Monograph 92. US Government Printing Office, Washington, DC.

Berman, a. and R. Ramos (1980). Pioneer Venus occultation radio science data generation, *IEEE Trans. Geosci. Rem. Sens.* **GE-18**, 18.

Brand, J.C.D., J.C. James and A. Rutherford (1953). Dielectric dispersion in sulfuric acid, *J. Chem. Soc.* 2447-2456.

Cimino, J.B., C. Elachi, A.J. Kliore, D.J. McCleese and I.R. Patel (1980). Polar cloud structures as derived from the Pioneer Venus orbiter, *J. Geophys. Res.* **85**, 8082-8088.

Colin, L. (1980). The Pioneer Venus program, *J. Geophys. Res.* **85**, 7575-7598.

Counselman, C.C., S.A. Gourevitch, R.W. King, G.B. Loriot and E.S. Ginsberg (1980). Zonal and meridional circulation of the lower atmosphere of Venus as determined by radio interferometry, *J. Geophys. Res.* **85**, 8026-8030.

Debye, (1929). *Polar Molecules*. Dover Publications, Inc.

Dunne, J.A. (1974). Mariner 10 Venus encounter. *Science* **183**, 1289-1291.

Eshleman, V. (1975). Jupiter's atmosphere: problems and potential of radio occultation, *Science* **189**, 876-878.

Eshleman, V.R., D.O. Muhleman, P.D. Nicholson and P.G. Steffes (1980). Comment on absorbing regions in the atmosphere of Venus as measured by radio occultation, *Icarus* **44**, 793-803.

Essen, L. and Froome, K.D. (1951). The refractive indices and dielectric constants of air and its principal constituents at 24000 M_c/S, *Proc. Roy. Soc. B* **64**, 862-875.

Fasullo, O.T. (1965). *Sulfuric Acid: Use and Handling*. McGraw-Hill Book Co., New York and San Francisco.

Fjeldbo, G. and V.R. Eshleman (1968). The atmosphere of Mars analyzed by integral inversion of the Mariner IV occultation data, *Planet. Space Sci.* **16**, 1035-1059.

Fjeldbo, G., A.J. Kliore, V.R. Eshleman (1971). The neutral atmosphere of Venus as studied with the Mariner V radio occultation experiments, *Astronom. J.* **76**, 123-140.

Flowers, R.H., R.J. Gillespie, E.A. Robinson and C. Solomons (1960). Solutions in sulfuric acid. Part XXXII. Molar conductivities of some acids and bases. Proton-transfer conduction by the H_3SO^{4+} and HSO_4^- ions, *J. Chem. Soc.*, Part 4, 4327-4339.

Frohlich, H. (1949). *Theory of Dielectrics*. Clarendon Press, Oxford.

Gmitro, J.I. and T. Vermuelen (1963). Vapor-liquid equilibrium for aqueous sulfuric acid. Filed with American Documentation Institute.

Hall, D.G. and R.H. Cole (1978). Kinetic depolarization in sulfuric acid, *J. Chem. Phys.* **68**, 3942-3943.

Hansen, J.E. and J.W. Hovenier (1974). Interpretation of the polarization of Venus, *J. Atmos. Sci.* **31**, 1137-1160.

Hasted, J.B. (1973). *Aqueous Dielectrics*. Chapman and Hall, London.

Hidy, G.M., W.F. Hall, W.N. Hardy, W.W. Ho, A.C. Jones, A.W. Love, M.J. Van Melle, H.H. Wang and A.E. Wheeler (1972). Development of a satellite microwave radiometer to sense the surface temperature of the world oceans, NASA CR-1960.

Ho, W., I.A. Kaufmann and P. Thaddeus (1966). Laboratory measurements of microwave absorption in models of the atmosphere of Venus, *J. Geophys. Res.* **21**, 5091-5108.

Ho, W. and W.F. Hall (1973). Measurements of the dielectric properties of seawater and NaCl solutions at 2.65 GHz, *J. Geophys. Res.* **27**, 6301-6315.

Hoffman, J.H., R.R. Hodges, T.M. Donahue and M.B. McElroy (1980a). Composition of the Venus lower atmosphere from the Pioneer Venus mass spectrometer, *J. Geophys. Res.* **85**, 7882-7890.

Hoffman, J.H., V.I. Oyama and U. von Zahn (1980b). Measurements of the lower atmosphere composition: A comparison of results, *J. Geophys. Res.* **85**, 7871-7881.

Holton, J.R. (1979). *An Introduction to Dynamic Meteorology*, 2nd edition. Academic Press, San Francisco.

Howard, H.T., G.L. Tyler, G. Fjelbdo, A.J. Kliore, G.S. Levy, D.L. Brunn, R. Dickinson, R.E. Edelson, W.L. Martin, R.B. Postal, B. Seidel, T.T. Sesplaukis, D.C. Shirley, C.T. Stelzried, D.N. Sweetnam, A.I. Zygielbaum, P.B. Esposito, J.D. Anderson, I.I. Shapiro and R.D. Reasenberg (1974). Venus: Mass, gravity field, atmosphere and ionosphere as measured by the Mariner 10 dual-frequency radio system, *Science* **183**, 1297-1301.

Hubbard, W., D. Hunten and A. Kliore (1975). Effect of Jovian oblateness on Pioneer 10/11 radio occultation, *JRL* **2**,265-268.

Janssen, M.A. (1972). The 20-36 GHz Venus microwave emission. Ph.D. Thesis, University of California, Berkeley.

Janssen, M.A. and M.J. Klein (1981). Constraints on the composition of the Venus atmosphere near 1.35 cm wavelength, *Icarus* **46**, 58-69.

Janssen, M.A. and Poynter (1981). The microwave absorption of SO_2 in the Venus atmosphere, *Icarus* **46**, 51-57.

Kliore, A.J. (1972). Current methods of radio occultation data inversion. In *Mathematics of Profile Inversion* (L. Lolin, ed.). NASA TM X-62 150, 3-2, 3-17.

Kliore, A.J. and I.R. Patel (1980). Vertical structure of the atmosphere of Venus from Pioneer Venus Orbiter radio occultations, *J. Geophys. Res.* **85**, 7957-7962.

Kliore, A.J., C. Elachi, I.R. Patel and J.B. Cimino (1977). Microwave absorption characteristics of the clouds of Venus from Mariner 10 radic occultation in "Space

Research XVIII," (M.R. Rycroft, ed.), Pergamon Press, Oxford, in press.

Kliore, A.J., C. Elachi, I.R. Patel and J.B. Cimino (1979). Liquid content of the lower clouds of Venus as determined from Mariner 10 radio occultation, *Icarus* **37**, 51-72.

Kliore, A.J., C. Elachi, and I.R. Patel (1980). Reply to comment on absorbing regions in the atmosphere of Venus as Measured by radio occultation by V.R. Eshleman et al., *Icarus* **44**, 804-806.

Knollenberg, R., L. Travis, M. Tomasko, P. Smith, B. Ragent, L. Esposito, D. McCleese, J. Martonchik and R. Beer (1980). The clouds of Venus: A synthesis report, *J. Geophys. Res.* **85**, 8059-8081.

Knollenberg, R.G. and D.M. Hunten (1980). The microphysics of the clouds of Venus: Results of the Pioneer Venus particle size spectrometer experiment, *J. Geophys. Res.* **65**, 8039-8058.

Kuczkowski, R.L., R.D. Suenram and F.J. Lovas (1981). The microwave spectrum, structure and dipole moment of sulfuric acid, in press.

Kurt, V.G. and V.S. Zhegulev (1979). Preliminary results of research performed on the Venera 11 and 12 spacecraft, *Kosmicheskie Issledovaniya* **17**, 643-645.

Lipa, B. and G.L. Tyler (1979). Statistical and computational uncertainties in atmopsheric profiles from radio occultation: Mariner 10 at Venus, *Icarus* **29**, 192-208.

Marov (private communication) through Jacques Blamont, Centre Nationale, d'Etudes Spatiales, 129 rue de l'Universite', 75007 Paris, tel. 555–91–21, January 31, 1978.

Mie, G. (1908). *Ann. Physik* **25**, 377.

Montgomery, C.G. (1947). Technique of microwave measurements. In *Radiat. Lab. Ser.*, Vol. 7. McGraw Hill, New York.

Morov (private communication) through Jacques Blamont, Centre Nationale, d'Etudes Spatiales, 129 rue de l'Universite', 75007 Paris, tel. 555–91–21, January 31, 1978.

Moroz, V.I., B.E. Moshkin, A.P. Ekonomov, N.F. Sanko, N.A. Parfent'er and Y.M. Golovin (1979a). Spectrometric experiment on board the Ververa-11,12 descenders: Some results of the analysis of the Venus day-side spectrum, (in Russian), Publ 117, Space Res. Inst., USSR Acad. of Sci., Moscow.

Moroz, V.I., N.A. Parfent'ev and N.F. Sanko (1979b). Spectrophotometric experiment on the Verera 11 and Verera 12 descent modules, *Kosmicheskic Issledovaniya* **17**, 727-742.

Muhleman, D.O., G.S. Orton and G. Berge (1978). A model of the Venus atmosphere from radio, radar, and occultation observations.

Nicholson, P.D. and D.O. Muhleman (1978). Independent radio-occultation studies of Venus' atmosphere. *Icarus* **33**, 89-101.

Oyama, V.I., G.C. Carle, F. Woeller, J.B. Pollack, R.T. Reynolds and R.A. Craig (1980). Pioneer Venus gas chromatography of the lower atmosphere of Venus, *J. Geophys. Res.* **85**, 7891-7902.

Pollack, J.B., D.W. Strecker, F.C. Witteborn, E.F. Erickson and B.J. Baldwin (1978). Properties of the clouds of Venus, as inferred from airborn observations of its near infrared reflectivity spectrum, *Icarus* **34**, 28-45.

Ragent, B. and J. Blamont (1980). The structure of the clouds of Venus: Results of the Pioneer Venus nephelometer, *J. Geophys. Res.* **85**, 8089-8106.

Rossow, W.B. and C. Sagan (1975). Microwave boundary conditions in the atmosphere and clouds of Venus, *J. Atmos. Sci.* **32**, 1164-1176.

Seiff, A., B. Kirk, R.E. Young, R.C. Blanchard, J.T. Findlay, G.M. Kelly and S.C. Sommer (1980). Measurements of thermal structuare and thermal contrasts in the atmosphere of Venus and related dynamical observations: Results from the four Pioneer Venus probes, *J. Geophys. Res.* **85**, 7903-7933.

Seinfeld, J.H. (1975). *Air Pollution, Physical and Chemical Fundamentals*. McGraw-Hill Book Co., San Francisco.

Sill, G. (1972). Sulfuric acid in Venus clouds, *Commun. Lunar Planet. Lab.* **9**, 191.

Spiro, C. and H. Lass (private communication) (1973).

Steffes, P.G. and V.R. Eshleman (1981). Laboratory measurements of the microwave opacity of sulfur dioxide under simulated conditions for the middle atmosphere of Venus, *Icarus*, in press.

Stewart, A.I., D.E. Anderson, Jr., L.W. Esposito and C.A. Barth (1979). Ultraviolet spectroscopy of Venus: Initial results from the Pioneer Venus orbiter, *Science* **203**, 777-779.

Stratton, J.A. (1941). *Electromagnetic Theory*. McGraw-Hill Book Co., New York.

Taylor, F.W., R. Beer, M.T. Chahine, D.J. Diner, L.S. Elson, R.D. Haskins, D.J. McCleese, J.V. Martonchik, P.E. Reichley, S.P. Bradley, J. Delderfield, J.T. Schofield, C.B. Farmer, L. Froidevaux, J. Leung, M.T. Coffey and J.C. Gille (1980). Structure and meteorology of the middle atmosphere of Venus: Infrared remote sensory from the Pioneer orbiter, *J. Geophys. Res.* **85**, 7963-8006.

Timmermans, J. (1960). *The Physico-Chemical Constants of Binary Systems in Concentrated Solutions*, vol. 4. Interscience Publishers, Inc., New York.

Van de Hulst, H.C. (1957). *Light Scattering by Small Particles*. John Wiley and Sons, Inc., New York.

Van Beek, L.K.H. (1967). *Progress in Dielectric* **7**, 69.

Von Hippel, A.R. (1954). *Dielectrics and Waves*. John Wiley and Sons, Inc., New York.

Von Hippel, A.R. (ed) (1954). *Dielectric Materials and Applications*. Technology Press of MIT and John Wiley and Sons, Inc., New York.

Woo, R., J.W. Armstrong and A. Ishimaya (1980). Radio occultation measurements of turbulence in the Venus atmosphere determined by radio interferometry, *J. Geophys. Res.* , 8031-8038.

Young, A.T. (1973). Are the clouds of Venus sulfuric acid?, *Icarus* **18**, 564.

CRC Handbook of Chemistry and Physics, 58th edition, R.C. Weast, editor (1977-1978). CRC Press, Inc., Cleveland, Ohio.

JANAF Thermodynamical Tables, 2nd edition, Stull, D.R. and H. Prophet (project directors) (1971). Nat. Stand. Ref. Data Ser., National Bureau of Standards (US).

Sulphur Data Book, The, Tuller, W.M. (ed.) compiled by technical staff *Freeport Sulphur Company* (1954). McGraw-Hill Book Co., Inc., New York.

From a fortune cookie eaten during the last few weeks of finishing this thesis:

Forget the details if they cloud the picture.